Kisoensingh Arvind

Sensitivity analysis on numerical modeling to simulate the flexural shear failure for reinforced concrete beams without stirrups

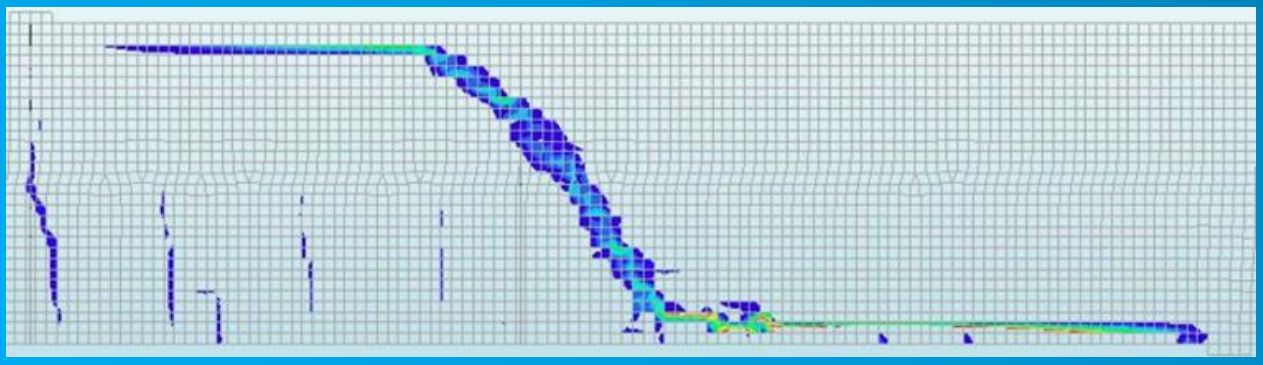

TUDelft

Sensitivity analysis on numerical modeling to simulate the flexural shear failure for reinforced concrete beams without stirrups

By

Kisoensingh Arvind

In partial fulfillment of the requirements for the degree of

Master of Science
in Applied Physics

at the Delft University of Technology
to be defended publicly on Wednesday, May 3rd, 2023, at 15:00

Student number	5145821	
Project duration	February 8th, 2022	May 3rd, 2023
Supervisor:	Ir. N. Kostense	Delft University of Technology
Thesis committee:	Prof. Dr. Ir. J.G. Rots	Delft University of Technology
	Dr. Ir. M. Pari	Delft University of Technology
	Dr. Ir. M. Poliotti	Delft University of Technology

TU Delft

Abstract

Flexural shear failure is a brittle failure mode that can occur in reinforced concrete (RC) beams without stirrups due to the combination of flexural and shear stresses. The failure mode begins with vertical flexural cracks at the bottom of the RC beam central span area due to flexural tensile stresses, followed by diagonal cracks. During stabilization, a diagonal crack enlarges, leading to flexural shear failure. The failure mode is brittle due to the significant bearing capacity reduction making it more difficult to predict.

Accurately predicting the capacity of concrete structures is important for ensuring their safety, especially in the case of brittle failures. Various design codes are available to design and assess such structures, but an advanced numerical method called the Non-Linear Finite Element Analysis (NLFEA) is an alternative to these codes. NLFEA allows for more detailed and accurate modeling of the structure behavior by considering material, geometry, and boundary conditions nonlinearity. By using NLFEA, engineers can optimize their design and gain a deeper understanding of the behavior of RC beams without stirrups. The NLFEA model requires several modeling decisions to accurately simulate the structures' behavior.

Sensitivity analysis on different modeling aspects is crucial to obtain a numerical model that can accurately simulate the RC beam. To be considered accurate, the numerical model should simulate approximately the same damage progression, failure mode, and failure load compared to the experiments. The sensitivity analysis is performed to modeling aspects with uncertainties identified during the literature review. These uncertainties are in the constitutive model, finite element discretization, and analysis procedure modeling aspects. Sensitivity analysis on various modeling aspects is performed using four experimental beams with distinct geometrical sizes, while some material configurations differ. This research investigates whether, using sensitivity analysis, a numerical model can be obtained that accurately simulates flexural shear failure for RC beams without stirrups.

The total strain crack models' crack orientation sensitivity analysis shows that the rotating crack orientation can suffer from over-rotation, which causes delamination of the concrete cover. Over-rotation also shows a strong correlation with many non-converged steps. In addition, the fixed crack orientation simulates a more realistic representation of the experimental failure mode. The compression-compression confinement sensitivity analysis shows that this modeling aspect does not influence simulations for cases with flexural shear failure much and can thus be excluded. A slightly lower failure load is simulated with the confined numerical model for one of the four cases. The sensitivity analysis on the FIB bond-slip relation and Shima bond-slip relation reveals that the former has a lower initial stiffness when using the same material configurations for their modeling assumptions. Due to the lower initial stiffness, there is a higher relative displacement between the concrete and reinforcement. In some cases, this results in either increased convergence problems, a higher possibility of dowel failure, a lower failure load, or a combination of them.

For the fourth sensitivity analysis modeling aspect, the full Newton-Raphson (NR) iteration scheme simulations are slightly more representative of the experiment than the Secant iteration scheme. This result is obtained despite the full NR scheme having more convergence problems during the initial crack. In addition, for a few cases, the Secant iteration scheme simulates symmetrical flexural shear failure due to failing to include material nonlinearity.

Sensitivity analysis of the reinforcement elements shows that simulations with truss elements are more accurate than beam elements. The beam elements models show compatibility issues when combined with plane stress elements. The interface elements fail to correctly tie the beam elements' extra rotational degree of freedom to the transitional degree of freedom. This incompatibility results in convergence problems. Also, higher relative displacements and a higher stiffness after the initial crack is noticed in some cases compared to the experiment. The final sensitivity analysis reveals that the element size sensitivity increases with an increase in the geometrical beam size. Too-large element sizes decrease the accuracy of simulations. In contrast, too-small element sizes increase the computational cost but can also simulate irregular crack patterns not representative of the experiment. A formula is introduced from the sensitivity analysis for beams up to a depth of 1200 mm to predict an appropriate element size.

The sensitivity analysis reveals that the most accurate numerical model is a fixed crack orientation and the Shima bond-slip relation combined with truss elements using the full NR iteration scheme. The sensitivity analysis is followed by a quantitative analysis of 76 experimental cases to verify the accuracy of the obtained numerical model for a broad range of differently configured experimental cases. Analysis shows that dowel failure can get captured due to an excessive change in the damage-based shear retention factor using the obtained numerical model. However, decreasing sensitive load step sizes to very small ones results in flexural shear failure. Also, the quantitative simulations show that the numerical model simulations are largely accurate, with 62 simulated cases below a failure load percentage difference of 10 % compared to the experiment. The average percentage difference is 6 % between the simulations and the experiment.

Analysis shows that this research successfully obtains a numerical model that accurately simulates flexural shear failure for RC beams without stirrups. The information obtained from this research can be used to make modeling choices. In addition, some uncertainties for other modeling aspects are introduced for future research. These modeling aspects are the shear retention model, concrete elements compatibility with the reinforcements beam elements, and the global element size for beams deeper than 1200 mm.

Keywords:
Element size, Flexural shear failure, Modeling aspect, Nominal shear strength, Non-Linear Finite element Analysis, Numerical modeling, Quantitative analysis, Reinforced concrete beams without stirrups, Sensitivity analysis, Size effect

Preface

With this thesis report, I conclude my Master of Science program in Structural Engineering with a specialization in Structural Mechanics at Technische Universiteit Delft. I am pleased to present my thesis, "Sensitivity analysis on numerical modeling to simulate the flexural shear failure for reinforced concrete without stirrups." This research investigates whether, using sensitivity analysis, a numerical model can be obtained that accurately simulates flexural shear failure for RC beams without stirrups. In addition, pilot research will be done for initial expressions on capturing the size effect numerically.

I have been privileged to learn from esteemed professors and researchers during my academic journey. Their teachings have helped me gain immense knowledge and inspired my research efforts. I am incredibly grateful to Prof. Dr. Ir. J.G. Rots for taking the time to discuss thesis subjects and help formulate the thesis topic. My main supervisor Ir. N. Kostense supervised me throughout the research process. I would also like to thank my other supervisor, Dr. Ir. M. Pari, for his invaluable help with the finite element analysis in DIANA FEA and for always being available to answer my questions. Additionally, I am thankful to my third supervisor, Dr. Ir. M. Poliotti, for sharing his immense knowledge of the size effect. This knowledge was instrumental in the research approach and method for the pilot research. During this research, the most challenging part was structurally communicating my findings in the report, with which the entire thesis committee helped me immensely.

I want to thank my parents, brother, and sister for their unwavering support during stressful times, love, and memorable moments during my academic journey. Relatives and friends have also always supported me, for which I am incredibly grateful. Finally, I would like to thank the faculty staff of the department of Structural Engineering, especially Iris Nederhof-van Woggelum, for their friendly conversations and constant help throughout the thesis process.

I hope that the findings presented in this thesis will be of value to future researchers in structural mechanics. This research highlights the difficulties with numerical modeling choices in DIANA FEA, and the findings could benefit future researchers. Additionally, the research on this topic can be furthered with the initial expression of the size effect using the numerical method during the pilot research.

Kisoensingh Arvind
Delft, May 2023

Contents

List of Figures

List of tables

List of equations

Notations

L	(Effective) length
a	(Effective) span
V_{ai}	Aggregate interlock shear force
k_{dg}	Aggregate size factor
α_E	Aggregate type-dependent scaling factor
N_{ed}	Axial force (from loading)
$\emptyset$	Bar diameter
M	Bending moment
β	Brittleness numbers (Gustafsson, Hillerborg, and Carpinteri)
S_{xx}, S_{xy}	Cauchy stresses
σ_{pu}	Cement matrix compressive strength
$f_{p0.1k}$	Characteristic 0.1% proof stress
f_{ck}	Characteristic concrete compressive strength
f_{pk}	Characteristic tensile strength
μ	Coefficient of friction
G_{Ck}, G_c	Compressive fracture energy
Ac	Concrete area
V_c	Concrete compression zone shear force
$f_{c,c}$	Concrete compressive cube strength
f_c	Concrete compressive strength
A_x, A_y	Contact areas
w	Crack opening
δ	Crack sliding
E_{cw}	Crack width
w_b	Crack width at the bottom of a crack
G_{Cr}	Decayed shear stiffness
H	Depth
$V_{rd,c}$	Design shear resistance (member without stirrups)
c_{clear}	Distance between reinforcement ribs
Δe	Distance neutral axis and center of the internal lever arm
c	Distance point loads (four-point experiment)
d	Effective depth
ε_x	Effective shear depth longitudinal strain (mid-depth)
a/d	Effective span-to-depth ratio
h	Equivalent length, crack bandwidth
V_{EC2}	Eurocode 2 shear force
α	Failure mode index
$V_{MC\ 2010}$	FIB Model Code 2010 shear force
G_F	Fracture energy
G_{Fk}	Fracture energy
s_{cr}	Height of a fully developed crack
S_0	Initial/linear slip (section 0)
S	In-plane principal strain

β_{σ}^{min}	Lateral cracking minimum reduction factor compressive strength
z_c	Lever arm
A_{sl}	Longitudinal reinforcement area
ρ	Longitudinal steel ratio
$\alpha_{cc}k_t$	Long-term effect coefficient × concrete determination reduction factor
β_{min}	Lower bound reduction factor
$f_{ctk;0.05}$	Lower-bound characteristic tensile strength
E_1	Maximal principal strain
d_g	Maximum aggregate size
da	Maximum aggregate size
h_{max}	Maximum equivalent length
τ_{max}	Maximum shear stress
f_{cm}	Mean compressive strength
σ_{cp}	Mean compressive stress (from axial force)
f_{ctm}	Mean tensile strength
$G_{\mathrm{f}}^{\mathrm{I}}$	Mode-I fracture energy
Kn	Normal stiffness
σ	Normal stress
$V_{numerical}$	Numerical shear force
ε_{nn}^{peak}	Peak elastic strain
v	Poisson ratio
v^*	Reduced Poisson's ratio
E^*	Reduced stiffness
D	Reinforcement diameter
Δu_t	Relative displacement (slip)
S_1,S_2,S_3	Relative slip sections 1, 2, and 3
V_{cr}	Residual tensile stresses shear force
V_s	Shear force (shear direction)
V	Shear force at the support
β	Shear retention Factor/ reduction factor FIB Model Code 2010
η_a	Shear span to effective depth
Ks	Shear stiffness
V_u	Shear strength
τ	Shear stress
t_t	Shear traction
ls	Side length
k	Size effect factor
b_w	Smallest width cross-section
fyk	Steel characteristic yield strength
γ_s	Steel safety coefficient
ε_{nn}^{cr}	Strain at the crack
α_c	Strain at the peak compressive strain
k_v	Strain effect and member size factor
σ_{nn}^{cr}	Stress at the crack
f_t	Tensile strength
b_n	The clear width of the beam

σ_N	The nominal strength of the specimen
V_d	The shear force from the dowel action
α_u	The ultimate strain
t, b_w	Thickness/ width
STS_x	Total interface shear traction
d_0	Transitional size
τ_f	Ultimate shear stress
$\varepsilon_{nn.ult}^{cr}$	Ultimate strain at the crack
z	Uncracked compression zone height/ internal lever arm
Δ	Vertical displacement
E_{cm}	Young's modulus after 28 days

Abbreviations

BC	Boundary condition
BFGS	Broyden-Fletcher-Goldfarb-Shanno
DPC	Demerit Point Classification
EC2	Eurocode 2
FCFTN	Confined compression-compression behavior fixed crack orientation and the FIB bond-slip relation with truss elements using the full Newton-Raphson iteration scheme
FEA	Finite Element Analysis
FEM	Finite Element Method
FUFBN	Unconfined compression-compression behavior fixed crack orientation and the FIB bond-slip relation with beam elements using the full Newton-Raphson iteration scheme
FUFTN	Unconfined compression-compression behavior fixed crack orientation and the FIB bond-slip relation with truss elements using the full Newton-Raphson iteration scheme
FUSBN	Unconfined compression-compression behavior fixed crack orientation and the Shima bond-slip relation with beam elements using the full Newton-Raphson iteration scheme
FUSsTN	Unconfined compression-compression behavior fixed crack orientation and the Shima bond-slip-strain relation with truss elements using the full Newton-Raphson iteration scheme
FUSTN	Unconfined (compression-compression) fixed crack orientation and the Shima bond-slip relation with truss elements using the full Newton-Raphson iteration scheme
FUSTS	Unconfined compression-compression behavior fixed crack orientation and the Shima bond-slip relation with truss elements using the Secant iteration scheme
HSC	High-strength concrete
LE	Linear Elastic
LoA	Level of Approximation
LSC	Low-strength concrete
LVDT	Linear Variable Differential Transformer, a sensor used to measure deformations and deflections in a single direction
MC 2010	Model code 2010
MNR	Modified Newton-Raphson
MSEL	Modified Size Effect Law
NLFEA	Non-Linear Finite Element Analysis
NR	Newton-Raphson
NSC	Normal-strength concrete
QNR	Quasi-Newton-Raphson
RBK	Richtlijnen Beoordeling Kunstwerken
RC	Reinforced concrete
RCFTN	Confined rotating crack orientation and the FIB bond-slip relation with truss elements using the full Newton-Raphson iteration scheme
RTD	Rijkswaterstaat Technical Document
RUFTN	Unconfined rotating crack orientation and the FIB bond-slip relation with truss elements using the full Newton-Raphson iteration scheme
RUSsTN	Unconfined rotating crack orientation and the Shima bond-slip-strain relation with truss elements using the full Newton-Raphson iteration scheme
RUSTN	Unconfined rotating crack orientation and the Shima bond-slip relation with truss elements using the full Newton-Raphson iteration scheme
SD	Standard deviation

SEL	(Bažant) Size Effect Law
ULS	Ultimate Limit State

1 Introduction

1.1 Background

Flexural shear failure is a brittle failure mode commonly observed in reinforced concrete (RC) beams, caused by the combination of flexural and shear stresses. The brittle nature of the flexural shear failure mode makes it more difficult to predict and requires great care. Accurately predicting the capacity of concrete structures is crucial for ensuring their safety, and designing such structures can be done using various design codes. The different design codes use analytical, empirical, or mechanical models. However, an advanced numerical method called the Non-Linear Finite Element Analysis (NLFEA) can be used as an alternative to these design codes. The RC beams without stirrups failing from flexural shear failure exhibit non-linear behaviors, which can be modeled using NLFEA. NLFEA allows for more detailed and accurate modeling of the behavior of RC beams without stirrups, considering material, geometry, and boundary conditions nonlinearity [1]. NLFEA is especially useful for large structures, structures consisting of complex boundary conditions, or structures where a brittle failure mode is expected. By using NLFEA, engineers can gain a deeper understanding of the behavior of RC beams without stirrups and optimize their design for improved performance and safety.

The NLFEA model relies on logical, numerical modeling decisions to accurately simulate the structures' behavior. These modeling choices affect the various shear transfer mechanisms contributing to the shear capacity of RC beams without stirrups. The mechanisms are aggregate interlock, residual tensile stresses, concrete compression zone, and dowel action. To make informed modeling choices, a theoretical analysis is necessary to gain a deeper understanding of these mechanisms and the modeling choices they influence. The modeling choices can significantly impact simulation results, potentially leading to either underestimating or overestimating the structural capacity. The best way to validate the modeling assumptions and uncertainties is by performing sensitivity analysis on the numerical model and validating the simulations with a wide range of differently configured cases. These uncertainties are in the constitutive model, finite element discretization, and analysis procedure. A reference numerical model found from past research and guidelines [2] must be introduced first, after which modeling aspects can be analyzed. Sensitivity analysis on numerical models is crucial to improve the accuracy and successfully simulate different RC beams without stirrups failing from the flexural shear failure cases.

The study numerically simulates RC beams without stirrups failing from flexural shear failure for cases with different geometrical and material configurations. Investigating and comparing different configurations is essential to verify the numerical model's accuracy and limitations. As a boundary for the experiment selection, only experiments that fail due to the flexural shear failure mode are implemented using NLFEA for this report. The shear capacity predicted by design equations proposed in some codes of practice is also compared to the numerical model simulations. Two codes that will be used are the Eurocode 2 (EC2) [3] and FIB Model Code 2010 (FIB MC 2010) [4].

This study aims to obtain a numerical model using sensitivity analysis to simulate flexural shear failure for differently configured RC beams without stirrups. The failure mode, correct damage progression, and failure load are used to judge the reliability of this model for a wide range of differently configured beams and should also be applicable for future research. In addition, as pilot research, this report will also address initial expression on capturing the size effect for the RC beams without stirrups using NLFEA. The size effect is a phenomenon that describes the decrease in nominal shear strength as the structure size increases [5] [6]. When analyzing geometrically large beams, the size effect is essential, as it can be severe for such structures. Various theories have been proposed to account for the size effect, with no widely accepted consensus. With all the capabilities of the NLFEA, it is hoped that this advanced numerical method can capture this effect.

1.2 Research question

This research investigates whether, using sensitivity analysis, a numerical model can be obtained that accurately simulates flexural shear failure for RC beams without stirrups. Thus, the main research question for this thesis is:
Can a numerical model be obtained using sensitivity analysis to simulate the flexural shear failure for RC beams without stirrups?

Four sub-questions must be answered to get a conclusion on the main research question and pilot research. These sub-questions also help logically construct the report. The sub-questions include a brief description for each of them and are given below:

Sub-question 1: What is the flexural shear failure for RC beams without stirrups, and how are experimental cases selected to study this failure mode on the beam with numerical simulations?

Flexural shear failure is a brittle failure mode for RC beams without stirrups and is caused by a combination of flexural and shear stresses. Different requirements should be met before experimental cases are selected for numerical analysis. The following three requirements are important:

- Firstly, the effective span-to-depth ratio for selected RC beams without stirrups cases should be within a boundary. This boundary is because the flexural shear failure mode, which is the focus failure mode in this research, heavily depends on the effective span-to-depth ratio.
- Secondly, the selected experimental cases should comprise beams with various geometrical and material configurations. This requirement will allow a statement based on the quantitive simulations with different configurations after sensitivity analysis of the numerical model.
- Thirdly, a set of selected experimental cases should be geometrically scaled beams. These beams will be used during the pilot research to determine if the numerical method can capture the size effect.

Sub-question 2: Does model uncertainty during the numerical model sensitivity analysis cause inaccurate results?

In the past, different studies have been done on model uncertainty. These studies hoped to reduce the model uncertainty bias from numerical models. However, getting a robust model for specific cases is still challenging, from only reports and guidelines. Therefore, a reference numerical model will be set up with recommendations from reports and guidelines and then analyzed. Sensitivity analysis is done for the constitutive model, finite element discretization, and analysis procedure. The model uncertainty reason causing inaccuracy should be stated if the numerical model results in inaccurate results for the experimental simulations after sensitivity analysis.

Sub-question 3: How do the numerical model simulations compare to the experimental results?

From previous reports, appropriate cases will be applied to study the accuracy of the obtained numerical model from sensitivity analysis. A comparison with the experimental results using the failure load percentage difference will show the performance of the numerical mode for all cases. Design codes (EC2 and FIB MC 2010) will also be used to compare the numerical model performance.

Sub-question 4: According to the pilot research, can numerical analysis capture the size effect for the RC beams without stirrups that fail due to flexural shear failure?

The size effect is described as a decrease in the nominal shear strength with a geometrical increase in the structure. The nominal shear strength is a parameter dependent on the size effect, as there is no size effect if the nominal shear strength is independent of the structure size. A set of geometrically scaled experimental cases will be used to show initial expressions on if the numerical method can capture the size effect.

1.3 Objectives and deliverables

At the end of this research, whether a numerical model is successfully obtained using sensitivity analysis to simulate the flexural shear failure for RC beams without stirrups is answered. If the model results are inaccurate, the reasoning for this should be given. In addition, pilot research will be done for initial expressions on capturing the size effect numerically. With the initial expression, the research on the size effect can be furthered.

1.4 Research approach

Now that the research question, objective, and deliverables hoped to be obtained are known, a research approach is put together. A step-by-step overview of the research method in the correct order is given below.

Firstly, the literature review is done on some important topics. Understanding the flexural shear failure for RC beams without stirrups and the damage progression during a failure is crucial. The reason for understanding this well is that the numerical model should replicate this behavior during its simulation. Because of the flexural shear failure, the shear capacity is vital, which is contributed by the four shear transfer mechanisms. The four shear transfer mechanisms are the aggregate interlock, residual tensile stresses, concrete compression zone, and dowel action. Also, when modeling the numerical model, including these four shear transfer mechanisms is essential.

After understanding the failure mode and different mechanisms that affect the shear capacity, the size effect is also explained. The size effect must be included in the analysis of RC beams without stirrups that fail in shear, especially for large beams. In addition, because design codes will be used for comparison with the numerical model, understanding their respective theories on the structures' capacity and calculations is important. Finally, in the literature review, the numerical model can be addressed. The advanced numerical method, "Non-Linear Finite Element Analysis"(NLFEA), will simulate the experimental cases. It should be kept in mind that the numerical method depends on logical, numerical modeling assumptions to include certain behaviors. Some structures will also have specific requirements to result in accurate simulations. Numerical modeling consists of the constitutive model, finite element discretization, and analysis procedure. Guidelines and past reports can help significantly in modeling assumptions but also help identify the model uncertainties.

Before the numerical model sensitivity analysis can be done to get a robust numerical model, experimental cases on RC beams without stirrups should be selected for the numerical analysis. The experimental cases will be chosen based on beams with different geometrical configurations, material configurations, and the effective span-to-depth ratio boundary. The reason for selecting cases based on the effective span-to-depth ratio is that only cases with flexural shear failure are chosen, with the failure mode depending on the ratio. A wide range of cases with different configurations is needed for the cases. This approach should produce a numerical model verified with various configurated beams. Also, a series of geometrically scaled beams should be included, as these will be used for the pilot research on size effect analysis. Here the beam geometry is an important parameter in the beam selection, as geometrically small and large beams are required for the size effect analysis.

Following the selection of experimental cases, the next step is to validate the modeling assumptions and reduce model uncertainties. The best way to do this is by qualitatively performing multiple sensitivity analyses of the numerical model with some experimental cases. These initial cases should be differently configured beams. The numerical model sensitivity analysis is done for different modeling aspects from the constitutive model, discretized model, and analysis procedure. This analysis should lead to a robust numerical model that successfully simulates the flexural shear failure for RC beams without stirrups. With the numerical model found, the remaining experimental cases are simulated and compared to see if the results are acceptable from a quantitative analysis. These simulations should also show the limitations of the obtained numerical model. The accuracy is based on the correct damage progression, failure mode, and failure load. In addition, the numerical model cannot be used if performance is unsatisfactory and sensitivity analysis should be performed further.

Finally, the size effect analysis can be performed, and an initial expression is found on whether the size effect can be captured with the numerical approach. The set of geometrically scaled experimental cases is simulated with the numerical model for the size effect analysis. During the size effect analysis, comparisons will be made to the experimental results, Size Effect Laws, and design codes to identify limitations or shortcomings in the performances of the methods mentioned.

Finally, the report can conclude whether a numerical model is found using sensitivity analysis that can successfully simulate the flexural shear failure for RC beams without stirrups. In addition, for the pilot research, the results of the initial expression on whether the size effect can be captured with the numerical method are addressed.

1.5 Thesis outline

This report is structured with five main chapters, which help reach the research goal. The first Chapter introduces the thesis background, research question, objectives, and approach. A brief overview of the other main Chapter is given below:

2 Literature review:
The failure mode, size effect, design codes, and shear transfer mechanisms are explained during the literature review. In addition, the background for the numerical model, assumptions from previous reports, and model uncertainties are addressed. These steps for the numerical model help with a reference numerical model and identify the model uncertainties.

3 Experimental case selection for numerical simulations:
A selection is made for experimental cases using boundaries introduced during the literature review. The boundaries are based on RC beams without stirrups with flexural shear failure having different geometrical and material configurations. Also, the effective span-to-depth ratio boundary should be kept in mind, and a set of experimental cases should be geometrically scaled to study the size effect.

4 Numerical model:
The literature review has helped with a reference numerical model consisting of assumptions and model uncertainties. The uncertainties should be reduced to get a robust numerical model for the size effect analysis. Sensitivity analyses on the numerical model can do this elimination of uncertainties until a robust model is obtained with the initial cases. After that, the other experimental cases were simulated for a quantitive analysis of the obtained numerical model to check its accuracy and limitations. Lastly, this Chapter will use the geometrically scaled experimental cases for the size effect analysis. During this analysis, the behavior of the nominal shear strength is of great importance.

5 Conclusion and recommendations:
The final Chapter summarizes all findings during the study to answer all sub-research questions. At last, the main research question can be answered with a conclusion, and recommendations for future work will follow this.

2 Literature review

This chapter performs a literature review, giving background information and explaining essential topics for this report. The chapters' content is specified in the order they will be presented, along with the motivation for the subjects:

- **Physical structure**
  This study focuses only on RC beams without stirrups where flexural shear failure occurs. There are more possible failure modes for the beams, but only experiments that fail due to flexural shear failure are selected for analysis. This type of failure and its behavior will be explained before, during, and after the failure occurs. Next, all four shear transfer mechanisms will be discussed to understand the theoretical background and their contribution to the shear capacity. The four shear transfer mechanisms are the aggregate interlock, residual tensile stresses, concrete compression zone, and dowel action. This knowledge will help include the mechanisms in the numerical model. Besides this, this Chapter will also explain the size effect, which increases with the beam size.
- **Numerical model**
  The numerical model is an essential aspect of the literature review. This topic will consist of three sections: constitutive model, finite element discretization, and analysis procedure. For each section, modeling aspects will also be identified that require sensitivity analysis.
- **Design codes**
  This section will discuss the design codes, EC2 and FIB MC 2010. These codes will be compared with the numerical model in Chapter 4.

2.1 Physical structure

2.1.1 Reinforced concrete beams subjected to flexural shear failure

The introduction briefly explained the flexural shear failure, but this Chapter will describe it more in-depth. For RC beams without stirrups, different failure modes can be found. Experiments show that the parameter effective span-to-depth ratio is critical for the failure mode with concentrated loading. According to Nawy [1], the possible failure types depend on the effective span-to-depth ratio, and their relation is given in Table 1. In addition, Slobbe et al. [2] combined experiments from two studies [3] [4] in their research to get the relation between the effective span-to-depth ratio and the failure mode, which is given in Table 1.

Table 1 Effective span-to-depth ratio and failure modes relation: Nawy (left) [1] and Slobbe et al. (right) [2]

Failure	***a/d (According to Nawy)***	***a/d (According to Slobbe et al.)***
Flexure failure	Exceeds 5.5	≥ 7.0
Flexural shear failure	Between 2.5 and 5.5	Between 3.0-7.0
Shear compression failure	Between 1 and 2.5	< 2.5

The flexural shear failure begins with vertical flexural cracks, also called main cracks, at the bottom of the RC beam central span area due to flexure tensile stresses. The main cracks also cause the rotation of the principal stresses. Following the cracks, the bond between the longitudinal reinforcement and surrounding concrete gets destroyed at the support. Next, brittlely, a couple of diagonal cracks develop at approximately 1.5*d* to 2*d* away from the surface of the beam's support. During stabilization, one of the diagonal cracks enlarges. This tensile crack is towards the top compression fibers of the beam where the point load is active. As a result of further propagation of the diagonal tensile crack, the flexural shear failure mode is caused. The diagonal tensile crack is caused due to the development of secondary cracks. According to Yang et al. [5], the critical diagonal crack starts from the last flexural crack. As a result of unstable secondary cracks, there is a fast drop in bearing capacity and increased deflection as the flexural shear crack opens.

In short, the flexural shear failure mode results from the combination of the flexural and shear stresses. This failure mode is brittle due to the significant bearing capacity reduction. Figure 1 shows the flexural shear failure crack pattern for an experiment. The right side shows the crack pattern around the reinforcement in the same figure.

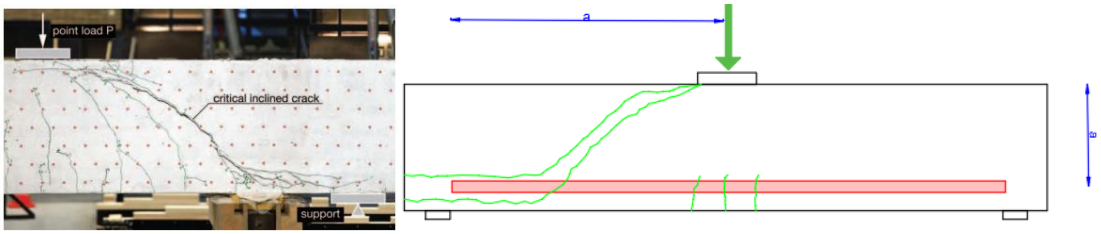

Figure 1 Flexural shear failure crack pattern: experimental [6] (left) along the longitudinal reinforcement visualized [1] (right)

During the simulation of the numerical cases, the failure mode behavior described above should be captured to get flexural shear failure. Luo et al. [7] studied the crack pattern of different beam depths. During the numerical analysis, the expected crack patterns are essential for this report to know what crack pattern output to expect from the simulations. The different crack patterns for the varying beam depths are given in Figure 2:

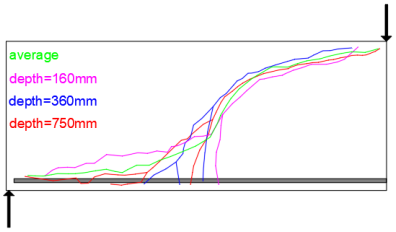

Figure 2 Crack pattern for varying beam depths [7]

2.1.2 Shear transfer mechanisms

The early shear strength predicting models used to be based on geometrical theories. There are two geometrical model types: arch action and beam action. The type of model depends on the effective span-to-depth ratio. Kim et al. [8] state that beams with an effective span-to-depth ratio smaller than 2.5 are determined by the arch action and are called large beams. Beams with a ratio larger than 2.5 are dominated by the beam action and are called slender beams. An overview of these two model types is shown in Figure 3:

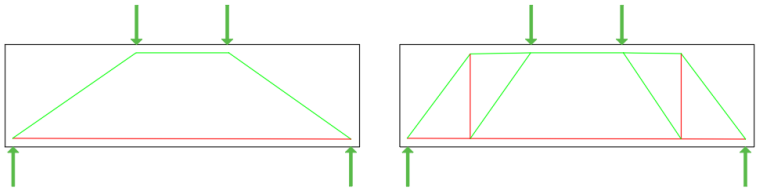

Figure 3 Arch action (left) and beam action (right) [9]

A downside of the geometrical theories is the absence of all shear transfer mechanisms. The mechanisms govern the shear failure for slender beams. This chapter's section will explain the four types of shear transfer mechanisms. According to Košćak et al. [10], the critical shear crack shape is correlated with the crack opening and sliding behavior. The shear sliding behavior is typical for reinforced concrete at the ultimate limit state (ULS). These behaviors, in turn, depend on the shear transfer mechanisms.

An overview of the four shear transfer mechanisms and the location they are active are given in Figure 4.

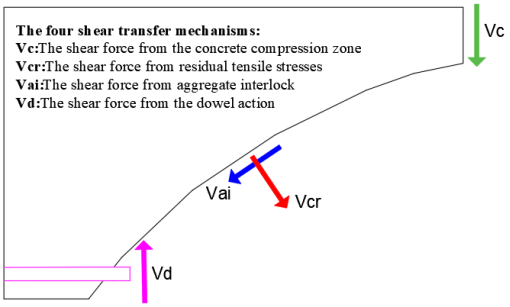

Figure 4 Four shear transfer mechanisms [11]

Garnica [12] states that some shear transfer mechanism grows in importance during the crack propagation while others lose their significance. It should be said that these average results can be vastly different depending on the case configuration in question. As will be seen further in this section, the shear transfer mechanisms depend on many factors. Košćak et al. [10] found the average contributions of these four mechanisms for RC beams without transverse reinforcement and are given in Table 2:

Table 2 Shear transfer mechanisms contribution [10]

Shear transfer mechanism	Average contribution
Aggregate interlock	62.7 %
Residual tensile stresses	23.2 %
Concrete compression zone	13.8 %
Dowel action	6.5 %

2.1.2.1 Aggregate interlock

The aggregate interlock mechanism can occur if the aggregate size is larger than the crack width, as shear forces can be transferred [2]. Walraven [13] described aggregate interlocking as an effect that allows for the development of shear and compressive stresses caused by the tangential and normal direction displacements between two cracked surfaces. The stresses are developed due to the "interlock" of two opposite faces as the bulging aggregates cause this interlock. According to Huber et al. [14], the potential shear transfer between two opposing crack surfaces depends on the crack kinematics/pattern and the roughness of the crack surface. Important parameters for this mechanism are the concrete's fracture mode, compressive strength, aggregate size, and crack width.

Several models for this mechanism have been developed over the years, but the Walraven model has a physical basis. This model relates the crack sliding (δ) and crack opening (w) to the shear stress (τ) and compressive stress (σ). The mentioned stresses are visible in Figure 5 and calculated with the formula in Equation [I] [15]:

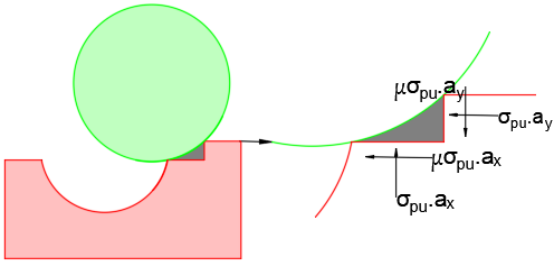

Figure 5 Aggregate interlock mechanism [16]

$$\begin{pmatrix}\sigma\\ \tau\end{pmatrix} = \sigma pu * \begin{pmatrix}Ax + \mu\ Ax\\ Ay - \mu\ Ay\end{pmatrix},$$

Equation [I]

With:

$$\sigma pu = 6.39\ fc^{0.56}$$

The effect of aggregate interlock can be studied with experiments such as roughness, push-off, and shear tests. Beams with shear cracks close to the point load show higher shear strength and more significant contribution from aggregate lock than beams with only cracks at the center of the shear span. Jayasinghe et al. [11] say the best way to safeguard the aggregate interlock mechanism is by using stirrups. However, in this thesis, beams with stirrups will be neglected.

2.1.2.2 Residual tensile stresses

According to Hordijk [17], the residual tensile strength of concrete consists of its ability to transfer tensile stresses after the concrete has cracked. These tensile stresses are created near the tip of the concrete and soften as the crack opening increases. A popular model to express the tension-softening behavior of concrete is Hordijk's exponential stress-crack width model, visible in Figure 6.

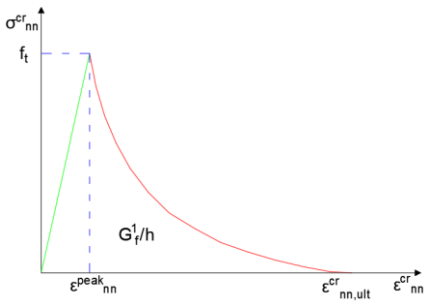

Figure 6 Hordijk softening curve stress-strain relation [17]

The smaller the crack width, the more significant the residual tensile stress contribution. After crack widths of 0.1 mm, the aggregate interlocking mechanism dominates the residual tensile stress. According to Yang [6], the total interlocking effect on the shear resistance is ten times greater than that of the tension-softening force after 0.1 mm, making the residual tensile stress effect negligible. Further information about Hordijk's exponential stress-crack width model will be explained during the literature review of the numerical model.

2.1.2.3 Concrete compression zone

The stress distribution in uncracked reinforced concrete is based on elasticity theory. The shear stress in the compression zone of uncracked concrete can be calculated if the boundary conditions are known. Axial compression increases the shear resistance, while axial tension decreases the shear resistance. According to Slobbe et al. [2], if there is no axial compression, the contribution of the concrete compression zone to the shear capacity is small. If the beam depth does not show large deviations along the length, it can be assumed that the flexural cracks form a tooth structure. The tooth structure is shown in Figure 7.

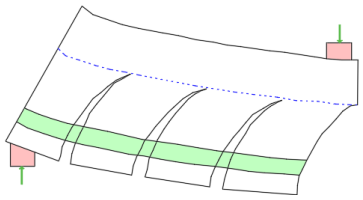

Figure 7 Concrete tooth model [18]

The beams analyzed in this study have a continuous depth along the length of the beam, making it possible to use the model based on Mörsch's formula [19]. This model accurately predicts the shear force in the uncracked concrete zone (Vc). Mörsch predicts the maximum shear stress to be reached at the neutral axis. A parabolic stress distribution is expected above the neutral axis. Constant stress from the neutral axis to the level of flexural reinforcement is expected below the neutral axis.

The classical beam theory can describe the concrete's compression zone stress distribution during the stabilized cracking phase. It is assumed that the entire uncracked contributes to the uncracked compressive zone. The shear contribution from the uncracked compression zone for slender beams becomes small. This small contribution is because of the small depth of the compression zone.

2.1.2.4 Dowel action

The final shear transfer mechanism is the dowel action. The dowel action refers to the capacity of the flexural reinforcement to transfer shear forces across the crack. According to Vintzēleou [20], this action resists the opening and sliding of the crack. In the case of RC beams, the flexural reinforcements are the longitudinal reinforcements, which must follow a transverse displacement to activate the dowel action. The longitudinal reinforcement transverse displacement happens when the beam deflects due to axial loading causing the concrete's displacement around the bar. Therefore, the more significant the longitudinal reinforcement amount, the larger the dowel action contribution, which is also said by Slobbe et al. [2]. According to Paulay et al. [21], three mechanisms can cause dowel action: bending, shearing, and kinking. Dowel failure is decided by concrete splitting, where the effective area of the concrete under tension is essential. Vintzēleou et al. [22] say concrete splitting is more common in RC beams if the concrete cover is less than 6-7 times the bar diameter. For thin concrete covers, the splitting cracks may be present either at the faces of the section or the bottom.

The analytical approach used for the dowel action is based on the beam on an elastic foundation analogy [22]. Steel bars and the concrete below them are considered a beam elastically supported by the concrete above them.

2.1.3 Size effect

According to Bažant et al. [23] [24], the size effect should be accounted for flexural shear failure for RC beams without stirrups. The size effect is described as the phenomenon due to which the nominal shear strength (σ_N) decreases as the beam size increases [25] [24]. According to Bažant et al. [26], the nominal shear strength is calculated with the formula in *Equation [II]*:

$$\sigma_N = \frac{V}{bd}$$

Equation [II]

One of the main influencing factors of the size effect is the release of stored energy during crack propagation. The release of stored energy correlates with the fracture zone length and area size. Yang et al. [27] found that an increased beam depth or decrease in the effective span-to-depth ratio has a higher energy release rate. Due to the higher energy release rate, crack width increases, a more brittle failure occurs, and the nominal shear strength decreases. With the increase of the beam depth, there is less contribution from the aggregate interlock to the shear capacity due to the increasing crack width. The relation of the size effect to the increasing beam depth was already well known. However, the dependence on the effective span-to-depth ratio is also confirmed by Zararis et al. [28].

The release of stored energy is not the only source that affects the size effect but the most dominant one for quasi-brittle materials. Bažant et al. [29] also identified that another significant source of the size effect is the statistical size effect caused by differences in the material strength. Ghannoum [30] found that the size effect can be seen in both normal-strength (NSC) and high-strength concrete (HSC). However, this study also found that the strength of concrete shows almost equal shear stresses at failure for the same reinforcement ratios. In contrast to Ghanoum's finding, El-Sayed et al. [31] found a higher size effect for HSC due to a higher brittleness. HSC is well known to be more brittle than LSC. Bentz et al. [32] also support this finding and state that the size effect increases with increased concrete strength. The higher the concrete strength, the more vulnerable the structure is to aggregate fracture, decreasing the aggregate interlock [33]. An analysis of concrete strength is vital due to its impact on the brittleness of the beam.

According to An et al. [34], the bond effect of steel and concrete is a critical source that controls the shear behavior and size effect. A stronger bond helps the steel yield before the crack reaches the critical depth. For flexural shear failure, the steel will not be expected to yield. Supporting this finding, Carmona et al. [35] found that the reinforcement and bond effect of steel and concrete can affect the size effect. The effect of the bond on the size effect can be studied by varying the reinforcement ratio and concrete strengths. An increase in longitudinal steel reinforcement can increase the shear stresses by controlling the crack width. A low longitudinal reinforcement ratio reduces the shear capacity because an increase in the crack width results in lower aggregate interlock stress transfer along the crack.

In addition, a lower reinforcement ratio also decreases the dowel action. The beam size relation to the longitudinal reinforcement is also significant. For deeper RC beams, the longitudinal reinforcement ratio's effectiveness decreases.

Next, the fracture mechanics-based Bažant SEL will be addressed below. This law uses the analytical method to describe nominal shear strength changes between geometrically scaled beams for the size effect analysis. In addition, a brief history of Bažant SEL and its research development over the years is given. According to Bažant, the size effect should be accounted for with the ultimate failure calculation instead of calculations for diagonal shear cracks. The ultimate failure calculation should be accounted for because the latter does not provide a sufficient safety margin against the safety load. Bažant proposed the SEL, which had modifications over the years from new findings.
Initially, in 1984, Bažant presented the following SEL [23]:

$$vu = \frac{10\ \sqrt[3]{\rho}}{\sqrt{1+\frac{d}{25\ da}}}\left(\sqrt{fc'}+3000\sqrt{\frac{\rho}{\alpha^5}}\right)$$

Equation [III]

With:
$\alpha = \frac{Vu\ d}{Mu}$ *(For concentrated loads:* $\alpha = \frac{a}{d}$*)*

In 1996 this law was modified by Kim et al. [36] and was called the modified Bažant SEL. The modified law agreed better with experimental data than any other law during that time. The modified Bažant SEL is given below:

$$vu = 3.5\ fc'^{\alpha/3}\rho^{3/8}\ \left(0.4+\frac{d}{a}\right)\left(\frac{1}{\sqrt{1+0.008d}}+0.18\right)$$

Equation [IV]

With:
$\alpha = 1\ for\quad \frac{a}{d} \geq 3$
$\alpha = 2-\frac{a/d}{3}\ for\quad \frac{a}{d} < 3$

Bažant et al. [26] state that the size effect of concrete could not be different from that of other quasi-brittle materials. The assumptions are that the failure load is controlled by the fracture energy Gf and the cohesive fracture parameters. In addition, another explanation of the size effect is the profile of the compressive stresses. The inclined compressive stress transfers a large part of the shear force at maximum load from the zone above the flexural crack. In large beams, the profile of the compressive stresses is very confined but uniform for slender beams. Bažant proposed the following design code, which was obtained with least-square regression:

$$vu = \mu\ \rho^{\frac{3}{8}}\left(1+\ \frac{d}{a}\right)\sqrt{\frac{fc'}{1+\frac{d}{d0}}}$$

Equation [V]

With:
$d0 = \kappa\ fc'^{-2/3}$
$\kappa = 3.800\sqrt{da},\qquad if\ da\ is\ not\ known:\ \kappa = 3.330$
$\mu = 13.3\ \ for\ the\ best\ fit$
$\mu = 10\ \ for\ the\ best\ design$

In 2009, Bažant et al. [37] introduced the Universal size effect, where two types of size effect laws are identified. The purpose of this law was to get a smooth description of the complex transition between the Weibull statistical size effect [38] and the energetic deterministic size effect. The occurrence for each law is given below:

- Type I SEL: occurs when the crack is initiated on a smooth surface of the beam. The structures do not have a not or pre-existing crack.
- Type II SEL: takes place from a deep notch or crack in the beam.
- Universal SEL: This law must ensure a smooth transition from type I to type II for quasi-brittle materials failure. The asymptotic size effect law occurs and captures the Weibull statistical size effect.

The nominal strength for the type I size effect is sensitive to material randomness, and the Weibull statistical size effect is considered. This material randomness can be ignored for the type II size effect. SEL type II considers the release of stored energy during failure as the cause of the size effect for quasi-brittle materials, not the statistical size effect. In *Figure 8*, the size effect is expressed by the transitional behavior between the strength criterion and the LEFM. The figure on the right is the type I size effect, while the figure on the left is the type II size effect.

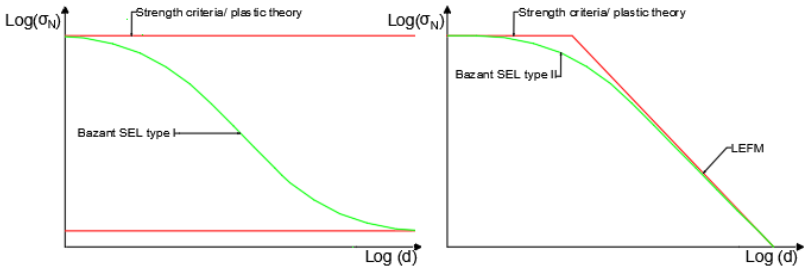

Figure 8 Bažant Size effect Law: type I (left) and type II (right) [37]

According to the Bažant SEL type II, the figure exists of 3 sections which are:

- The strength criteria from the strength theory.
- The nonlinear fracture mechanics section has an asymptotic slope between -1 and -0.5 caused by the influence of the size effect.
- The linear elastic fracture mechanics section with a slope of -0.5 is also recognizable as the steepest slope in the log-log plot.

Bažant et al. [39] researched the failure probability if SEL type II is not considered. The results suggested that the failure probability was 10^{-6} for small beams. However, this probability increased to an unsafe value of 10^{-3} for large beams. SEL type II considers the release of stored energy during failure as the cause of the size effect. The Bažant type II SEL is expressed by Equation [VI].

$$\sigma_N = \frac{B\, f_t'}{\sqrt{1 + \frac{d}{Do}}},$$

Equation [VI]

$With$:
$\sigma_N = \frac{P}{b\, d}: the\ nominal\ stress\ [MPa]$
$d: effective\ depth\ [mm]$
$ft: tensile\ strength\ [MPa]$
$B, Do: dimensional\ parameters$

During the calculation of the shear capacity using the design code EC2, the size effect factor has also been included. The formula for the shear capacity will be given in Chapter 2.3, but below the size effect factor k is given:

$$k = 1 + \sqrt{\frac{200}{d}}$$

Equation [VII]

k is called the size effect factor, which considers the size effect by decreasing the shear resistance for an increased effective depth. This factor is formulated from experimental research data. The influence of the size effect factor with increasing beam depth can be seen in *Figure 9*.

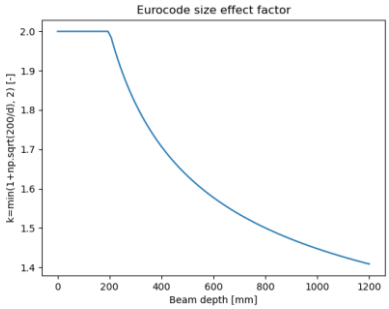

Figure 9 Eurocode 2 size effect factor influence [40]

Yang [6] argues that the size effect depends on different mechanisms, each having different contributions. Expressing the size effect with geometrical scaling relationships is not feasible. Yang et al. formed a new theory for RC beams without stirrups to calculate the shear capacity. This theory will not be used during the comparisons but does help understand the shear transfer mechanisms and shear capacity formulas mentioned previously better. A summarization of this theory is given in Annex I.

2.2 Numerical model

Chapter 2.2 of this section is a literature review on the numerical model but also consists of numerical modeling decisions that need to be made for the numerical model. Combined with the numerical model sensitivity analysis in Chapter 4.2, these decisions should lead to a robust numerical model that can be applied to all cases. The initial solution strategy decisions will be based on information from previous reports and personal experience with DIANA FEA, as the scope of this topic is broad. Reports from past years which will mainly be used as the normative guideline for the choices are from Hendriks et al. [41], Belleti et al. [42], Putter [43] [44], Lang [45], Yang et al. [5], and Garnica et al. [46]. Finally, the most accurate robust model will be chosen, while some limitations will be addressed.

According to Putter et al. [44], if the solution strategies are not considered to depend on the type of FEA software, differences in solutions may still be present in the FEA software. Therefore, solution strategy choices will be made to get the best robust model to simulate the flexural shear failure for RC beams without stirrups in the software DIANA FEA. In addition, Putter also states that any slight change in the constitutive model, discretized model, and analysis choices can cause a shift in model accuracy for a brittle model. It should be noted that beams without stirrups are more sensitive to solution strategy choices. This sensitivity makes it difficult to get a robust model based on only literature for a specific case.

Before the constitutive models are explained for the materials concrete and reinforcement in the following section, it is crucial to know how the material properties are chosen for the numerical models. These are calculated with the help of EC2 [40], FIB MC 2010 [47], and Richtlijnen Beoordeling Kunstwerken (RBK) [48]. A summary of the concrete and reinforcement material properties is given in Table 3 and Table 4, respectively. In addition to the tables, in DIANA FEA for concrete, the isotropic linear elastic model should be based on Young's Modulus *E* with $E > 0$ and Poisson's ratio v with $0 \leq v \leq 0.5$. Hendriks et al. [41] found that concrete's initial Young's Modulus should be reduced by 0.85 due to initial cracks.

Table 3 Material properties of concrete [41]

Concrete	
Mean compressive strength	$f_{cm} = f_{ck} + \Delta f, \quad \Delta f = 8\ MPa$
Compressive strength minimum reduction factor (From lateral cracking)	$\beta_\sigma^{min} = 0.4; \beta \geq \beta_\sigma^{min}$
Lower-bound characteristic tensile strength	$f_{ctk;0.05} = 0.7 f_{ctm}$
Mean tensile strength	$\leq \frac{C50}{60}: f_{ctm} = 0.3 f_{ck}^{\frac{2}{3}}$ $> C50/60: f_{ctm} = 2.12 ln\,(1 + 0.1 f_{cm})$
Fracture energy	$G_{Fk} = 0.7 \times 0.073 f_{cm}^{0.18}$
Compressive fracture energy	$G_{Ck} = 250 \times f_{ck}/f_{cm} \times 0.073 f_{cm}^{0.18}$
Young's modulus after 28 days	$E_{cm} = 22000(0.1 f_{cm})^{0.3}$
(Initial) Poisson ratio	*v = 0.20*
Density plain concrete	*ρ = 2400 kg/m³*
Density reinforced concrete	*ρ = 2500 kg/m³*
Long-term effect coefficient × Concrete determination reduction factor	$\alpha_{cc} k_t = 1.0$

Table 4 Material properties of reinforcement [41]

Reinforcement	
Poisson ratio	*v = 0.3*
Density steel	*ρ = 7850 kg/m³*
Steel safety coefficient	$\gamma_s = 1.1$

2.2.1 Constitutive model

To effectively mimic the behavior of the experimental cases, correct choices for the constitutive model must be employed to capture the material's correct behavior. Therefore, the constitutive model literature review will be done for the concrete and reinforcement in the sections below.

2.2.1.1 Concrete

The constitutive model for concrete will be explained in five sections. The sections will be the following:
- Model types
- Tensile behavior
- Compressive behavior
- Reduction due to interaction
- Equivalent length.

Each of the sections can be found in the order below:

Model types:
The total strain crack model will be used to model the concrete. This model is categorized under the smeared crack model and describes a material's tensile and compressive behavior using a single stress-strain relationship. The stresses in this model are computed depending on the crack directions. The total strain crack model can be used with the following three types of crack models:
- The rotating crack orientation
- The fixed crack orientation
- The rotating to fixed crack orientation, which is a rotating and fixed crack orientation hybrid

The rotating and fixed crack orientations will be investigated and used for the model sensitivity analysis during this study. If correct results are not found with one of these crack models, the rotating to fixed crack orientation will also be used for the sensitivity analysis. However, Løvli [49] has found that this model acts between the rotating and fixed crack orientations. Due to this behavior, when neither the rotating nor fixed crack orientation gives accurate results, nor will the rotating to fixed crack orientation. For the two crack orientation models in focus, earlier studies have shown diverse responses for RC beams without stirrups cases. The different response results (with pros and cons) are shown in Table 5. The crack model behaviors from Table 5 will be given special attention during the model sensitivity analysis. Overlapping advantages and disadvantages will be omitted. Also, remedies will be suggested for some problems introduced in the table.

Table 5 Fixed and rotating crack orientation: pros and cons

	Rotating crack orientation	***Fixed crack orientation***
Advantage	• Not affected by stress-locking	• For beams without stirrup, limited variation is shown in the obtained coefficient of variations [44] • The crack pattern is captured more realistic [5] • Included aggregate interlock (due to the shear retention model)
Disadvantage	• Over-rotation of cracks and struts results in a higher capacity than in reality [44] • Requires visual inspection of the rotated cracks and force-displacement behavior to get the failure moment [43]	• Dependence on the shear retention model (this can cause an overestimation of the failure load) [44] • Unable to solve sufficient change in the principal stress-strain above the reinforcement (causing premature failure) [45] • Accounts for additional [44]

The fixed crack orientation saves the principal tensile strains, compressive strain, and crack orientation as parameters. Once the tensile strength of concrete is reached in an orthogonal coordinate system, the orientation in a fixed crack strain model is captured and evaluated. The crack gets followed by this coordinate system, and because this system is fixed, shear stresses can also occur. This model analyzes normal and shear stresses on the crack surface. It thus can reproduce the physical behavior of concrete cracks more precisely than the rotating crack orientation. The rotating crack orientation assumes that the orientation of the cracks rotates continually in response to changes in the axis of the principal strains. The way both crack models' crack orientation work is displayed in Figure 10.

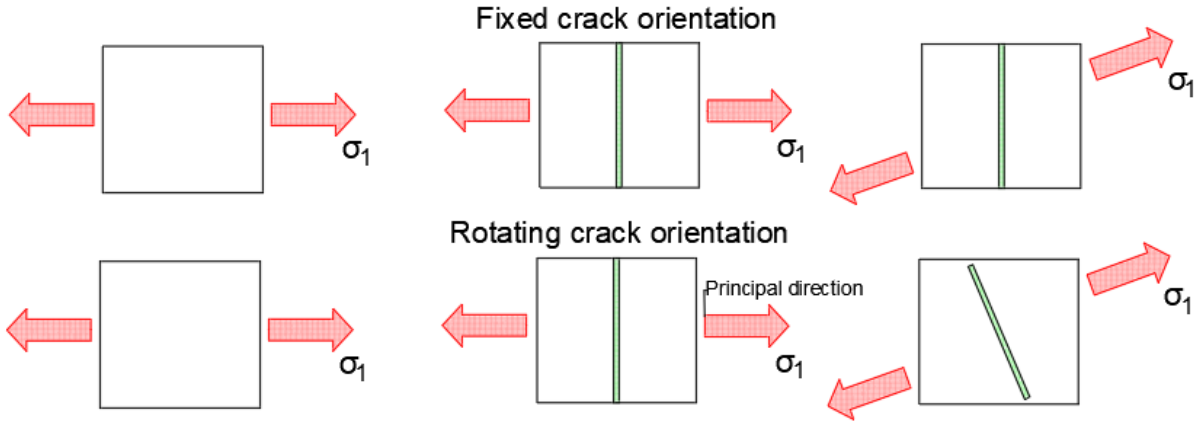

Figure 10 T total strain crack model: fixed (top) and rotating crack orientation (bottom) [50]

Shear stresses are present in the fixed crack orientation, as shown in Figure 10. This model requires a reduction of the shear stiffness along the crack using a shear retention model. As previously mentioned, the fixed crack orientation result of the load capacity will depend on the type of shear retention model. According to Slobbe et al. [2], including a constant shear retention factor in the model can be interpreted as the aggregate interlock mechanism. DIANA FEA offers seven types of shear retention models, which are:

- Aggregate Size-Based Shear Retention: shear retention is based on aggregate size.
- Al-Mahaidi shear retention function: the shear stiffness reduction depends on the normal total strain.
- Constant Shear Retention: The shear retention factor is introduced in the shear retention model to describe the residual shear stiffness of the crack. Araujo et al. [51] suggested using $\beta = 0.01$, as the contribution of the shear strength from the crack is small on the structure's shear crack.
- Damage-Based Shear Retention: shear retention is based on the damage due to cracking.
- Maekawa shear retention curves: two types of shear retention curves by Professor Maekawa are offered in DIANA FEA.
- Normal Crack Strain Based Shear Retention: multi-linear diagram of shear retention factors and the normal crack strains.
- Variable Shear Retention: shear retention varies with shear strain.

Recently multiple studies have been done on the shear retention models using DIANA FEA. Because of the large amount of available data, no sensitivity analysis for the shear retention model is required. The damage-based shear retention model will be used, which causes a reduction of the shear stiffness at a rate like that of the normal stiffness. From some reports, the following main conclusions were found in favor of the damage-based shear retention mode:

- The variable shear retention model is more consistent than the constant shear retention model [52].
- The damage-based shear retention model works well for RC beams without stirrups. In contrast, the other tested shear retention models led to more significant sensitivities [44].
- The aggregate-sized shear retention model fails to capture shear and mixed-mode failure, resulting in stiffer simulations than the experiment [53].
- The problem of over-rotation is avoided with the damage-based shear retention model [54].

Lang [45], however, states that the damage-based tension model can result in excessive loss of the shear retention factor. As a result of these problems with the shear retention model, Slobbe et al. [2] point out the advantage of the rotating crack orientation. With this choice, picking a shear retention model can be avoided, which avoids the possibility of shear stress locking.

Tensile behavior:
According to Marzec et al. [55], during flexural shear failure, the tensile parameters' effects dominate over the compressive parameters. At the same time, the reverse situation is the case for compressive shear failure. Concrete is a material with low tensile strength, where the crack occurs perpendicular to the maximum tensile stress and in a brittle manner. The tensile softening behavior is related to the mode-I fracture energy $G_{\mathrm{f}}^{\mathrm{I}}$ [56]. Sucharda says [57] fracture energy is vital for NLFEA but extremely hard to calculate with experiments.

DIANA FEA offers multiple softening curves, but Hendriks et al. (8) recommend using an exponential-type or exponential softening diagram. This softening curve is preferable because it simulates more localized cracks and, as a result, avoids broad areas of diffuse cracking. The Hordijk softening curve [58], an exponential-type softening diagram, is chosen due to the high amount of backing from reports with similar cases. The softening curve selected is shown previously in Figure 6.

Each part of the stress-strain relation curve and additional information is given below:

- In the first part, the concrete acts elastically until the tensile strength f_t, after which the tensile softening starts.
- The elastic part ends at the strain peak $\varepsilon_{nn}^{\mathrm{peak}}$. At the ultimate strain $\varepsilon_{nn.ult}^{\mathrm{cr}}$, the stress in the crack $\sigma_{nn}^{\mathrm{cr}}$ becomes zero, after which the crack is fully open.
- The area in the graph is equal to $\frac{G_{\mathrm{f}}^{\mathrm{I}}}{h}$.
- The damage-based reduction model should also be applied when modeling the tensile behavior. This model reduces the Poisson's ratio after the crack.

The formula for this curve is given below:

$$\frac{\sigma_{nn}^{cr}(\varepsilon_{nn}^{cr})}{f_t} = \begin{cases} \left(1 + \left(c_1 \frac{\varepsilon_{nn}^{cr}}{\varepsilon_{nn\cdot cr}^{cr}}\right)^3\right) exp\left(-c_2 \frac{\varepsilon_{nn}^{cr}}{\varepsilon_{nn\cdot ult}^{cr}}\right) & \cdots \\ -\frac{\varepsilon_{nn}^{cr}}{\varepsilon_{nnn.ult}^{cr}}(1 + c_1^3)\, exp(-c_2) & , \textit{if } 0 < \varepsilon_{nn}^{cr} < \varepsilon_{nn\cdot ult}^{cr} \\ 0 & , \textit{if } \varepsilon_{nn\cdot ult}^{cr} < \varepsilon_{nn}^{cr} < \infty \end{cases}$$

Equation [VIII]

The following reduced & simplified formula is found for the tensile strength:

$$f_t = \left(0.739 \frac{G_f^I E}{h}\right)^{\frac{1}{2}},$$

Equation [IX]

With:
h: equivalent length/ crack bandwidth.

Compressive behavior:
Numerical studies from Hasegawa et al. [59] [60] have shown that accounting only for the concrete tensile behavior is sufficient to capture the flexural shear failure for deep RC beams. However, because a compressive failure mode is possible, this should not be excluded by modeling only the tensile behavior. According to Hendriks et al. [41], the following points are essential about concrete compressive behavior:

- Concrete shows a pressure-dependent behavior.
- Concrete's post-peak behavior depends on the boundary conditions.
- Influence by lateral cracking should cause a reduction of compressive strength.
- To reduce element size sensitivity, the softening behavior based on the compressive fracture energy G_c should be modeled.

The parabolic curve recommended by Feenstra [61] to model this behavior is in Figure 11. In addition, the formulas for the Feenstra model are also given in Equation [X].

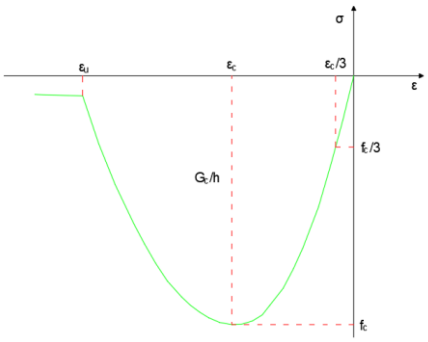

Figure 11 Concrete compressive behavior parabolic curve [61]

$$f = \begin{cases} -f_c \frac{1}{3} \frac{\alpha_j}{\frac{\alpha_c}{3}}, \text{ if } \alpha_{c/3} < \alpha_j \leq 0 \\ -f_c \frac{1}{3}\left(1 + 4\left(\frac{\alpha_j - \alpha_{c/3}}{\alpha_c - \alpha_{c/3}}\right) - 2\left(\frac{\alpha_j - \alpha_{c/3}}{\alpha_c - \alpha_{c/3}}\right)^2\right), \text{ if } \alpha_c < \alpha_j \leq \alpha_{c/3} \\ -f_c\left(1 - \left(\frac{\alpha_j - \alpha_c}{\alpha_u - \alpha_c}\right)^2\right), \text{ if } \alpha_u < \alpha_j \leq \alpha_c \\ 0, \text{ if } \alpha_j \leq \alpha_u \end{cases}$$

Equation [X]

With:

Strain at the peak compressive strain: $\alpha_c = -\frac{1}{3}\frac{f_{cf}}{E} - \frac{4}{3}\frac{f_c}{E}$

Reduction due to interactions:

The concrete's compressive strength should be reduced for two types of interactive behaviors. These two interactive behaviors are tension-compression and compression-compression behavior.

The first interactional behavior discussed is the tension-compression interaction. According to Vecchio et al. [62], for this behavior, the concrete strength and stiffness decrease after it cracks. This behavior is also called compressive behavior with lateral cracking. After the cracks, the concrete loses its full compressive strength. Excluding the compressive strength reduction around the cracked elements caused by cracks would not be conservative for the numerical model with the flexural shear failure mode and thus must be included. An example of different reduction models available is shown in Figure 12.

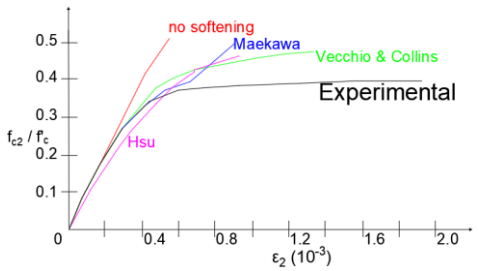

Figure 12 Tension-compression interaction reduction model [62]

The reduction model proposed by Vecchio & Collins [62] will be applied, which can be considered with the following reduction factor:

$$\beta_{\sigma_{cr}} = \frac{1}{1+K_c} \leq 1, \text{ with } K_c = 0.27\left(-\frac{\alpha_{l_a}}{\varepsilon_0} - 0.37\right)$$

Equation [XI]

The reduction factor due to lateral cracking can also be used, which Belletti et al. [42] suggest being β_{min}=0.6. However, Japan Society of Civil Engineers [63] found that 0.2 can be subtracted from this value if there is potential reverse cyclic loading until a significant tensile strain occurs. A β_{min} of 0.4 will be implemented, which is also the lower bound of the reduction factor. According to Salah et al. [64], β_{min}=0 would result in over-stiff behavior from the structure.

The second interactive behavior is the compression-compression behavior, also known as the compressive behavior with lateral confinement. During the compression-compression interaction, confinement can be considered but also skipped depending on the numerical model. In this report, confinement does not play a significant role in the chosen 2D numerical cases with expected flexural shear failure. According to Putter [43], it is recommended to use an unconfined model. However, to know if modeling this behavior is necessary, sensitivity analysis will be performed for this in Chapter 4. An unconfined numerical model and a numerical model with confinement will be used for sensitivity analysis. The confinement model used for the sensitivity analysis is the Shelby & Vecchio model [65].

Equivalent length:
Recent studies have suggested that the equivalent length is critical for the shear capacity of RC beams without stirrups. DIANA FEA offers three methods to calculate the equivalent length/crack bandwidth: the user-specified method, the Rots element-based method, and Govindjee's projection method. According to Hendriks et al. [41], the user-specified crack width method can be inaccurate while increasing the number of modeling factors for the numerical model. On the other hand, the Rots element-based method has accuracy problems for distorted or high aspect-ratio elements. Govindjee's method [66] has the least problems and is best suited. This method automatically decides the equivalent length. The formula for Govindjee's projection method is given below:

$$h_g(\boldsymbol{x}) = \left(\left[\sum_{i=1}^{n} [\partial_{\boldsymbol{x}} N_i(\boldsymbol{x}) \phi_i] \right] \cdot \boldsymbol{n}(\boldsymbol{x}) \right)^{-1}$$

Equation [XII]

With:

$$\phi_i = \frac{(\boldsymbol{x}_i - \boldsymbol{x}_c) \cdot \boldsymbol{n}(\boldsymbol{x}) - \phi_{min}}{\phi_{max} - \phi_{min}}$$

A problem with this method is that directional mesh bias can occur. This problem occurs when the localized band direction and mesh lines are not aligned, causing the strain localization to depend on the mesh orientation [67]. Through the years, updated versions of these Govindjee's projection method have been created. The newer version also has an added orientation factor, improving this method. However, because the new methods are not a part of the current version of DIANA FEA (version 10.5), the updated methods will be excluded from this thesis.

2.2.1.2 Reinforcement

Reinforcement has an elastic-plastic behavior, as shown in Figure 13. This figure shows that the yield point is the elastic limit, while hardening starts after the yield point till the ultimate strength. To include the non-linear mechanism, the Von Mises plasticity model will be used as the non-linear model. Here the ultimate stress will reach before the steel fails. According to Hendriks et al. [41], rupture can be modeled by specifying sharp, softening branches. Alternatively, a post-processing check should be done if rupture is not modeled.

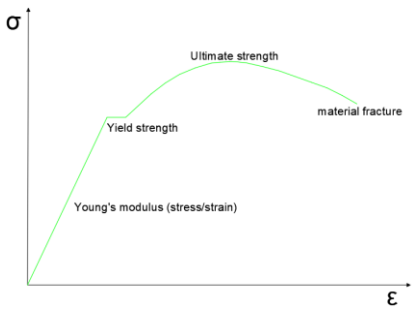

Figure 13 Reinforcement elastic-plastic model [68]

Hardening is beyond ideal plasticity and should also be introduced into the model as strain-isotropic hardening. Giuliano [74] explains that isotropic hardening is when the material yield surface expands under plastic deformation. An alternative to isotropic hardening is kinematic hardening. The difference between the two hardening types is the “Bauschinger effect.” Both hardening types are based on the strain-hardening hypothesis [69]. In Figure 14, an overview of the two hardening types is given. The two stress-strain relation diagrams show the change in the yield surface.

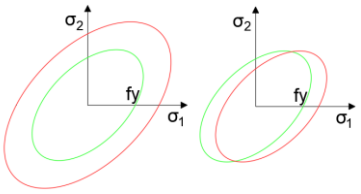

Figure 14 Isotropic (left) and kinematic hardening (right) [69]

The concrete-reinforcement interaction is the primary mechanism driving the stress redistribution after cracking. This mechanism can be modeled in multiple ways using DIANA FEA. Putter [43] recommends using the bond-slip relation as the most dependable. In addition, Yang et al. [5] state that this model improves the simulation results. The bond-slip relation describes the slip between concrete and reinforcement. DIANA FEA offers several bond-slip relations, which are listed below:

- The quadratic function proposed by Dörr.
- Power Law relation proposed by Noakowski.
- Bond-slip relationship presented by Shima.
- Bond-slip-strain relationship presented by Shima.
- CEB-FIB 2010 bond-slip relation.

The Shima bond-slip and CEB-FIB 2010 models are often used. Putter [43] has found that the CEB-FIB 2010 model works best for RC beams without stirrups-specific cases. He explains that the failure load is overestimated due to the higher bond stress at which the stiffness decreases significantly for the Shima bond-slip relation. Still, a numerical model sensitivity analysis will be done between the two bond-slip relations to decide which performs best for the specific cases in this report. Chapter 4.2.1.2, Figure 54 compares a stress-displacement graph using both models during the model sensitivity analysis. For now, the theoretical background of both models is explained below.

The first model discussed is the Shima bond-slip relation [70]. This model is defined by the formula in Equation [XIII]. This formula is a function of the concrete strength and reinforcement diameter, and a curve can be plotted from it. Also, the stiffness of this model is infinite.

$$t_t = 0.9 f_c^{\left(\frac{2}{3}\right)} \left(1 - e^{-40\left(\frac{\Delta ut}{D}\right)^{0.6}}\right) [MPa]$$

Equation [XIII]

The CEB-FIB 2010 bond-slip curve is unique from the other models because of the unloading and reloading behavior. This behavior uses linear stiffness until the opposite stress value is reached. Because of this, the calculations are done in four phases, shown in Figure 15. Each phase is also described in the figure.

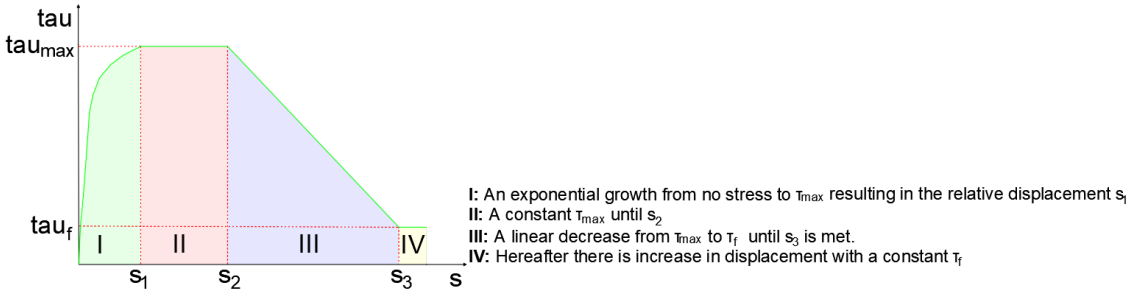

Figure 15 CEB-FIB 2010 bond-slip curve based on pull-out [47]

The following calculations in Table 6 are important for the phases when modeling the bond-slip relation because of multiple modeling conditions. Good bond-slip conditions for the pull-out failure will be considered in this report.

Table 6 FIB bond-slip model bond-stresses considering good conditions [47]

Bond stresses (with good conditions)	**Boundaries (Relative displacements)**	**Pull-out failure: Ribbed bars**	**Pull-out failure: Smooth bars**
$\tau_0 = \tau_{max} (\frac{s}{s2})^{\alpha}$	0≤s≤s1		
$\tau_0 = \tau_{max}$	s1≤s≤s2	s1=1mm	s1=0.01mm
$\tau_0 = \tau_{max} (\tau_{max} - \tau_f) \frac{s-s2}{s3-s2}$	s2≤s≤s3	s2=2mm	s2=s1
τ_f	s3>s	s3=c_{clear}	s3=s1
Additional formulas:		$\tau_{max}=2.5\sqrt{fck}$	$\tau_{max}=0.1\sqrt{fcm}$
		α=0.4	α=0.5
		$\tau_f=0.4\ \tau_{max}$	$\tau_f=\tau_{max}$

The element should have a neglectable initial deformation compared to the continuum element. High initial stiffness is introduced as a solution for the normal and shear stiffness. For the stiffnesses, the following formula is used:

- Normal stiffness *(Kn)*=$\frac{100*E}{h}$
- Shear stiffness *(Ks)=0.1*Kn*

2.2.2 Finite element discretization

In the earlier section, the constitutive models were discussed. With the information gathered till now, the next step is finite element discretization. By discretizing the experimental cases, the experimental cases can then be approximated as closely as possible with the help of NLFEA. The discretization will be done for the concrete, reinforcement, mesh, loading, and boundary conditions below.

2.2.2.1 Concrete

Because the RC beam model will be made in 2D, 2D plane-stress elements, also called membrane elements, can be used with all nodes in-plane. Shun summarized [71] characteristics of the 2D plane-stress elements, which are:

- The elements make use of the XY coordinate system.
- Transitional displacement takes place in the x-direction and y-direction.
- Strain components are: ε_{xx}, ε_{yy} and the shear component γ_{xy}.
- A small thickness compared to the length and width dimensions.
- Stresses σ_{zz} and strains ε_{zz} perpendicular to the face (z-direction) equals zero.

The specified thickness is vastly different for this type of element. It is enough to specify the thickness at one node for uniform-thickness cases. For non-uniform thickness cases, the thickness needs to be specified for every node, as shown in Figure 16:

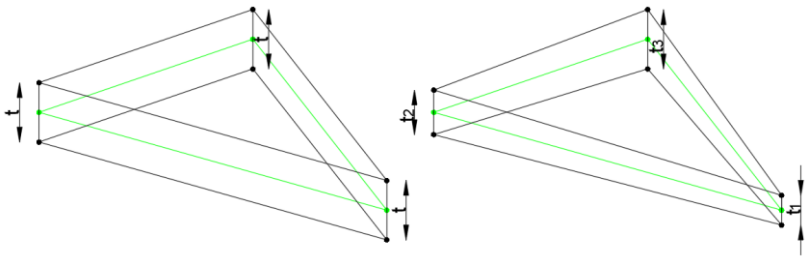

Figure 16 Plane-stress element thickness: uniform (left) and non-uniform (right) [71]

Hendriks et al. [41] recommend quadratic elements over linear elements giving more deformation modes and preventing locking. In addition, Borst et al. [72] state that these elements should be fully integrated to avoid spurious modes due to extensive cracking. The element recommended for the 2D RC beam model is an eight-node-quadrilateral element. The element that fits this recommended in DIANA FEA is CQ16M, displayed in Figure 17.

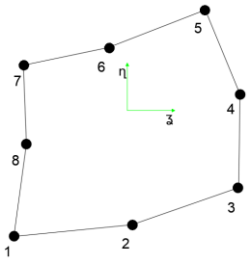

Figure 17 CQ16M plane-stress element [71]

Essential facts and choices about CQ16M are listed below:

- The polynomial equation for the displacement:

$$u_i(\xi,\eta) = a_0 + a_1\xi + a_2\eta + a_3\xi\eta + a_4\xi^2 + a_5\eta^2 + a_6\xi^2\eta + a_7\xi\eta^2$$

Equation [XIV]

- ε_{xx} varies linearly in the x-direction and quadratic in the y-direction.
- ε_{yy} varies linearly in the y-direction and quadratic in the x-direction.
- γ_{xy} varies quadratically in the x-direction and y-direction.
- This element uses an isoparametric quadratic scheme and makes use of numerical integration.
- A 3x3 Gaussian integration scheme will be used instead of a 2x2 Gaussian one. Because DIANA FEA has a 2x2 reduced integration in the default settings, this must be adjusted.
- The element pairs well with embedded elements and grid elements for longitudinal reinforcement.

2.2.2.2 Reinforcement

From the earlier sections, some considerations need to be made before doing the finite element discretization for the reinforcement. As mentioned in the last section, the bond-slip relation will be modeled and can be done in DIANA FEA with truss or beam elements.

The advantage of embedded reinforcement with truss elements is that the reinforcement does not require a modification in the connectivity of the concrete elements. Hendriks et al. [41] state that slip can be modeled explicitly due to the combination of the embedded reinforcement with interface elements. However, unfortunately, the truss element cannot be used to model the dowel action, as this element only takes up axial stresses.

Beam elements can describe axial forces, shear forces, in-plane moments, and out-of-plane moments. These descriptions give axial deformation, shear deformation, curvature, and torsion. However, Shun [71] points out that the dimensions perpendicular to the bar length must be minor compared to the bar length. An advantage of the beam elements is that it also considers bending stiffness, making it possible for the concrete to withstand shear stresses with the dowel effect. Cook et al. [73] found that the beam elements limit freedom in meshing due to the characteristic of sharing nodes with continuum elements. DIANA FEA offers the following three classes for beam elements:

- Class-I beam element: from the classical beam theory, it works well for linear and non-linear geometrical analysis.
- Class-II beam element: numerically integrated from the classical beam theory. This element works well for linear and non-linear geometrical + physical analysis.
- Class-III beam element: numerically integrated from the Mindlin beam theory. This element works well for linear and non-linear geometrical + physical analysis. This class of beam elements also includes shear deformation.

Due to this, the element includes shear deformation, consisting of 3 nodes and 9 degrees of freedom. The geometrical nonlinearity of the dowel action should be considered. This nonlinearity should be considered due to the change in the line of action. According to Slobbe et al. [2], this inclusion works well with Class-III beam elements. The displacement variables can be derived from Equation [XV].

$$u_x(\xi) = a_0 + a_1\xi + a_2\xi^2$$
$$u_y(\xi) = b_0 + b_1\xi + b_2\xi^2$$
$$\phi_z(\xi) = c_0 + c_1\xi + c_2\xi^2$$

Equation [XV]

According to Putter et al. [43] [44], the best results for RC beams without stirrup cases are found for the beam element combined with CEB-FIB 2010 bond-slip relation for the fixed crack orientation. However, convergence difficulties have been found for beam elements during the analysis using the CEB-FIB 2010 bond-slip relation on the force norm. Compared to the CEB-FIB 2010 bond-slip relation with the Shima-bond-slip relation, the Shima-bond-slip relation did not result in many convergence difficulties. The analysis found the convergence difficulty is because, unlike the Shima-bond-slip relation, the CEB-FIB 2010 bond-slip relation requires bond stresses during the increase of the strain. As a result, this causes an increase in the residual force. Because many modeling aspects are still undecided for the numerical model, choosing based on just this information from the literature review is not ideal. From a theoretical perspective, both reinforcement element types have advantages and disadvantages. A numerical model sensitivity analysis will be done with the truss and beam elements. The reinforcement element type will be chosen depending on the better results during the sensitivity analysis.

2.2.2.3 Mesh

The element size must be chosen based on the beam dimensions to avoid element size sensitivity problems. Over the years, various element size sensitivity analyses have been performed, and recommendations for the formula have been given. However, whether these recommendations will accurately work for all numerical cases in this report is still unknown. The suggestions below highlight information over the years, from which an initial element size can be decided. This initial element size, in turn, will be optimized with an element size sensitivity analysis for beams with different dimensions.

Correct element sizes benefit the dowel crack initiation and propagation rate, as they depend on the element size. Also, the element size cannot be more extensive than 1.5 times the maximum aggregate size. In 2020 Hendriks et al. [41] proposed the formula ($min\left(\frac{l}{50}, \frac{d}{6}\right)$) to calculate the element size for 2D RC beam models. In addition, a second formula for the maximum element size has been given, which says $h\,max \leq \frac{Leq}{2}$. The reasons for the maximum size are the following:

- Avoid snap-back post-peak behavior caused by the softening materials.
- Avoid stress distribution jumps to keep it as smooth as possible.
- Capture damage distribution.

Putter [43] found that elements with the size $\frac{d}{20}$ gave the best results. It was also shown that cases on beams without stirrups over 600mm showed mesh dependence when analyzing with element sizes $\frac{d}{20}, \frac{d}{30}, \frac{d}{40}, \frac{d}{60}$. The report states the analysis for beams without stirrups should still be done with great care due to their sensitivity. Especially in large beams, finer element sizes resulted in overestimating the resistance. It should be noted that the largest element size is already tiny.
Even larger element size could also have been assessed during this report's sensitivity analysis, as the most significant size was chosen as the best. Lang [45] did some element size sensitivity analysis, and recommendations were made to make the element size smaller than $\frac{d}{15}$ to simulate the flexural shear failure. However, a much smaller element size resulted in a longer computation time with no significant improvements, so making the element size smaller is not required. Gedik et al. [74] showed that an element size is sufficient between 10 mm and 30 mm. Adhikary et al. [75] parametric study shows that an element size smaller than 25 mm no longer improves the result.

Because the initial cases will be based on experiments from Stevin lab, special attention is given to a report by Teshome [53]. In this report, similar beams were studied and used an element size of 25 mm. The recommendations from Lang [45] are also remarkably close to the element size of 25 mm for the initial cases. With the information found till now, the initial element size will be chosen to be 25 mm. During the element size sensitivity analysis in Chapter 4.2.3.2, the element size will be decreased and increased until an optimum element size is found for a specific beam depth.

2.2.2.4 Loading, boundary conditions, and symmetry

Applying point loads and constraints for the boundary conditions can result in high-stress concentrations in the model. The high-stress concentration can affect the numerical model simulations, which should be avoided. Hendriks et al. [41] suggest that loading and support plates are a satisfactory solution to avoid this. Distributed loads can also be placed on the plate as an alternative instead of applying point loads that cause high-stress concentrations. The right boundary conditions are critical because they influence specimen stress distribution. Hasegawa [76] says the shear capacity, post-peak behavior, and failure type can all be affected. In addition, placing supports over the entire plate length as a boundary condition can cause a crack near the plate.

Symmetry can reduce computational costs for a numerical simulation but has its problems and restrictions. A fundamental problem with using symmetry is that it is assumed that failure occurs symmetrically. Therefore, symmetry can only be applied if the structure, loads, and constraints are symmetrical. The user should also remember that the load gets halved when symmetry is used, and the load is applied midspan. Because of these restrictions and an expected non-symmetric failure type (flexural shear failure), symmetry will not be applied to the model. An overview of the numerical model with the proper loading conditions, boundary conditions, and non-symmetry is shown in Figure 18.

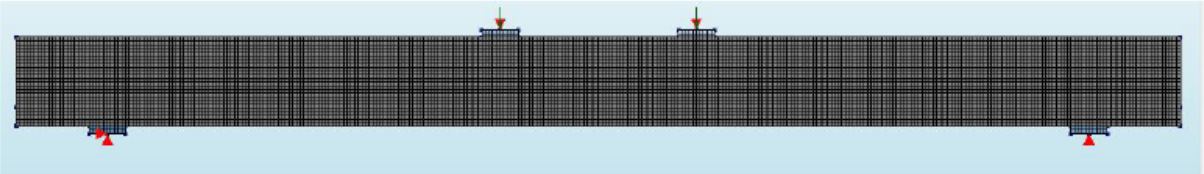

Figure 18 Beam boundary conditions: loading plates (top) and loading supports (bottom)

2.2.3 Analysis procedure

During NLFEA, the force and displacement have a non-linear relation. Due to this, equilibrium cannot be reached directly, and the analysis must be done with the correct analysis procedures. The simulation is run with the incremental-iterative procedure. According to Putter [44], the procedure's choice can affect the result. However, this effect is not as dominant as the constitutive assumptions.

2.2.3.1 Incremental-iterative procedure

DIANA FEA offers different methods for the incremental-iterative procedure. Lang [45] states that the various methods form the global stiffness matrix differently, affecting the excessive change of the principal stress-strain. The different methods offered by DIANA FEA are explained by Borst et al. [69] and are listed below:

- Newton-Raphson (NR) iteration scheme: The prediction depends on this scheme's last unknown or last found situation. Also, the stiffness is updated after every iteration, which can be time-consuming.
- Modified Newton-Raphson (MNR) iteration scheme: It is unnecessary to set up the stiffness matrix every time for this scheme. Because of this, doing more iterations than the standard version is necessary but iterates faster. The prediction depends on the converged equilibrium state.
- Quasi-Newton-Raphson (QNR) iteration scheme: this scheme does not entirely set up a new stiffness matrix every iteration but uses information from the previous results. This scheme is perfect for unconstrained optimization and often combined with the line search method.
- Linear-Elastic (LE) iteration scheme: as the scheme name says, it uses the linear stiffness matrix. Even though this scheme is robust, stability problems can occur at bifurcation points.

Hendriks et al. [41] recommend the standard (full) NR iteration scheme as the results were accurate and sufficient (if combined with the arc-length control). A disadvantage of the NR type of iteration schemes (NR, MNR, and QNR) is its limited radius of convergence. However, this radius can be enlarged with the line search method. This method improves the incremental displacement vector by scaling the vector to get the point of lowest potential energy along the search direction to represent the equilibrium. With this, the current iteration procedure creates a more robust model with increased convergence.

Multiple reports [2] [77] have used the Secant iteration scheme while using the displacement method. The scheme can be based on the Broyden-Fletcher-Goldfarb-Shanno (BFGS), Broyden, or Crisfield algorithm. The BFGS algorithm will be chosen if the Secant iteration scheme is used, as this algorithm has been applied in the previously mentioned reports. Akram et al. [78] researched the two discussed schemes and concluded that the full NR iteration scheme is the fastest available, while the Secant iteration scheme is the most effective. Both schemes will be used for sensitivity analysis in Chapter 4.2.2. In Figure 19, the difference between both schemes can be seen.

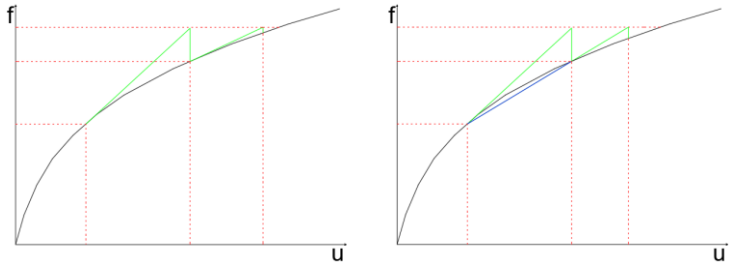

Figure 19 NR iteration scheme (left) and Secant iteration scheme (right) [69]

2.2.3.2 incremental procedure

Applying the external load depends on how the equilibrium path is sought after with increments. According to Borst et al. [69], this choice helps control the load and get convergence for each step. Applying the external load can be done in three ways using DIANA FEA and is listed below, with also an overview of them in Figure 20:

- Load control: here, the load is applied directly on the beam in several steps.
- Displacement control: prescribing the displacements, giving nodal forces that must be summed up for the external force. This one is more stable but not recommended for structures with multiple loads [41].
- Arc-length control: the incremental displacements are constrained to a prescribed value by adapting the increment size during iteration.

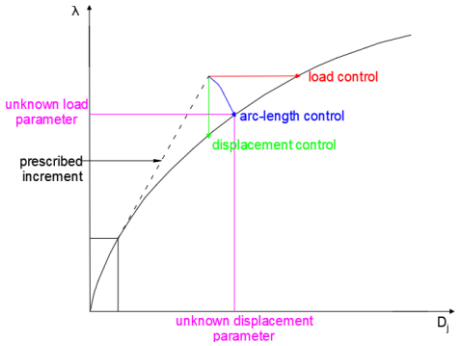

Figure 20 Force, displacement, and arc-length control [79]

Lang [45] recommends using the arc-length control combined with the line search method, as the force-controlled analysis did not capture the softening behavior. Putter [44] also used the same combination to trace the post-peak load paths. The arc-length control method [80] helps find the equilibrium path while dealing with limit and bifurcation points. Unfortunately, the load control method stumbles at limit points, while the displacement method cannot manage snap-back behavior. However, negative load steps can be prescribed to overcome the snap-back problem for the displacement method.

Hasegawa [81] did research on the methods for RC beams without stirrups and found the following:

- Arc-length control with indirect displacement does not get the bifurcation path for flexural shear failure.
- Direct displacement method: branch-switching was captured for the correct bifurcation point. However, this method will require the Secant stiffness.

Yang et al. [82] also report that the arc-length method may fail near or at limiting points for softening materials.

2.2.3.3 Convergence criteria

Complete equilibrium cannot be reached but can be calculated to a sufficient tolerance while accepting a small error. For this, the convergence criteria are used. DIANA FEA offers four types of convergence criteria, namely:

- Force norm: the norm can be solved directly for convergence but is not recommended for linear elastic regimes.
- Displacement norm: the norm requires an additional iteration to reach convergence.
- Energy norm: the norm is composed of internal forces and relative displacements. This norm also requires an additional iteration to reach convergence.
- Residual norm: like the force norm, this norm considers the out-of-balance forces vector and the constrained degrees of freedom values.

The user gives the maximum number of iterations allowed to avoid too many. The iterations stop if convergence has been met, the maximum number of iterations is reached, or divergence occurs. Putter [43] recommends using at least 100 iterations per step for cases like the ones important for this report. Reaching the maximum number of iterations cannot be seen as convergence. Lang [45] states that always getting convergence for each step is unnecessary if reliable results for shear failure have been found. Yang et al. [5] do, however, state that lack of convergence can cause unstable propagation of the flexural shear crack. This unstable propagation will affect the deformation and stresses in the structure. The convergence logs generated during the simulation should always be studied to avoid such a problem.

The iteration schemes should converge for at least one of the norms to be considered sufficient. The following norms have been advised where the convergence of one of the norms is considered sufficient:

- The energy norm with a tolerance of 0.001
- The force norm with a tolerance of 0.01

According to Hendriks et al. [41], using the displacement norm alone is considered inappropriate for the analysis.

2.3 Design codes

In the final part of the report, predictions from design codes will also be compared to the numerical simulations to compare the predicted shear capacity. The design code is from EC2 guidelines [40] and FIB MC2010 [47]. The EC2 guidelines analytical design code evaluates the shear resistance (*Vrd,c)* while including the size effect with the formula in *Equation [XVI]*.

$$VRd,c = (CRd,c\ k \left(100\ \rho l\ fck\right)^{\frac{1}{3}} + k1\ \sigma cp\Big] bwd,$$

Equation [XVI]

$$With\ the\ requirement\ that$$
$$VRd,c \geq (vmin + k1\ \sigma cp)\ bwd$$

Equation [XVII]

$$Where:$$
$$k = 1 + \sqrt{\frac{200}{d}}$$
$$\rho l = \frac{Asl}{bwd} \leq 0.02$$
$$\sigma cp = \frac{Ned}{Ac}$$

The importance of the factor *k* has been given in Chapter 2.1.3. A minimum requirement is also given in the formulas above for the VRd,c. This requirement is meant as a minimum for scenarios where the reinforcement ratio is low.

Another second design code chosen for this report is the FIB MC 2010, which is based on a physical-mechanical model instead of an analytical model. The formulas for the shear strength based on a level of approximation (LoA) III for beams without stirrups are given in Equation [XVIII]:

$$V_c = k_v \cdot \sqrt{f_c} \cdot b_w \cdot z,$$

Equation [XVIII]

$$With:$$
$$k_v = \frac{0{,}4}{1 + 1500 \cdot \varepsilon_x} \cdot \frac{1300}{1000 + k_{dg} \cdot z}$$
$$k_{dg} = \frac{32}{16 + d_g} \geq 0.75$$
$$\beta = \begin{cases} 1 & \text{if } a_v \geq 2d_\ell \\ a_v/2d_\ell & \text{if } 0.25d_\ell \leq a_v \leq 2d_\ell \\ 0.5 & \text{if } a_v \leq d_\ell \end{cases}$$
$$\varepsilon_x = \frac{1}{2E_sA_s}\left(\frac{M_{Ed}}{z} + V_{Ed} + N_{Ed}\left(\frac{1}{2} \pm \frac{\Delta e}{z}\right)\right)$$

Because the design codes are not the focus of this report, a simplified LoA II will be used. The design codes are used for comparison purposes with the numerical simulations. It should be remembered that the LoA II introduces simplifications, causing a reduction in the model's accuracy. The following simplifications are done for the LoA II:

- ε_x, which is the strain at the midsection will be assumed to be:

$$\varepsilon_x = \frac{fyk}{2E_s}$$

Equation [XIX]

The aggregate size factor k_{dg} is assumed to equal the lower bound factor of 0.75. It was initially believed that k_{dg} equals 1.25, which is also recommended. However, with the initial assumption, the results are too conservative and have a high failure load percentage difference.

2.4 Summary

This chapter's section will summarize essential information gathered in the previous sections of this Chapter to make numerical modeling choices. In addition, this summary also helps to decide which modeling aspect requires sensitivity analysis in Chapter 4. With sensitivity analysis using numerical cases, it is hoped to get a robust numerical model, which will be applied to all experimental cases. These experimental cases will be given in the next chapter. The numerical model also hopes to account for the four shear transfer mechanisms as much as possible to improve its accuracy. Before moving to the shear transfer mechanisms, a summation of occurrences during the flexural shear failure is given:

- Vertical flexural cracks formed.
- Longitudinal reinforcement and concrete bonds are destroyed.
- Diagonal cracks developed.
- A diagonal crack enlarges.
- Flexural shear failure occurs.

This failure mode is fundamental and has a significant bearing capacity reduction. This failure mode occurs for beams with an effective span-to-depth ratio between 2.5 and 7.0. This condition will be applied while selecting the experimental cases in Chapter 3. Bažant et al. [23] [24] state that the size effect should be accounted for such cases. The size effect on beams will be analyzed by geometrically scaling beams and comparing the nominal shear strength.

Now that the failure mode and size effect is summarized, a summation of the four shear mechanisms and numerical modeling choices is combined given below:

- Dowel action:
  - The dowel action's parameters are the element size, reinforcement element, constitutive reinforcement model, and reinforcement ratio. Most importantly, the reinforcement ratio will decide the contribution of the dowel action. The larger this is, the more significant the contribution.
  - The element size should be small enough to start the dowel crack and its propagation.
  - Truss elements do not include the dowel action. Beam elements are required to model the dowel action. In addition, the geometrical nonlinearity of the dowel action must also be included.
- Aggregate interlock & residual tensile stresses:
  - This aggregate interlock is dominant for a crack width greater than 0.1mm. At the same time, the residual tensile stress is dominant if the crack width is smaller than 0.1mm.
  - If the fixed crack orientation is used, the shear retention model has to be included. This model can be interpreted as the aggregate interlock.
  - The residual tensile stress is included in the Hordijk fictitious crack model, including localized cracks.
  - For the aggregate interlock, the most critical parameters are the aggregate size and concrete strength.
  - Like the dowel action, the contribution of these two mechanisms is small for large beams.
- Concrete compression zone:
  - The importance of this mechanism lies in the beam depth, which influences the uncracked area. Understandably, the slenderer the beam is, the smaller the contribution.
  - Compression-compression confinement can also influence this mechanism.

The inclusion and effects of the four shear transfer mechanisms on the numerical model depend on the constitutive case and finite element discretization. Figure 21, Figure 22, and Figure 23 show an overview of the obtained reference numerical model and modeling choices from the literature review on the next page. The reference model exists of the components: constitutive model, finite element discretization model, and analysis procedure.

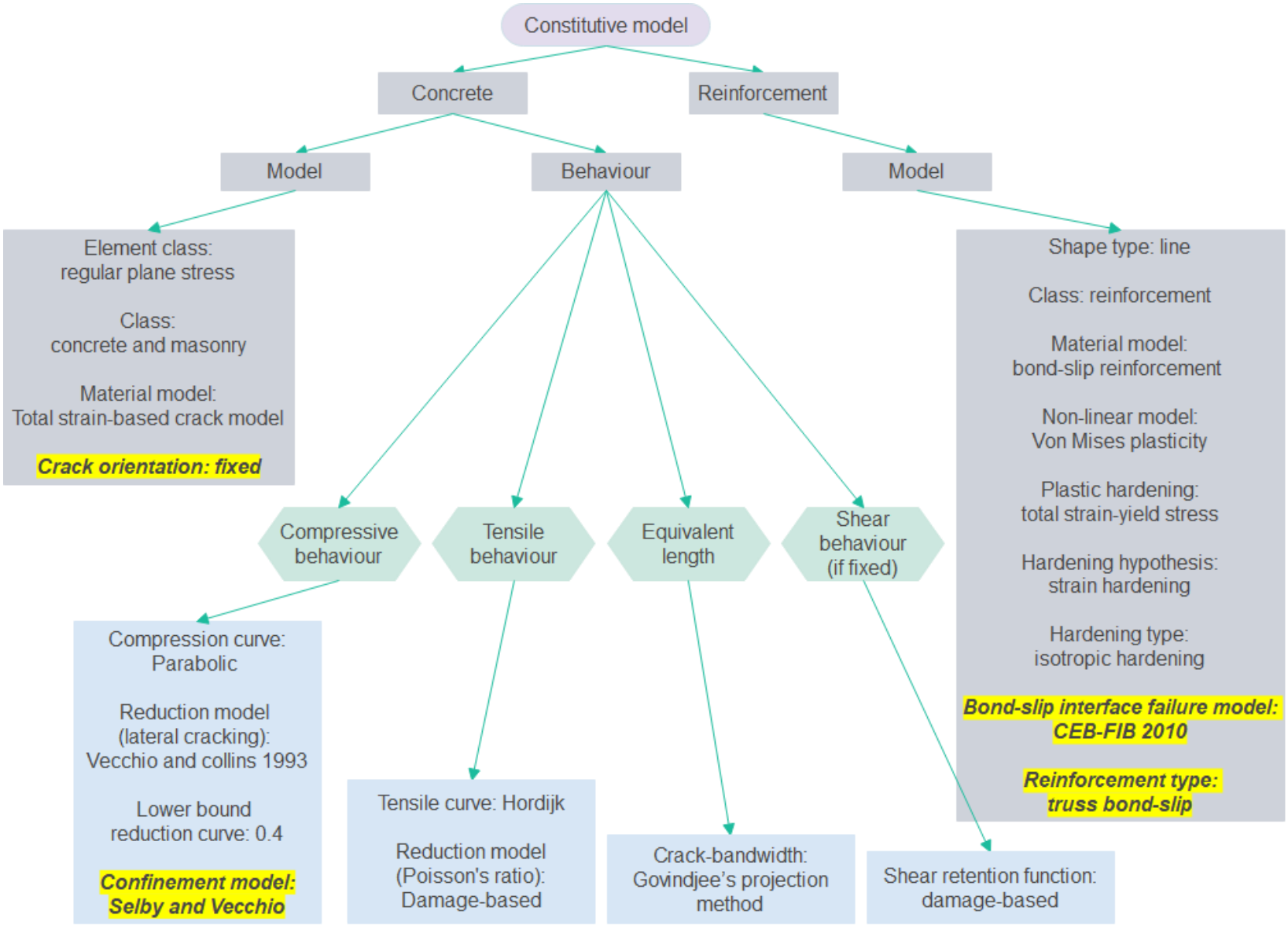

Figure 21 Reference numerical model: constitutive model

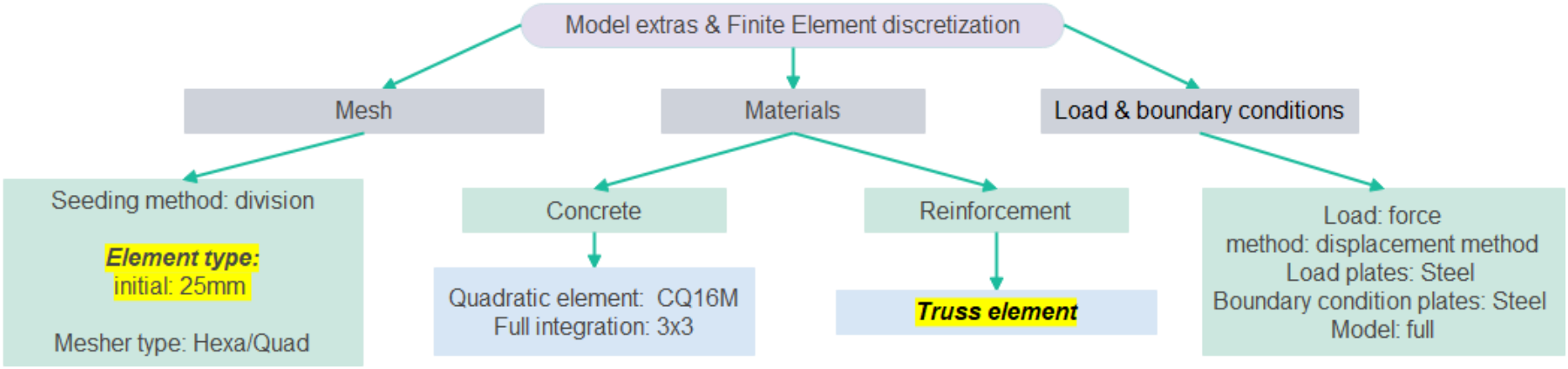

Figure 22 Reference numerical model: finite element discretization

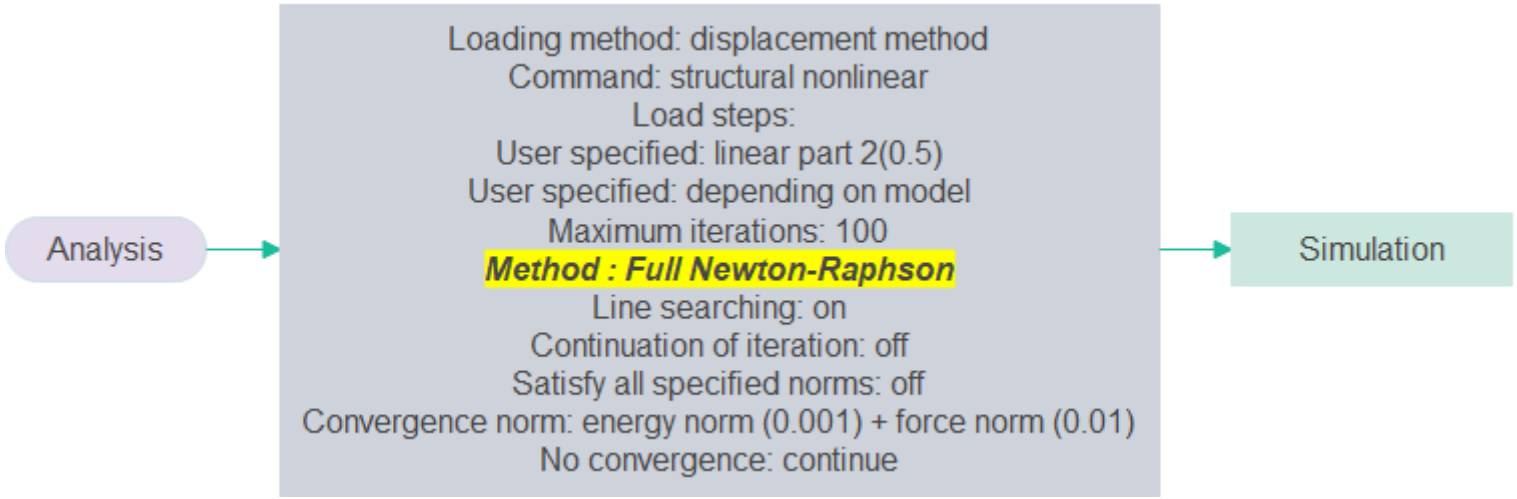

Figure 23 Reference numerical model: analysis procedure

3 Experimental case selection for numerical simulations

The experimental cases will be chosen based on boundaries for the effective span-to-depth ratio, based on different geometries and material configurations to increase the variety in configurations for the cases from Chapter 2. The reason for selecting cases depending on the effective span-to-depth ratio is that only cases with flexural shear failure are chosen. The boundary archived from the literature review in Chapter 2 for the effective span-to-depth ratio is between 2.5 and 7. In addition, the effective depth will be restricted to a maximum beam depth of 1200 mm. This restriction is because geometrically large beams are very mesh sensitive but are important for the pilot research. In Chapter 4.2.3.2, the element size sensitivity analysis will be done for beams with a depth of up to 1200 mm. A basic overview of the models and the naming of the dimensions are given in Figure 24:

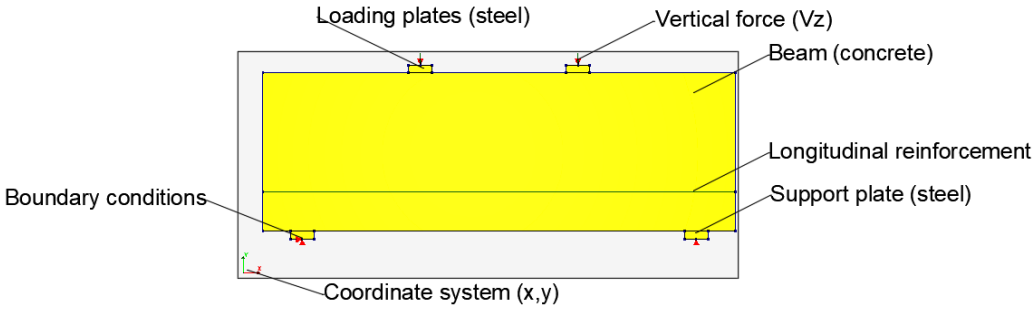

Figure 24 RC beams without stirrups numerical model

All the experimental cases from the reports below will be used to see if the robust numerical model found in Chapter 4 can simulate accurate results. Simulations of these cases with enough variety in the configurations will show the accuracy and limitations of the numerical model. The initial cases are summarized below, with their properties in Annex II. The first four reports given below are given with their original reference. However, they are also summarized in the report by Dunkelberg et al. [83]. These cases are based on a single geometrical or material variation. Their simulations can indicate if the increase in a single configuration can cause inaccurate results for the numerical model.

3.1 Geometrically scaled beam cases

This report by Bhal [84] was selected due to its inclusion of geometrically scaled beams. This set of experiments will also be used for the size effect analysis as there are geometrically scaled beams required for the size effect analysis. Some important geometrical and material configurations have the following ranges:

- Effective depth: (300 mm - 1200 mm)
- Effective span-to-depth ratio: (2.94)
- Concrete strength: ($f_{c,c}$: 22.02 MPa - 28.12MPa)
- Reinforcement ratio: (1.26 %)

These cases consist of four beams with effective depths: 300mm, 600 mm, 900mm, and 1200mm.

A four-point test configuration is used for the beams, as shown in Figure 25. A new geometrical parameter (c) is also introduced, which gives the distance between the two-point loads. The four-point experiment setup also applies to the following three reports.

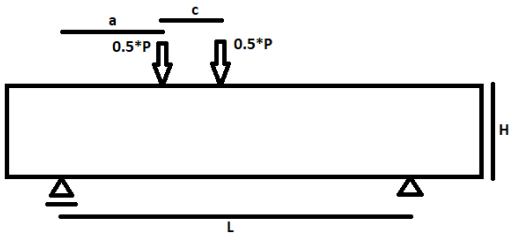

Figure 25 Four-point experiment configuration [83]

3.2 Cases with variation in reinforcement ratio

This report [85] tested twenty-six reinforced HSC beams without stirrups to determine the diagonal cracking and ultimate shear capacity. Out of these twenty-six cases, a selection was made for cases with only variation in the reinforcement ratio. Some important geometrical and material configurations have the following ranges:

- Effective depth: (184.15 mm - 208.03 mm)
- Effective span-to-depth ratio: (4.00)
- Concrete strength: ($f_{c,c}$: 74.09 MPa - 81.59 MPa)
- Reinforcement ratio: (1.77 % - 6.64 %)

All cases have a depth of 254 mm, but the effective depth is slightly different due to the reinforcement area. The cases have the following reinforcement ratios: 1.77%, 2.25%, 3.26%, 3.93%, 5.03%, and 6.64%. This selection gives a broad range for reinforcement ratio variation to assess the accuracy of the numerical model.

3.3 Cases with variation in effective span-to-depth ratio

In Krefeld et al. report [86], over 200 RC beam cases have been tested. However, from these cases, the cases with stirrups are neglected. Also, cases with variations in the beam depth, reinforcement ratio, concrete class, and distributed loading are disregarded. Only beams with concentrated loading will be chosen to stay consistent with the experimental case selection. Finally, the effective span-to-depth ratio range will be kept within the boundaries for which the flexural shear failure occurs. With these restrictions, some important geometrical and material configurations have the following ranges:

- Effective depth: (250.44 mm)
- Effective span-to-depth ratio: (3.40 – 7.05)
- Concrete strength: ($f_{c,c}$: 40.54 MPa – 45.62 MPa)
- Reinforcement ratio: (4.15 %)

The effective span-to-depth ratios studied will be 3.40, 4.61, 5.83, and 7.05.

3.4 Cases with variation in concrete strength

Mphonde et al. report [87] will be used to study the numerical model performance for the concrete strength variation. This report studied the concrete strength using three different series, for which the effective span-to-depth ratio differed for each. The first series was chosen with a constant effective span-to-depth ratio of 3.49. It was essential to have a broad range of cases with different concrete strengths available due to its role during flexural shear failure for the beam. For the first series of cases from the report, some important geometrical and material configurations have the following ranges:

- Effective depth: (298.45 mm)
- Effective span-to-depth ratio: (3.49)
- Concrete strength: ($f_{c,c}$: 25.29 MPa - 114.10 MPa)
- Reinforcement ratio: (3.34 %)

The concrete compressive cube strengths are 25.29 MPa, 45.88 MPa, 50.70 MPa, 90.91 MPa, 99.07 MPa, 111.85 MPa, and 114.10 MPa.

3.5 Cases with variations in geometrical and material configurations

The following experimental cases based on two reports from the Stevin lab were recommended by the supervisors and used for analysis. These cases have a detailed analysis for each test, making them beneficial for a quality analysis during the numerical model sensitivity analysis in Chapter 4. Each analysis in this report is supported with sufficient information about the tests, photos of the test, a load time curve, a load-displacement curve, and LVDT measurements. With the help of detailed measurements in the reports, the damage progression and failure load analysis can be done in more detail. The detail in these reports is also why some experimental cases from them are chosen during the (qualitative) sensitivity analysis.

Koekkoek et al. [88] report aimed to study the transition between flexure failure and shear failure for RC beams without stirrups. From reviewing the report, it was found that some of the experimental beams did consist of stirrups. Therefore, beams, where results were affected by the stirrups, will be neglected. Some important geometrical and material configurations that were varied have the following ranges:

- Effective depth: (269.50 mm - 762.50 mm)
- Effective span-to-depth ratio: (2.54 - 5.49)
- Concrete strength: ($f_{c,c}$: 23.70 MPa - 91.10 MPa)
- Reinforcement ratio: (0.58 % - 1.17 %)

From the results of these experiments, beam configurations were varied. A three-point test was applied here, and Figure 26 can be used to get an overview of the test.

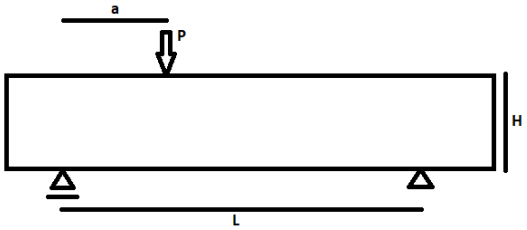

Figure 26 Three-point experiment configuration [83]

Garnica et al. [89] report was a follow-up study to Koekkoek's work [88], where the experiment analysis took place similarly at Stevin Lab. This report varies the same configurations as the earlier one but studied only geometrically large beams with the beam depth kept at 800mm or 1200 mm. Beams of 1200 mm have not been studied during the Koekkoek report. Some important geometrical and material configurations that were varied have the following ranges:

- Effective depth: (765.00 mm - 1160.00 mm)
- Effective span-to-depth ratio: (3.27 - 3.92)
- Concrete strength: ($f_{c,c}$: 81.25 MPa - 89.16 MPa)
- Reinforcement ratio: (0.27 % - 0.85 %)

Because the "Garnica and Yang" report is a follow-up to the "Koekkoek and Yang" report, both will be referred together further as the "Garnica & Koekkoek" report during this research. Fifty-one cases (37 + 14) will be simulated and studied from these two reports.

3.6 Experimental cases overview

An overview of the experimental cases is given in this chapter. Before the selection of the experimental cases, the following boundaries are considered:

- The effective span-to-depth ratio between 2.5 and 7.0 to capture the flexural shear failure
- A maximum effective depth of 1200 mm to simulate geometrically large/deep beams

The selected experiments were with three-point or four-point setups. Besides the boundaries, cases with different geometrical and material configurations were used. This approach would allow verifying the numerical model for various case configurations. The figure below gives a schema with the experimental cases and the main variation in their configuration.

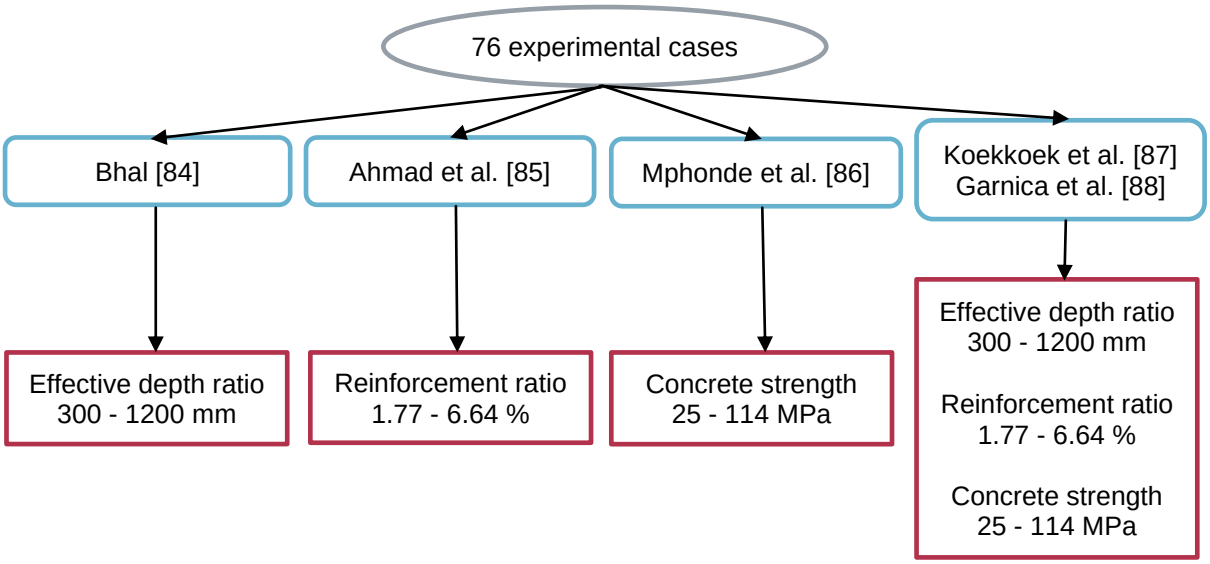

Figure 27 Experimental cases overview

4 Numerical modeling, analysis, results, and sensitivities

Before analyzing to see whether the numerical model can simulate the flexural shear failure for RC beams without stirrups, it is required to have a robust numerical model. Such a model can be obtained with sensitivity analysis using a numerical reference model. This model should represent most configurations of different RC beams without stirrups subjected to flexural shear failure while reducing as much model uncertainty as possible. Castaldo et al. [90] state that some model uncertainty characterizes the NLFEA. In addition, specific requirements should be met with the numerical model for RC beams without stirrups to simulate the flexural shear failure. Neglecting some requirements in the model will cause the neglection of a behavior. An example is that neglecting a nonlinear material behavior during numerical modeling required to simulate the flexural failure mode will lead to capturing a wrong failure mode.

In this chapter, the following topics are addressed:

1. **Reference numerical model:**
   The reference numerical model obtained from the literature review is first introduced in the section. In addition, information on initial cases for the numerical model sensitivity analysis using DIANA FEA is also provided here. These cases are a selection of differently configured (material and geometrical configurations) experimental cases from Chapter 3.5.
2. **Sensitivity analysis numerical model:**
   The sensitivity analysis for the numerical model is done on various modeling aspects of the constitutive model, finite element discretization, and analysis procedure. An analysis of the compression-compression confinement, two bond-slip relations in combination with two types of crack orientations are done for the constitutive model. Following that, two schemes of the incremental iteration procedure are analyzed. Finally, analysis is done on the reinforcement element type and element size for the finite element discretization. After the sensitivity analysis, the numerical model should be able to capture the correct damage progression, failure mode, and close enough failure load compared to the experiment.
3. **Quantitative analysis:**
   After the sensitivity analysis with the initial experimental cases simulates satisfactory results, a quantitative analysis can be done. This analysis will include all experimental cases from Chapter 3. This analysis obtains a general performance overview of the numerical model, and the model's limitations are identified.
4. **Size effect analysis:**
   During the size effect analysis, a set of geometrically scaled experimental cases will be used to show initial expressions on if the numerical method can capture the size effect. These cases will be based on experimental cases from Chapter 3.1.

4.1 Reference numerical model

The assumptions and modeling choices from the literature review are the foundation for the reference numerical model. The reference numerical model is given in Chapter 2.4 (Figure 21, Figure 22, and Figure 23), with the different modeling choices for sensitivity analysis marked with **Bold text**. In addition, the reference numerical model is also given in the tables from Table 7, Table 8, and Table 9 for a more ordered overview.

Table 7 Reference numerical model: constitutive model a

Concrete	***Modeling choice***
Class	Concrete and masonry
Material model	Total-strain crack model
Crack orientation	Fixed
compressive curve	Parabolic
Reduction model lateral cracking	Vecchio and Collins 1993
Lower bound reduction curve	0.4
Compressive-compressive confinement	Selby and Vecchio
Tensile curve	Hordijk
Reduction model Poisson's ratio	Damage-based
Crack-bandwidth	Govindjee's projection method
Shear retention function	Damage-based

Table 8 Reference numerical model: constitutive model b

Reinforcement	***Modeling choice***
Class	Reinforcement
Material model	Bond-slip reinforcement
Non-linear model	Von Mises plasticity
Plastic hardening	Total strain-yield stress
Hardening hypothesis	Strain hardening
Hardening type	Isotropic hardening
Bond-slip interface model	CEB-FIB 2010
Reinforcement type	Truss bond-slip

Table 9 Reference numerical model: finite element discretization

Concrete	***Modeling choice***
Quadratic element	CQ16M
Integration	Full: 3x3
Reinforcement	***Modeling choice***
Element	Truss element
Mesh	***Modeling choice***
Element size	Initially 25 mm
Mesher type	Hexa/ Quad
Seeding method	division

Table 10 Reference numerical model: analysis procedure

Analysis procedure	***Modeling choice***
Loading method	Displacement method
Command	Structural non-linear
Load steps	Start with 0.5 (linear part)
User specified	Depending on model
Maximum iterations	100
Incremental-iterative procedure	Full NR
Line searching	On
Continuation of iteration	Off
Satisfy all specified norms	Off
Convergence norm	Energy norm (0.001) and force norm (0.01)
No convergence	Continue

The sensitivity analysis will be done on the following modeling aspects:

- **The use of compression-compression confinement:**
  - Modeling aspect choices: “Selby and Vecchio” confinement and unconfined.
  - Motivation: this modeling aspect is critical for beams that fail in compression. Although the flexural shear failure is a tensile failure, it would still be interesting to see how this modeling aspect impacts concrete behavior during this failure mode.
- **The reinforcement bond-slip relation:**
  - Modeling aspect choices: the FIB bond-slip relation or the Shima bond-slip relation.
  - Motivation: according to Yang et al. [32], the crack pattern is more realistic when compared to a perfect bond assumption by including a bond-slip in the reinforcement modeling. The bond-slip relation allows relative displacement between the reinforcement and concrete, increasing cracks' progression. The main difference between the two bond-slip relations mentioned is that the FIB bond-slip relation accounts for a decrease in the bond stress if high slip values are increased further. The behavior discussed between the two models is shown in Figure 54. Besides decreasing the shear traction, the figure shows that the Shima bond-slip relation has a higher traction capacity.
- **The total strain crack models’ crack orientation:**
  - Modeling aspect choices: the fixed crack orientation or the rotating crack orientation.
  - Motivation: these two crack modeling choices will be combined with the compression-compression confinement and bond-slip constitutive modeling aspects. These combinations will result in eight different variations for the constitutive model, out of which the best-performing model can be chosen while still reviewing only a single aspect. An overview of the combinations is given in Figure 28.
- **The reinforcement element type:**
  - Modeling aspect choices: truss elements or beam elements.
  - Motivation: both reinforcement elements are combined with the plane stress element used for concrete in a numerical model. Interest is shown in these two elements because the beam elements include bending stiffness, making it possible for the concrete to withstand shear stresses with the dowel effect. As a result of using this element, the dowel action can be included. The truss elements do not include the dowel action.
- **Incremental-iterative procedure**:
  - Modeling aspect choices: the full NR iteration scheme or the Secant-iteration scheme.
  - Motivation: in the past, various sensitivity studies have been done on these two schemes. The results, however, have different opinions about the better scheme due to the different numerical models and situations for their respective analyses. It would be interesting to determine which scheme is the most accurate for RC beams without stirrups to simulate the flexural shear failure.
- **Global element size:**
  - Motivation: because beams with different dimensions are used during this research, this can become a crucial factor in deciding the accuracy of the numerical model. As seen later during the sensitivity analysis, the element size depends on the beam geometry (depth and length). This dependence on geometry is also reflected in many recommendation formulas for the element size mentioned in the literature review. Using too small elements is not a correct choice as this can result in high computational time. On the other hand, using a large element size reduces the model accuracy and can cause jumps between elements caused by a discontinuous stress field.

Four numerical cases are used for numerical model sensitivity analysis. The cases are based on “Garnica & Koekkoek” experiments and have geometrical and material properties variations. The properties are found in Table 11 with the names A122B1, B701B2, R804A1, and H601A. Some more cases with comparable properties for cases A122B1, R804A1, and H601A are included in the table to enhance the quality of the sensitivity analysis.

Sensitvity analysis cases' properties table:

Table 11 Sensitivity analysis cases properties

Test	Date:	Length L [mm]	Depth H [mm]	Effective span-to-depth ratio a [mm]	Effective depth d [mm]	α/d [-]	fc,cube [MPa]	reinforcement ratio ρ [%]	Rebar [mm]
A121A3	2015	5000	300	1000	270	3.7	78	1.17	3Ø20
A122B1	2015	5000	300	1000	271	3.7	79	1.16	3Ø20
A123A1	2015	5000	300	1000	270	3.7	79	1.16	3Ø20
B701B2	2015	5000	500	1500	472	3.18	81	0.67	3Ø20
R804A1	2016	8000	800	3500	755	4.64	85	0.65	3Ø25
R804B1	2015	8000	800	3500	755	4.64	85	0.65	3Ø25
H601A	2019	9000	1200	4500	1158	3.89	86	0.57	4Ø25
H602A	2019	9000	1200	4500	1158	3.89	86	0.57	4Ø25

A visualization of the three-point experimental test setup used for these cases is visible in Chapter 3, Figure 26. The initial element size for all cases A122B1, B701B2, and R804A1 is 25 mm. This element size is chosen based on the results of Chapter 2.2.2.3, but most importantly, Teshome [53] previously used this element size for beams from the "Garnica & Koekkoek" reports. Teshome also used an element size of 50 mm, which is too big according to the other recommendations from Chapter 2.2.2.3. For case H601A, the element size is 40 mm. The reasoning for not using an element size of 25 mm is given in Chapter 4.2.1.1. Finally, in this section, some notes regarding the four experimental cases are given below:

- R804A1, R804B1, and H601A were done with cyclic loading, which can influence the experimental results.
- A steel plate was added to R804B1, which was unfortunately deformed, causing an additional reduction of the global stiffness. This difference in stiffness is visible between experimental cases R804A1 and R804B1 (Figure 36), which have the same geometrical and material configurations.
- Figure 99 from Annex II explains the naming of the experimental cases for the "Garnica & Koekkoek" report.

After the numerical model sensitivity analysis, all the remaining cases mentioned in Chapter 3 are simulated and analyzed quantitatively. Once an accurate numerical model is found from the sensitivity analysis and quantitative numerical simulations, the use of the model can be furthered for the pilot research on the size effect.

4.2 Sensitivity analysis numerical model

The sensitivity analysis for the numerical model will be done with the following three modeling sections and order:

- The constitutive model
- Finite element discretization
- Analysis procedure

4.2.1 Constitutive model

Sensitivity analysis of the constitutive model analysis is done on the crack orientation, compressive lateral confinement, and bond-slip. The last two modeling aspects mentioned will be applied to the fixed and rotating crack orientations creating eight different numerical model combinations, as shown in Figure 28 below. The red arrows show which models will be compared to each other during the analysis.

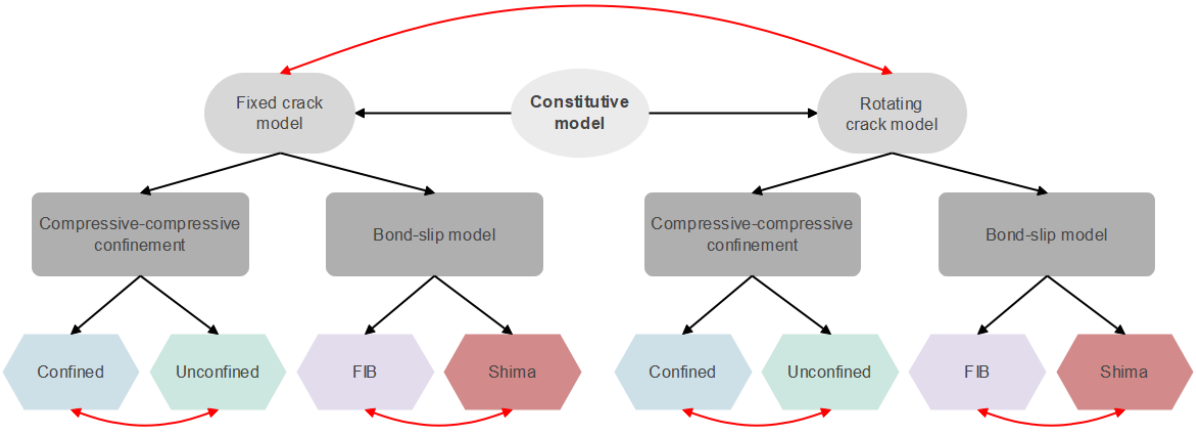

Figure 28 Constitutive model modeling aspects for sensitivity analysis

4.2.1.1 Crack orientation and compressive-lateral confinement

In this section, with variations in crack orientations and compressive-lateral confinement effects, the following four models are used for simulation:

- Confined compression-compression behavior fixed crack orientation and the FIB bond-slip relation with truss elements using the full NR iteration scheme (FCFTN)
- Unconfined compression-compression behavior fixed crack orientation and the FIB bond-slip relation with truss elements using the full NR iteration scheme (FUFTN)
- Confined rotating crack orientation and the FIB bond-slip relation with truss elements using the full NR iteration scheme (RCFTN)
- Unconfined rotating crack orientation and the FIB bond-slip relation with truss elements using the full NR iteration scheme (RUFTN)

Fixed crack orientation with variation in confinement

Confined variation

The reinforcement did not yield in any of the four cases for the confined fixed crack orientation numerical model (FCFTN). Also, most of the four cases' failure modes resembled the flexural shear failure description. An in-depth analysis is done below. The force-displacement graph's different marker meanings are introduced first, which also applies to other plots of this chapter. The force-displacement graphs consist of dots in the graph, which show the non-converged steps. Also, for cases A122B1 (Figure 29), B701B2 (Figure 33), and R804A1 (Figure 37), the failure load is at the plotted black cross, after which non-converged steps followed, and the simulation could not be trusted from that point on. Case H601A (Figure 38) does not have a black cross to show the failure step as the failure load is at the maximum load, after which a steep force decline was noticed. All four numerical cases are discussed next.

Figure 29 presents the force-displacement graph for case A121A3.

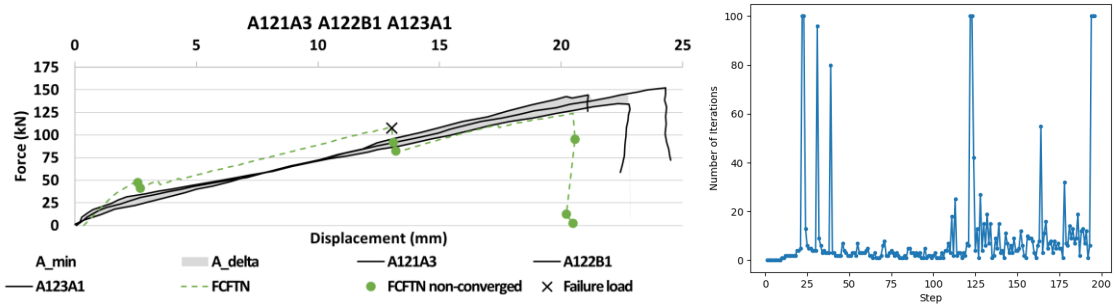

Figure 29 A121A3 confined fixed crack orientation sensitivity analysis: force-displacement graph (left) and convergence log (right)

The A122B1 with confined fixed crack orientation (FCFTN) numerical simulation does not have the same initial stiffness (before the first crack) as the experimental results. This stiffness result is because of previous experiments on the cantilever beam. The previous loading effect is not accounted for with the numerical model. As a result, the numerical models will show a lower displacement caused by its higher stiffness. The numerical stiffness captured after the first crack is like the experimental one. Figure 30 summarizes how the cases from the reports ([88] and [12]) were tested during the experiment to explain why some experimental cases have lower initial stiffnesses than those found by the numerical simulations. In the figure, options one and two are taken after shear failure is reached during testing. Option one strengthens the part on which shear failure occurs, and the support is moved to the undamaged parts for more tests. For option two, however, instead of fixing the undamaged part, the beam is tested at the other undamaged end of the beam. The two initial experimental stiffnesses from case R804A1 in Figure 37 also show this point in the result, even though both have the same geometrical and material configurations.

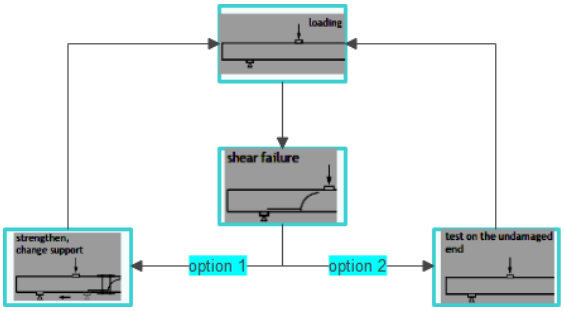

Figure 30 "Koekkoek and Garnica" experimental testing sequence [88]

For case A122B1 with confined fixed crack orientation, the maximum load is found at the cross plotted in the graph, after which the beam fails. There is a low failure load in the case of the fixed crack orientation here. This behavior will also be noticed in some of the other upcoming cases. The fixed crack orientation is combined with the damage-based shear retention factor. This factor is based on damage due to cracking, where the shear stress reduces as fast as the tensile stresses. Substantial changes in the shear retention factor of the fixed crack orientation explain the possible premature failure. For case A121A3, the change in the factor is visible in Figure 31, where Gknt represents the change in the shear retention factor.

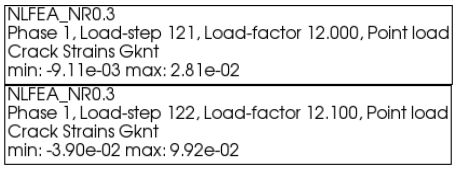

Figure 31 A121A3 confined fixed crack orientation: before (left) and at failure crack stress (right)

In Figure 32, the maximum principal strain is for further analysis.

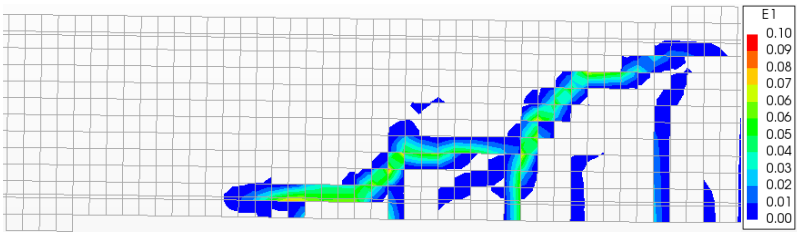

Figure 32 A121A3 confined fixed crack orientation sensitivity analysis: maximum principal strain

The failure mode for case A121A3 is recognized as flexural shear failure. The failure load is captured when failure of the beam occurs, and the force decreases. The steps plotted after in the force-displacement graph are non-converged, and its results are not trustable anymore. This case simulation will be mentioned later during the following case analysis for more findings. The force-displacement graph for case B701B2 with confined fixed crack orientation is shown below:

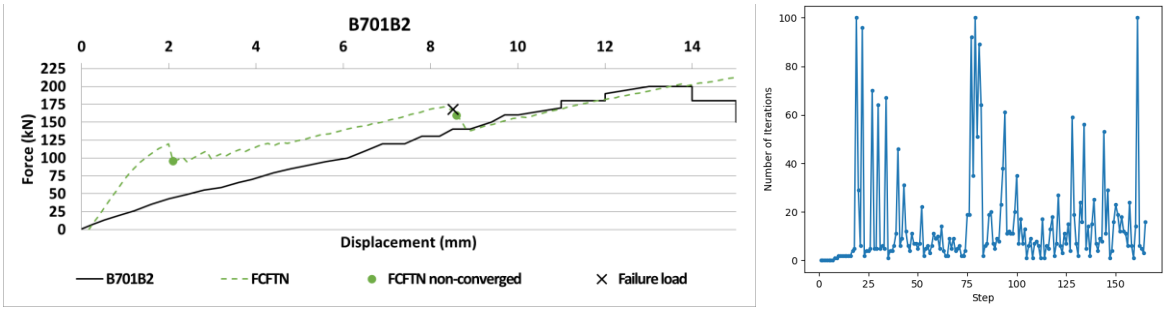

Figure 33 B701B2 confined fixed crack orientation sensitivity analysis: force-displacement graph (left) and convergence log (right)

Similarly to case A122B1 with confined fixed crack orientation, case B701B2 with the same numerical modeling aspects failure load is at the black cross plotted in the force-displacement graph. Further analysis after the failure load is not required due to the unreliable non-converged steps (dots) after this load. The failure load has been discussed till now, but the failure mode is also important. The plot of the principal strain can be found in the figure below.

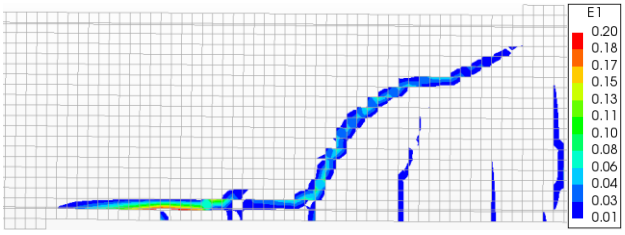

Figure 34 B701B2 confined fixed crack orientation sensitivity analysis: maximum principal strain

Case B701B2 with confined fixed crack orientation is subjected to dowel failure, indicated by the large concentration of cracks along the reinforcement. The difference between flexural shear failure and dowel failure can be seen in Figure 35.

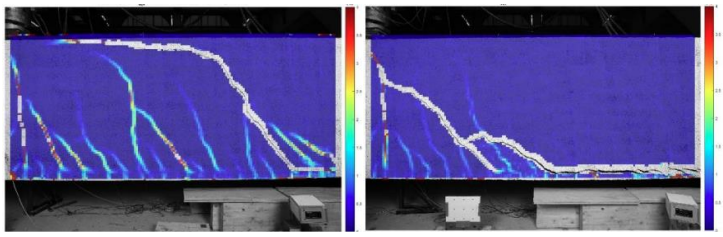

Figure 35 Flexural shear (left) and dowel failure (right) [12]

The flexural shear failure originates from a critical inclined crack that develops two secondary branches. The specimen loses its capacity when the unstable secondary branches develop. In contrast, dowel failure is characterized by the detachment of the tensile reinforcement from a flexural crack. No secondary branch develops in the compression zone [12]. From Figure 32 for case A121A3, a small secondary branch is visible in the compression zone related to the flexural shear failure.

Different potential causes can contribute to the cause of dowel failure. Firstly, due to significant changes in the shear retention factor in the elements near the reinforcement. As a result, the numerical model cannot solve the excessive change in the factor, the cracks propagate, and (premature) dowel failure occurs. Secondly, due to the element size, as crack propagation rate depends on its size. Lastly, due to the bond-slip sensitivity from the FIB bond-slip relation and elements used. These reasons may have led to further crack propagation along the reinforcement. However, they should be studied further with more sensitivity analysis on different modeling aspects to find the cause. The upcoming sensitivity analysis on other aspects will help with the reasoning for these two cases on the correct damage progression and failure mode. Next, case R804A1 is analyzed with its force-displacement graph given below.

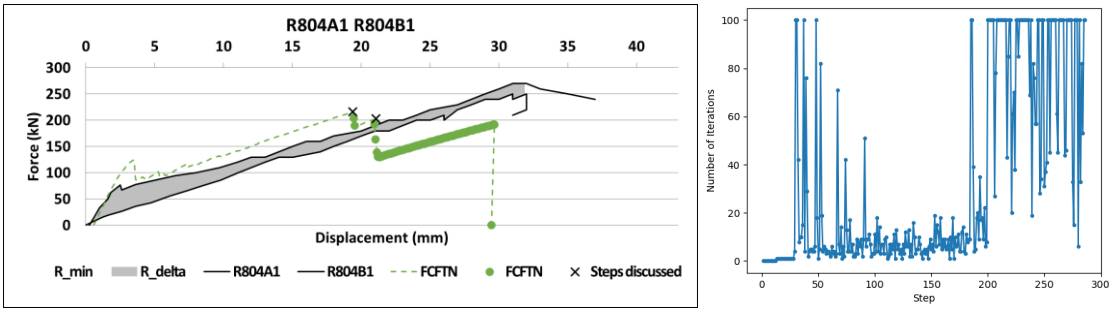

Figure 36 R804A1 confined fixed crack orientation sensitivity analysis: force-displacement graph (left) and convergence log (right)

During the experiments in the lab, two specimens were experimented on with the same configurations. The numerical model simulation with confined fixed crack orientation has the same pre-cracking and post-cracking stiffness as the first experimental R804A1 specimen. However, the specimen tested afterward has a lower initial stiffness. This stiffness is due to the testing sequence explained in Figure 37. For case R804A1 with confined fixed crack orientation, two crosses are plotted at load steps 184 and 199, followed by multiple non-converged steps (green dots) plotted along the force-displacement graph. Analysis shows failure occurs during the second maximum load (second cross), while diagonal cracks formed at the first maximum step. The last segment of the force-displacement graph is not usable for analysis due to the convergence difficulties shown by the plotted dots. The principal strain is plotted below to analyze the crack pattern for case R801A.

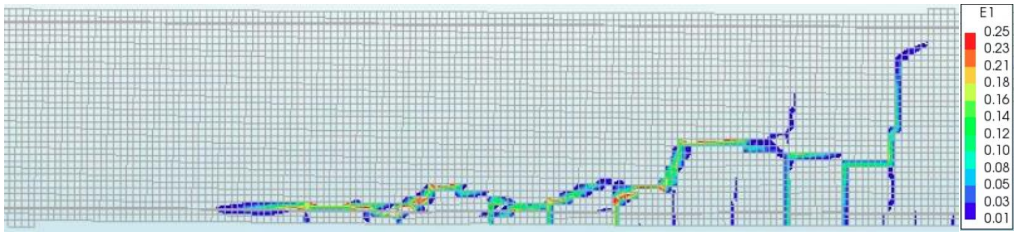

Figure 37 R804A1 confined fixed crack orientation sensitivity analysis: maximum principal strain

For R804A1 with confined fixed crack orientation, the most damage is along the reinforcement, indicating dowel failure instead of flexural shear failure. From previous experience, irregular crack patterns (the jumps in the cracking pattern) can be due to a too-small element size. A too-small element size does not always simulate the most accurate results, as numerical instabilities can occur. However, this statement is not a conclusion and will be addressed during the element size sensitivity analysis. The element size of 25 mm will be used until the element size sensitivity analysis. This approach helps keep the analysis consistent during comparison with the upcoming sections.

Finally, the last case (H601A) can be analyzed, with its force-displacement graph given below.

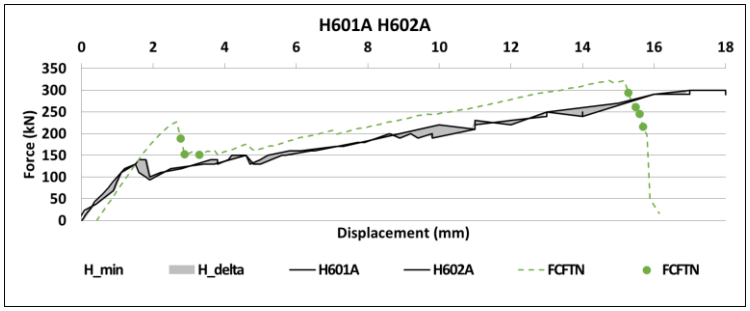

Figure 38 H601A confined fixed crack orientation sensitivity analysis: force-displacement graph

Special attention is required for case H601A. For the other cases, acceptable results were found using an element size of 25 mm during this and other upcoming sensitivity analyses, even if not yet accurate. Unfortunately, case H601A showed element size sensitivity issues (irregular crack patterns due to a too-small element size) with an element size of 25 mm during all modeling aspects' sensitivity analyses. This issue resulted in wrong damage progression and over-predictions of the failure load. Because none of the modeling aspects' sensitivity analysis results was practical for conclusions due to the issues faced, the element size was changed to 40 mm. Hereafter, the modeling aspects sensitivity analysis was simulated for case H601A with a new element size. Avoiding changing to an appropriate element size would make the simulated results from case H601A mediocre and give inaccurate conclusions on a modeling aspect. Only for this case the element size is changed before Chapter 4.2.3.2. For cases A122B1, B701B2, and R804A1, an element size of 25 mm is maintained. The element size of 40 mm, obtained from a pre-element size sensitivity analysis, also be applied to the other modeling aspects' sensitivity analysis only for this case. From the results of the new element size, the correct damage progression, failure mode (flexural shear failure), and an acceptable failure load were found with this numerical setup. The same pre-cracking and post-cracking stiffness was also found for the simulation and experiment. While the force-displacement graph is visible in the figure above, the flexural shear failure is visible below. In the initial branch there of the force-displacement graph, overshooting of the failure load occurs before the first crack. This overshooting can be due to concrete modeling aspects, reinforcement modeling aspects, or a modeling aspect of finite element discretization. The overshooting of the initial branch will be addressed during the other modeling aspect sensitivity analysis when more information is known to get better observations and a conclusion on this problem.

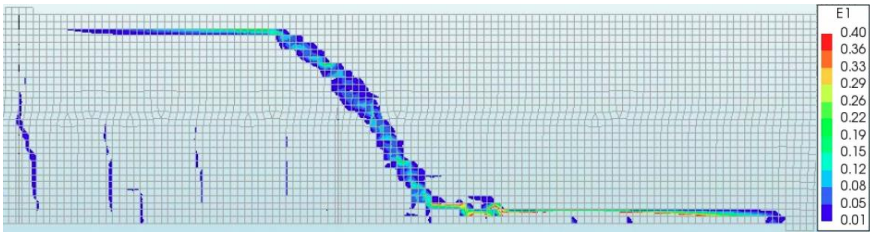

Figure 39 H601A confined fixed crack orientation sensitivity analysis: principal strain

Unconfined variation

For the following numerical analysis, the concrete compression-compression behavior is unconfined to study the modeling aspects' effect on the numerical model. The unconfined numerical model will be compared to the confined one from the previous section.

The force-displacement graphs of all four cases can be seen in Figure 40, with blue lines showing the unconfined results and green lines showing the confined results.

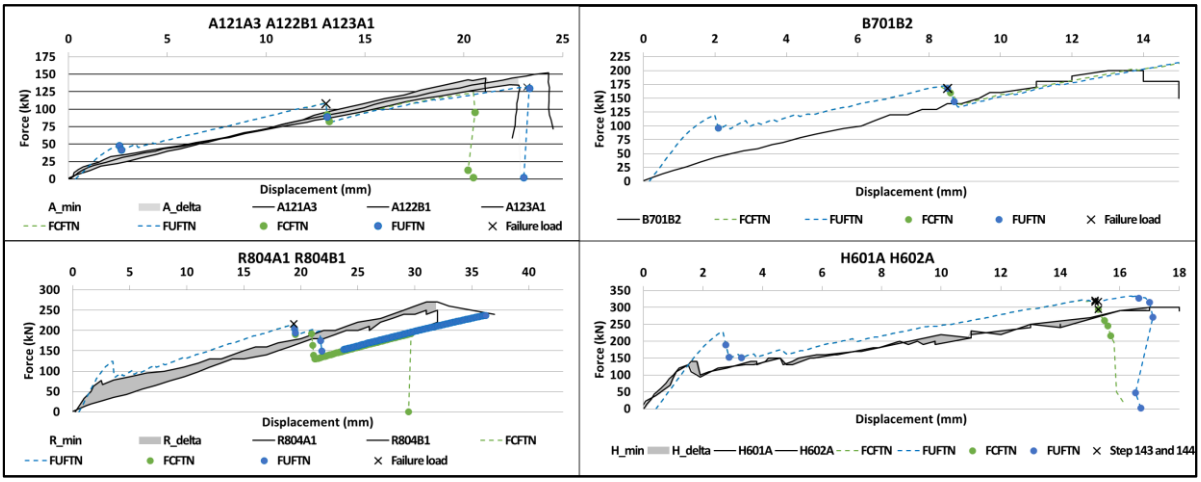

Figure 40 Force-displacement graphs: confined and unconfined fixed crack orientation

As for the confined fixed crack orientation (FCFTN) beams, the same situation occurs for all unconfined (FUFTN) beams regarding stiffness. Both numerical model configurations have similar stiffnesses along the path of the force-displacement graphs. It is immediately observed from the force-displacement graphs above that the unconfined cases “A122B1, B701B2, and R804A1” have a similar displacement and failure load as the confined ones. In Annex III, the maximum strain figures are plotted with a comparison of the confined and unconfined fixed crack orientation cases.

The same result for the confined and unconfined beams is not the situation for case H601A, as the confined numerical model failed earlier. Case H601A confined numerical model and unconfined numerical model in-plane principal stresses are shown at the confined numerical model failure load step and step after to study the difference between the numerical models. In the force-displacement graph (Figure 40), load steps 143 and 144 were plotted with black crosses.

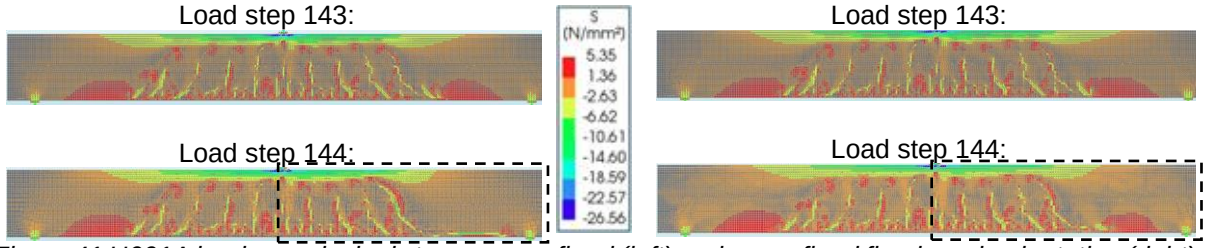

Figure 41 H601A in-plane principal stresses: confined (left) and unconfined fixed crack orientation (right)

At load step 143, the stresses are similar for the confined and unconfined numerical simulation. However, the confined model has sudden high stresses along the reinforcement at step 144. The formation of these stresses causes earlier development of the flexural shear crack, leading to the confined numerical model failing earlier than the unconfined one. The force-displacement graph also reflects the failure load difference, with a slight difference of 0.03 % between the two numerical models. The results suggest that modeling the confinement for cases with flexural shear failure cases is unnecessary. In addition, the analysis output and non-converged steps (dots in the force-displacement graph) also suggest that the unconfined state is preferred due to being slightly more accurate for simulations of such cases.

Below, the maximum principal strain plot is given where the flexural shear failure is recognized for both cases. (Because flexural shear failure is not a compressive failure type but a brittle shear-tension failure, there is no dependence on concrete crushing).

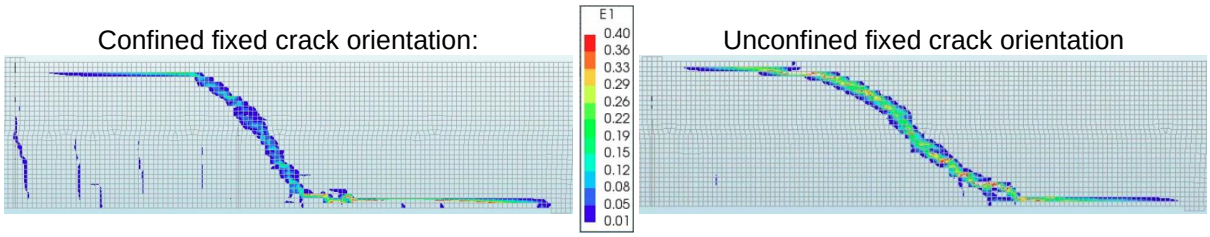

Figure 42 H601A maximum principal strain: confined (left) and unconfined fixed crack orientation (right)

Rotating crack orientation with variation in confinement

Confined variation

The fixed crack orientation from the previous analysis is changed to the rotating crack orientation for this numerical model. This change is made to see if an improvement can be made to the numerical model by changing the crack orientation. This section will compare the confined rotating crack orientations (RCFTN) model to the confined fixed crack orientation (FCFTN). This approach changes one modeling aspect between the two numerical models, making an easy comparison possible. The force-displacement and maximum principal strain graphs are below for cases A121A3 and B701B2 with the two confined rotating crack orientations (Figure 43 and Figure 44). The two cases analysis is done together as the same difference in response and conclusions are found due to change in the crack orientation of the numerical model.

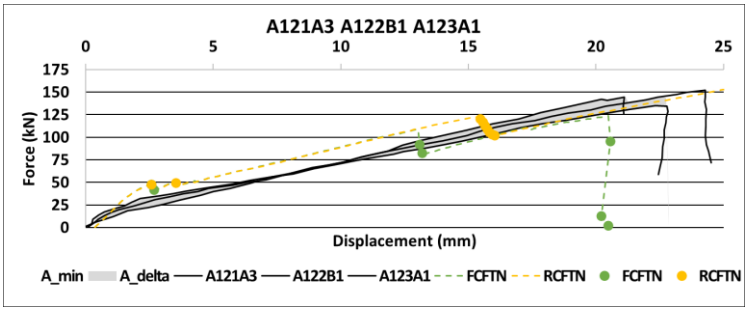

Figure 43 A121A3 confined rotating crack orientation sensitivity analysis: force-displacement graph

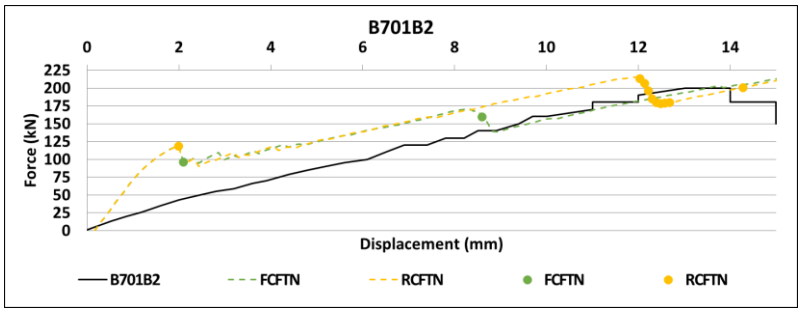

Figure 44 B701B2 confined rotating crack orientation sensitivity analysis: force-displacement graph

The force-displacement graph shows that the failure load and displacement predictions are more accurate with the rotating crack model than the fixed crack orientation model. Even though there are some non-converged steps (dots in the force-displacement graph) for the rotating numerical model, these steps are after the model has been successfully simulated to failure. The flexural shear failure for both models occurs after the first maximum load and is followed by the non-converged steps. Thus, damage progression, the failure mode, and the failure load itself is not affected by the non-converged steps.

The maximum principal strain for both models is given below:

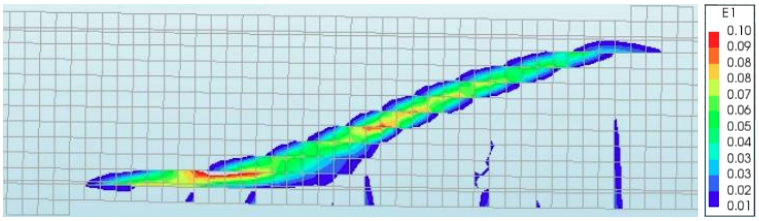

Figure 45 A121A3 confined rotating crack orientation sensitivity analysis: maximum principal strain

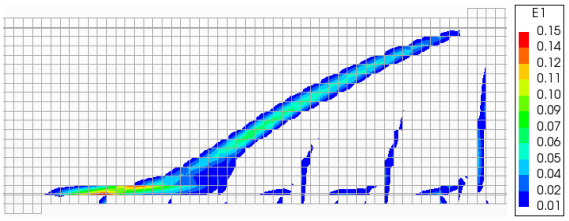

Figure 46 B701B2 confined rotating crack orientation sensitivity analysis: maximum principal strain

A121A3 and B701B2 confined rotating crack orientations models capture the same failure mode as the numerical models with a fixed orientation. However, as expected, the rotating crack orientation model's crack does not simulate the experimental crack (Figure 100 and Figure 101) as accurately as the fixed crack orientation model (Figure 29 and Figure 33). The reason for a more accurate crack pattern is that the fixed crack orientations' crack orientation is constant. The fixed orientation is more suitable for brittle materials due to the material's cracking behavior. The next analysis is done for case R804A1 with the force-displacement graph and non-converged steps log below (Figure 47).

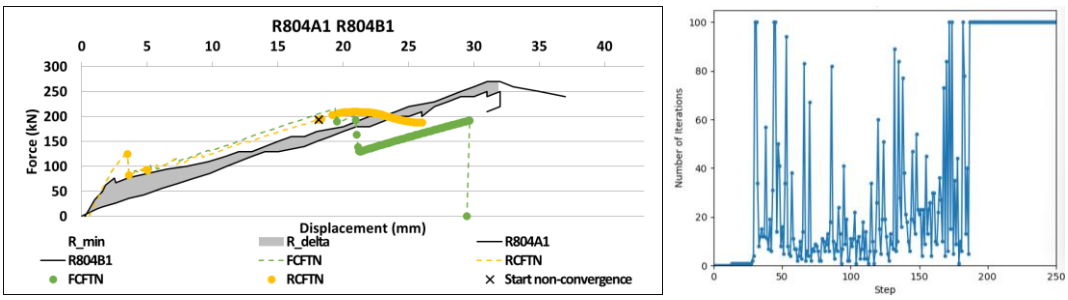

Figure 47 R804A1 confined rotating crack orientation: force-displacement graph (left) and converged steps log (right)

The result from R804A1 with confined rotating crack orientations cannot be trusted as many convergence difficulties exist before the failure load is reached. The yellow dots in the plot are the non-converged steps, while the black cross shows the first steps before the series of non-converged steps. The high number of non-converged steps is due to over-rotation caused by the rotating crack orientation. In previous research, Løvli [49] found a direct correlation between over-rotation and the number of non-converged steps. Stability issues accompany the over-rotation during simulation, and a wrong failure mode is also captured instead of the expected flexural shear failure from the experiment. For R804A1 with confined rotating crack orientations, this can be seen in Figure 48, where there are large strains around the reinforcement and concrete cover.

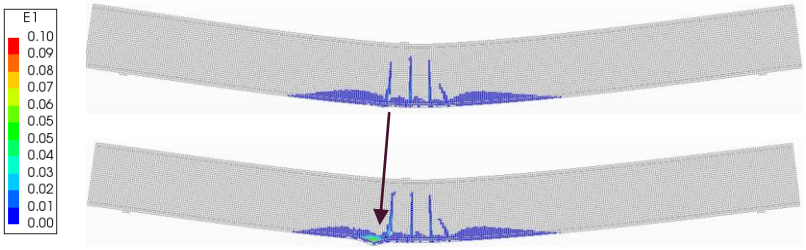

Figure 48 R804A1 confined rotating crack orientation: delamination

The failure is the delamination of the concrete cover caused by cracking along the reinforcement. In addition, the crack runs more vertically than diagonally (diagonal crack) toward the loading point. The figure plot is for the first non-converged step (black cross marker) and some steps after with an already extremely high maximum principal strain. The element is already dissolved before the maximum load is reached. The in-plane principal stress has also been plotted at the delamination location in Figure 49 to support the claim on excessive over-rotation of the crack orientation.

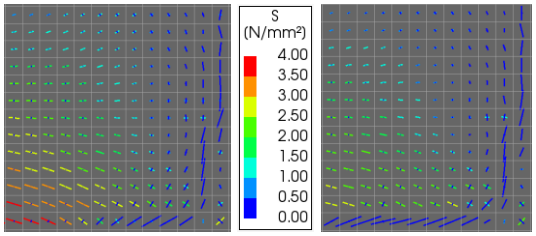

Figure 49 R804A1 confined rotating crack orientation: in-plane principal stress

For case R804A1, the experimental failure mode found in Figure 102 shows that no delamination should occur. Just like for case R804A1 with confined rotating crack orientations, the same delamination problem due to over-rotation was observed from the analysis of case H601A with confined rotating crack orientations. Thus, an in-detail analysis will be left out for case H601A as this will be redundant.

Unconfined variation

For the comparison of the unconfined rotating crack numerical model (RUFTN), the confined rotating crack orientation (RCFTN) model will be used. There is a neglectable difference between the results of the two models. To keep this section short, cases A121A3 and B701B2 are analyzed together, where both simulated acceptable results. The force-displacement graphs with a comparison between the confined and unconfined rotating crack orientation models are shown below for both cases:

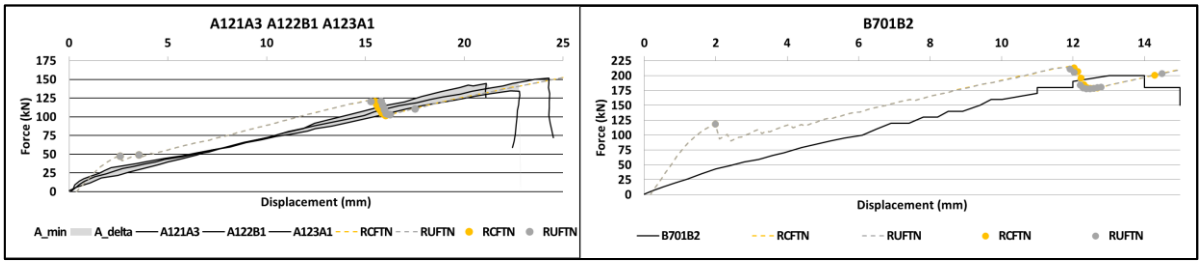

Figure 50 Force-displacement graphs confined rotating crack orientation: A121A3 (left) and B701B2 (right)

As seen for cases A121A3 and B701B2 with unconfined rotating crack orientation from Figure 50, there is almost negligible difference between the force-displacement graphs of the confined and rotating unconfined rotating crack orientation numerical model. for the two cases. The crack of both models is also similar. Thus Figure 43 and Figure 44 can be used to visualize the unconfined model crack. Next, case R804A1 with unconfined rotating crack orientation is analyzed. Previously this case for the confined numerical model resulted in delamination due to over-rotation. For analysis of case R804A1 with an unconfined rotating crack orientation, the force-displacement graph is shown in Figure 51. The unconfined numerical model runs more stable than the confined model (also found for the fixed crack orientation). The convergence problems do occur, but at a later stage than the confined numerical model, thus simulating a higher failure load.

Below, the force-displacement graph and the convergence log are shown.

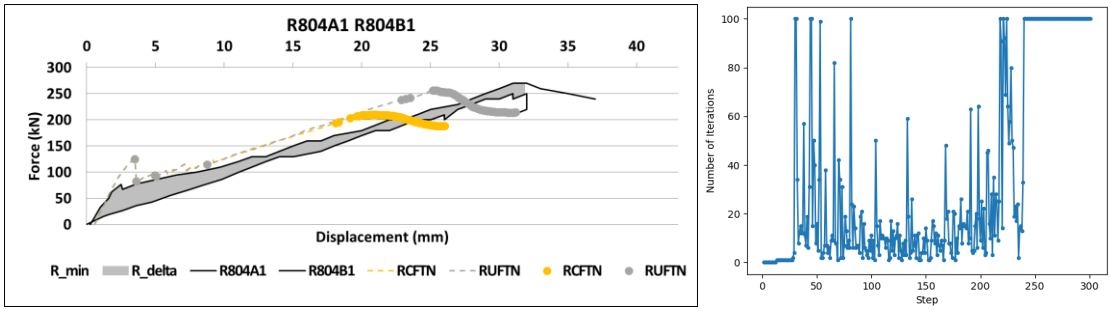

Figure 51 R804A1 unconfined rotating crack orientation: force-displacement graph (left) and convergence log (right)

Unfortunately, just like for case R804A1 with the confined rotating crack orientation numerical model, the unconfined model is also subjected to over-rotation before the failure load is reached, thus resulting in delamination of the concrete cover. The delamination is visible in Figure 52 below. The results show a strong correlation between the non-converged steps and over-rotation.

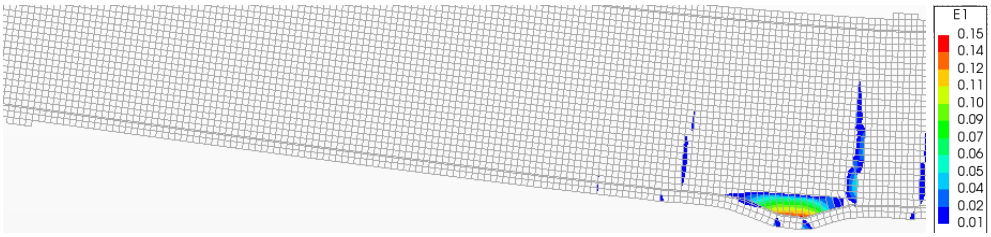

Figure 52 R804A1 unconfined rotating crack orientation: delamination

The over-rotation for case H601A gets worse. The difference between case R804A1 and H601A is the geometrical size. The results show that the rotating crack orientation numerical model results in over-rotation for RC beams without stirrups when applied to geometrically large beams (R804A1) and worsens as the beam size increases (H601A). Therefore, this research cannot use the rotating crack orientation without including the compression-compression confinement.

Below is a table summarizing Chapter 4.2.1.1 results for the confined and unconfined fixed crack orientation numerical model for an overview of this section. The results of the rotating crack orientation are neglected as results for some cases were loaded with non-converged steps overshooting the norms and thus not acceptable.

Table 12 Confinement with the fixed crack orientation sensitivity analysis summary

Test	A121A3	A122B1	A123A1	B701B2	R804A1	R804B1	H601A	H602A
Vexperiment [kN]	145	152	137	202	269	250	306	306
FCFTN Vnumerical [kN]	109	109	109	168	216	216	322	322
FCFTN $\frac{Vexperimental}{Vnumerical}$ [-]	1.33	1.40	1.25	1.20	1.25	1.16	0.95	0.95
FUFTN Vnumerical [kN]	108	108	108	173	216	216	333	333
FUFTN $\frac{Vexperimental}{Vnumerical}$ [-]	1.34	1.41	1.26	1.17	1.25	1.16	0.92	0.92

4.2.1.2 Crack orientation and bond-slip relation

This section will replace and compare the Shima bond-slip relation with the FIB bond-slip relation in the numerical model. Analysis of the modeling aspect will be combined with the fixed crack and rotated crack orientation models. The following four numerical models will be used to compare the Shima and FIB bond-slip relation:

- Unconfined compression-compression behavior fixed crack orientation and the FIB bond-slip relation with truss elements using the full NR iteration scheme (FUFTN)
- Unconfined compression-compression behavior rotating crack orientation and the FIB bond-slip relation with truss elements using the full NR iteration scheme (RUFTN)
- Unconfined compression-compression behavior fixed crack orientation and the Shima bond-slip relation with truss elements using the full NR iteration scheme (FUSTN)
- Unconfined compression-compression behavior rotating crack orientation and the Shima bond-slip relation with truss elements using the full NR iteration scheme (RUSTN)

Fixed crack orientation with variation in bond-slip relation

This section will discuss the fixed crack orientation numerical models combined with the Shima bond-slip relation (FUSTN) and compare them to the FIB bond-slip (FUFTN) models. Comparing the Shima bond-slip relation performance to the FIB bond-slip relation is essential for the interaction between the concrete and reinforcement. The comparison is hoped to successfully conclude which bond-slip relation is more accurate in representing the experimental results and should be used for the constitutive model. The load-displacement graphs for all four cases with both bond-slip relation numerical models are plotted in Figure 53 for comparison. The green line shows the model with the FIB bond-slip relation, while the blue line shows the model with the Shima bond-slip relation.

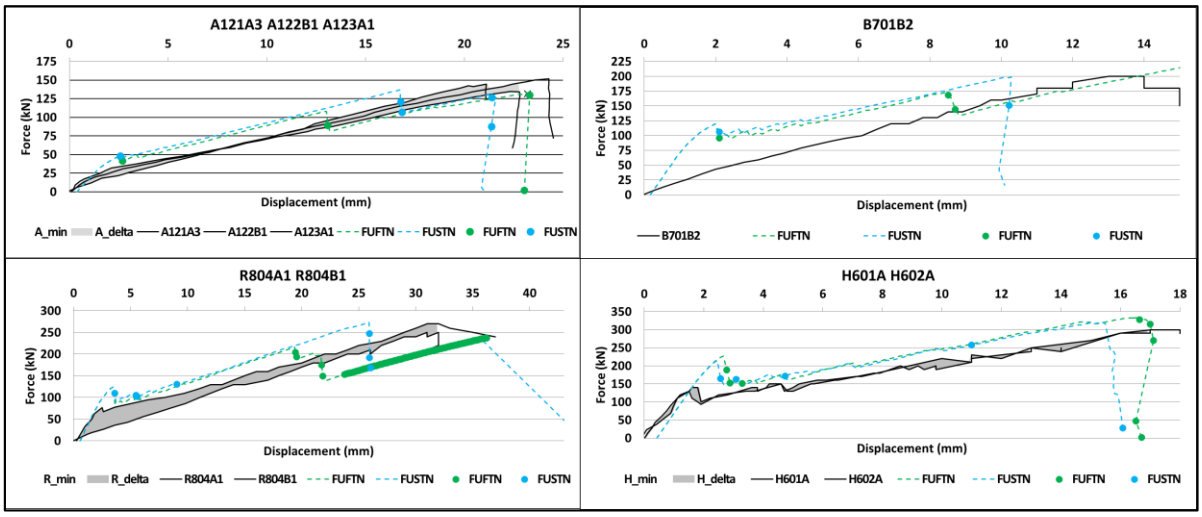

Figure 53 Force-displacement graph: FIB and Shima bond-slip relation

In the force-displacement graphs, cases A121A3, B701B2, and R804A1 instantly increased and improved the failure load and displacement with the Shima bond-slip relation. The failure load and displacement simulations with the Shima bond-slip relation are closer to the experimental failure loads. An in-depth analysis is performed to determine why there is such a difference by changing the bond-slip relation for the numerical model. Because the analysis conclusions for the bond-slip relation of these three cases (cases A121A3, B701B2, and R804A1) were almost similar, one of them is picked for a detailed explanation in this chapter. During the previous sensitivity analysis, the most explanation was done on cases A121A3 and R804A1, so now case B701B2 is chosen for the in-detail sensitivity analysis.

Case H601A, in contrast to the other three cases, showed a decrease in failure load and displacement with the Shima bond-slip relation. However, the simulated failure load of the Shima bond-slip relation is also closer to the experimental failure load for this case. Case B701B2 and case H601A will be primarily focused on during this sensitivity. This approach helps avoid overcrowding this section with results from all four cases, helps spot differences between case B701B2 and case H601A, and includes all important observations/conclusions. However, at the end of the in-depth analysis, a summarizing table will be shown with results for all four cases. A sensitivity analysis on case B701B2 is done first.

For case B701B2 (from Figure 53 force-displacement graph), the Shima-bond-slip relation failure load is close to the experimental one. In the force-displacement graph, the Shima bond-slip relation also has a steeper drop in force. This steeper drop mimics the brittle nature of the flexural shear failure better. A 'traction and slip' relation in Figure 54 is plotted for case B701B2 to understand the difference between the bond-slip relation from a theoretical perspective. The plot was made using Shima et al. calculations for the Shima bond-slip relation and the CEB-FIB 2010 calculations for the FIB bond-slip relation, found in Chapter 2.2.1.2. The same material values were used for the calculations of this plot by entering these values in their respective formulas. Three interesting findings are introduced from the figure while using the same material configurations for bond-slip relations modeling assumptions. First, the FIB bond-slip relation decreases the bond stress at high slip values. Secondly, the Shima bond-slip relation has a higher shear traction capacity. Lastly, a higher initial stiffness for the Shima bond-slip relation is another important difference between the two models.

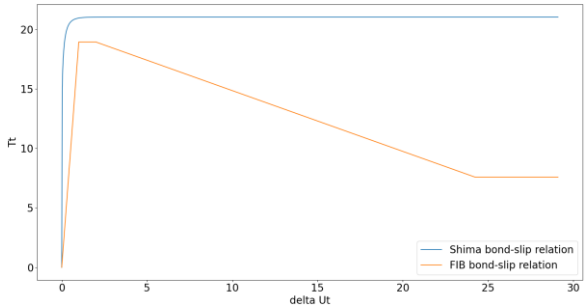

Figure 54 B701B2: FIB and Shima bond-slip relation curves

Next, the numerical models' reinforcement results (Cauchy stresses, total interface traction, interface relative displacements) are analyzed. The results of the two bond-slip relation numerical models and their respective failure loads found in the force-displacement graph (Figure 53) have been plotted below. The traction and relative displacement results have been zoomed in at the location where the failure crack occurs instead of showing the full beam to better spot the differences between the bond-slip relations.

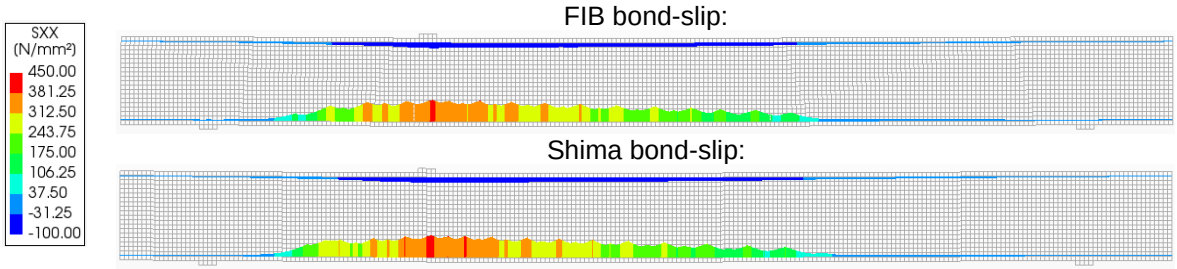

Figure 55 B701B2 reinforcement stresses: FIB (top) and Shima bond-slip relation (bottom)

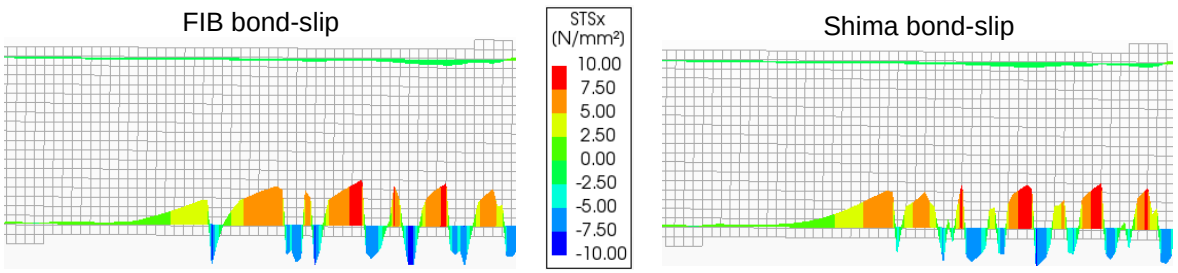

Figure 56 B701B2 interface shear traction: FIB (left) and Shima bond-slip relation (right)

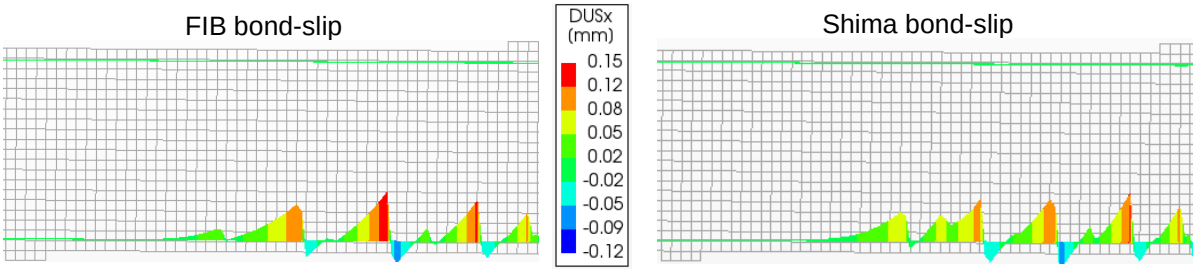

Figure 57 B701B2 interface relative displacement: FIB (left) and Shima bond-slip relation (right)

When comparing, there are no apparent differences between the maximum stresses and tractions results of the two bond-slip relation models. However, the Shima bond-slip relation model has lower relative displacements at its failure load than the FIB bond-slip relation model, even though the latter failed earlier. The maximum shear traction for the bond-slip relations has not been reached at this stage, as visible in the figures' legend. Due to the higher initial stiffness, the Shima bond-slip relation allows for less relative displacement between the materials. Because of the lower initial stiffness, a larger relative displacement is caused, resulting in faster crack propagation for the FIB bond-slip relation. The numerical model could not deal with the FIB bond-slip relation model's high crack propagation rate at the failure load. The behavior is also reflected in the non-converged step after this point. The maximum principal strains for case B701B2 are given in Figure 58 below to show the failure mode and strains:

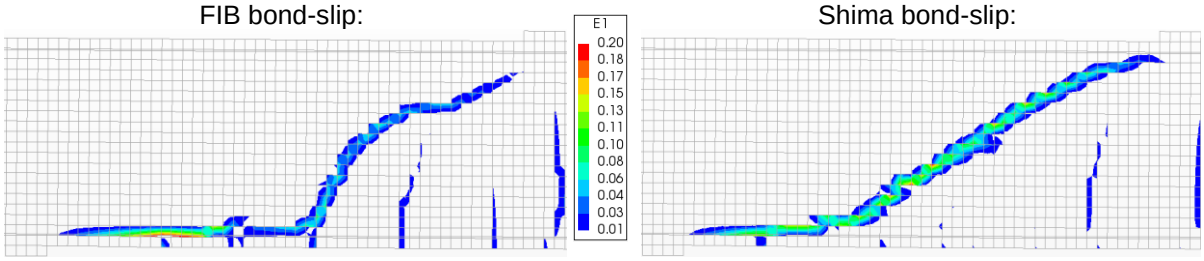

Figure 58 B701B2 maximum principal strains: FIB (left) and Shima bond-slip relation (right)

During the Shima bond-slip relation sensitivity analysis, the s small secondary branch in the compression zone is developed, with less concentrated stresses along the reinforcement. Looking at the experimental specimen crack pattern (Annex III, Figure 101), the pattern is mimicked better with the Shima bond-slip relation.

The sensitivity analysis results for case H601A (Figure 53) are discussed now. The force-displacement graph for this case showed a large overshot in the initial branch using the FIB bond-slip relation. The overshooting has been reduced with the Shima bond-slip relation. After the initial overshooting, both bond-slip relation numerical models return to a similar location in the force-displacement graph and follow an almost identical path. This behavior shows that the overshooting does not impact the simulation for further load steps. The improvement in the branch is related to the activation of the reinforcement and concrete interaction after the initial crack. At the initial crack, there is a case of non-convergence for both schemes. During other modeling aspects sensitivity analyses, more analysis will be done on the cause of the overshooting, as this might depend on more modeling aspects than only the bond-slip relation. Unlike the previous numerical case, H601A does not differ much between the Shima bond-slip relation and the FIB bond-slip relation in failure load. The reinforcement ratio is only 0.57 % for this case, explaining the small difference between the bond-slip relations. Even though the bond between the reinforcement and concrete is essential to transfer the stresses between them, the bond-slip relations' influence decreases as the reinforcement ratio is low. There is less surface area for the bond between the two materials. Compared to the case's experimental result, the bond-slip relations slightly overpredict the failure load (Shima by 5 kN and FIB by 15 kN). The results show that the Shima bond-slip relation overpredicts less than the FIB bond-slip relation, with the difference between the two numerical models' failure loads being a marginal 1.04%.

Below, the reinforcement stresses, shear tractions, and relative displacement are plotted to analyze the bond-slip relation influence. The plots are made at the failure load of each bond-slip relation numerical model.

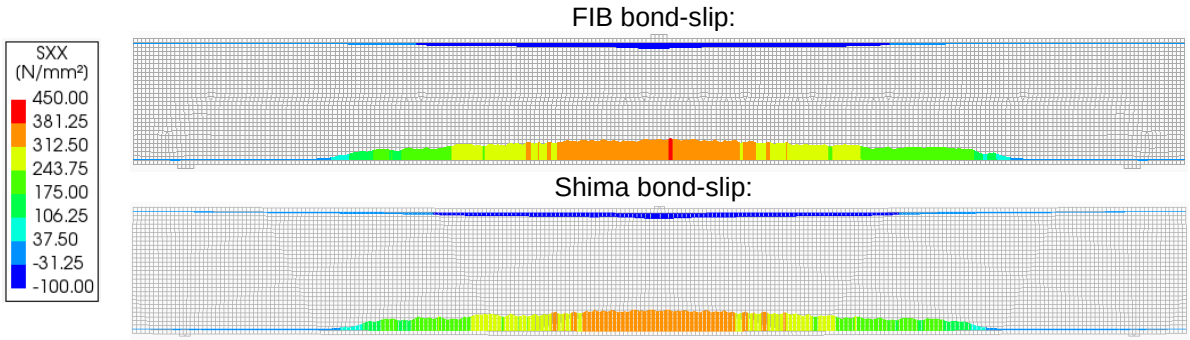

Figure 59 H601A reinforcement stresses: FIB (top) and Shima bond-slip relation (bottom)

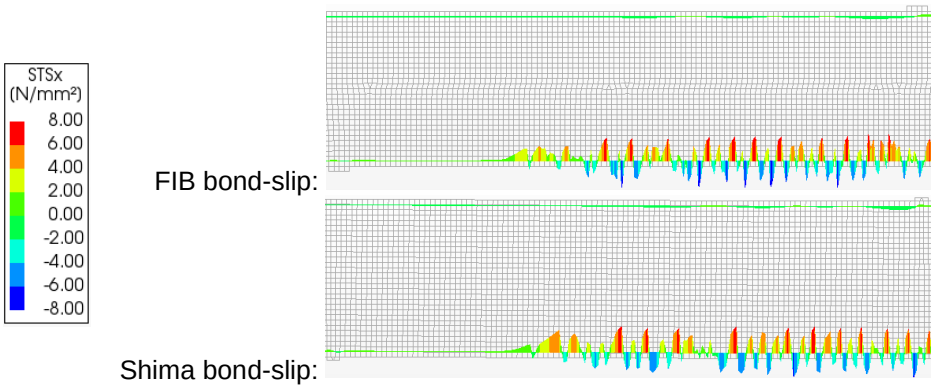

Figure 60 H601A interface shear traction: FIB (top) and Shima bond-slip relation (bottom)

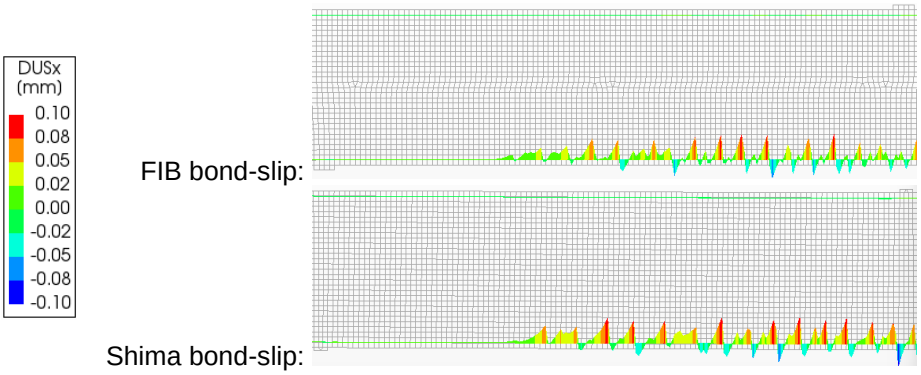

Figure 61 H601A interface relative displacement: FIB (top) and Shima bond-slip relation (bottom)

When the results at the numerical model's respective failure loads are studied, the FIB bond-slip relation numerical model relative displacements from the plots are slightly larger. The higher value is logical as the FIB bond-slip relation deforms more and has a slightly higher failure load, as seen in the force-displacement graph. Due to the higher initial stiffness for the Shima bond-slip relation, the shear tractions appear slightly higher. The maximum tractions have not yet been reached for the bond-slip relation numerical models with a relative displacement of less than 0.1 mm. The simulation with FIB bond-slip relation results in acceptable values.

An interesting behavior is noticed by comparing the relative displacement of the bond-slip relations between case B701B2 and H601A. If there is not too high of a relative displacement occurring (this happens with the FIB bond-slip relation model), the numerical model has an easier time coping with the changes in the model during each step for the brittle failure mode cases. Also, this is reflected in the small number of non-converged steps. For case H601A, the Shima bond-slip relation, and the FIB bond-slip relation only have non-converged steps during the initial cracking. The other non-converged steps are found after successfully simulating the correct failure mode. These non-converged steps are visible with the dots in the force-displacement graph (Figure 53). The slight difference between the bond-slip relation models is also due to the low reinforcement ratio for this specific case (H601A), causing the reinforcement ratio to contribute less to the beam capacity. Lastly, the maximum principal crack strain is given where the simulation of the flexural shear failure is seen for both bond-slip relations.

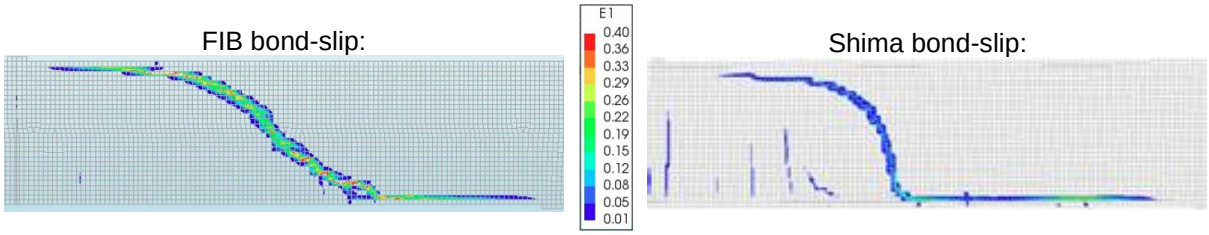

Figure 62 H601A maximum principal strains: FIB (top) and Shima bond-slip relation (bottom)

Rotating crack orientation with variation in bond-slip relation

In this unconfined rotating crack orientation numerical model, the FIB bond-slip relation (RUFTN) is replaced with the Shima bond-slip relation (RUSTN) and used to analyze the bond-slip relations. Many convergence difficulties were found during the analysis for the numerical simulations of all four cases (A121A3, B701B2, R804A1, and H601A) using the Shima bond-slip relation. For case A121A3, the non-converged steps log and the force-displacement graph has been plotted in Figure 63.

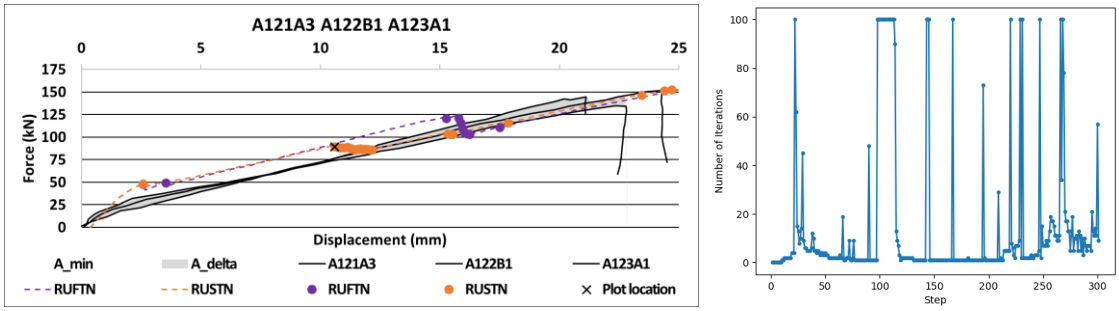

Figure 63 A121A3 rotating crack orientation with Shima bond-slip relation: force-displacement graph (left) and convergence log (right)

Also, Figure 64 includes the crack width plot to understand what happened because of the convergence problems. It should be noted that the crack width plotted at the load step is large (location shown with a cross in the force-displacement graph), and the element is already dissolved. However, plotting at this loading step was chosen to demonstrate the delamination. A plot with a small crack width would not demonstrate the delamination visually clearly. In addition, the delamination increases to exceedingly high crack widths in a few steps.

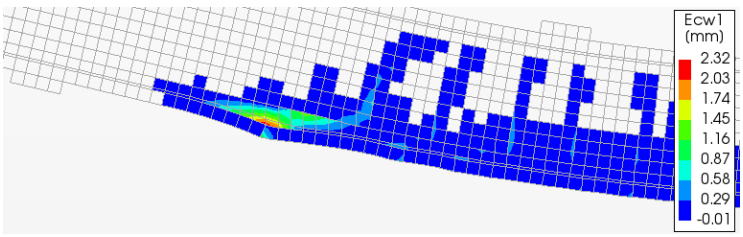

Figure 64 A121A3 rotating crack orientation with Shima bond-slip relation: delamination

From analysis, the wrong results were caused by over-rotation, a known problem with the rotating crack orientation. The causation of this problem was already discussed for the rotating crack orientation and the FIB bond-slip relation, and the same applies here. There is a strong correlation between the number of non-converged steps and over-rotation, visible in Figure 63. The crack width figure shows that the Shima bond-slip relation at an early load step already shows an impending delamination failure. The plot location is given with a cross on the force-displacement graph. Delamination is the cause of failure for all four initial cases, which is the wrong failure mode.

Like with the FIB bond-slip relation, in the case of the rotating crack orientation and the Shima bond-slip relation, the convergence difficulty increases as the geometrical beam size increases. As the element sizes are the same and the over-rotation is in the element, the larger the beams, the more elements over-rotate. The increase in convergence difficulties results from B701B2 are shown in Figure 65 and Figure 66 to prove it. The number of non-converged steps has increased, while the step load at which the delamination occurred was early in the force-displacement graph. In the crack width plot, a considerable maximum crack width is shown to make the delamination visible in the figure. After the plots, the conclusion section below (Table 13) will summarize the results between the two bond-slip relations for comparison.

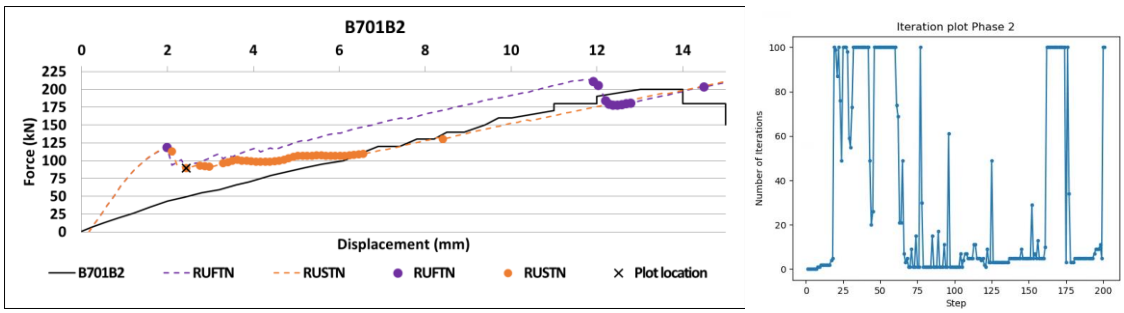

Figure 65 B701B2 rotating crack orientation with Shima bond-slip relation: force-displacement graph (left) and convergence log (right)

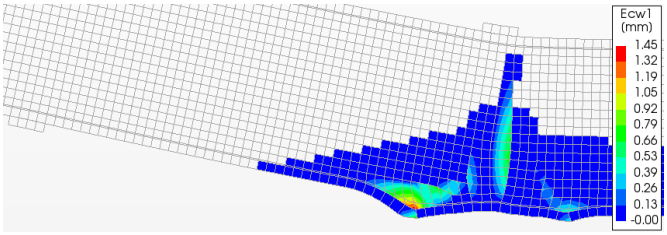

Figure 66 B701B2 rotating crack orientation with Shima bond-slip relation: delamination

4.2.1.3 Conclusion

Chapters 4.2.1.1 and 4.2.1.2 are summarized to conclude the sensitivity analysis for the constitutive model. Sensitivity analysis investigated the influence of the compression-compression confinement behavior and bond-slip relation with the total strain crack models' crack orientation for the constitutive model. The following variations were used for the aspects mentioned:

- Compression-compression confinement behavior: "Selby and Vecchio" confinement and unconfined.
- Bond-slip relation: FIB bond-slip relation and Shima bond-slip relation.
- The total strain crack models' crack orientation: the fixed crack orientation or the rotating crack orientation

Below in Table 13, a summary of the constitutive model sensitivity analysis failure loads is shown where the fixed crack orientation was applied. The results of the rotating crack orientation are not shown, as the simulated results were awful in multiple cases. The rotating crack orientation model resulted in many non-converged steps with high force and energy norm differences. This problem would sometimes occur long before the failure load was even simulated. Thus, the rotating crack orientation is not an option for RC beams without stirrups that fail due to flexural shear failure.

Table 13 Constitutive model sensitivity analysis summary

Test	A121A3	A122B1	A123A1	B701B2	R804A1	R804B1	H601A	H602A
Vexperiment [kN]	145	152	137	202	269	250	306	306
FCFTN Vnumerical [kN]	109	109	109	168	216	216	322	322
FCFTN $\frac{Vexperimental}{Vnumerical}$ [-]	1.33	1.40	1.25	1.20	1.25	1.16	0.95	0.95
FUFTN Vnumerical [kN]	108	108	108	173	216	216	333	333
FUFTN $\frac{Vexperimental}{Vnumerical}$ [-]	1.34	1.41	1.26	1.17	1.25	1.16	0.92	0.92
FUSTN Vnumerical [kN]	137	137	137	198	274	274	312	312
FUSTN $\frac{Vexperimental}{Vnumerical}$ [-]	1.06	1.11	1.00	1.02	0.98	0.91	0.98	0.98

The findings for each modeling aspect during the constitutive model sensitivity analysis are also given below:

Fixed crack orientation or Rotating crack orientation:

- The fixed crack orientation has a more realistic representation of the (flexural shear) failure crack.
- The rotating crack orientation can be subjected to delamination of the concrete cover (especially for geometrically large beams). The delamination is caused by over-rotation from the rotating crack orientation. In addition, a strong correlation was found between over-rotation and a high number of non-converged steps.
- The rotating crack orientation can also be sensitive to dowel failure due to over-rotation of the elements above the reinforcement. Dowel failure is characterized by the detachment of the tensile reinforcement from a flexural crack. For this failure mode, no secondary branch develops in the compression zone.
- The fixed crack orientation can also be sensitive to dowel failure due to excessive change in the damage-based shear retention factor. This excessive change in the factor can also lead to premature failure of the beam and requires very small steps for the sensitive step sizes.

Confined or unconfined:

- In a small number of cases, the unconfined numerical model had a higher failure load (for both the fixed and rotating crack orientations). However, there is not much difference in failure load between the confined and unconfined numerical models.
- The compression-compression confinement had a sudden concentration of high stresses along the reinforcement in one of the four, thus capturing the wrong failure mode (dowel failure).
- The compression-compression confinement is not a modeling requirement for cases with a brittle shear-tension failure mode, such as flexural shear failure.

FIB bond-slip relation or Shima bond-slip relation:

- The Shima bond-slip relation has a higher bond stress capacity and initial stiffness than the FIB bond-slip relation with the same material configurations for the modeling assumptions. In addition, the later bond-slip relation accounts for a decrease in bond stress at high slip values, which does not happen for the Shima bond-slip relation.
- Due to the higher initial stiffness, the Shima bond-slip relation allows for higher shear tractions at less relative displacement between the materials than the FIB bond-slip relation.
- The lower initial stiffness of the FIB bond-slip model increases the relative displacement, thus having a bigger crack (propagation). As the numerical model cannot deal with the rate of changes in the model, convergence problems occur.
- The FIB bond-slip relation is found to be more sensitive to capturing dowel failure mode. The larger relative displacement between the concrete and reinforcement causes the reinforcement to detach. This detachment is a characterization of dowel failure.
- The Shima bond-slip relation more accurately captures the flexural shear failure crack pattern.
- The Shima bond-slip relation with the fixed crack orientation simulates the most accurate results. In three cases of four, the Shima bond-slip relation model simulated a higher failure load than the FIB bond-slip relation model. In contrast, the Shima bond-slip relation had a lower failure load in one case. However, the Shima bond-slip relation showed more accurate results for all four cases than the FIB bond-slip model when compared to the experimental results.

From the analysis and the table overview, the constitutive model sensitivity analysis results in " unconfined (compression-compression behavior) fixed crack orientation and the Shima bond-slip relation" as the best-performing numerical model.

4.2.2 Analysis procedure

During the sensitivity analysis of the analysis procedure, the full NR iteration scheme is compared to the Secant iteration scheme. The advantages and disadvantages of both schemes have already been discussed in Chapter 2. The simulated results of the four numerical cases will be displayed below to see if there is a difference between the two schemes. The non-converged steps in this section are shown with dots in the force-displacement graph and logged on the right in tables for an overview and analysis. Only the non-converged steps before failure are displayed in the log, and if no non-converged steps are shown for a scheme, it is because the scheme does not consist of non-converged steps. Cases First, case A121A3 is analyzed and discussed. The force-displacement graph plotted in the figure shows the non-converged steps with their out-of-balance force and energy variation. Because the Secant iteration scheme did not consist of non-converged before reaching the failure load, no steps are included for this iteration scheme in the log.

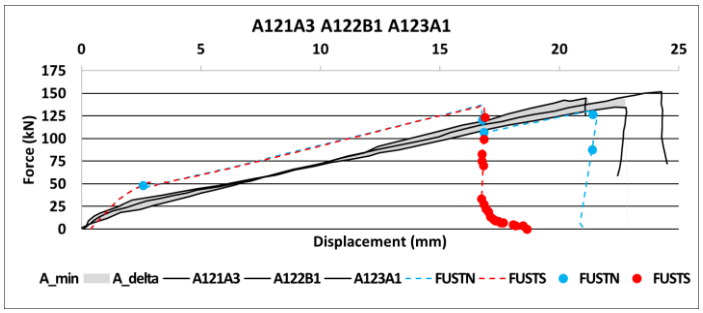

Case	A121A3-NR
Step	22
Force norm	0.01
Out-of-balance forces	0.028
Energy norm	0.001
Energy variation	0.002

Figure 67 A121A3 iteration schemes: Force-displacement graph (left) and non-converged steps (right)

Both schemes have almost equivalent force-displacement path progression till the failure load. More important than the non-converged steps are the size of the out-of-balance forces and relative energy variation. The force norm considers only the force with a criteria size of 0.01. In addition, the energy norm considers both the displacement and force with a criterion of 0.001. For case A121A3 at step 22 using the full NR iteration scheme, the convergence of both norms is not met using a step size of 0.1. However, the overshooting of the norms is by a factor of 1.8 (force norm) and 1 (energy norm) and can easily be reduced with smaller load steps or more maximum iterations. Currently, the maximum iterations are set to 100, which is not incredibly high. The experimental and numerical results of the strain are provided in Figure 68 for further analysis.

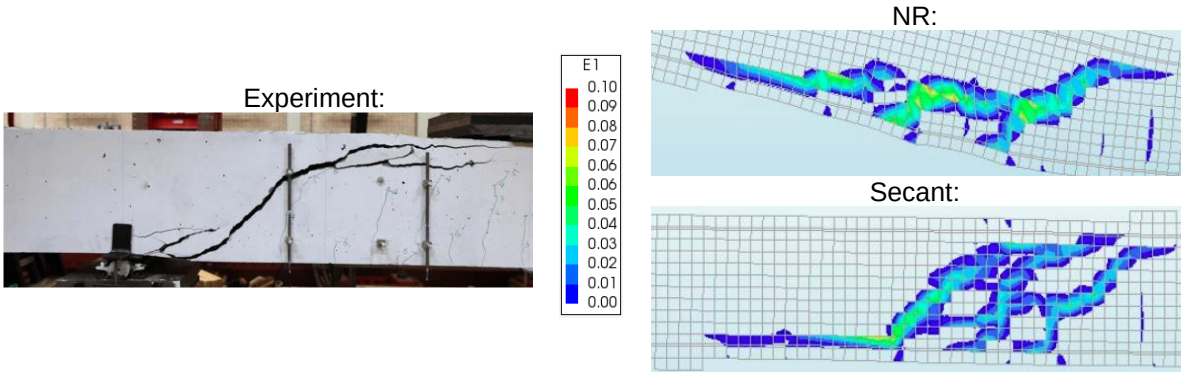

Figure 68 A121A3 iteration schemes maximum principal strain: NR (top) and Secant scheme (bottom)

From a comparison between the flexural shear crack pattern and the experimental pattern, the full NR iteration scheme does not mimic the cracks for case A121A3. The Secant model does come closer to the experimental pattern. A change in element size might improve the crack pattern as it influences its accuracy. This statement will be researched more during the element size sensitivity analysis in Chapter 4.2.3.2.

Next, case B701B2 is addressed. First, the force-displacement graph and non-converged steps are given.

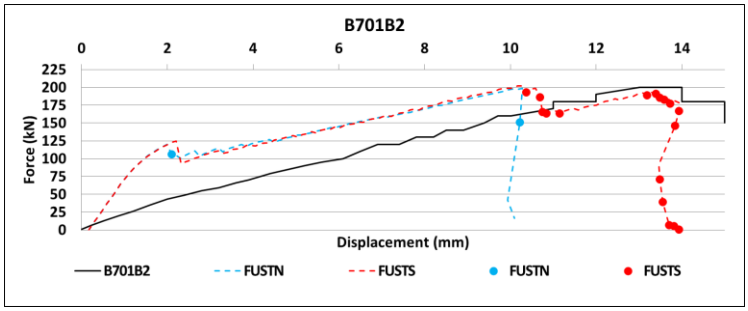

Case	B701B2-NR
Step	19
Force norm	0.01
Out-of-balance forces	0.221
Energy norm	0.001
Energy variation	0.123

Figure 69 B701B2 iteration schemes: Force-displacement graph (left) and non-converged steps (right)

The force-displacement graph does not show a vast difference between the iteration schemes, but the full NR iteration scheme does consist of one non-converged step at the initial crack. The results for case B701B2 using the full NR iteration scheme at step 19 are unacceptable as the results greatly overshoot the norm for this specific step. Reducing the step size at the initial cracks will reduce the considerable overshooting of the norm. However, the correct damage progression takes place after the load step, and accuracy for case B701B2 was not impacted for the full NR iteration scheme due to the already small load step of 0.1. Below, the maximum principal strain is also given for case B701B2:

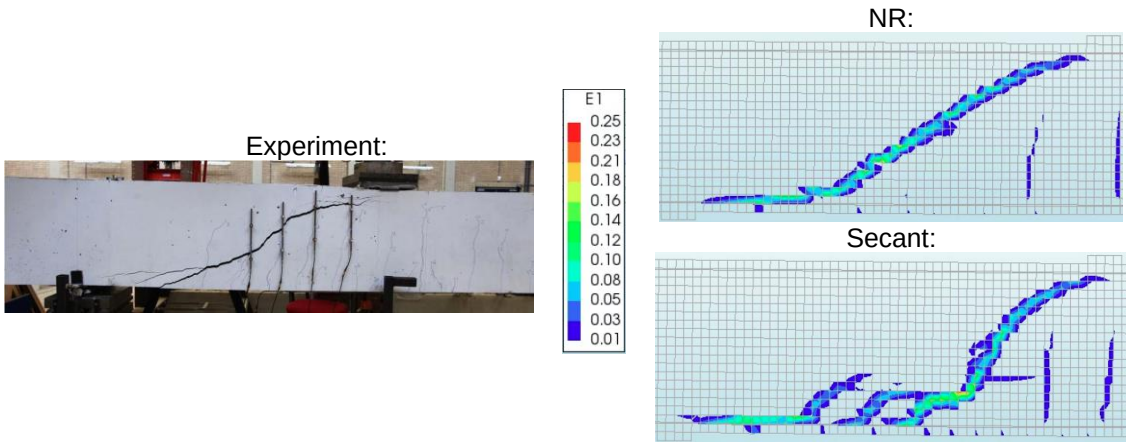

Figure 70 B701B2 iteration schemes maximum principal strain: NR (top) and Secant scheme (bottom)

For the B701B2 case, both models come close to the experimental flexural shear pattern. However, the full NR iteration scheme mimics the experimental crack better. In contrast, the cracks along the reinforcement are spread and have developed some large diagonal cracks along the reinforcement for the Secant iteration scheme. The two cases analyzed until now, A121A3 and B701B2 (Figure 67 and Figure 69), barely show any difference in their force-displacement graph between the two iteration schemes. Next, R804A1 is analyzed, but first, the force-displacement graph is given in Figure 71, and the non-converged steps in Table 14:

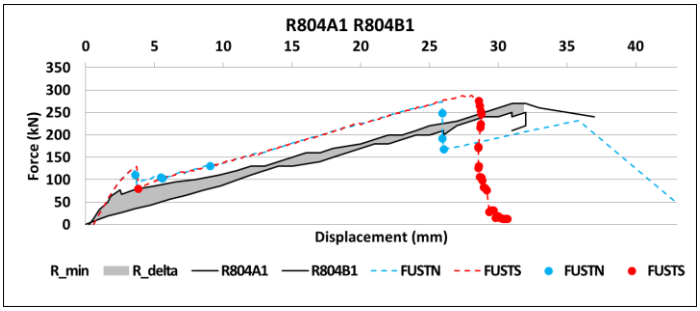

Figure 71 R804A1 iteration schemes: force-displacement graph

Table 14 R804A1 Non-converged steps: NR and Secant iteration schemes

Iteration scheme	R804A1 step	Force norm	Out-of-balance forces	Energy norm	Energy variation
Secant	33	0.010	0.167	0.001	0.003
Newton - Raphson	31	0.010	0.371	0.001	0.097
	49	0.010	0.166	0.001	0.009
	50	0.010	0.072	0.001	0.001
	84	0.010	0.138	0.001	0.006

For case R804A1, the full NR iteration scheme has a lower failure load than the Secant iteration scheme. The higher number of non-converged steps is a disadvantage for the full NR iteration scheme, as visible by the dots in the graph. While the Secant iteration scheme consists of only one non-converged step before failure, the full NR iteration scheme consists of four steps. The results of the non-converged steps are based on analysis with a step size of 0.1. The full NR iteration scheme's out-of-balance force and energy variation overshoot the norms at some steps. For load step 31, the energy variation result is almost ninety-five times larger than the norm. In addition, the out-of-balance forces are thirty-six times larger than the norm. Also, a reduction in the step size did not lead to an improvement in the overall result. In the numerical model, the non-converged steps are when the flexural cracks open. Even though there is a difference in the number of non-converged steps, both iteration schemes followed the same force-displacement path. Their overlapping path in the force-displacement graph is visible above. While the Secant iteration scheme is more stable according to the literature review and during the simulation does not run into many convergence problems during the simulations compared to the full NR iteration scheme, the full NR iteration scheme's failure load is closer to the experimental failure load. Observations show that the Secant iteration scheme slightly overestimates the failure load (14kN). Next, the maximum principal strain is shown in Figure 72 for case R804A1.

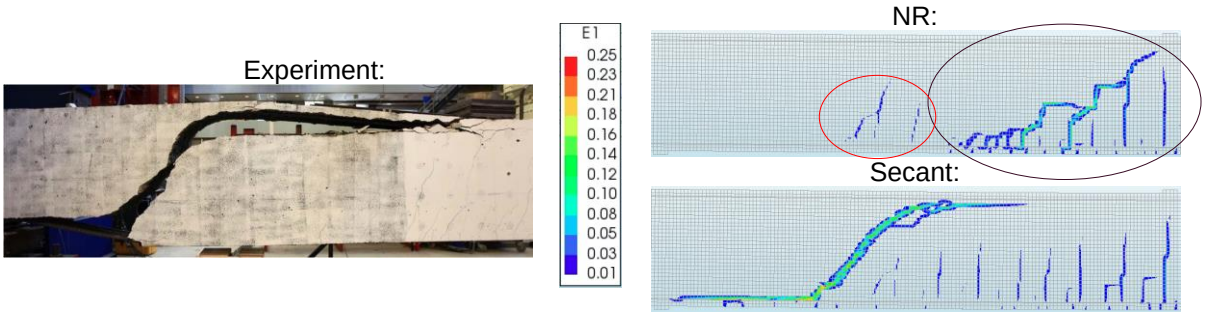

Figure 72 R804A1 maximum principal strain: NR (top) and Secant scheme (bottom)

For case R804A1, the Secant iteration scheme flexural shear failure crack closely matches the experimental result. However, the full NR iteration scheme crack pattern is incorrect, and its pattern has no smooth transition. Strains formed from the last crack for the full NR iteration scheme are shown with the red circle in the plot. However, unexpectedly irregular cracks are formed due to large strains transferring from one element to another horizontally or vertically. The wrong failure mode problem seems to be caused due to the element properties or its size rather than the full NR iteration scheme only. This statement will be researched further during the element size sensitivity analysis. The last case that is analyzed for the iteration schemes is H601A, with its force-displacement graph and non-converged steps given:

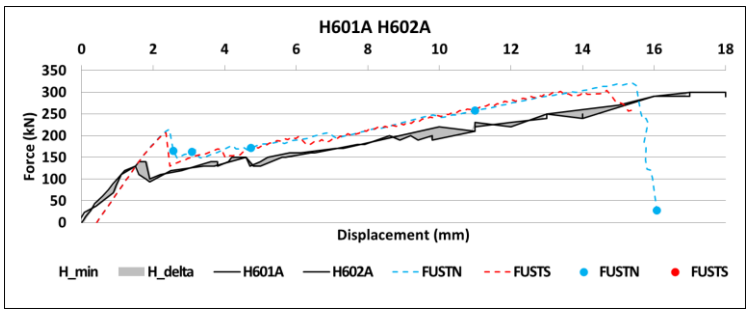

Figure 73 H601A iteration schemes: force-displacement graph

Table 15 H601A Non-converged steps: NR iteration scheme

H601A step	Force norm	Out-of-balance forces	Energy norm	Energy variation
22	0.010	0.165	0.001	0.010
27	0.010	0.090	0.001	0.004
43	0.010	0.080	0.001	0.003
103	0.010	0.156	0.001	0.030

H601A with the Secant iteration scheme does not consist of non-converged steps before the flexural shear failure is successfully simulated. This reason is why no steps are included in the table. In contrast, the full NR iteration scheme consists of four non-converged steps before failure. Some of the results in the table are unacceptable from analysis, like with R801A1, for a step size of 0.1. Still, because this step size is already small, the accuracy of the numerical model was not influenced by the NR method. The method followed a similar force-displacement path as the Secant iteration scheme at these steps. The maximum principal strain is also given below:

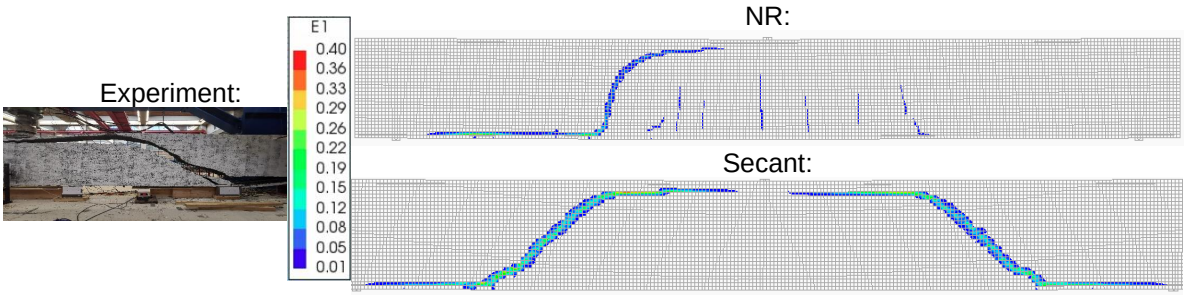

Figure 74 H601A maximum principal strain: NR (top) and Secant scheme (bottom)

While the flexural shear failure gets nicely captured for H601A using the full NR and Secant iteration schemes, the latter captures a symmetrical failure. However, flexural shear failure is known to be a non-symmetrical failure mode due to the mechanical behavior of RC beams taking up several types of non-linearities. A probable reason for the symmetrical failure is that the Secant iteration scheme fails to include material nonlinearity due to the symmetrical modeling of the structure. Changing the step size for the Secant method did not fix this issue. The full beam's NR iteration scheme result demonstrated correct non-symmetric failure. Only a half beam will be shown in plots during further analysis figures unless a symmetric failure occurs. Comparisons for the numerical failure loads and experimental failure of the four discussed cases are below in Table 16 for both schemes to give an overview of their performance.

Table 16 Iteration schemes sensitivity analysis summary

Test	A121A3	A122B1	A123A1	B701B2	R804A1	R804B1	H601A	H602A
Vexperiment [kN]	152	137	202	269	250	306	306	152
FUSTN Vnumerical [kN]	137	137	198	274	274	312	312	137
FUSTN $\frac{Vexperimental}{Vnumerical}$ [-]	1.06	1.11	1.00	1.02	0.98	0.91	0.98	0.98
FUFTS Vnumerical [kN]	136	136	202	284	283	301	301	136
FUFTS $\frac{Vexperimental}{Vnumerical}$ [-]	1.06	1.12	1.00	1.00	0.95	0.88	1.02	1.02

To summarize this modeling aspect, both schemes had almost equivalent failure loads and displacements for cases A121A3 and B701B2. However, when comparing the schemes, the other two cases (R804A1 and H601A) showed differences in the force-displacement graphs. The main difference between the four cases is their geometrical size. Increased sensitivity from the iteration schemes appears to occur with increased geometrical size. This table shows that the full NR iteration scheme gives slightly more accurate results while mostly successfully capturing the flexural failure crack. This conclusion was found, despite the Secant iteration scheme having fewer non-converged steps for all four cases.

In addition, there was one case with symmetric failure for the Secant iteration scheme. The symmetrical failure is wrong as the flexural shear failure is a non-symmetrical failure mode, even though the simulated crack pattern is accurate. Case R804A1 had problems simulating the flexural shear failure, but the failure load was accurate. The findings indicated that the problem is possibly due to the element (size) and the iteration scheme used. In Chapter 4.2.3.2, element size sensitivity will demonstrate if the correct failure mode for case R804A1 with the full NR iteration scheme can be captured. This case was the only case with much better results for the Secant iteration scheme due to the failure mode. During the element size sensitivity analysis, more analysis will be done on both schemes as there is not much difference between the results. With such a slight difference in this modeling aspect simulations, concluding the appropriate iteration scheme for the numerical model is impossible. In addition, the schemes also appear to depend on the geometrical structure size and the finite element discretized model elements. Besides, the global element size also depends on the geometrical size. With this approach, a better conclusion can be found regarding the schemes, and a link between the iteration scheme and element size can be identified.

4.2.3 Finite element discretization

The finite element discretization modeling aspects are the last ones for the sensitivity analysis. First, the reinforcement element is addressed, and then the element size.

4.2.3.1 Reinforcement element

During this section's analysis, the truss elements are replaced with beam elements for reinforcement in the numerical model. Unfortunately, due to a numerical error during simulation, the Shima bond-slip relation combined with beam elements for the reinforcement cannot be reviewed. The problem is purely caused due to changes in the reinforcement element. For future research, it would be interesting to see if using another concrete element with beam elements would have solved this problem. A change in the concrete element is avoided during this research to keep consistency in the concrete element for the reference numerical model. Changing the reinforcement and concrete elements together makes it difficult to study a single modeling aspect (in this case, the reinforcement element) during the sensitivity analysis.

The bond-slip relation sensitivity analysis in Chapter 4.2.1.2 shows that the Shima bond-slip relation performs better than the FIB bond-slip relation. Still, the FIB bond-slip relation is applied to analyze the numerical model for reinforcement element variation due to the numerical problem (error) found with the Shima bond-slip relation. There is a possibility that a change in reinforcement element can cause better accuracy for the FIB bond-slip relation with beam elements compared to the Shima bond-slip relation combined with truss elements. The reinforcement element sensitivity analysis is performed with the following numerical models:

- Unconfined compression-compression behavior, fixed crack orientation, and the FIB bond-slip relation with beam elements using the full NR iteration scheme (FUFBN).
- Unconfined compression-compression behavior, fixed crack orientation, and the FIB bond-slip relation with truss elements using the full NR iteration scheme (FUFTN).
- Unconfined compression-compression behavior, fixed crack orientation, and the Shima bond-slip relation with truss elements using the full NR iteration scheme (FUSTN).

Comparing the FIB bond-slip relation with beam elements model and the Shima bond-slip relation with truss elements models on the reinforcement elements are challenging to analyze due to the difference in two modeling aspects instead of one. Thus first, the FIB bond-slip relation with beam elements model will be compared to the FIB bond-slip relation with truss elements model to analyze the influence of a change in reinforcement elements between the models. Afterward, the failure load simulation and crack pattern accuracy between the three numerical models are compared. During the comparisons of the bond-slip relations in Chapter 4.2.1.2, the B701B2 and H601A cases were used for detailed analysis. The choice is made to use these two cases again for the in-depth analysis of the reinforcement elements to make more accessible cross-references to the Shima bond-slip relation with truss elements. However, the analysis results of cases A121A3 and R804A1 will also be included at the end of this section. The force-displacement graph for case B701B2 is given in Figure 75 for the first case sensitivity analysis of the reinforcement type.

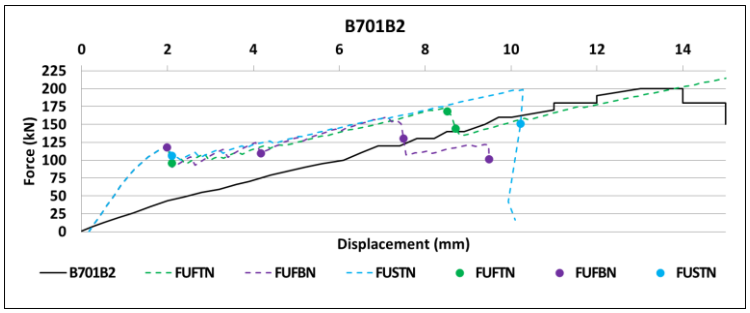

Figure 75 B701B2 Force-displacement graph: FIB bond-slip relation with truss elements, Shima bond-slip relation with truss elements, and FIB bond-slip relation with beam elements

For the beam elements model, there is an earlier failure than the two truss element models. Because of the inclusion of the dowel action contribution to the shear capacity, one would expect that the beam elements model would have a higher failure load simulation and a more accurate representation of the experimental result. However, this does not happen here, as the failure load is drastically underestimated for the model with beam elements. Besides the force-displacement graph, the reinforcement stresses, shear tractions, and relative displacements are also below for further analysis. The plots below are located at the failure load step of each numerical model. The shear stresses for both element types are included in Annex III, Figure 107. The figure displays that beam elements include these stresses to account for the dowel action.

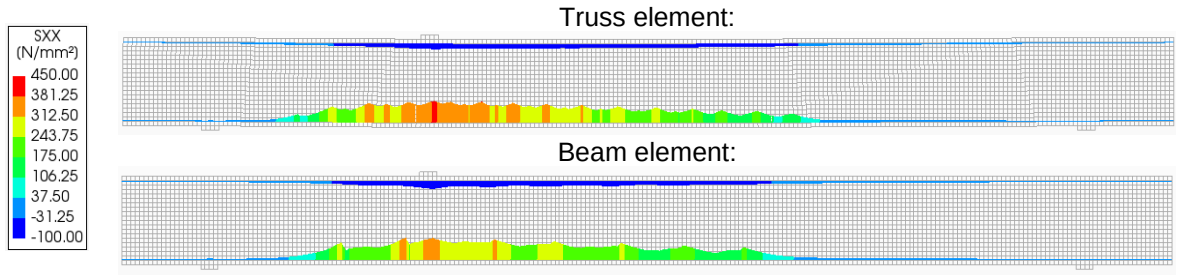

Figure 76 B701B2 Reinforcement stresses: FIB bond-slip relation with truss (top) and beam elements (bottom)

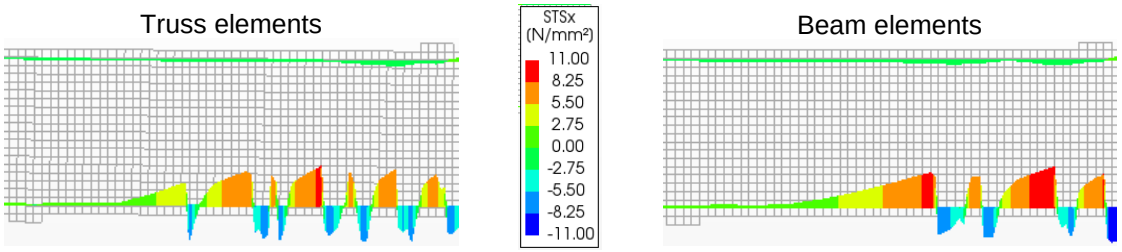

Figure 77 B701B2 bond-slip relation interface shear traction: FIB bond-slip relation with truss (left) and beam elements (right)

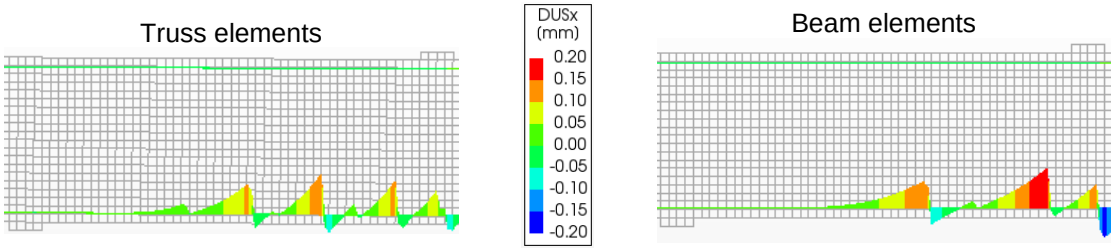

Figure 78 B701B2 bond-slip relation interface relative displacement: FIB bond-slip relation with truss (left) and beam elements (right)

While the reinforcement stresses reached for the truss elements model are higher than that of the beam elements model, this is expected as the truss elements model also fails after reaching a higher capacity. However, the beam elements' shear tractions and relative displacements show much larger values while having similar material inputs for the FIB bond-slip relation. To understand better why this happens by changing the reinforcement element, a side-by-side overview of all elements used for the numerical model is given:

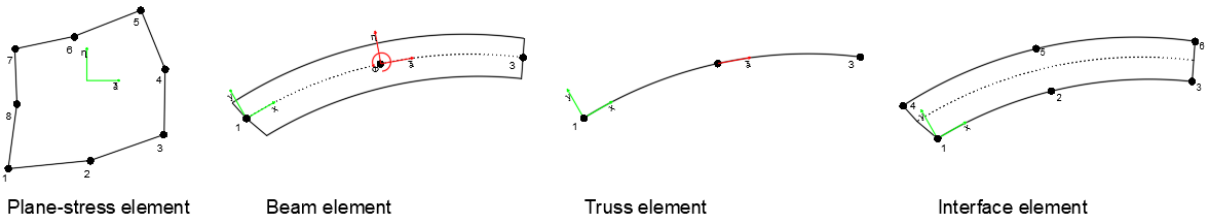

Figure 79 Finite element discretization: numerical model elements

The reinforcement elements are used together with plane stress elements for concrete. If plane stress elements are connected to beam elements directly, then the rotating degree of freedom must be tied to the translational degree of freedom for compatibility. DIANA FEA automatically takes care of the procedure. However, unfortunately, the applied interface element between the reinforcement and concrete is not ideal as it is not successful at dealing with the rotational degree of freedom. In the force-displacement diagram, there are also more non-converged steps for the beam elements model due to the incompatibility between elements. As a result of this problem, high shear tractions and relative displacement between the two materials occur with beam elements for reinforcement. The maximum principal strain is given below to review the failure mode and strains:

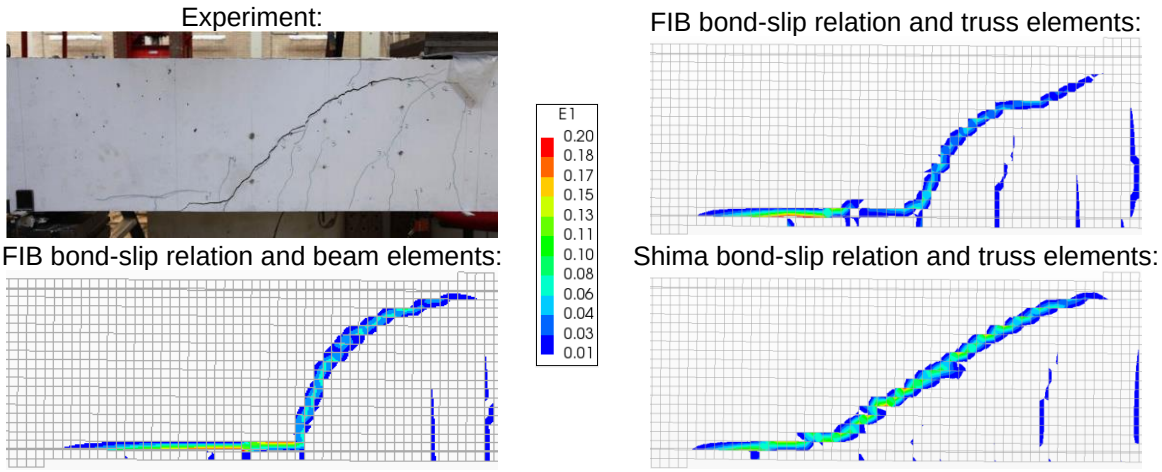

Figure 80 B701B2 strains with the combinations: FIB bond-slip with truss elements (top right), FIB bond-slip with beam elements (bottom left), and Shima bond-slip with truss elements (bottom right)

The FIB bond-slip relation combined with the beam elements shows high strains along the reinforcement. The large strains along the reinforcement before the diagonal crack fully developed were observable for the FIB bond-slip model with truss elements but increased with beam elements. The too-large relative displacements cause increased strain along the reinforcement. Also, the transition between the diagonal crack during failure and detached reinforcement (strains along reinforcement) is not smooth. The Shima bond-slip relation combined with truss elements has the best crack pattern and failure load simulation of the three numerical models. One way to tackle the incompatibility problem is by replacing the plane stress element with a more suitable element or manually tying the rotational degree of freedom. The previous sensitivity analysis shows this is also the better bond-slip relation. The next case analyzed is H601A, with the force-displacement graph for the case below.

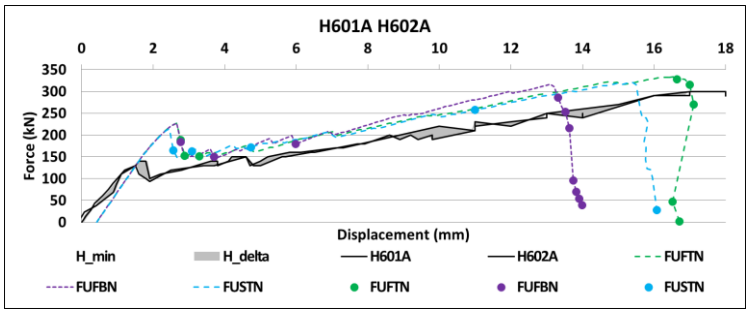

Figure 81 H601A Force-displacement graph: FIB bond-slip relation with truss elements, Shima bond-slip relation with truss elements, and FIB bond-slip relation with beam elements

Case H601A for the model with beam elements has a slightly higher global stiffness following the initial crack than the two models with truss elements and the experiment in the force-displacement graph. The higher stiffness causes the beam element model to get an increased failure load and decreased displacement. While the failure load is acceptable, the wrong stiffness shows that the simulation does not accurately represent the experimental result. The force-displacement graph displays the truss elements giving more reliable results.

Below, the reinforcement stresses, tractions, and relative displacement at each numerical model failure load are also given. In Annex III, Figure 108, a plot of shear stresses is included to show that the beam elements account for the dowel action.

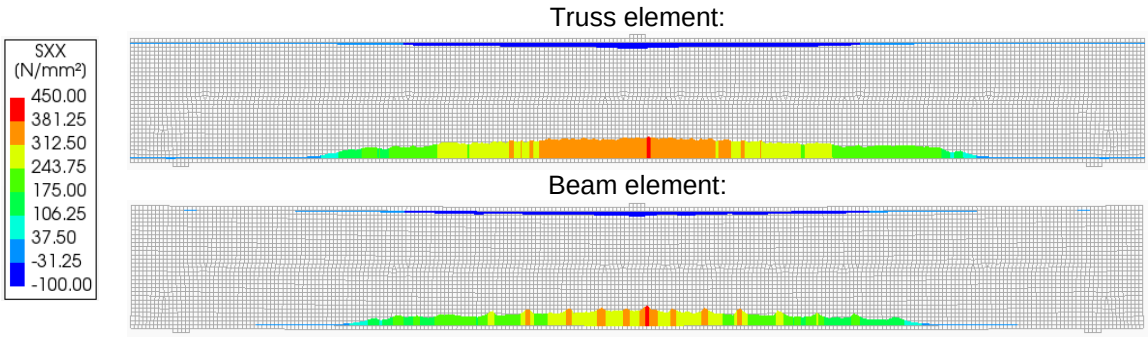

Figure 82 H601A Reinforcement stresses: FIB bond-slip relation with truss (top) and beam elements (bottom)

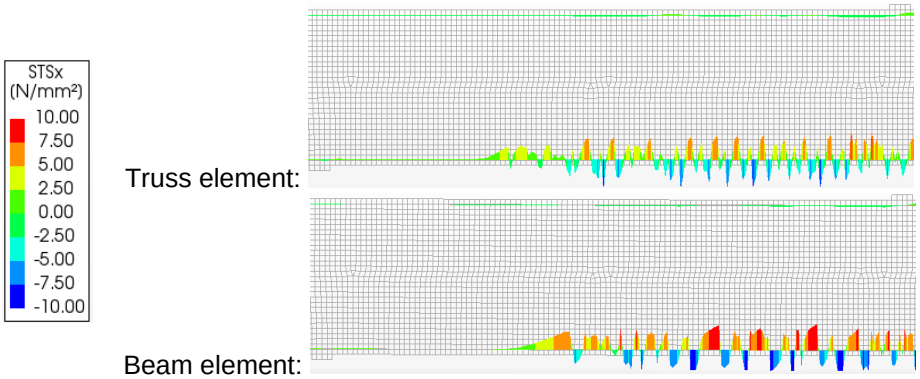

Figure 83 H601A bond-slip relation interface shear traction: FIB bond-slip relation with truss (top) and beam elements (bottom)

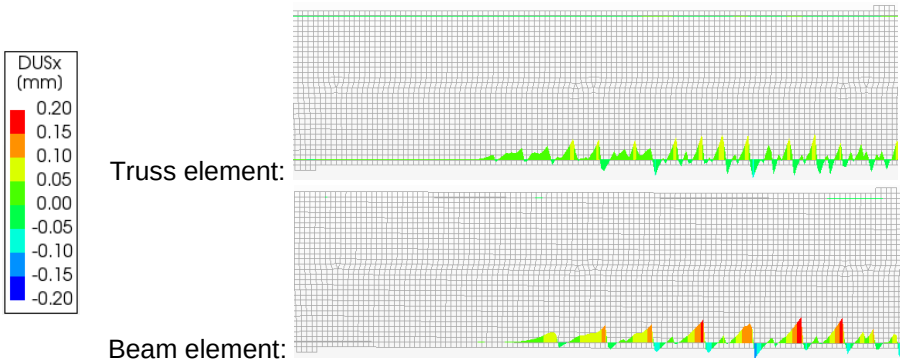

Figure 84 H601A bond-slip relation interface relative displacement: FIB bond-slip relation with truss (top) and beam elements (bottom)

Like the previous case, the reinforcement stresses are higher for the simulation with truss elements. Also, like in the previous case, the shear tractions and relative displacements from the numerical model with beam elements are larger than those with the truss elements. However, in the case of H601A, the difference is even more pronounced than in values (traction and relative displacement) B701B2. Both case properties were compared to find the main configurations that make both cases different. Table 11 shows that the beam geometry is the biggest difference between the B701B2 and H601A cases. With a larger beam, there are more elements. Thus, the effect caused by incompatibility between plane stress elements and beam elements is increased.

Finally, the maximum principal strain for case H601A is given in Figure 85.

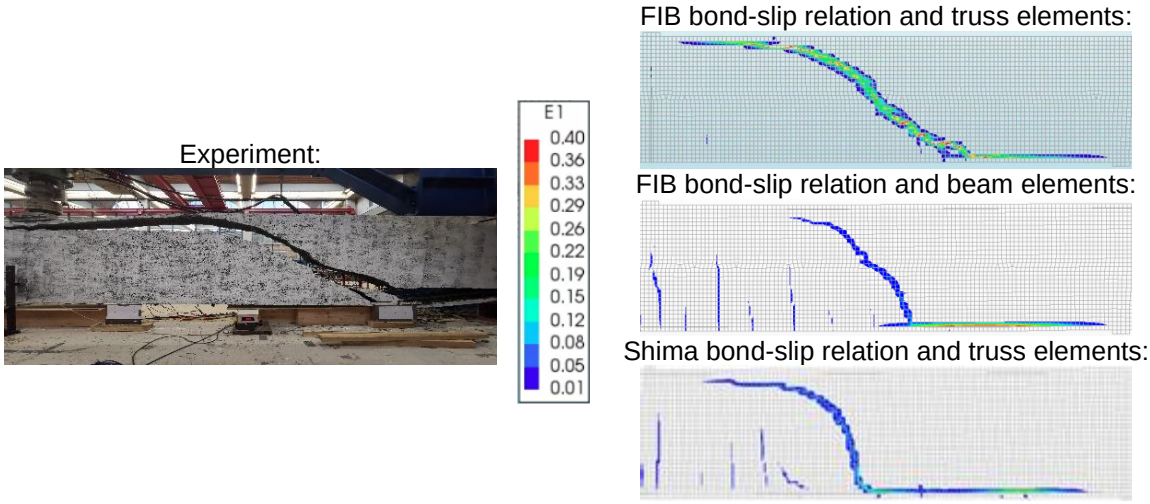

Figure 85 H601A strains with the combinations: FIB bond-slip with truss elements (top) and FIB bond-slip with beam elements (middle), and Shima bond-slip with truss elements(bottom)

The figure shows high strains along the reinforcement for the numerical model with beam elements. The detachment of the tensile reinforcement is a sign of dowel failure. Beam elements show to be prone to high stresses along the reinforcement when combined with regular plane stress elements. For this case, if we compare the (FIB and Shima bond-slip relation with) truss element models, the flexural shear failure crack pattern is captured for both cases. However, based on the failure load and crack propagation of the other three numerical cases (A121A3, B701B2, and R804A1), the Shima bond-slip relation with truss elements is recommended. The force-displacement graphs are given for cases A121A3 and R804A1 in Annex IV, Figure 109, and Figure 110. In addition, in the annex, Table 59 shows an overview of the differences in maximum reinforcement stresses and relative displacements using the two element types for all cases.

For this section, a summary of all failure loads is in the table below. The table results show more accurate simulations of the (Shima bond-slip relation with) truss elements over the numerical model with beam elements. One interesting behavior for the four cases with beam elements was noticed. A pattern is observed in the difference in inaccurate estimations depending on the structure size. Using beam elements in the numerical model, the geometrically smallest case (A121A3) had the largest underestimation of the failure load. This failure load underestimation was reduced as the beam geometry increased (B701B2). However, after a certain geometry (R804A1 and H601A), the model started overestimating the failure load with increased structure geometry. The difference in failure load between the element types can be found in the force-displacement graphs of the four cases (Figure 107, Figure 109, Figure 110, and Figure 108).

Table 17 Reinforcement element sensitivity analysis: FIB bond-slip & truss elements, Shima bond-slip & truss elements, and FIB bond-slip & beam elements

Test	A121A3	A122B1	A123A1	B701B2	R804A1	R804B1	H601A	H602A
Vexperiment [kN]	145	152	137	202	269	250	306	306
FUFTN Vnumerical [kN]	108	108	108	173	216	216	333	333
FUFTN $\frac{Vexperimental}{Vnumerical}$ [-]	1.34	1.41	1.26	1.17	1.25	1.16	0.92	0.92
FUSTN Vnumerical [kN]	137	137	137	198	274	274	312	312
FUSTN $\frac{Vexperimental}{Vnumerical}$ [-]	1.06	1.11	1	1.02	0.98	0.91	0.98	0.98
FUBTN Vnumerical [kN]	103	103	103	160	264	264	316	316
FUBTN $\frac{Vexperimental}{Vnumerical}$ [-]	1.4	1.48	1.32	1.26	1.02	0.95	0.97	0.97

4.2.3.2 Element size

The final sensitivity analysis is for the element size, which is done in this chapter. The global element size sensitivity analysis will use the unconfined compression-compression behavior of fixed crack orientation and the Shima bond-slip relation combined with the truss elements model. This analysis is essential, especially for cases with large geometry, as these are known to be more sensitive to the element size. The analysis will be done in the order from the geometrically largest beam (H601A) to the geometrically smallest beam (A121A3). The global element size sensitivity analysis for each case will help to determine the optimal element size. Initial assumptions from the literature review for the element size are specified first, after which the approach for the element size sensitivity analysis is explained. Two studies that made recommendations using DIANA FEA for the simulations recommended the following:

- According to Putter [43], special attention must be given to beams with a depth greater than 600 mm, as it found severe mesh dependency and recommended 20 elements over the beam depth.
- Lang [45] found that less than 15 elements of the beam depth do not successfully capture the flexural shear failure. The maximum element size used for simulations will be limited to the finding from Lang unless required otherwise.

After the sensitivity analysis, the largest element size that successfully and accurately simulates the flexural shear failure will be chosen out of all the sizes. Choosing the largest element size in this way helps reduce computational time while providing accurate results. The initial element size was 25 mm for cases A121A3, B701B2, and R804A1. For case H601A, the initial element size was 40 mm for reasons explained in Chapter 4.2.1. The initial element size used resulted in the following number of elements over beam depth:

Table 18 Reference numerical model: number of elements over the beam depth

Case	A121A3	B701B2	R804A1	H601A
Number of elements of beam depth [-]	12	20	32	30

As an approach for the element size sensitivity analysis, the following approach is used:

1 Start analyzing simulations with the initial element size.
2 Add five elements from the initial number of elements over the beam depth and run simulations with the smaller element size.
3 Subtract five elements from the initial number of elements over the beam depth and run simulations with the larger element size.
4 After the simulations are completed, analyze their accuracy.
5 If element size sensitivity for the different sizes is noticed due to too large elements, subtract five elements again. If no element size sensitivity is noticed for the different sizes, add five elements again for simulations with larger elements.
6 Run simulations with the new element size and analyze it.
7 Repeat steps 5 and 6 or stop with the sensitivity analysis if an optimal element size is found from step 6.

Results from Chapter 4.2.2 show that the full NR iteration scheme works slightly better than the Secant iteration scheme. However, not much difference was found between both iteration schemes. However, both schemes showed different failure loads and damage progression for cases R804A1 and H601A. The iteration scheme sensitivity analysis introduced suspicions that both schemes depend on the element type and dimensions. Because of this suspicion, element size sensitivity analysis is performed initially using both iteration schemes. First, case H601A is analyzed, followed by R804A1, followed by B701B2, and finally, A121A3.

H601A element size sensitivity analysis:
Unlike the other three cases, for case H601A, an element size of 40 mm was used for the modeling aspects sensitivity analysis till now instead of 25 mm. The reasoning for this is included in Chapter 4.2.1. However, the initial results obtained with an element size of 25 mm are also included in the sensitivity analysis. For case H601A, all the different element sizes used for the element size sensitivity analysis are given in Table 19. Hereafter plots of the force-displacement graphs and crack patterns are given in Figure 86 and Figure 87. In the force-displacement graph, a high element sensitivity is discovered for case H601A (which is a geometrically large case).

Table 19 H601A element sizes sensitivity analysis

Depth [mm]	1200	1200	1200	1200	1200	1200
Number of elements [-]	48	40	30	25	20	15
Element size [mm]	25	30	40	48	60	80

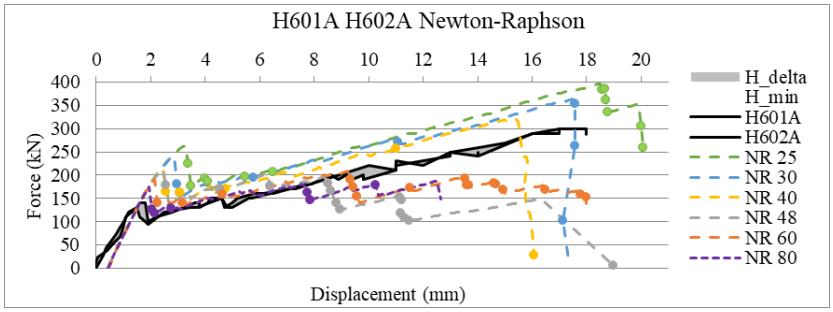

Figure 86 H601A element size sensitivity analysis: force-displacement graph

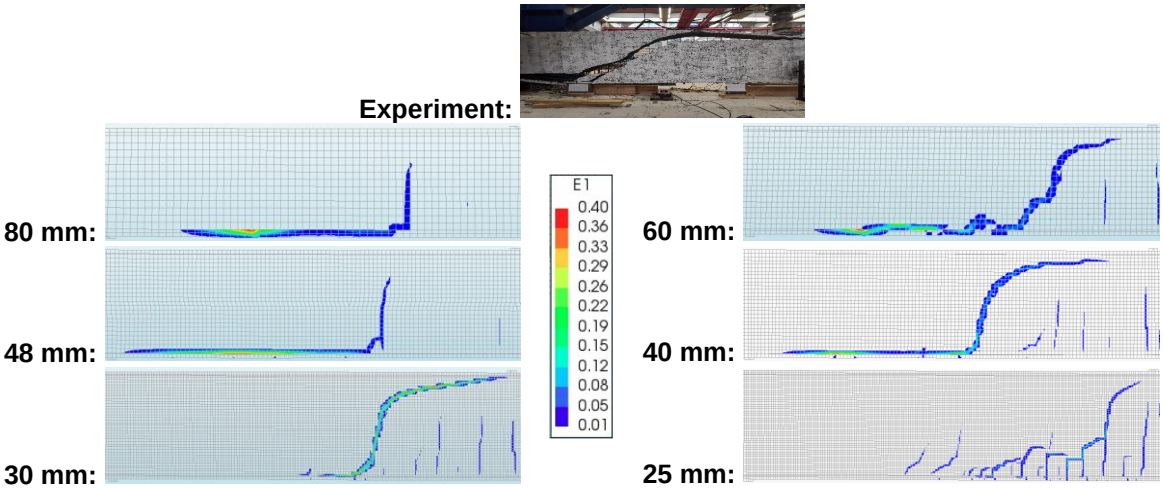

Figure 87 H601A element size sensitivity analysis: crack pattern

The figures above show why the exception was made not to initially use the element size of 25 mm for this case. Overpredictions of the failure load and, more importantly, irregular crack patterns would constantly occur during the sensitivity analysis due to the element size of 25 mm. Thus, reliable analysis and conclusions for the previous modeling aspects would not be possible with an element size of 25 mm. A closer analysis was done for the simulation with this element size using the figure below from the step at its failure load:

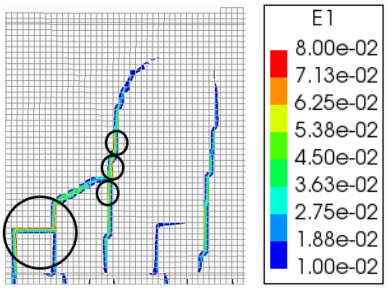

Figure 88 H601A irregular crack pattern: maximum principal strain

The plot shows that for an incredibly small element size, huge strains show at the sides of some elements. These strains are transferred horizontally or vertically to the next element, thus creating horizontal or vertical strains running over several elements. Due to this, the numerical model results in an irregular crack pattern instead of a smooth flexural shear failure pattern, as found in experiments. This pattern shows that the damage progression has been captured incorrectly. The element sizes 40 mm and 30 mm have shown the correct damage progression and captured the flexural shear failure crack close to the experimental crack pattern. However, the element size of 30 mm overpredicts the failure load by 16 % compared to the experiment. Closer analysis displays signs of forming an irregular crack pattern with an element size of 30 mm. At the same time, the element size of 40 mm overpredicts the failure load by only 4 % while closely resembling the experimental beam behavior. Based on the current findings, the element size of 40 mm is shown to be the optimal element size for beams with this depth.

Also, element sizes 48-, 60-, and 80-mm show that if the crack pattern is analyzed, they were chosen too large by capturing the wrong failure load. This failure mode is called dowel failure and can be identified by dowel cracks along the reinforcement running toward the support. The reason for this failure mode is the dependence of the dowel crack propagation on the element size. The larger the element size, the more sensitive the crack propagation rate. The element size of 80 mm showed an underprediction in the failure load with a factor of 1.6. For case H601A, the element size is a sensitive modeling aspect. A similar element size sensitivity analysis is also done for the Secant iteration scheme to see how this analysis scheme performs but also to see if the large element size sensitivity still preserves. The force-displacement graph and crack patterns using the Secant iteration scheme are given in Figure 89 and Figure 90 below:

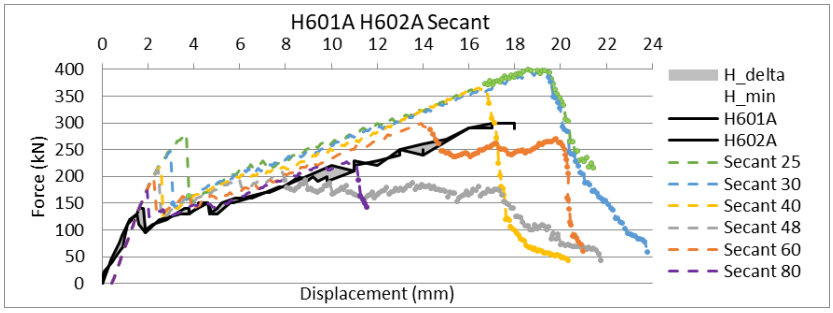

Figure 89 H601A element size sensitivity analysis: force-displacement graph

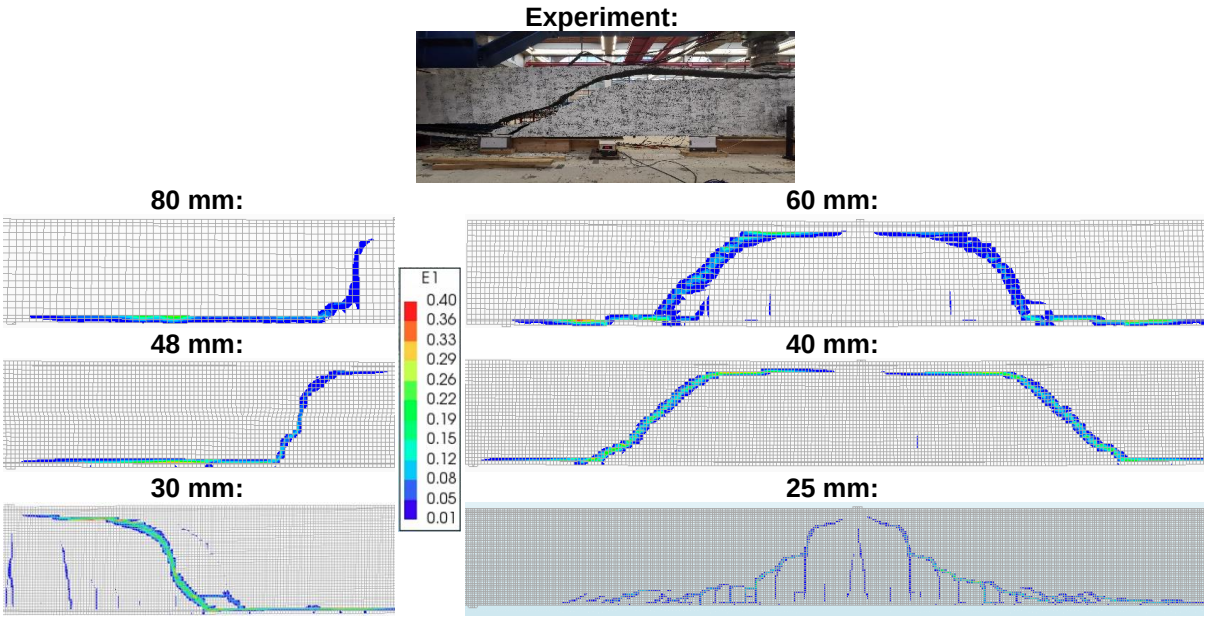

Figure 90 H601A element size sensitivity analysis: crack pattern

Like the full NR iteration scheme, the Secant iteration scheme also captures the dowel failure for some element sizes. However, unlike the full NR iteration scheme, the Secant iteration scheme successfully captures flexural shear failure with an element size of 60 mm. Unfortunately, symmetrical failure occurs for the simulation with this element size and an element size of 40 mm. However, the simulated result for the element size of 60 mm comes closest to the experimental failure load and failure mode out of all simulations. The reasoning for the symmetrical failure mode problem and a recommendation to fix this problem has been addressed in Chapter 4.2.2. With the Secant iteration scheme, the element size of 25 mm also fails to capture the correct failure mode while suffering from an irregular crack pattern due to too small mesh elements. This simulation shows that, independent of the analysis scheme, an irregular crack pattern with an overestimation of the failure load can be captured if the element size is too small. An overview of all the H601A element size sensitivity analyses by comparing the experimental failure load for both iteration schemes is given in Table 20:

Table 20 H601A element size sensitivity analysis summary

H601A	Elements [-]	NR: V [kN]	NR: V_{exp}/V_{num} [-]	Secant: V [kN]	Secant: V_{exp}/V_{num} [-]
Experiment	-	306	-	306	-
25	**48**	397	0.77	405	0.75
30	**40**	363	0.84	402	0.76
40	**30**	312	1.02	367	0.83
48	**25**	213	1.43	208	1.47
60	**20**	208	1.47	298	1.03
80	**15**	187	1.64	227	1.35

The table shows the high sensitivity of the element size for the numerical simulations. The element sizes were chosen based on the beam depth. Because element size sensitivity is a complex topic, as seen from the analysis, choosing an element size based on only one case simulation result for beam depth is inconvenient. Due to this, a similar element size sensitivity analysis was done on more beams with a depth of 1200 mm. The properties for the following cases, "H404A, H121A, H851C, and H852A," with a beam size of 1200 mm, are given in Table 40 from Annex II. These cases will be used for further element size sensitivity analysis for beams with a depth of 30 mm. The element size sensitivity analysis results are in Annex III (Figure 117, Figure 118, and Figure 119) for these cases. Table 21 summarizes only the best-performing element sizes used for simulation to avoid overcrowding the graphs with too many results. All cases capture the flexural shear failure with an element size of 40 mm, just like case H601A. In addition, the full NR iteration scheme gives the best overall result for this element size and not the Secant iteration scheme.

Table 21 Element size sensitivity analysis of 1200 mm cases: NR and Secant iteration schemes

Experiment	H121A V [kN]	V_{exp}/V_{num} [-]	H404A V [kN]	V_{exp}/V_{num} [-]	H851C V [kN]	V_{exp}/V_{num} [-]	H852A V [kN]	V_{exp}/V_{num} [-]
Failure load	341	-	269	-	421	-	406	-
FUSTN 30	380	0.90	265	1.02	479	0.88	479	0.85
FUSTS 30	399	0.86	269	1.00	490	0.86	490	0.83
FUSTN 40	368	0.93	244	1.10	404	1.04	404	1.01
FUSTS 40	395	0.86	256	1.05	431	0.98	431	0.94
FUSTN 60	325	1.05	207	1.30	322	1.31	322	1.26
FUSTS 60	274	1.24	184	1.46	357	1.18	357	1.14

The remaining three cases for the element size sensitivity analysis are addressed next. Too much focus on the Secant iteration scheme will not be emphasized for these cases because the full NR iteration scheme has proven more dependable for the 1200 mm deep beams. Also, a slightly better performance was observed for the full NR iteration scheme during the modeling aspects' sensitivity analysis. For the cases with a depth of 1200 mm, wrongly capturing a symmetric failure is also identified for the Secant iteration scheme. The Secant iteration scheme is not more dependable than the full NR iteration scheme and thus will not be used for an in-depth analysis. However, the Secant iteration scheme results are included in the summary tables below to give an overview of the simulations done.

R804A1 element size sensitivity analysis:
This case is also a geometrically large beam and has a depth of 800 mm. The element sizes 20 mm, 25 mm, 80/3 mm, 32 mm, and 40 mm was analyzed for this case. The strains and force-displacement graph will be placed in Annex III for this case. The same will also be done for the other two cases (A121A3 and B701B2). The annex shows the case results in Figure 111 and Figure 112. A summary of the failure loads from the element size sensitivity analysis, including a comparison with the experimental failure loads, is given in Table 22.

Table 22 R804A1 element size sensitivity analysis summary

R804A1	Elements [-]	V [kN]	V_{exp}/V_{num} [-]	V2 [kN]	V_{exp}/V_{num} [-]
Experiment	-	269	-	250	-
FUSTN 20	40	285	0.95	285	0.88
FUSTS 20	40	293	0.92	293	0.85
FUSTN 25	32	274	0.98	284	0.91
FUSTS 25	32	288	0.94	288	0.87
FUSTN 80/3	30	268	1.01	268	0.93
FUSTS 80/3	30	266	1.01	266	0.94
FUSTN 32	25	263	1.03	263	0.95
FUSTS 32	25	240	1.12	240	1.04
FUSTN 40	20	248	1.09	248	1.01
FUSTS 40	20	280	0.96	280	0.89

The simulated plots in Figure 111 shows that element sizes 80/3, 25, and 20 mm cannot be used due to capturing either the dowel failure or an irregular crack pattern. However, their failure load predictions are acceptable compared to the experimental failure loads. While case R801A1 also captures the dowel failure and irregular crack patterns, this case is less sensitive to the element size when predicting the failure load than case H601A. During previous modeling aspect sensitivity analysis, an element size sensitivity issue was suspected using an element size of 25 mm for the R804A1 case. The element size of 25 mm was causing over predictions but, more importantly, an irregular crack pattern. This element size was still used, as not all numerical models during sensitivity analysis suffered from this. Keeping the same element size helps to avoid changing multiple modeling aspects for a numerical model during a section. Numerous modeling aspect changes would make it challenging to review differences caused by the central modeling aspect for the sensitivity analysis.

Element sizes 32 mm and 40 mm are sufficiently accurate for this case using the full NR and the Secant iteration schemes. These element sizes successfully capture the flexural shear failure while showing a logical and expected damage progression. One thing to note is that the two experimental specimens (V1 and V2) have a difference of 20 kN in failure load. Thus, the lower accuracy in column V2 is visible in the table. Even though the sensitivity in element size is reduced, additional numerical analyses will be done on new cases with the same beam depth before the end of this chapter, as was done for case H601A. This approach will help get an optimal element size for a specific beam depth using multiple cases to increase the quality of the element size recommendation. Similarly, additional cases will be analyzed on the element size for cases A121A3 and B701B2.

B702B1 element size sensitivity analysis:
The third case analyzed on the element size sensitivity is B702B1. The previously used element size of 25 mm already captured the damage progression and failure mode. However, performing an element size sensitivity analysis can help find the optimum element size for the case. The optimum element size should reduce unnecessary computational costs while maintaining an approximate similar numerical simulation accuracy. The simulated results can be found in Figure 113 and Figure 114 from Annex III. For case B701B2, all the numerical element size configurations successfully capture the flexural shear failure. A summary of the different element sizes, number of elements over the beam depth, and simulated failure loads are given in Table 23 to study the accuracy of the failure load simulations.

Table 23 B702B1 element size sensitivity analysis summary

B701B2	Elements [-]	V [kN]	V_{exp}/V_{num} [-]
Experiment	-	202	-
FUSTN 50/3	30	200	1.01
FUSTS 50/3	30	213	0.95
FUSTN 20	25	205	0.99
FUSTS 20	25	208	0.98
FUSTN 25	20	198	1.02
FUSTS 25	20	202	1.00
FUSTN 100/3	15	156	1.29
FUSTS 100/3	15	222	0.91

The force-displacement graph in the annex and the table above are reviewed. These results show that the simulation underpredicts the failure load for the element size of 100/3 due to a too-large element size. The too-large element size decreases the accuracy of the simulation. Thus, no further increase in element size was performed. Besides analysis for the element sizes of 20 mm and 25 mm, another analysis was added with the element size of 50/3. These three element sizes resulted in failure loads close to the experimental result. The maximum difference between the three simulated failure loads of different element sizes is 6 %. This additional element size sensitivity analysis was performed to show the decrease in element size sensitivity with a decrease in the beam dimensions (depth).

A121A3 element size sensitivity analysis:
Finally, the smallest beam (A121A3) is analyzed for element size sensitivity, for which there were suspicions that the element size of 25 mm was already large. However, an element size sensitivity analysis for elements of 30mm was also done to see how much the inaccuracy increases with an even larger element size. The simulated results are in Annex III, Figure 115, and Figure 116. The summary of this simulation using the numerical and experimental failure load can be seen in Table 24 below.

Table 24 A121A3 element size sensitivity analysis summary

A121A3	Elements [-]	V [kN]	V_{exp}/V_{num} [-]	V2 [kN]	V_{exp}/V_{num} [-]	V3 [kN]	V_{exp}/V_{num} [-]
Experiment	-	145	-	152	-	137	-
FUSTN 12	**25**	158	0.92	158	0.97	158	0.87
FUSTS 12	**25**	160	0.91	160	0.95	160	0.85
FUSTN 15	**20**	144	1.00	144	1.06	144	0.95
FUSTS 15	**20**	139	1.04	139	1.10	139	0.99
FUSTN 20	**15**	137	1.06	137	1.12	137	1.00
FUSTS 20	**15**	137	1.05	137	1.11	137	1.00
FUSTN 25	**12**	137	1.06	137	1.11	137	1.00
FUSTS 25	**12**	113	1.28	113	1.35	113	1.21
FUSTN 30	**10**	109	1.33	109	1.40	109	1.25
FUSTS 30	**10**	136	1.06	136	1.12	136	1.00

First, simulations were done with elements sizes of 20, 25, and 30 mm. As suspected, the element size of 30 mm proved too large, causing incorrect damage progression. The table above shows an underprediction of the failure load for an element size of 30 mm due to decreased accuracy. The element size of 30 mm had 10 elements over the beam depth, which Lang [45] also did not recommend for the flexural shear failure. After analyzing the element sizes 20 and 25, it can be said that they capture the correct damage progression and successfully capture the flexural shear failure. However, between element sizes 20 and 25, it was found that element size 20 delivered the more accurate representation of the experiment, as also reflected in Table 24. Next, tests were done with reduced element sizes of 12 mm and 15 mm to determine if the size could be optimized even more over an element size of 20 mm. The maximum principal strain plots are in Figure 115.

Element size 15 had the most accurate result with a correct crack progression, an almost similar crack pattern to the experiment, and an accurate failure load prediction for all three experimental specimens. Interestingly, like the previous cases, tiny element sizes can start overpredicting and show signs of an irregular crack pattern. In this case, after element sizes 25, 20, and 15 mm simulated comparable results, the element size of 12 mm overpredicted the failure load due to being too small. This result shows that tiny element sizes increase the computational cost and decrease the accuracy after a particular small element size. Next, an additional element size sensitivity analysis will be done for other cases with a similar beam depth using element sizes 15 and 20 mm. This analysis will make it clear which element size is more optimal.

Additional cases element size sensitivity analysis:
Previously additional element size sensitivity analysis was done for multiple experimental beams with a depth of 1200 mm. Case H601A showed considerable sensitivity, and choosing an element size for a beam with a depth based on only one simulation is not ideal. As the beam depths (R804A1, B701B2, and A121A3) decreased, the element size sensitivity appeared to decrease. However, because of the considerable sensitivity of the element size, more sensitivity analysis will still be done for cases with a depth of 800 mm, 500 mm, and 300 mm. With this approach, choosing an element size based on one numerical simulated case per beam depth is avoided. Previously for the three cases, accurate results with acceptable computational time were simulated with the following element sizes:

- R804A1 with element sizes of 32 and 40 mm
- B701B2 with element sizes of 20 and 25 mm
- A121A3 with element sizes of 15 and 20 mm

The additional case with their beam depths is also given below:

- R803A1 with a beam depth of 800 mm
- B502A2 with a beam depth of 500 mm
- A751B1 with a beam depth of 300 mm

Below are three tables (Table 25, Table 26, and Table 27), which summarize the additional cases' element size sensitivity analysis results. In addition, figures of the simulated results are placed in Annex III (Figure 120, Figure 121, and Figure 122).

Table 25 R803A1 element size sensitivity analysis summary

R803A1	Elements [-]	V [kN]	V_{exp}/V_{num} [-]	V2 [kN]	V_{exp}/V_{num} [-]
Experiment	-	279	-	308	-
FUSTN 20	**40**	294	0.95	294	1.05
FUSTN 25	**32**	296	0.94	296	1.04
FUSTN 80/3	**30**	274	1.02	274	1.13
FUSTN 32	**25**	313	0.89	313	0.98
FUSTN 40	**20**	282	0.99	282	1.09

Table 26 B502B2 element size sensitivity analysis summary

B502A2	Elements [-]	V [kN]	V_{exp}/V_{num} [-]	V2 [kN]	V_{exp}/V_{num} [-]
Experiment	-	174	-	173	-
FUSTN 20	**25**	178	0.98	178	0.98
FUSTN 25	**20**	171	1.02	171	1.02
FUSTN 100/3	**15**	183	0.95	183	0.95

Table 27 A751B1 element size sensitivity analysis summary

A751B1	Elements [-]	V [kN]	V_{exp}/V_{num} [-]
Experiment	-	107	-
FUSTN 12	**25**	125	0.86
FUSTN 15	**20**	116	0.92
FUSTN 20	**15**	109	0.98

Because the numerical sensitivity analysis results and problems due to the sensitivity have already been addressed, a detailed explanation will be left out for the additional cases. However, the main points that are found for the element size sensitivity analysis for these cases are the following:

- None of the cases was subjected to failure due to reinforcement yielding.
- For the additional cases, not all simulations with element sizes that could capture the flexural shear failure previously resulted in this failure mode again.
- Case A751B1 captures the flexural shear failure for element sizes 15 mm and 20 mm accurately. However, considering computational cost, an element size of 20 mm is preferred for beams with a depth of 300 mm. There is no need to increase the computational time if no significant improvement is found in the simulation.
- For case B502B2 in Figure 121 force-displacement graph two experimental specimen results are shown. While one specimen has the same initial stiffness as the numerical model, the other has a lower initial stiffness. The lower initial stiffness is due to a previous experiment on the beam, as explained in Figure 30. However, what is essential is that the post-initial crack stiffness of both experiments resembles each other and is accurately replicated by the numerical simulation. The same reasoning can be used for the case of R803A1 if the force-displacement graph is reviewed in Figure 122.
- Case B502B2, unfortunately, does not capture the flexural shear failure with all element sizes used in the analysis. The element size of 20 mm is subjected to the wrong failure mode due to the element size being too small. The element size of 25 mm is good enough to simulate the flexural shear failure for beams with a depth of 500 mm. A larger element size with five fewer elements over the beam depth also captures the right failure load. However, a slight underestimation of the failure load was noticed for the larger element sizes during the analysis of case B701B2. This underestimation of the failure load is due to a decrease in accuracy caused by the increased element size.
- Just as it was noticed for case R804A1, for R803A1, the best-performing element size was 40 mm. According to the literature, beams with depths greater than 600 mm are known for increased element size sensitivity. The flexural shear failure for element size 40 successfully captures the correct failure mode and resembles the experimental cracks. The 80/3 mm and 32 mm element sizes also accurately capture the failure load. However, when describing the crack pattern, these two element sizes have element size sensitivity problems causing irregular crack patterns.

Element size sensitivity analysis: summary

There is a lack of element size recommendations from previous studies regarding geometrically large beams, with many suggesting further research for such beams [45] [43]. The mesh sensitivity analysis found that the 800 mm and 1200 mm beams, considered large, get the most accurate representation of the experiment with an element size of 40 mm. Figure 91 will be used as a guideline to estimate the element size for the remaining cases for this research. These element sizes will be adopted as the standard size for upcoming beams with a depth of up to 1200 mm.

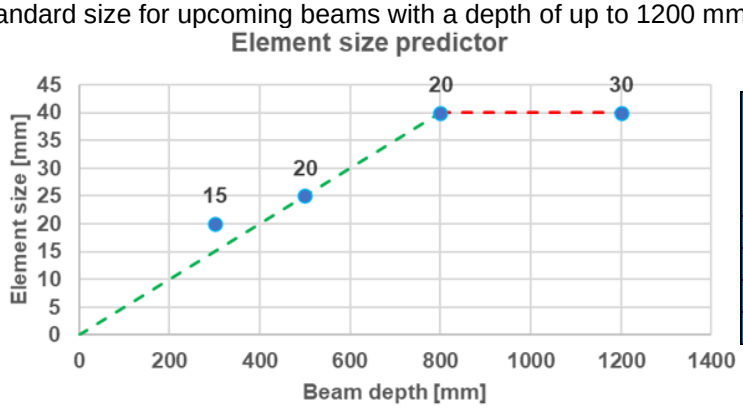

Beam depth [mm]	Element size [mm]	Number of elements over beam depth [-]
300	15	20
500	20	20
800	40	20
1200	40	30

Figure 91 Optimal element size predictor (left) and element size prediction for different depths (right)

In Figure 91, markers show the number of elements over beam height. The green line does not go through the plotted marker for the beam with a depth of 300 mm. The plotted dot for this beam depth shows an element size recommendation of 20 mm. However, the green line is plotted like this because the element size of 15 mm gave as accurate results as for element size of 20 mm during the mesh sensitivity analysis. The only reason the element size of 20 mm got initially chosen as the optimal one was the lower computational time.

Also, an overview of the improvement in result for the initial cases when applying the element size predictor is shown in Table 28.

Table 28 Sensitivity analysis cases with element size predictor

$V_{experimental}/V_{numerical}$:	Initial element size	Element size predictor
A121A3	1.06	1.00
A122B1	1.11	1.06
A123A1	1.00	0.95
B701B2	1.02	0.99
R804A1	0.98	1.09
R804B1	0.91	1.01
H601A	0.98	0.98
H602A	0.98	0.98

The RTD guidelines recommend calculating the element size depending on a minimum number of elements over the beam length and depth. For all the cases till now, the element size calculated over the beam length was not governing. The elements over the beam length were larger than those recommended over the beam depth, and the smaller size of these two was chosen as the governing one. The formula over the beam length advised by the RTD guidelines is 50 elements over the beam length. However, the elements over the beam length will also be accounted for in the upcoming cases from the following simulations, as this element size may be the governing one for some cases.

4.3 Quantitative analysis

This section quantitively compares numerical simulations to experimental results. The numerical model is based on the model found after sensitivity analysis on multiple modeling aspects in Chapter 4.2. The numerical model is an unconfined (compression-compression) fixed crack orientation and the Shima bond-slip relation combined with truss elements using the full NR iteration scheme. This model can also be found summarized in the figures from Annex IV. A quantitative analysis is done for all cases from Chapter 3, with their properties specified in Annex II. From the quantitative analysis, the numerical model consistently gave satisfactory results for most cases, with a few exceptions. A few cases did not successfully result in the correct failure mode.

The geometrically smaller beams resulted in the correct failure mode for every simulation. However, a typical wrong failure mode that would often be captured was the dowel failure for geometrically large beams. As found during the modeling aspect sensitivity analysis of the fixed crack model, the dowel failure mode is caused by an excessive change in the damage-based shear retention factor. During simulations, the change in the shear retention factor should be closely monitored. Sensitive steps for the change in the factor are especially before and during failure and can be located from the force-displacement graph. The excessive change in the damage-based shear retention factor is controlled by reducing the step size of the analysis procedure when close to the failure load during the simulation. Even though it can be cumbersome to decrease the step size to tiny steps as there is an increase in the computational time, the flexural shear failure gets successfully captured.

The reduction of the step size approach did not work for only one case, namely case H301A, where the step size was reduced to 0.001. This experiment was found in Garnica et al. report [89], and the case properties, including results, can be found in Annex II. Further research was done on this case, and interesting findings were found in the report. After the experiment on case H301A was performed at Stevin lab, another experiment on a case with the same material properties and dimensions was performed. This case is called H302A and resulted in dowel failure during the experiment. Analyzing its failure mode, this overlapped with the numerical simulation. The same failure mode for the numerical simulation and case H302A during the experiment can be seen in Figure 92. Compared to H302A experimental results, the numerical model found the correct damage progression, failure load, and failure mode. Another remark on case H301A is that this experiment was stopped midway through the testing and, after that, resumed. Case H302A was performed without interruptions, making this a more reliable experiment.

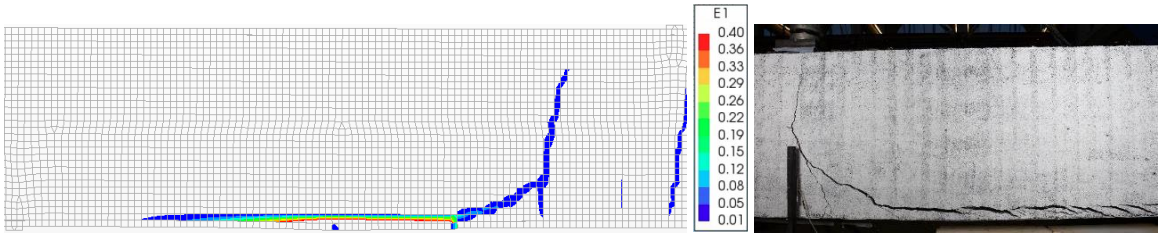

Figure 92 H302A dowel failure: simulation (left) and experiment (right)

The numerical simulations' accuracy can be analyzed on their safety by the percentage difference between the experimental and simulated failure loads. Also, using the results of this method, an overview of the accuracy can be given in histograms. The quantitive numerical simulations of cases are also displayed in Annex II for the different experimental cases. The percentile result for the numerical model is specified in the histogram of Figure 93 on the next page. A similar histogram is also made for the design codes EC2 and FIB MC 2010. The results for the FIB MC2010 are based on an LoA II, introduced in Chapter 2.3. The design code percentile differences are specified in Figure 94, with the legend from Figure 93 also applied to the design code figure.

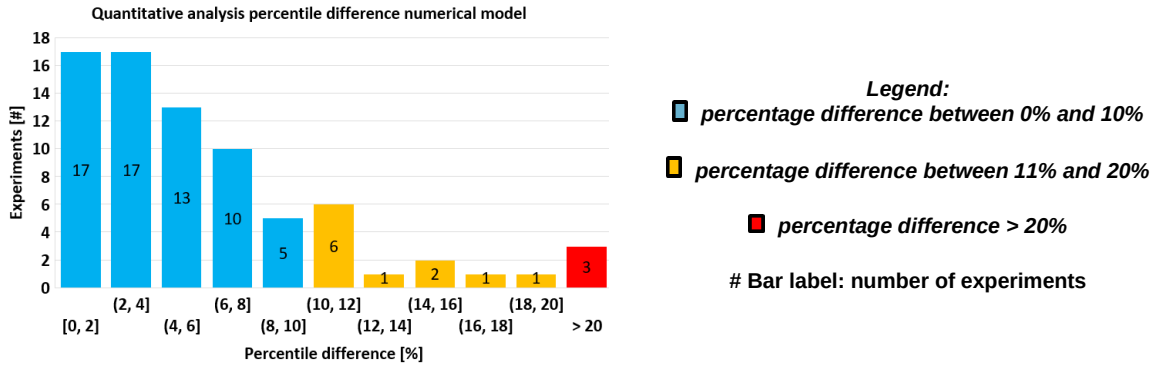

Figure 93 Quantitive analysis percentile difference: Numerical model (top left)

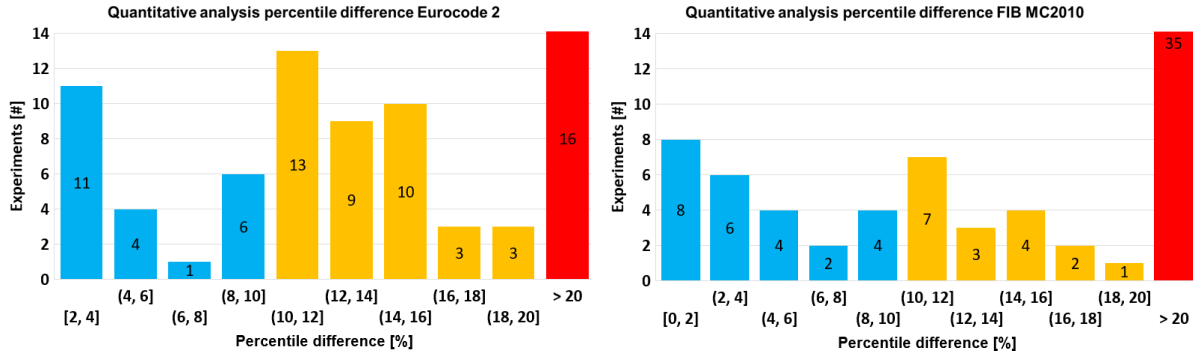

Figure 94 Quantitive analysis percentile difference: EC2 (bottom left), and FIB MC2010 (bottom right)

According to the percentile differences, the numerical model simulations are satisfactory, with only 3 simulated cases over a 20% difference. All these 3 cases consisted of low reinforcement ratios and being geometrically large. The EC2 resulted in better predictions compared to the FIB MC2010. However, if for the FIB MC2010 the LoA III were applied instead of the simplified LoA II, the physical-mechanical model results from FIB MC2010 would be improved. The simplified LoA was used as the design codes are not the focus of this study, and not all required data for LoA III were available. The numerical method and design codes have the following average failure load percentage differences with the experiment:

- Numerical simulations: 6%
- EC2 predictions: 14%
- FIB MC2010 predictions: 19%

The plot in Figure 95 below gives an overview of the experimental failure load compared to the numerical simulations:

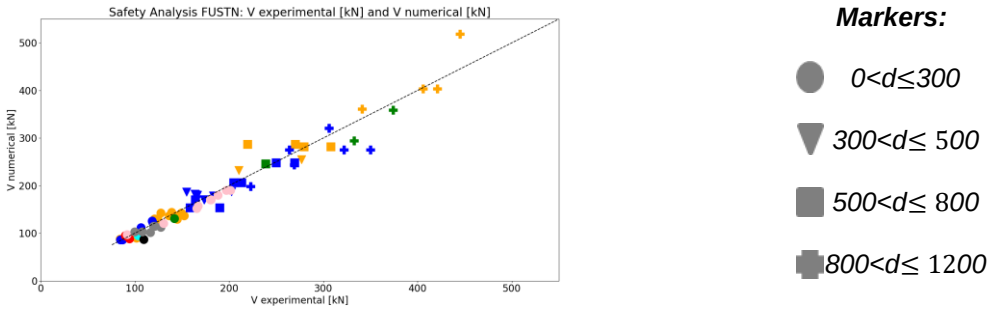

Figure 95 Simulated and experimental failure loads

The numerical analysis comparison in Figure 95 shows that the smaller case simulations are close to the experimental result. However, as the beam size increases, the difference between the compared models in failure load does increase in some cases. The largest failure loads are for beams with a depth of 1200 mm and can be recognized from the plus markers. These were also the largest geometrical beams out of all simulated cases. While the numerical results stay close to the plotted midline, some under and overestimations exist. An alternative method called the DPC method was also used for a similar comparison. The results of this method can be found in Annex VI. In the annex, six cases were unacceptable in their failure load predictions according to the DPC method and in the annex. A short analysis is also done on the design codes predictions. The plot Figure 96 below has been made to give an overview of the experimental failure load to the design code predictions:

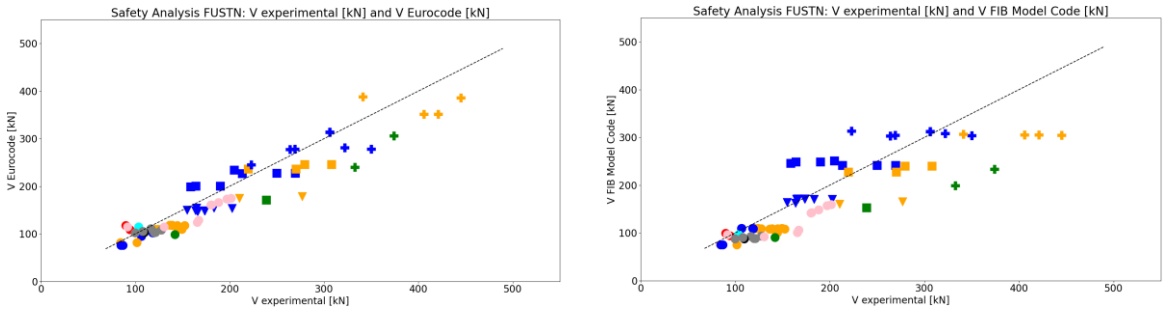

Figure 96 "EC2 and experimental" (left) and "FIB MC2010 Simulated experimental failure loads" (right)

The analytical result from the Eurocode sometimes underestimates the failure load with high differences from the experiment. The results of these predictions can be explained due to the safety threshold introduced in the analytical design code to keep the calculations safe. The physical-mechanical model from FIB MC2010 shows large over and underestimations for the geometrically large beams. Most results found for geometrically small beams are underestimated. Overestimation of the failure load can be dangerous and was looked at more in-depth. Three cases (E401B1, E402B, and H301A) are subjected to the highest overestimations. All three cases have one thing in common, they are all large beams (1200 mm) and have low reinforcement ratios (0.41 %, 0.41 %, and 0.27 %, respectively). These beams should be looked at more in-depth without the simplified LoA. Using LoA III will improve results as the simplifications are eliminated.

4.4 Size effect analysis

Finally, this section performs numerical simulations for the size effect analysis. These results will give an initial expression of whether the numerical method can capture the size effect. The size effect is investigated on RC beams without stirrups by scaling them geometrically. The cases are based on experiments from Bhal [84] and have an effective depth of 300 mm, 600 mm, 900 mm, and 1200 mm. The four cases were also part of the quantitative analysis, and their simulations are accurate compared to experimental results. Detailed information regarding the four experimental cases from this report can be found in Annex II. In addition, the overview of the experimental setup is given in Figure 25.

The simulated failure load and displacement of the Bhal experiments increase when the beams' geometrical size is increased. This behavior is shown in the force-displacement graph in Annex VII (Figure 134). However, the nominal shear strength is required to know if the size effect is captured. A log-log scale plot with the nominal shear strength and the effective depth is plotted to study the size effect. The log-log plot can be seen in Figure 97 for the Bhal cases. This figure will show how accurately the numerical model captures the size effect compared to the experiment and multiple analytical models. Each analytical model used for comparison was explained during the literature review.

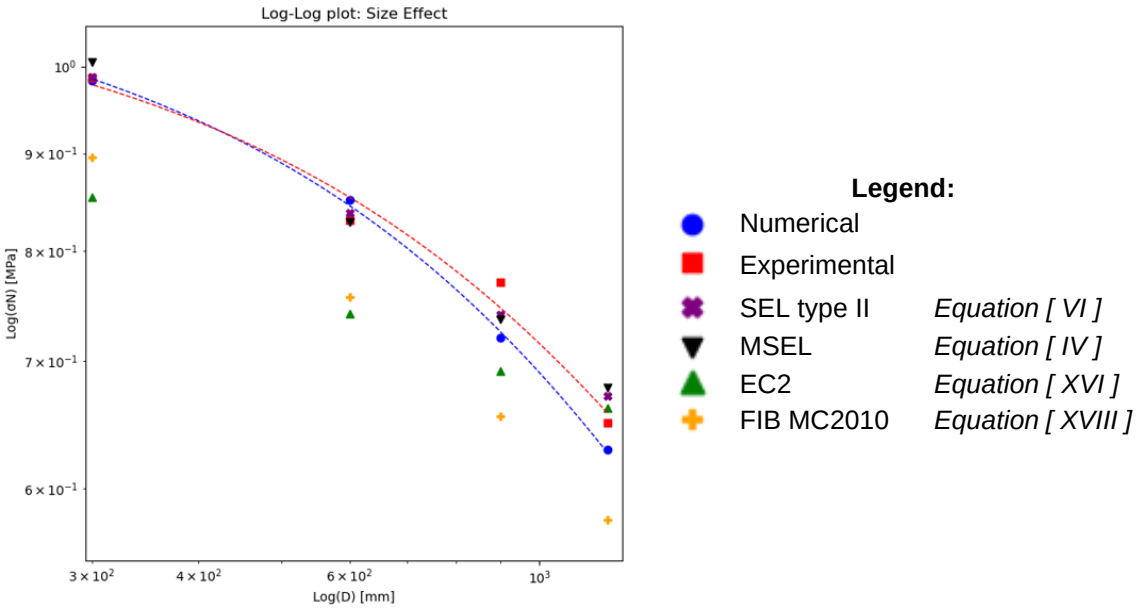

Figure 97 Size effect analysis: nominal shear strength and effective depth

The markers in the figure above show the nominal shear strength values. For the experiment and numerical model, these markers have been connected with a second-order curve fitted line to show better the decreasing relation. The numerical model's decrease in the nominal shear strength can be seen in the figure with increased effective depth and constant values for all other geometrical and material configurations. This decrease in nominal shear strength proves the inclusion of the size effect for the set of geometrically scaled beams. However, it is important to know if the size effect is captured accurately with the numerical method by comparing this to the experimental result.

The experimental nominal shear strengths (red square markers) do not entirely align with the curve fitting. There are small jumps from the markers below and above the fitted line. Looking at the fitted line of the numerical method and experimental result, the nominal shear strength of the numerical simulation (blue circle markers) closely follows the experimental results. While the small beams have the same approximate nominal shear strength, there is a slightly increasing underestimation of the value as the beam depth increases. This underestimation of nominal shear strength indicates a slightly higher size effect found with simulations compared to the experiments. However, this underestimation is within acceptable boundaries as the relative difference in numerical and experimental nominal shear strength for the largest beam (d = 1200 mm) is 3%. There is a possibility that the size effect can be overestimated more for geometrically scaled beams bigger than the one from this set. Future research on even larger beams can make this remark clearer. The relative difference in the nominal shear strength between the smallest (d = 300 mm) and largest beams (d=1200 mm) is 17 %.

Results of the numerical model and experiments for the decreasing nominal shear strength as the beam size increases show that the numerical model has captured the size effect. Next, the SELs and design code predictions are analyzed. The Bažant SEL (purple cross markers) predictions show that this model best captures the size effect. However, the disadvantage of the SEL should also be considered, as the geometrical parameters to calculate the size effect are unknown in advance. The MSEL predictions (black triangle markers) also show promising results, even though they are not as accurate as Bažant SEL. The nominal shear strength results closely follow the experimental results and numerical simulations with this SEL. There is a case of underestimation of the nominal shear strength for the design codes (EC2 and FIB MC2010 with LoA II). Analytical models have a conservative region included, causing lower predictions. The FIB MC2010 with LoA II is predicting the size effect well. The decrease in the nominal strength with an increase in beam depth is like the experimental and numerical one. Unfortunately, the EC2 underestimates the size effect as the beam size increases. For geometrically scaled beams deeper than 1200 mm, this will lead to exaggerated predictions of the nominal shear strength.

Another aspect of capturing the size effect is being consistent with the failure mode pattern of the geometrically scaled beams. The crack pattern for all four cases is extrapolated on one beam for comparison in Figure 98. The figure shows that the correct failure mode (flexural shear failure) has been captured in all cases, but most importantly, the patterns do not differ much.

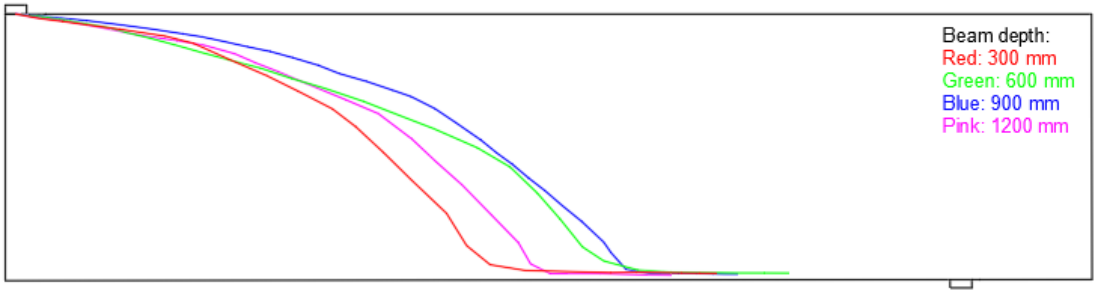

Figure 98 Size effect analysis: geometrically scaled beams crack pattern

Before moving to the chapter conclusion, more analysis is done on the behavioral influence on the beam caused by the effective depth. An important observation was the relationship between the increasing effective depth and the reinforcement stresses. As the beam depth increases, the tensile stresses in the reinforcement decrease. Beams with lower tensile strains are linked to a more brittle response during failure.

The analysis shows that the numerical method captures the size effect with varying effective depths by geometrically scaling the beams. According to the literature review, reinforcement ratio, effective span-to-depth ratio, and concrete strength are other possible factors influencing the size effect. The influence of a parameter on the size effect is studied as done previously, using log-log curves for the nominal shear strength over the effective depth with fictitious beams. The results can be found in Annex VIII.

4.5 Discussion and conclusion

Numerous sensitivity analysis was done on different modeling aspects to get the best numerical model. During the analysis, the correct damage progression, failure mode, and failure load were required to be found or, at the very least, be acceptable. For this, sensitivity analysis was performed on a selection of cases using the following modeling aspects:

- The use of compression-compression confinement
- The reinforcement bond-slip relation
- The total strain crack models' crack orientation
- The reinforcement element type
- Incremental-iterative procedure
- Global element size

The tables below summarize the most important numerical model's failure load simulations. After all sensitivity analyses for the modeling aspects were performed, the suggested numerical model in the table's final row was obtained.

Table 29 Compression-compression confinement sensitivity analysis summary

$\frac{V_{experimental}}{V_{numerical}}$:	Confined	Unconfined
A121A3	1.33	1.33
A122B1	1.40	1.41
A123A1	1.25	1.26
B701B2	1.20	1.17
R804A1	1.25	1.25
R804B1	1.16	1.16
H601A	0.95	0.92
H602A	0.95	0.92

Table 30 Total strain crack models' crack orientation sensitivity analysis summary

$\frac{V_{experimental}}{V_{numerical}}$:	Fixed	Rotating
A121A3	1.33	1.20
A122B1	1.40	1.26
A123A1	1.25	1.13
B701B2	1.20	0.94
R804A1	1.25	1.28
R804B1	1.16	1.19
H601A	0.95	Delamination
H602A	0.95	Delamination

Table 31 Bond-slip relation sensitivity analysis summary

$\frac{V_{experimental}}{V_{numerical}}$:	FIB	Shima
A121A3	1.33	1.06
A122B1	1.40	1.11
A123A1	1.25	1.00
B701B2	1.20	1.02
R804A1	1.25	0.98
R804B1	1.16	0.91
H601A	0.95	0.98
H602A	0.95	0.98

Table 32 Iteration scheme sensitivity analysis summary

$\frac{V_{experimental}}{V_{numerical}}$:	Full NR	Secant
A121A3	1.06	1.06
A122B1	1.11	1.12
A123A1	1.00	1.00
B701B2	1.02	1.00
R804A1	0.98	0.95
R804B1	0.91	0.88
H601A	0.98	1.02
H602A	0.98	1.02

Table 33 Reinforcement element sensitivity analysis summary

$\frac{V_{experimental}}{V_{numerical}}$:	Truss	Beam
A121A3	1.06	1.40
A122B1	1.11	1.48
A123A1	1.00	1.32
B701B2	1.02	1.26
R804A1	0.98	1.02
R804B1	0.91	0.95
H601A	0.98	0.97
H602A	0.98	0.97

Table 34 Global element size sensitivity analysis summary

$\frac{V_{experimental}}{V_{numerical}}$:	Initial	Predictor
A121A3	1.06	1.00
A122B1	1.11	1.06
A123A1	1.00	0.95
B701B2	1.02	0.99
R804A1	0.98	1.09
R804B1	0.91	1.01
H601A	0.98	0.98
H602A	0.98	0.98

Using sensitivity analysis, a numerical model is obtained that can accurately simulate the flexural shear failure for RC beams without stirrups. Previously a summary of the constitutive model modeling aspects findings was given in Chapter 4.2.1.3. A summary of the constitutive model numerical choices is given in the two tables below:

Table 35 Robust numerical model: concretes' constitutive mode

Aspect	***Modeling choice***
Element class	Regular plane stress (quadratic)
Class	Concrete and masonry
Material model	Total-strain crack model
Crack orientation	Fixed
compressive curve	Parabolic
Reduction model lateral cracking	Vecchio and Collins 1993
Lower bound reduction curve	0.4
Compressive-compressive confinement	Unconfined
Tensile curve	Hordijk
Reduction model Poisson's ratio	Damage-based
Crack-bandwidth	Govindjee's projection method
Shear retention function	Damage-based

Table 36 Robust numerical model: reinforcements' constitutive model

Aspect	***Modeling choice***
Shape type	Line
Class	Reinforcement
Material model	Bond-slip reinforcement
Non-linear model	Von Mises plasticity
Plastic hardening	Total strain-yield stress
Hardening hypothesis	Strain hardening
Hardening type	Isotropic hardening
Bond-slip interface model	Shima
Reinforcement type	Truss bond-slip

The findings for the modeling aspects from sensitivity analysis will be specified below. The findings mentioned below are an extension of the conclusion found for the constitutive model to avoid repeating the constitutive model results. The critical findings for the remaining sensitivity analysis are the following:

Newton Raphson iteration scheme or Secant iteration scheme:

- The full NR iteration scheme has more convergence problems than Secant's during the initial crack. However, this should not be a problem as the overshot of the (force and energy) norms are analyzed for the non-converged steps in the convergence log generated by DIANA FEA.
- Both iteration schemes simulate the same result for geometrically small beams. However, with an increase in the beam size, the simulated cases become more sensitive to the iteration scheme used, and the difference between simulated results can increase.
- Most of the time, the full NR iteration scheme captures the flexural shear failure more accurately.
- Both iteration schemes require different load steps and sometimes different element sizes for optimal results.
- Secant's iteration scheme can symmetrically give the flexural shear failure for some simulations. The Secant iteration scheme fails to include material nonlinearity due to the symmetrical modeling of the structure, causing this type of failure.

Beam element or Truss element:

- The beam elements applied can withstand shear stresses with the dowel effect, but this benefit is missing for truss elements.
- Incompatibility between the beam and plane stress elements is found due to the extra rotational degree of freedom of the beam element, which the plane stress element does not have. The interface element must tie this rotational degree of freedom to the transitional degree of freedom. However, the interface element automatically used by DIANA FEA is not ideal for such a tying of degrees of freedom. Thus, higher shear tractions, relative displacements, and more convergence problems occur for beam elements.
- The numerical model with truss elements reaches higher reinforcement stresses than beam elements because the latter model often fails at lower loads.
- The numerical model with beam elements sometimes overpredicts the stiffness after the initial cracks. There were also high strains along the reinforcement for these cases, making the numerical model with beam elements more sensitive to dowel failure.

The global element size:

During element size sensitivity analysis, a larger element size sensitivity was found for geometrically large beams. Because the crack propagation rate depends on the element size, the wrong failure mode was often captured. While it is well known that too-large element sizes can decrease the simulation accuracy, some interesting findings are also addressed for too-small element sizes. When the element size is too-small, huge strains appear at the sides of some elements. These large strains are transferred horizontally or vertically from element to element, thus creating horizontal or vertical crack patterns. As a result, the numerical model simulates an irregular crack pattern instead of a smooth flexural shear failure pattern. Thus, besides increasing unnecessary computational costs, a too-small element size should not be chosen to avoid capturing irregular crack patterns. The optimal element size from the sensitivity analysis for different beam depths is given in Figure 91 in an element size predictor and Table 38 below. The element size predictor should be used for calculations over the beam depth to predict the element size for beams. In addition, a formula advised by the RTD guidelines (50 elements over the beam length) should also be considered. However, this element size is not expected to be the governing as the element size predictor's element size is almost always smaller. The smaller element size from the formulas is chosen as the governing element size and applied to the numerical model.

The best numerical model from all the sensitivity analyses is an unconfined (compression-compression) fixed crack orientation and the Shima bond-slip relation with truss elements using the full NR iteration scheme. Figures from Annex V and tables in this chapter (Table 35, Table 36, Table 37, Table 38, and Table 39) provide a complete overview of the numerical model configurations. Some of the tables are given below:

Table 37 Robust numerical model: finite element discretization a

Elements	***Modeling choice***
Concrete Element	Quadratic element
Concrete Integration	3x3
Reinforcement Element	Truss element

Table 38 Robust numerical model: finite element discretization b

Mesh	***Modeling choice***
Element size	$minimum\left(\begin{Bmatrix} {}^{h}/_{20},\ if\ h \le 800\ mm \\ 40\ mm,\ if\ 800 \le h \le 1200\ mm \end{Bmatrix},\ {}^{L}/_{50}\right)$
Mesher type	Hexa/ Quad
Seeding method	division

Table 39 Robust numerical model: analysis procedure

Analysis procedure	***Modeling choice***
Loading method	Displacement method
Command	Structural non-linear
Load steps	Start with 0.5 (linear part)
User specified	Depending on model
Maximum iterations	100
Incremental-iterative procedure	Full NR
Line searching	On
Continuation of iteration	Off
Satisfy all specified norms	Off
Convergence norm	Energy norm (0.001) and force norm (0.01)
No convergence	Continue

Following the sensitivity analysis, a quantitative analysis is performed for all experimental cases mentioned in Chapter 3, which are 76 cases. The properties for all the cases can be found in Annex II. The numerical model from different modeling aspects' sensitivity analysis consistently gave satisfactory results for most cases, with a few exceptions. A few cases did not successfully result in the correct failure mode. For these cases, the dowel failure mode is caused by an excessive change in the damage-based shear retention factor. During analysis, the change in the shear retention model should be closely monitored, especially close to the sensitive steps. Sensitive load steps are especially before and during failure. Reducing the load step to tiny steps close to the sensitive load steps increases the computational time greatly but avoids capturing the dowel failure. As a result, the flexural shear failure will be successfully captured.

The percentage difference between the simulation and experimental failure load was used to get an overview of the simulated failure load accuracy compared to the experimental failure loads from the quantitative analysis. Most of the cases were at a low percentile difference. From the quantitative analysis, the following percentages were found:

- 0 % ≤ percentage difference ≤ 10 %: 62 cases
- 10 % < percentage difference ≤ 20 %: 11 cases
- Percentage difference > 20 %: 3 cases

In addition, the average failure load percentage difference was 6 % for all cases for the numerical simulations, while the EC2 average difference was 14 %.

Lastly, the pilot research on the size effect was performed. An initial expression of whether the numerical method can capture the size effect is obtained from this analysis. After simulating the geometrically scaled beams, this was followed by analyzing the changes in the nominal shear strength. An increase in the beam size led to a decrease in the nominal shear strength, which shows that the numerical model successfully captures the size effect. The nominal shear strength decrease between the largest and smallest cases caused by the size effect is 17 %. The same nominal shear strength was found for the geometrically smaller beams when comparing the numerical simulation with the experimental result. However, the nominal shear strength is slightly underestimated in the simulations as the beam size increases. This result indicates an overestimation of the size effect with the numerical method. However, the size effect prediction from the numerical method is acceptable, with a relative difference of only 3 % with the experimental result for the largest beam (H601A). An analysis with some size effect theories showed that Bažant SEL and MSEL show almost similar nominal shear strength as the experimental result. Lastly, it was also important that an almost identical crack pattern was captured for the size effect. The crack patterns of the four cases have been merged into one figure (Figure 98), which shows that all the cases successfully captured the flexural shear failure.

5 Conclusion and recommendations

5.1 Conclusion

This research investigates whether, using sensitivity analysis, a numerical model can be obtained that accurately simulates flexural shear failure for RC beams without stirrups. During this research, first, sensitivity analysis was performed to reduce the model uncertainty for multiple modeling aspects. After that, a quantitative analysis with many cases followed to verify if the numerical model previously obtained is accurate for such simulations. Below, the important findings from this research are given.

The modeling aspects:
Sensitivity analysis was done on multiple modeling aspects for the numerical model with four experimental cases. All four cases had different geometrical sizes, while some material parameters differed. Having differences in the case configuration increases the sensitivity analysis quality. The different findings for each aspect are discussed below:
1. The total strain crack models' crack orientation:
The sensitivity analysis shows that the rotating crack orientation can suffer from delamination of the concrete cover due to over-rotation of the crack. The delamination is recognized by cracking of the concrete cover along the reinforcement. Over-rotation has also been shown to correlate strongly with a high number of non-converged steps. In addition, the fixed crack orientation has a more realistic representation of the experiment failure mode.
2. The use of compression-compression confinement:
This modeling aspect is kept unconfined for the numerical model because compression-compression confinement is not a modeling requirement for cases with a brittle shear-tension failure mode. In addition, for one of the four sensitivity analysis cases, a slightly lower failure load was found for the confined numerical model. In this case, high stresses were suddenly introduced along the reinforcement.
3. The reinforcement bond-slip relation:
The main difference between the Shima bond-slip relation and FIB bond-slip relation is the inclusion of a decrease in bond stress at high slip values for the latter relation. Also, the Shima bond-slip relation has a higher bond capacity and initial stiffness when using similar material configurations for the modeling assumptions. Due to the FIB bond-slip relation's lower initial stiffness, a bigger relative displacement occurs between the concrete and reinforcement. As a result, the cracks are larger with this bond-slip relation, and the simulation also underestimates the failure load. In addition, due to the higher relative displacement between the materials of the FIB bond-slip model, this model is more sensitive to capturing dowel failure as the tensile reinforcement detaches. Overall, the Shima bond-slip model captures the correct failure mode and failure load more accurately.
4. Incremental-iterative procedure:
The full NR and Secant iteration scheme for geometrically small beams simulate almost the same results. However, the simulations' differences increase as the beam's geometrical size increases. Analysis shows the full NR iteration scheme can have more convergence problems during the initial crack. However, its simulations after the initial cracks are more representative of the experiment. In addition, in a few cases, the Secant iteration scheme gave symmetrical flexural shear failure due to failing to include material nonlinearity.

5. The reinforcement element type:
The beam elements used consider bending stiffness, making it possible for the concrete to withstand shear stresses with the dowel effect, which truss elements do not. These reinforcement elements are combined with plane stress elements for concrete, where the beam elements also have a rotational degree of freedom besides the transitional ones. For plane stress elements and beam elements to be compatible, the interface element must tie the extra degree of freedom to the transitional degree of freedom. However, the interface element DIANA FEA applies fails to do this successfully, causing incompatibility issues. As a result, simulations with beam elements have been shown to consist of simulations with more convergence problems and higher relative displacements than truss elements. Due to the higher relative displacements, a numerical model with beam elements between the materials can be more sensitive to dowel failure. In addition, comparisons between the experiment and numerical simulations with beam elements show that the stiffness was slightly overpredicted after the initial cracks.
6. Global element size:
The global element size is a modeling aspect whose sensitivity has been observed to increase as the beams' geometrical size increases. More experimental cases were added to the sensitivity analysis for the element size due to the high sensitivity of this modeling aspect. A too-large element size can decrease the accuracy of the simulations, and wrong failure modes can be captured as the crack propagation rate depends on the element size. While choosing a too-small element size can increase the computational time without improving the analysis quality, the numerical model can also capture irregular crack patterns. The irregular crack patterns are caused due to large strains at the end of the elements. Next, the large strains are horizontally or vertically transferred to the neighboring elements, thus causing an irregular crack pattern. From the sensitivity analysis, the following element size formula is recommended for beams up to a depth of 1200 mm:

$$element\ size = minimum\left(\begin{Bmatrix} {}^{h}/_{20},\ if\ h \le 800\ mm \\ 40\ mm,\ if\ 800 \le h \le 1200\ mm \end{Bmatrix},\ {}^{L}/_{50}\right)$$

Equation [XX]

The modeling aspects sensitivity analysis found that the best numerical model is an unconfined (compression-compression) fixed crack orientation and the Shima bond-slip relation with truss elements using the full NR iteration scheme.

The quantitative analysis:
After the sensitivity analysis was completed, a quantitative analysis was conducted for all 76 experimental cases. The model provided satisfactory results with the numerical model obtained from sensitivity analysis, except for a few cases where dowel failure occurred due to an excessive change in the shear retention factor. Load steps close to failure should be monitored closely and reduced to small steps (0.001) to avoid capturing dowel failure. A downside of this approach is the high computational time, but it does result in the correct failure mode. The failure mode percentage differences were 0 - 10 % for 62 cases, 10 - 20 % for 62 cases, and larger than 20 % for 3 cases. In addition, the average failure load percentage difference was 6 % for the numerical simulations, while the best-performing design code had an average of 14 %. The failure load percentage difference overview shows that a numerical model was successfully obtained using sensitivity analysis to simulate the flexural shear failure for RC beams without stirrups.

The pilot research:
With the pilot research, it was hoped to find out if numerical analysis can capture the size effect for the RC beams without stirrups that fail due to flexural shear failure. This pilot research gave an initial expression of the possibility. Analysis shows the numerical model nominal shear strength decreases as the beam geometrical size increases. The simulated nominal shear strength difference was 17 % between the geometrically smallest and largest beam. Compared to the experimental results, the numerical simulation slightly overestimated the size effect as the beams' geometrical size increased with a nominal shear strength difference of 3% for the largest beam (depth = 1200 mm). All four cases successfully captured almost identical flexural shear failure patterns, showing that the size effect has been successfully captured with these results.

5.2 Future research recommendations

Some pitfalls were met during the research, and questions outside this thesis's scope were identified. These points can be addressed in future research, improving the numerical model for simulations of the flexural shear failure for RC beams without stirrups. In addition, recommendations for the size effect are made to decrease ambiguity around this topic.

After the sensitivity analysis, the numerical model showed reliable results, and no further sensitivity analysis on modeling aspects was required to simulate cases accurately. However, some recommendations are still given regarding the model for the future:

1. In a few cases, the current numerical model would capture the dowel failure instead of the flexural failure and required large decreases in the load step size where the change in the shear retention factor was large to simulate the correct failure mode. Instead of increasing the computational time a lot, a more in-depth study can be done for a more appropriate shear retention model.
2. The global element size sensitivity analysis was performed for beams up to a depth of 1200 mm during this study. The analysis showed that this is still a complex topic, and the element size should be researched further for even larger beams than those used in this research.
3. The beam element combined with plane stress elements ran into some compatibility problems during the sensitivity analysis. The use of plane stress elements was already decided on for concrete. Thus no beam element with different concrete elements was simulated. However, further research with shell or plane stress elements with a rotational degree of freedom can identify the use of a better element for concrete for such numerical models.
4. Finally, the percentage difference was higher for simulations for geometrically large beams with a low reinforcement ratio than the other experimental. It would be interesting to see if another numerical model configuration can improve the results for such cases. In addition, simulations should be analyzed for cases with much lower reinforcement ratios than those used during the research (ρ = 0.26 %) to see if the model maintains high accuracy for such simulations.

Recommendations regarding (the pilot research on) the size effect are also made below:

1. An initial expression is found on whether the numerical method can capture the size effect for RC beams without stirrups that fail due to flexural shear failure. A conclusion can be found on this question with numerical simulations on a larger scale and more variety in the RC beams without stirrups geometrical and material configurations.
2. For the experimental (Bhal) cases, with an increasing beam size, a marginal overestimation of the size effect was noticed, with a nominal shear strength relative difference of 3% for the geometrically largest beam. In future research, it would be interesting to see if this relative difference increases to unacceptable percentages for much larger beams.

Bibliography

[1] G. N. J. Kani, "How Safe are Our Large Reinforced Concrete Beams?," *Journal Proceedings,* vol. 64, no. 3, pp. 128-141, 1967.

[2] Z. Bažant and M. Kazemi, "Size Effect on Diagonal Shear Failure of beam without stirrups," *ACI Structural Journal,* pp. 268-276, 1991.

[3] N. Bhal, "Über den Einfluß der Balkenhöhe auf die Schubtragfähigkeit von einfeldrigen Stahlbetonbalken mit und ohne Schubbewehrung," Otto-Graf-Institute, Stuttgart, 1968.

[4] Z. Bažant and Q. Yu, "Designing Against Size Effect on Shear Strength of Reinforced Concrete Beams Without Stirrups," *Journal of Structural Engineering,* vol. 331, no. 12, pp. 1886-1897, 2005.

[5] W. Weibull, "The phenomenon of rupture in solids," Proc. Royal Swedish Institute of Engineering Research, Stockholm, 1939.

[6] Z. P. Bažant, Y. Xi and S. G. Reid, "Statistical Size Effect in Quasi-Brittle Structures: I. Is Weibull theory applicable?," *Journal of Engineering Mechanics,* vol. 117, no. 11, pp. 2623-2640, 1991.

[7] Z. Bažant and J.-K. Kim, "Size Effect in Shear Failure of Longitudinally Reinforced Beams," *ACI Journal,* pp. 456-468, 1984.

[8] Z. Bažant, J.-L. Le and Q. Yu, "Statistical aspects of quasibrittle size effect and lifetime, with consequences for safety and durability of large structures," Northwestern University, Illinois, 2010.

[9] CEN/TC 250, Eurocode 2: Design of concrete structures, Delft: Nederlands Normalisatie-Instituut, 2005.

[10] F. S. A. G. 5, Model Code 2010, Lausanne: International Federation for Structural Concrete, 2012.

[11] Y. Yang, "Shear behaviour of reinforced concrete members without shear reinforcement," Delft University of Technology, Delft, 2014.

[12] R. Cook, D. Malkus, M. Plesha and R. Witt, Concepts and applications of finite element analysis, Madison: University of Wisconsin, 2001.

[13] A. Lubell, T. Sherwood, E. C. Bentz and M. Collins, "Safe Shear Design of Large Wide Beams," *Concrete International,* vol. 26, no. 1, pp. 66-78, 2004.

[14] D. Angelakos, D. Bentz and C. E.C., "Effect of Concrete Strength and Minimum Stirrups on Shear Strength of Large Members," *American Concrete Institute Structural Journal,* vol. 98, no. 3, pp. 291-300, 2001.

[15] E. G. Nawy, Reinforced Concrete: A fundamental Approach, New Jersey: Prentice Hall, 2004.

[16] A. Slobbe, M. Hendriks and J. Rots, "Sequentially linear analysis of shear critical reinforced concrete beams without shear reinforcement," *Finite Elements in Analysis and Design,* vol. 50, pp. 108-124, 2012.

[17] W. Kim and R. White, "Shear-critical cracking in slender reinforced concrete beams," *ACI Structural Journal,* vol. 96, no. S83, pp. 757-765, 1999.

[18] F. Vecchio and W.Shim, " Experimental and analytical reexamination of classic concrete beam tests," *Journal of Structural Engineering,* vol. 130, no. 3, pp. 460-469, 2004.

[19] Y. Yang, A. d. Boer and d. J. Uijl, "Postdiction of flexural shear capacity of a large beam without stirrups using NLFEM," *Structural Engineering International,* pp. 208-215, 2021.

[20] W. Luo, J.-L. Le, M. Rasoolinejad and Z. Bažant, "Coefficient of Variation of Shear Strength of RC Beams and Size Effect," Northwestern University, Illinois, 2020.

[21] H.-G. Kim, C.-Y. Jeong, M.-J. Kim, Y.-J. Lee, J.-H. Park and K.-H. Kim, "Prediction of shear strength of reinforced concrete beams without shear reinforcement considering bond action of longitudinal reinforcements," *Advances in Structural Engineering,* vol. 21, no. 1, pp. 30-45, 2018.

[22] Z.-Q. He, T. Xu and Z. Liu, "Decoupling of arch action and truss action in large beams by strain energy," *Structures: volume 26,* pp. 185-192, 2020.

[23] J. Košćak, D. Damjanović, M. Bartolac and I. Duvnjak, "Shear behavior of RC beams without transverse reinforcement: An analysis of crack kinematics and transfer mechanisms based on stereophotogrammetric measurements," University of Zagreb, Zagreb, 2022.

[24] T. Jayasinghe, T. Gunawardena and P. Mendis, "A comparative study on minimum shear reinforcement provisions in codes of practice for reinforced concrete beams," *Case Studies in Construction Materials,* p. 617, 2021.
[25] G. Garnica, "Analysis of shear transfer mechanisms in concrete members without shear reinforcement based on kinematic measurements," TU Delft, Delft, 2018.
[26] J. C. Walraven, "Aggregate Interlock: a theoretical and experimental analysis," Delft University of Technology, Delft, 1980.
[27] T. Huber, P. Huber and J. Kollegger, "Influence of aggregate interlock on the shear resistance of reinforced concrete beams without stirrups," *Engineering Structures 186,* pp. 26-42, 2019.
[28] J. C. Walraven, "Fundamental analysis of aggregate interlock," *Journal of the Structural Division,* pp. 2245-2270, 1981.
[29] F. Cavagnis, R. Fernández and A. Muttoni, "An analysis of the shear-transfer actions in reinforced concrete members without transverse reinforcement based on refined experimental measurements," *Structural concrete,* pp. 1-16, 2017.
[30] D. A. Hordijk, "Tensile and tensile fatigue behaviour of concrete: experiments, modelling and analysis," *HERON,* vol. 37, no. 1, pp. 1-79, 1992.
[31] D. Zhang, T. Ueda and H. Furuuchi, "Concrete cover separation failure of overlay-strengthened reinforced concrete beams," *Construction and Building Materials,* vol. 26, no. 1, p. 735–745, 2012.
[32] E. Mörsch, Concrete-Steel Construction (Der EisenBetonBau), London: The engineering news publishing company, 1909.
[33] E. Vintzileou, "Shear transfer by dowel action and friction as related to size effects," *CEB Bull,* pp. 53-77, 1997.
[34] T. Paulay, R. Park and M. Phillips, "Horizontal construction joints in cast in place reinforced concrete," *ACI Special Publications,* pp. 599-616, 1974.
[35] E. N. Vintzēleou and T. Tassios, "Mathematical models for dowel action under monotonic and cyclic conditions," *Magazine of Concrete Research,* pp. 13-22, 1986.
[36] K.-H. Yang, H.-S. Chung, E.-T. Lee and H.-C. Eun, "Shear characteristics of high-strength concrete large beams without shear reinforcement," *Engineering Structures,* vol. 25, p. 1343–1352, 2003.
[37] P. Zararis and G. Papadakis, "Diagonal shear failure and size effect in RC beams without web reinforcement," *Journal of Structural Engineering,* pp. 733-742, 2001.
[38] Z. P. Bažant and J. Planas, Fracture and Size Effect in Concrete and Other Quasibrittle Materials, Florida: CRC Press, 1998.
[39] W. M. Ghannoum, "Size Effect on Shear Strength of Reinforced Concrete Beams," McGill University, Montréal, 1998.
[40] A. El-Sayed and S. A. B., "Size effect on shear resistance of high strength concrete large beams," *Materials and Structures,* vol. 49, pp. 1871-1882, 2016.
[41] E. C. Bentz and S. Buckley, "Repeating a Classic Set of Experiments on Size Effect in Shear of Members without Stirrups," *ACI Structural Journal,* vol. 102, no. 6, pp. 832-838, 2005.
[42] T. Jayasinghe, T. Gunawardena and P. Mendis, "Shear strength of concrete members without transverse reinforcement: A comparative study between codes of practice and artificial neural network," *Case Studies in Construction Materials ,* vol. 16, no. 01102, pp. 1-20, 2022.
[43] X. An, K. Maekawa and H. Okamura, "Numerical Simulation of Size Effect in Shear Strength of RC beams," *Japan Society for Civil Engineers,* pp. 297-316, 1997.
[44] J. Carmona and G. Ruiz, "Bond and size effects on the shear capacity of RC beams without stirrups," *Engineering Structures,* pp. 45-56, 2014.
[45] J.-K. Kim and Y.-D. Park, "Prediction of Shear Strength of Reinforced Concrete Beams without Web Reinforcement," *Materials Journal,* vol. 93, no. 3, pp. 213-222, 1996.
[46] Z. P. Bažant and Q. Yu, "Universal Size Effect Law and Effect of Crack Depth," *Journal of Engineering Mechanics,* pp. 78-84, 2009.
[47] M. Hendriks and M. Roosen, "Guidelines for Nonlinear Finite Element Analysis of Concrete Structures," Rijkwaterstraat, 2020.
[48] B. Belletti, C. Damoni, M. Hendriks and A. d. Boer, "Validation of the Guidelines for Nonlinear Finite Element Analysis of Concrete Structure Part: Reinforced beams," Rijkswaterstaat Centre for Infrastructure, Delft, 2017.
[49] A. d. Putter, "Towards a uniform and optimal approach for safe NLFEA of reinforced concrete beams," Delft University of Technology, Delft, 2020.
[50] A. d. Putter, M. Hendriks, J. Rots, Y. Yang, M. Engen and A. v. d. Bos, "Quantification of the resistance modeling uncertainty of 19 alternative 2D nonlinear finite element approaches

benchmarked against 101 experiments on reinforced concrete beams," *Structural concrete,* pp. 1-15, 2022.
[51] Y. Lang, "Influence of Numerical Size Effect in Non-Linear Finite Element Analysis," Delft University of Technology, Delft, 2021.
[52] Z. Garnica, Y. Yang and E. Lantsoght, "Nonlinear finite element analysis of tests of reinforced concrete slabs," in *IABSE Congress Ghent 2021*, Delft & Quito, 2021.
[53] ROK, Richtlijnen Beoordeling Kunstwerken, Utrecht: Rijkwaterstaat, 2013.
[54] T. K. Løvli, "Nonlinear Analysis of Reinforced Concrete beams without shear reinforcement," Norwegian University of Science and Technology, Trondheim, 2022.
[55] V. A. Georgewill and B. E. Ngekpe, "Punching Shear Failure of Reinforced Concrete Flat Slab System-A Review," *European Journal of Advances in Engineering and Technology,* pp. 10-16, 2019.
[56] D. L. Araujo, L. C. Carmo, F. G. T. Nunes and R. D. T. Filho, "Modelagem computacional de vigas de concreto armado reforçado com fibras de aço submetidas a cisalhamento," *Revista IBRACON de Estruturas e Materiais,* pp. 68-94, 2010.
[57] P. Huber and J. Kolleger, "Numerical Simulation of Shear Behaviour of Reinforced Concrete Beams," in *fib PhD Symposium Quebec*, Quebec, 2014.
[58] T. T. Teshome, "Model Uncertainty of Non-Linear Finite Element Analysis of Reinforced Concrete Beams without Shear Reinforcement," TU Delft, Delft, 2019.
[59] Y. Yang and E. Lantsoght, "Nonlinear finite element analysis of tests of reinforced concrete slabs," in *Structural Engineering for Future Societal Needs*, Gent, 2021.
[60] I. Marzec, J. Tejchman and Z. Mróz, "Numerical analysis of size effect in RC beams scaled along height or length using elasto-plastic-damage model enhanced by non-local softening," *Finite Elements in Analysis and Design,* pp. 1-20, 2019.
[61] H. Schlangen, "Experimental and numerical analysis of fracture processes in concrete," Delft University of Technology, Delft , 1993.
[62] O. Sucharda, P. Mateckova and V. Bilek, "Non-Linear Analysis of an RC Beam Without Shear Reinforcement with a Sensitivity Study of the Material Properties of Concrete," *Slovak Journal of Civil Engineering,* pp. 33-43, 2020.
[63] D. A. Hordijk, "Local approach to fatigue of concrete," W.D. Meinema b.v., Delft, 1991.
[64] T. Hasegawa and K. Yoshitake, "Parametric study for size effect of reinforced concrete large beam on shear strength," in *Proceedings of the 55th annual conference of JSCE 5*, Japan, 2000.
[65] T. Hasegawa, "Size effect analysis of reinforced concrete large beam using Multi equivalent series phase model.," in *Proceedings of the 54th annual conference of JSCE 5*, Japan, 1999.
[66] P. Feenstra, "Computational Aspects of Biaxial Stress in Plain and Reinforced Concrete," Delft University of Technology, Delft, 1993.
[67] F. Vecchio and M. Collins, "Compression response of cracked reinforced concrete," *Journal of Structural Engineering,* pp. 3590-3610, 1993.
[68] Japan Society of Civil Engineers, "Standard Specifications for Concrete Structures," Japan Society of Civil Engineers: Guidelines for Concrete, Tokyo, 2007.
[69] K. Salah, C. Abdelhamid and N. Mohammed, "Nonlinear analysis of reinforced concrete structures using a new constitutive model," Revue Européenne des Éléments, 841-856, 2004.
[70] F. V. Robert Gordon Shelby, "Three-dimensional Constitutive Relations for Reinforced Concrete.," University of Toronto, Department of Civil Engineering, Toronto, 1993.
[71] S. Govindjee, G. Kay and J. Simo, "Anisotropic modeling and numerical simulation of brittle damage in concrete," *International Journal for Numerical Methods in Engineering,* pp. 3611-3633, 1996.
[72] A. Slobbe, M. Hendriks and J. Rots, "Systematic assessment of directional mesh bias with periodic boundary conditions: Applied to the crack band model," *Engineering Fracture Mechanics,* pp. 186-208, 2013.
[73] J. Kaczmarczyk and A. Grajcar, "Numerical Simulation and Experimental Investigation of Cold-Rolled Steel Cutting," MDPI, Gliwice, 2018.
[74] R. d. Borst and B. Sluys, Computational methods in Non-linear solid mechanics, Delft: Delft University of Technology, 2015.
[75] H. Shima, L.-L. Chou and H. Okamura, "Micro and Macro Models for Bond in Reinforced Concrete," *Journal of Faculty of Engineering,* vol. 39, no. 22, pp. 133-194, 1987.
[76] S. Chai, Finite Element Analysis for Civil Engineering with DIANA software, Nanjing: Nanjing University press, 2020.

[77] R. d. Borst and J. Rots, "Occurrence of spurious mechanisms in computations of strain-softening solids," *Engineering Computations,* pp. 272-280, 1989.
[78] I. Saether, "Structural behaviour of deteriorated and retrofitted concrete structures," Northern Research Institute Narvik, Norwegian University of Science and TechnologyFaculty of Engineering Science and TechnologyDepartment of Structural Engineering, Narvik, 2010.
[79] Y. H. Gedik, H. Nakamura, Y. Yamamoto and M. Kunieda, "Evaluation of three-dimensional effects in short large beams using a rigid-body-spring-model," *Cement & Concrete Composites,* pp. 978-991, 2011.
[80] S. D. Adhikary, B. Li and K. Fujikake, "Strength and behavior in shear of reinforced concrete large beams under dynamic loading conditions," *Nuclear Engineering and Design ,* p. 14–28, 2013.
[81] T. Hasegawa, "Finite Elements in Civil Engineering Applications," CRC press, Florida, 2002.
[82] M. G. Marques, E. A. Liberati, M. J. Pimentel, R. A. d. Souza and L. M. Trautwein, "Nonlinear finite element analysis (NLFEA) of reinforced concrete flat slabs with holes," *Structures,* pp. 1-11, 2020.
[83] S. Akram and Q. u. Ann, "Newton Raphson Method," *International Journal of Scientific & Engineering Research,* vol. 6, no. 7, pp. 1748-1752, 2015.
[84] U. Goud and S. Naidu, "Investigation on Buckling of Laminated Composite Plate," *Journal of Mechanical and Civil Engineering,* pp. 81-87, 2016.
[85] E. Riks, "The application of Newton's method to the problem of elastic stability," *Journal of Applied Mechanics,* pp. 529-551, 1972.
[86] T. Hasegawa, "Constitutive models and arc-length control method in analysis of branch-switching to bifurcation path for diagonal tension failure in reinforced concrete beams," in *International Conference on Fracture Mechanics of Concrete and Concrete Structures*, Tokyo, 2016.
[87] Z. Yang and D. Proverbs, "A comparative study of numerical solutions to non-linear discrete crack modelling of concrete beams involving sharp snap-back," *Engineering Fracture Mechanics ,* pp. 81-105, 2004.
[88] L. H. S. Z.-H. R. Daniel Dunkelberg, "The 2015 ACI-DAfStb database of shear tests on slender prestressed concrete beams without stirrups—Overview and evaluation of current design approaches," *Structural Concrete,* vol. 19, no. 6, pp. 1740-1759, 2018.
[89] W. J. Krefeld and C. W. Thurston, "Studies of the Shear and Diagonal Tension Strength of Simply Supported Reinforced Concrete Beams," *Journal of the American Concrete Institute,* vol. 63, no. 4, pp. 451-476, 1966.
[90] A. G. Mphonde and G. C. Frantz, "Shear Tests of High- and Low-Strength Concrete Beams Without Stirrups," *Journal of the American Concrete Institute,* vol. 81, no. 4, pp. 350-357, 1984.
[91] R. Koekkoek and Y. Yang, "Measurement Report on the Transition between Flexural and Shear Failure on RC Beams without Shear Reinforcements," Delft University of Technology., Delft, 2016.
[92] Z. Garnica and Y. Yang, "Measurement report on the Shear behaviour of 1.2 m deep RC slab strips," Delft University of Technology, Delft , 2018.
[93] D. G. G. B. G. M. Paolo Castaldo, "Partial safety factor for resistance model uncertainties in 2D non-linear finite element analysis of reinforced concrete structures," Department of Structural, Geotechnical and Building Engineering, Politecnico di Torino, 2018.
[94] T. Baumann and H. Rüsch, "Schubversuche mit indirekter Krafteinleitung : Versuche zum Studium der Verdübelungswirkung der Biegezugbewehrung eines Stahlbetonbalkens," *Heft / Deutscher Ausschuss für Stahlbeton, 210,* 1970.
[95] B. A. Podgorniak-Stanik, "The influence of concrete strength, distribution of longitudinal reinforcement, amount of transverse reinforcement and member size on shear strength of reinforced concrete members," University of Toronto, Toronto, 1998.

Annex

Annex I Critical shear displacement theory

The opening of a critical flexural shear crack is taken as the lower bound for the shear capacity. Displacement of an existing flexural crack can be used as a criterion for the unstable opening of the critical flexural shear crack.
This theory is based on three shear transfer mechanisms, namely:

- Aggregate interlock
- Concrete compressive zone
- Dowel action

The residual tensile stresses have been neglected in this theory because they are considered to have a neglectable influence.

Based on the Walraven model [13], the simplified formula below is used for rectangular RC beam cross-sections:

$$Vai = fc^{0.56}\ scr\ b\ \frac{0.03}{wb - 0.01}(-978\Delta^2 + 85\Delta - 0.27)$$

Equation [XXI]

With:
$wb \geq 0.04mm$
$fc \leq 60MPa$

Based on the Morsch formula [19], [6] derived the following simplified formulation for Vc:

$$Vc = \frac{2}{3}\frac{zc}{z}V = \frac{d - scr}{d + 0.5scr}$$

Equation [XXII]

The following was found for the dowel action by [91]:

$$Vd = \frac{\Delta}{0.08}Vdmax$$

Equation [XXIII]

$With$:
$Vdmax = 1.64\ bn\ \phi\sqrt[3]{fck}$
$bn = (b - n\phi)$

Since it is assumed that the maximum dowel force has been reached, the following formula can be derived:

$$Vd = Vd\max = 1.64\ bn\ \phi\sqrt[3]{fc}$$

Equation [XXIV]

The total shear force at the opening of the critical flexural shear crack equals:

$$V = Vc + Vai + Vd = \frac{d - scr}{d + 0.5scr} + fc^{0.56}\ scr\ b\ \frac{0.03}{wb - 0.01}(-978\Delta^2 + 85\Delta - 0.27) + 1.64\ bn\ \phi\sqrt[3]{fc}$$

Equation [XXV]

For an unknown applied force, iterations must be performed for Vai. Vai depends on wb, which in turn depends on M. The crack with the smallest $\frac{M}{Vd}$ ratio is the critical crack.

Annex II Experimental cases

Experimental case naming from "Garnica & Koekkoek" reports:

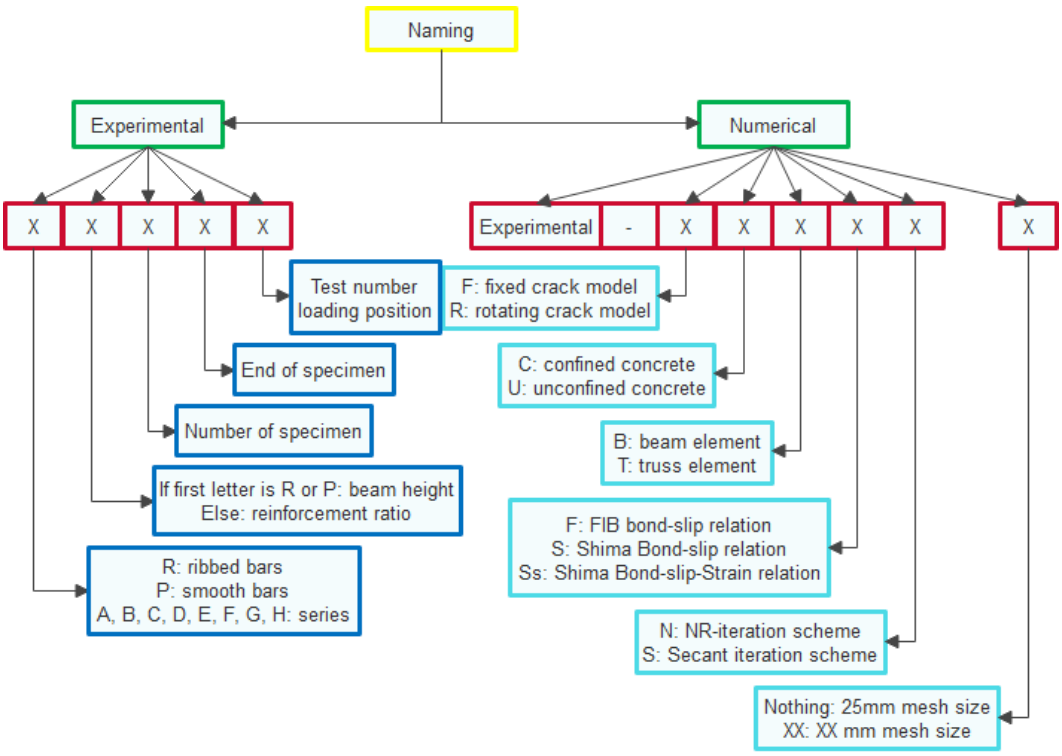

Figure 99 "Garnica & Koekkoek" cases naming pattern

Sensitivity analysis initial cases:

Table 40 Element size sensitivity analysis cases properties

Test	Date:	length L [mm]	depth H [mm]	a [mm]	Effective depth d [mm]	a/d [-]	fc,cube [MPa]	reinforcement ratio ρ [%]	Rebar [mm]
H404A	2018	9000	1200	4000	1158	3.45	82.04	0.42%	3Ø25
H121A	2018	9000	1200	3000	1145	2.6	84.12	1.14%	8Ø25
H851C	2018	9000	1200	4500	1150	3.91	82.99	0.85%	6Ø25
H852A	2018	9000	1200	4500	1150	3.91	82.99	0.85%	6Ø25
A751B1	2015	5000	300	800	274.5	2.91	78.5	0.37	603.19
B502A3	2015	5000	500	1700	472.5	3.6	81.9	0.59	829.38
B502B1	2015	5000	500	1700	472.5	3.6	81.9	0.59	829.38
R803A1	2015	8000	800	3500	762.5	4.59	83.3	0.82	1884.96
R803B1	2016	8000	800	3500	762.5	4.59	83	0.82	1884.96

“Garnica & Koekkoek” cases

Table 41 “Garnica & Koekkoek” cases properties and experimental results 1

Test [#]	Date (year)	L [mm]	H [mm]	t [mm]	ls [mm]	A [mm]	d [mm]	$\frac{a}{d}$ [-]	C [mm]	fc,cube [MPa]	P [%]	Rebar [mm]	fyk [MPa]	V experimental [kN]
A121A3	2015	5000.00	300.00	300.00	500.00	1000.00	269.50	3.70	no	77.70	1.17	3Ø20	550.00	144.60
A122B1	2015	5000.00	300.00	300.00	500.00	1000.00	270.50	3.70	no	78.50	1.16	3Ø20	500.00	152.30
A123A1	2015	5000.00	300.00	300.00	500.00	1000.00	270.00	3.70	no	79.20	1.16	3Ø20	500.00	136.50
A123A2	2015	5000.00	300.00	300.00	500.00	800.00	270.00	2.96	no	80.10	1.16	3Ø20	500.00	139.00
A122B2	2015	5000.00	300.00	300.00	500.00	750.00	270.50	2.77	no	78.50	1.16	3Ø20	500.00	139.10
A902B2	2015	5000.00	300.00	300.00	500.00	1000.00	276.00	3.62	no	78.50	0.90	1Ø12+2Ø20	500.00	124.20
A902A1	2015	5000.00	300.00	300.00	500.00	995.00	276.00	3.61	no	78.50	0.90	1Ø12+2Ø20	500.00	120.70
A901B1	2015	5000.00	300.00	300.00	500.00	880.00	274.00	3.21	no	78.50	0.90	1Ø12+2Ø20	500.00	127.50
A902A3	2015	5000.00	300.00	300.00	500.00	800.00	276.00	2.90	no	78.50	0.90	1Ø12+2Ø20	500.00	149.40
A901A3	2015	5000.00	300.00	300.00	500.00	750.00	274.00	2.74	no	78.50	0.90	1Ø12+2Ø20	500.00	145.00
A901B2	2015	5000.00	300.00	300.00	500.00	750.00	274.00	2.74	no	78.50	0.90	1Ø12+2Ø20	500.00	124.20
A752A2	2015	5000.00	300.00	300.00	500.00	850.00	273.00	3.11	no	78.50	0.74	3Ø16	500.00	119.00
A751B1	2015	5000.00	300.00	300.00	500.00	800.00	274.50	2.91	no	78.50	0.73	3Ø16	500.00	106.70
A751A2	2015	5000.00	300.00	300.00	500.00	750.00	274.50	2.73	no	78.50	0.73	3Ø16	500.00	118.40
A601B1	2015	5000.00	300.00	300.00	500.00	700.00	275.50	2.54	no	78.50	0.58	1Ø10+2Ø16	500.00	106.40
C901B1	2015	5000.00	300.00	300.00	500.00	1250.00	271.50	4.60	no	23.70	0.91	1Ø12+2Ø20	500.00	101.70
C901A3	2015	5000.00	300.00	300.00	500.00	1000.00	271.50	3.68	no	23.70	0.91	1Ø12+2Ø20	500.00	84.10
C751A2	2015	5000.00	300.00	300.00	500.00	1000.00	270.00	3.70	no	23.70	0.74	3Ø16	500.00	84.50
C751A3	2015	5000.00	300.00	300.00	500.00	1000.00	270.00	3.70	no	23.70	0.74	3Ø16	500.00	86.70
B701B2	2015	5000.00	500.00	300.00	500.00	1500.00	471.50	3.18	no	81.10	0.67	3Ø20	500.00	202.40
B702B1	2015	5000.00	500.00	300.00	500.00	1450.00	471.50	3.08	no	81.70	0.67	3Ø20	500.00	164.90
B702A1	2015	5000.00	500.00	300.00	500.00	1250.00	471.50	2.65	no	81.70	0.67	3Ø20	500.00	183.20
B501B1	2015	5000.00	500.00	300.00	500.00	1800.00	471.50	3.82	no	81.80	0.59	1Ø16+2Ø20	500.00	165.70
B501A2	2015	5000.00	500.00	300.00	500.00	1750.00	471.50	3.71	no	81.80	0.59	1Ø16+2Ø20	500.00	166.40
B502A3	2015	5000.00	500.00	300.00	500.00	1700.00	472.50	3.60	no	81.90	0.59	1Ø16+2Ø20	500.00	173.60
B502B1	2015	5000.00	500.00	300.00	500.00	1700.00	472.50	3.60	no	81.90	0.59	1Ø16+2Ø20	500.00	173.20

Table 42 "Garnica & Koekkoek" cases simulated results 1

Test [#]	V numerical [kN]	Failure mode [-]	DPC numerical [-]	DPC conclusion [-]
A121A3	136.52	Flexural shear failure	1.06	Sufficient
A122B1	136.52	Flexural shear failure	1.12	Sufficient
A123A1	136.52	Flexural shear failure	1.00	Sufficient
A123A2	144.42	Flexural shear failure	0.96	Sufficient
A122B2	138.77	Flexural shear failure	1.00	Sufficient
A902B2	130.46	Flexural shear failure	0.95	Sufficient
A902A1	130.46	Flexural shear failure	0.93	Sufficient
A901B1	143.02	Flexural shear failure	0.89	Sufficient
A902A3	143.02	Flexural shear failure	1.04	Sufficient
A901A3	129.76	Flexural shear failure	1.12	Sufficient
A901B2	129.76	Flexural shear failure	0.96	Sufficient
A752A2	121.91	Flexural shear failure	0.98	Sufficient
A751B1	106.70	Flexural shear failure	1.00	Sufficient
A751A2	125.87	Flexural shear failure	0.94	Sufficient
A601B1	111.89	Flexural shear failure	0.95	Sufficient
C901B1	90.16	Flexural shear failure	1.13	Sufficient
C901A3	88.02	Flexural shear failure	0.96	Sufficient
C751A2	85.91	Flexural shear failure	0.98	Sufficient
C751A3	85.91	Flexural shear failure	1.01	Sufficient
B701B2	187.63	Flexural shear failure	1.08	Sufficient
B702B1	181.12	Flexural shear failure	0.91	Sufficient
B702A1	178.85	Flexural shear failure	1.02	Sufficient
B501B1	170.38	Flexural shear failure	0.97	Sufficient
B501A2	179.77	Flexural shear failure	0.93	Sufficient
B502A3	170.60	Flexural shear failure	1.02	Sufficient
B502B1	170.60	Flexural shear failure	1.02	Sufficient

Table 43 "Garnica & Koekkoek" cases predicted results 1

Test [#]	V EC2 [kN]	DPC EC2 [-]	DPC EC2 conclu-sion [-]	V MC 2010 [kN]	DPC MC 2010 [-]	DPC MC 2010 [-]
A121A3	117.48	1.23	Insufficient	100.66	1.44	Insufficient
A122B1	117.92	1.29	Insufficient	108.11	1.41	Insufficient
A123A1	118.14	1.16	Sufficient	108.42	1.26	Insufficient
A123A2	118.64	1.17	Sufficient	109.04	1.27	Insufficient
A122B2	117.92	1.18	Insufficient	108.11	1.29	Insufficient
A902B2	110.05	1.13	Sufficient	109.93	1.13	Sufficient
A902A1	110.05	1.10	Sufficient	109.93	1.10	Sufficient
A901B1	109.43	1.17	Sufficient	109.27	1.17	Sufficient
A902A3	110.05	1.36	Insufficient	109.93	1.36	Insufficient
A901A3	109.43	1.33	Insufficient	109.27	1.33	Insufficient
A901B2	109.43	1.13	Sufficient	109.27	1.14	Sufficient
A752A2	102.23	1.16	Sufficient	108.94	1.09	Sufficient
A751B1	102.20	1.04	Sufficient	109.44	0.97	Sufficient
A751A2	102.20	1.16	Sufficient	109.44	1.08	Sufficient
A601B1	94.92	1.12	Sufficient	109.77	0.97	Sufficient
C901B1	82.03	1.24	Insufficient	75.45	1.35	Insufficient
C901A3	82.03	1.03	Sufficient	75.45	1.11	Sufficient
C751A2	76.24	1.11	Sufficient	75.10	1.13	Sufficient
C751A3	76.24	1.14	Sufficient	75.10	1.15	Sufficient
B701B2	153.83	1.32	Insufficient	170.21	1.19	Insufficient
B702B1	154.25	1.07	Sufficient	170.84	0.97	Sufficient
B702A1	154.25	1.19	Insufficient	170.84	1.07	Sufficient
B501B1	147.91	1.12	Sufficient	170.94	0.97	Sufficient
B501A2	147.91	1.12	Sufficient	170.94	0.97	Sufficient
B502A3	148.23	1.17	Sufficient	171.31	1.01	Sufficient
B502B1	148.23	1.17	Sufficient	171.31	1.01	Sufficient

Table 44 "Garnica & Koekkoek" cases properties and experimental results 2

Test [#]	Date (year)	L [mm]	H [mm]	t [mm]	ls [mm]	A [mm]	d [mm]	$\frac{a}{d}$ [-]	C [mm]	fc,cube [MPa]	P [%]	Rebar [mm]	fyk [MPa]	V experimental [kN]
R501A1	2015	5000.00	500.00	300.00	500.00	2500.00	455.00	5.49	no	80.50	1.15	5Ø20 (2 layers)	500.00	276.80
R501B1	2015	5000.00	500.00	300.00	500.00	1500.00	455.00	3.30	no	75.80	1.15	5Ø20 (2 layers)	500.00	210.20
R502B1	2016	5000.00	500.00	300.00	500.00	1750.00	465.00	3.76	no	77.10	0.68	3Ø20	500.00	154.90
R502A2	2016	5000.00	500.00	300.00	500.00	1600.00	465.00	3.44	no	75.60	0.68	3Ø20	500.00	163.90
R804A1	2016	8000.00	800.00	300.00	500.00	3500.00	755.00	4.64	no	85.10	0.65	3Ø25	500.00	269.40
R804B1	2015	8000.00	800.00	300.00	500.00	3500.00	755.00	4.64	no	85.10	0.65	3Ø25	500.00	249.90
R801A1	2015	8000.00	800.00	300.00	500.00	2000.00	762.50	2.62	no	84.00	0.64	3Ø25	500.00	213.10
R801B1	2015	8000.00	800.00	300.00	500.00	2000.00	762.50	2.62	no	91.10	0.64	3Ø25	500.00	204.80
R803A1	2015	8000.00	800.00	300.00	500.00	3500.00	762.50	4.59	no	83.30	0.82	6Ø20 (2 layers)	500.00	279.30
R803B1	2016	8000.00	800.00	300.00	500.00	3500.00	762.50	4.59	no	83.00	0.82	6Ø20 (2 layers)	500.00	307.90
R802A1	2015	8000.00	800.00	300.00	500.00	2000.00	755.00	2.65	no	75.80	0.83	6Ø20 (2 layers)	500.00	219.40
R802B1	2015	8000.00	800.00	300.00	500.00	2000.00	755.00	2.65	no	75.80	0.83	6Ø20 (2 layers)	500.00	270.20
E401B1	2018	9000.00	800.00	300.00	500.00	2500.00	765.00	3.27	no	86.74	0.41	3Ø20	500.00	158.70
E402A	2018	9000.00	800.00	300.00	500.00	2500.00	765.00	3.27	no	89.16	0.41	3Ø20	500.00	190.00
E402B	2018	9000.00	800.00	300.00	500.00	3000.00	765.00	3.92	no	89.16	0.41	3Ø20	500.00	164.00
H401A	2018	9000.00	1200.00	300.00	500.00	4500.00	1158.00	3.88	no	81.25	0.42	3Ø25	500.00	264.00
H402A	2018	9000.00	1200.00	300.00	500.00	4500.00	1158.00	3.88	no	84.12	0.42	3Ø25	500.00	322.00
H403A	2018	9000.00	1200.00	300.00	500.00	4500.00	1158.00	3.88	no	81.67	0.42	3Ø25	500.00	350.00
H404A	2018	9000.00	1200.00	300.00	500.00	4000.00	1158.00	3.45	no	82.04	0.42	3Ø25	500.00	269.00
H301A	2018	9000.00	1200.00	300.00	500.00	4000.00	1160.00	3.45	no	86.58	0.27	3Ø20	500.00	222.70
H601A	2019	9000.00	1200.00	300.00	500.00	4500.00	1158.00	3.89	no	86.40	0.57	4Ø25	500.00	306.00
H602A	2019	f9000.00	1200.00	300.00	500.00	4500.00	1158.00	3.89	no	86.08	0.57	4Ø25	500.00	306.00
H851C	2018	9000.00	1200.00	300.00	500.00	4500.00	1150.00	3.91	no	82.99	0.85	6Ø25	500.00	421.00
H852A	2018	9000.00	1200.00	300.00	500.00	4500.00	1150.00	3.91	no	82.99	0.85	6Ø25	500.00	406.00
H121A	2018	9000.00	1200.00	300.00	500.00	3000.00	1145.00	2.60	no	84.12	1.14	8Ø25	500.00	341.00
H123A	2018	9000.00	1200.00	300.00	500.00	4500.00	1145.00	3.93	no	82.99	1.14	8Ø25	500.00	445.00

Table 45 "Garnica & Koekkoek" cases simulated results 2

Test [#]	V numerical [kN]	Failure mode [-]	DPC numerical [-]	DPC conclusion [-]
R501A1	254.49	Flexural shear failure	1.09	Sufficient
R501B1	232.20	Flexural shear failure	0.91	Sufficient
R502B1	186.71	Flexural shear failure	0.83	Insufficient
R502A2	182.06	Flexural shear failure	0.90	Sufficient
R804A1	247.82	Flexural shear failure	1.09	Sufficient
R804B1	247.82	Flexural shear failure	1.01	Sufficient
R801A1	206.05	Flexural shear failure	1.03	Sufficient
R801B1	206.05	Flexural shear failure	0.99	Sufficient
R803A1	282.04	Flexural shear failure	0.99	Sufficient
R803B1	282.04	Flexural shear failure	1.09	Sufficient
R802A1	286.87	Flexural shear failure	0.76	Insufficient
R802B1	286.87	Flexural shear failure	0.94	Sufficient
E401B1	154.02	Flexural shear failure	1.03	Sufficient
E402A	154.02	Flexural shear failure	1.23	Insufficient
E402B	170.61	Flexural shear failure	0.96	Sufficient
H401A	275.08	Flexural shear failure	0.96	Sufficient
H402A	275.08	Flexural shear failure	1.17	Sufficient
H403A	275.08	Flexural shear failure	1.27	Insufficient
H404A	243.88	Flexural shear failure	1.10	Sufficient
H301A	198.41	Dowel failure	1.12	Sufficient
H601A	321.04	Flexural shear failure	0.95	Sufficient
H602A	321.04	Flexural shear failure	0.95	Sufficient
H851C	403.64	Flexural shear failure	1.04	Sufficient
H852A	403.64	Flexural shear failure	1.01	Sufficient
H121A	361.00	Flexural shear failure	0.94	Sufficient
H123A	518.17	Flexural shear failure	0.86	Insufficient

Table 46 "Garnica & Koekkoek" cases predicted results 2

Test [#]	V EC2 [kN]	DPC EC2 [-]	DPC EC2 conclu-sion [-]	V MC 2010 [kN]	DPC MC 2010 [-]	DPC MC 2010 [-]
R501A1	178.50	1.55	Insufficient	165.15	1.68	Insufficient
R501B1	174.56	1.20	Insufficient	160.26	1.31	Insufficient
R502B1	150.03	1.03	Sufficient	164.26	0.94	Sufficient
R502A2	148.94	1.10	Sufficient	162.66	1.01	Sufficient
R804A1	227.68	1.18	Insufficient	241.29	1.12	Sufficient
R804B1	227.68	1.10	Sufficient	241.29	1.04	Sufficient
R801A1	227.28	0.94	Sufficient	241.24	0.88	Sufficient
R801B1	234.15	0.87	Sufficient	251.23	0.82	Insufficient
R803A1	246.09	1.13	Sufficient	240.23	1.16	Sufficient
R803B1	245.76	1.25	Insufficient	239.80	1.28	Insufficient
R802A1	236.65	0.93	Sufficient	227.72	0.96	Sufficient
R802B1	236.65	1.14	Sufficient	227.72	1.19	Insufficient
E401B1	198.79	0.80	Insufficient	245.65	0.65	Insufficient
E402A	200.81	0.95	Sufficient	249.06	0.76	Insufficient
E402B	200.81	0.82	Insufficient	249.06	0.66	Insufficient
H401A	277.37	0.95	Sufficient	303.12	0.87	Sufficient
H402A	280.94	1.15	Sufficient	308.43	1.04	Sufficient
H403A	277.90	1.26	Insufficient	303.90	1.15	Sufficient
H404A	278.36	0.97	Sufficient	304.59	0.88	Sufficient
H301A	245.42	0.91	Sufficient	313.19	0.71	Insufficient
H601A	314.12	0.97	Sufficient	312.58	0.98	Sufficient
H602A	313.70	0.98	Sufficient	312.00	0.98	Sufficient
H851C	351.52	1.20	Insufficient	305.21	1.38	Insufficient
H852A	351.52	1.15	Sufficient	305.21	1.33	Insufficient
H121A	388.14	0.88	Sufficient	306.56	1.11	Sufficient
H123A	386.21	1.15	Sufficient	304.50	1.46	Insufficient

Bhal cases

Table 47 Bhal cases properties and experimental results

Test [#]	Date (year)	L [mm]	H [mm]	t [mm]	ls [mm]	A [mm]	d [mm]	$\frac{a}{d}$ [-]	C [mm]	fc,cube [MPa]	P [%]	Rebar [mm]	fyk [MPa]	V experimental [kN]
d_350	1905	1800.00	350.00	300.00	300.00	881.25	300.00	2.94	no	22.02	1.26	2Ø24	426.00	70.99
d_650	1905	3600.00	650.00	300.00	300.00	1762.50	600.00	2.94	no	28.12	1.26	4Ø24	426.00	119.48
d_950	1905	5400.00	950.00	300.00	300.00	2643.75	900.00	2.94	no	26.11	1.26	6Ø24	426.00	166.38
d_1250	1905	7200.00	1250.00	300.00	300.00	3525.00	1200.00	2.94	no	23.95	1.26	8Ø24	426.00	187.10

Table 48 Bhal cases simulated results

Test [#]	V numerical [kN]	Failure mode [-]	DPC numerical [-]	DPC conclusion [-]
d_350	70.80	Flexural shear failure	1.00	Sufficient
d_650	122.44	Flexural shear failure	1.02	Sufficient
d_950	155.55	Flexural shear failure	0.93	Sufficient
d_1250	181.00	Flexural shear failure	0.97	Sufficient

Table 49 Bhal cases predicted results

Test [#]	V EC2 [kN]	DPC EC2 [-]	DPC EC2 con-clusion [-]	V MC 2010 [kN]	DPC MC 2010 [-]	DPC MC 2010 [-]
d_350	53.38	0.75	Insufficient	45.33	1.57	Insufficient
d_650	92.71	0.78	Insufficient	76.60	1.56	Insufficient
d_950	129.72	0.78	Insufficient	99.46	1.67	Insufficient
d_1250	165.53	0.88	Sufficient	116.91	1.60	Insufficient

Ahmad et al. cases

Table 50 Ahmad et al. cases properties and experimental results

Test [#]	Date (year)	L [mm]	H [mm]	t [mm]	ls [mm]	A [mm]	d [mm]	$\frac{a}{d}$ [-]	C [mm]	fc,cube [MPa]	P [%]	Rebar [mm]	fyk [MPa]	V experimental [kN]
rho_1.7	1905	2070.61	254.00	300.00	152.40	832.10	208.03	4.00	406.40	74.09	1.77	2#5+1*#3	414.00	47.18
rho_2.2	1905	2070.61	254.00	300.00	152.40	832.10	208.03	4.00	406.40	81.59	2.25	3*#5	414.00	44.96
rho_3.3	1905	2058.42	254.00	300.00	152.40	826.01	206.50	4.00	406.40	78.34	3.26	3*#6	414.00	45.85
rho_3.9	1905	2032.00	254.00	300.00	152.40	812.80	203.20	4.00	406.40	74.09	3.93	2*#8	414.00	58.30
rho_5.0	1905	2019.81	254.00	300.00	152.40	806.70	201.68	4.00	406.40	81.59	5.03	2*#9	414.00	51.68
rho_6.6	1905	1879.60	254.00	300.00	152.40	736.60	184.15	4.00	406.40	78.34	6.64	4*#7	414.00	54.71

Table 51 Ahmad et al. cases simulated results

Test [#]	V numerical [kN]	Failure mode [-]	DPC numerical [-]	DPC conclusion [-]
rho_1.7	44.06	Flexural shear failure	0.93	Sufficient
rho_2.2	47.54	flexural shear failure	1.06	Sufficient
rho_3.3	48.54	flexural shear failure	1.06	Sufficient
rho_3.9	50.70	flexural shear failure	0.87	Sufficient
rho_5.0	47.44	flexural shear failure	0.92	Sufficient
rho_6.6	43.46	flexural shear failure	0.79	Insufficient

Table 52 Ahmad et al. cases predicted results

Test [#]	V EC2 [kN]	DPC EC2 [-]	DPC EC2 con-clusion [-]	V MC 2010 [kN]	DPC MC 2010 [-]	DPC MC 2010 [-]
rho_1.7	56.50	1.20	Insufficient	47.33	1.00	Sufficient
rho_2.2	60.79	1.35	Insufficient	49.67	0.91	Sufficient
rho_3.3	59.64	1.30	Insufficient	48.36	0.95	Sufficient
rho_3.9	57.84	0.99	Sufficient	46.38	1.26	Insufficient
rho_5.0	59.39	1.15	Sufficient	48.35	1.07	Sufficient
rho_6.6	53.61	0.98	Sufficient	43.76	1.25	Insufficient

Krefeld et al. cases

Table 53 Krefeld et al. cases properties and experimental results

Test [#]	Date (year)	L [mm]	H [mm]	t [mm]	ls [mm]	A [mm]	d [mm]	$\frac{a}{d}$ [-]	C [mm]	fc,cube [MPa]	P [%]	Rebar [mm]	fyk [MPa]	V experimental [kN]
dtsr_3.4	1905	1828.80	304.80	300.00	457.20	850.90	250.44	3.40	127.00	40.87	4.15	2*#10	366.00	60.70
dtsr_4.6	1905	2438.40	304.80	300.00	457.20	1155.70	250.44	4.61	127.00	40.54	4.15	2*#10	366.00	59.92
dtsr_5.8	1905	3048.00	304.80	300.00	457.20	1460.50	250.44	5.83	127.00	45.62	4.15	2*#10	366.00	63.76
dtsr_7.0	1905	3657.60	304.80	300.00	457.20	1765.30	250.44	7.05	127.00	40.13	4.15	2*#10	366.00	49.98
dtsr_7.0	1905	3657.60	304.80	300.00	457.20	1765.30	250.44	7.05	127.00	43.08	4.15	2*#10	366.00	53.94
dtsr_7.0	1905	3657.60	304.80	300.00	457.20	1765.30	250.44	7.05	127.00	43.08	4.15	2*#10	366.00	53.94

Table 54 Krefeld et al. cases simulated results

Test [#]	V numerical [kN]	Failure mode [-]	DPC numerical [-]	DPC conclusion [-]
dtsr_3.4	57.33	Flexural shear failure	0.94	Sufficient
dtsr_4.6	57.24	flexural shear failure	0.96	Sufficient
dtsr_5.8	56.14	Flexural shear failure	0.88	Sufficient
dtsr_7.0	51.40	Flexural shear failure	1.03	Sufficient
dtsr_7.0	51.40	Flexural shear failure	0.95	Sufficient
dtsr_7.0	51.40	Flexural shear failure	0.95	Sufficient

Table 55 Krefeld et al. cases predicted results

Test [#]	V EC2 [kN]	DPC EC2 [-]	DPC EC2 conclusion [-]	V MC 2010 [kN]	DPC MC 2010 [-]	DPC MC 2010 [-]
dtsr_3.4	55.57	0.92	Sufficient	44.31	1.37	Insufficient
dtsr_4.6	55.42	0.92	Sufficient	44.13	1.36	Insufficient
dtsr_5.8	57.64	0.90	Sufficient	46.82	1.36	Insufficient
dtsr_7.0	55.23	1.11	Sufficient	43.91	1.14	Sufficient
dtsr_7.0	56.55	1.05	Sufficient	45.50	1.19	Insufficient
dtsr_7.0	56.55	1.05	Sufficient	45.50	1.19	Insufficient

Mphone et al. cases

Table 56 Mphone et al. cases properties and experimental results

Test [#]	Date (year)	L [mm]	H [mm]	t [mm]	ls [mm]	A [mm]	d [mm]	$\frac{a}{d}$ [-]	C [mm]	fc,cube [MPa]	P [%]	Rebar [mm]	fyk [MPa]	V experimental [kN]
fc_25	1905	2133.60	336.55	300.00	152.40	1041.40	298.45	3.49	50.80	25.29	3.34	3*#8	414.00	65.27
fc_45	1905	2133.60	336.55	300.00	152.40	1041.40	298.45	3.49	50.80	45.88	3.34	3*#8	414.00	82.83
fc_50	1905	2133.60	336.55	300.00	152.40	1041.40	298.45	3.49	50.80	50.70	3.34	3*#8	414.00	83.46
fc_90	1905	2133.60	336.55	300.00	152.40	1041.40	298.45	3.49	50.80	90.91	3.34	3*#8	414.00	90.04
fc_90	1905	2133.60	336.55	300.00	152.40	1041.40	298.45	3.49	50.80	91.26	3.34	3*#8	414.00	90.36
fc_100	1905	2133.60	336.55	300.00	152.40	1041.40	298.45	3.49	50.80	99.07	3.34	3*#8	414.00	94.12
fc_115	1905	2133.60	336.55	300.00	152.40	1041.40	298.45	3.49	50.80	111.85	3.34	3*#8	414.00	98.51
fc_115	1905	2133.60	336.55	300.00	152.40	1041.40	298.45	3.49	50.80	114.10	3.34	3*#8	414.00	100.71

Table 57 Mphone et al. cases simulated results

Test [#]	V numerical [kN]	Failure mode [-]	DPC numerical [-]	DPC conclusion [-]
fc_25	60.46	Flexural shear failure	0.93	Sufficient
fc_45	76.26	Flexural shear failure	0.92	Sufficient
fc_50	78.64	Flexural shear failure	0.94	Sufficient
fc_90	85.17	Flexural shear failure	0.95	Sufficient
fc_90	85.17	Flexural shear failure	0.94	Sufficient
fc_100	90.05	Flexural shear failure	0.96	Sufficient
fc_115	95.27	Flexural shear failure	0.97	Sufficient
fc_115	95.27	Flexural shear failure	0.95	Sufficient

Table 58 Mphone et al. cases predicted results

Test [#]	V EC2 [kN]	DPC EC2 [-]	DPC EC2 con-clusion [-]	V MC 2010 [kN]	DPC MC 2010 [-]	DPC MC 2010 [-]
fc_25	62.07	0.95	Sufficient	45.94	1.42	Insufficient
fc_45	66.10	0.80	Insufficient	50.48	1.64	Insufficient
fc_50	68.34	0.82	Insufficient	53.06	1.57	Insufficient
fc_90	83.02	0.92	Sufficient	71.05	1.27	Insufficient
fc_90	83.13	0.92	Sufficient	71.19	1.27	Insufficient
fc_100	85.43	0.91	Sufficient	74.17	1.27	Insufficient
fc_115	88.96	0.90	Sufficient	78.81	1.25	Insufficient
fc_115	89.55	0.89	Sufficient	140.66	1.27	Insufficient

Annex III Numerical model sensitivity analysis

A121A3 A122B1 A123A1

Figure 100 Case A121A3: experimental flexural shear failure

B701B2:

Figure 101 Case B701B2: experimental flexural shear failure

R804A1 R804B1

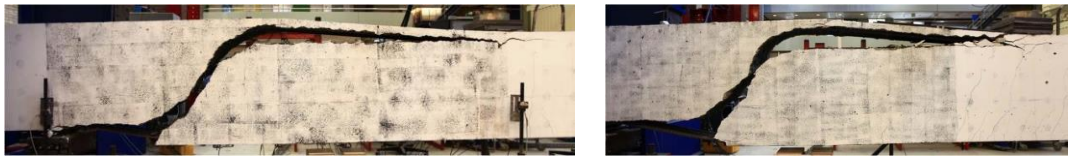

Figure 102 Case R804A1: experimental flexural shear failure

H601A H602A

Figure 103 Case H601A: experimental flexural shear failure

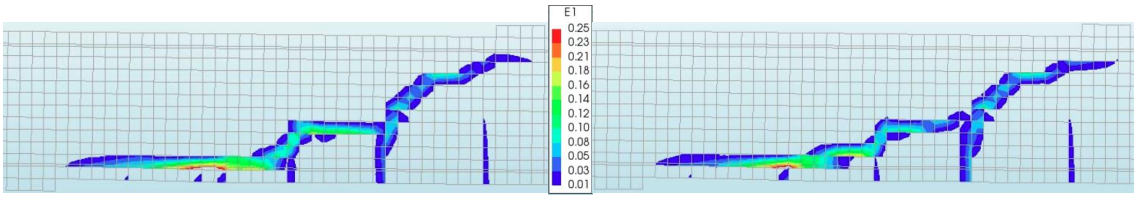

Figure 104 A121A3 maximum principal strain fixed crack orientation: confined (left) and unconfined (right)

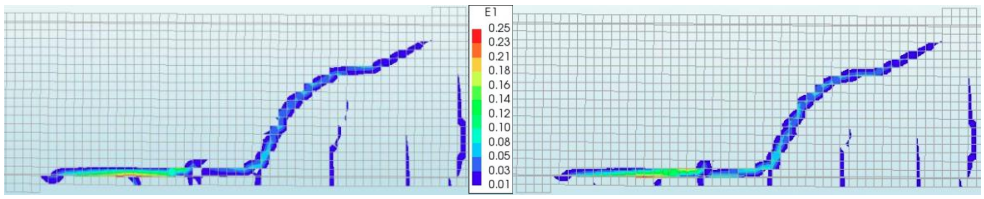

Figure 105 B701B2 maximum principal strain: confined (left) and unconfined (right)

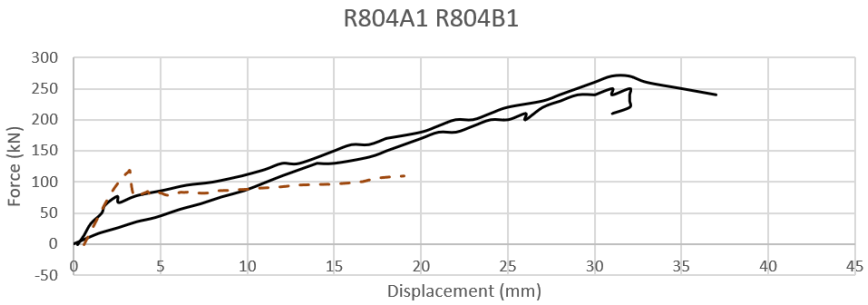

Figure 106 R804A1 Shima bond-slip-strain relation: force-displacement graph

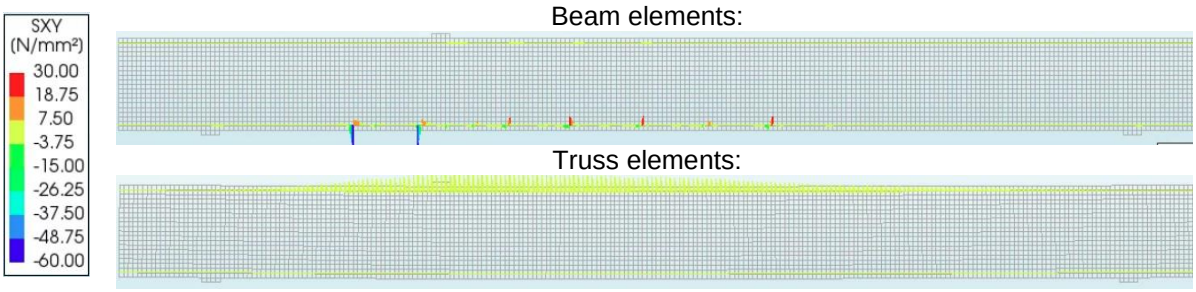

Figure 107 B701B2 Reinforcement shear stresses FIB bond-slip with beam (top) and truss elements (bottom)

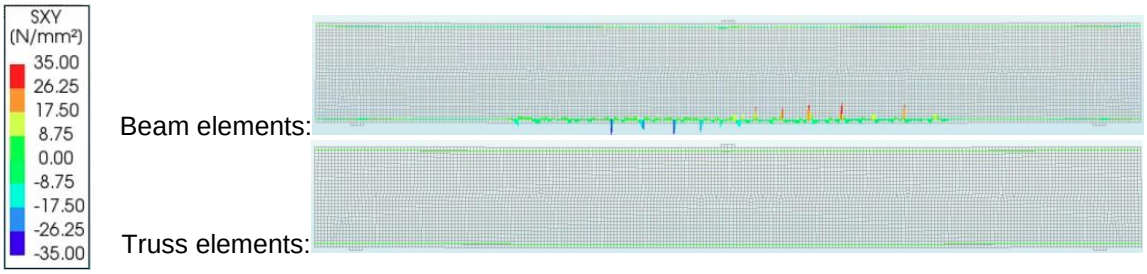

Figure 108 H601A reinforcement shear stresses: FIB bond-slip with beam (top) and truss elements (bottom)

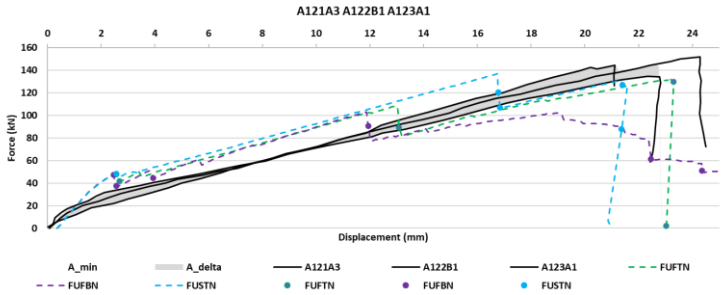

Figure 109 A121A3 Force-displacement graph: FIB bond-slip relation with truss elements, Shima bond-slip relation with truss elements, and FIB bond-slip relation with beam elements

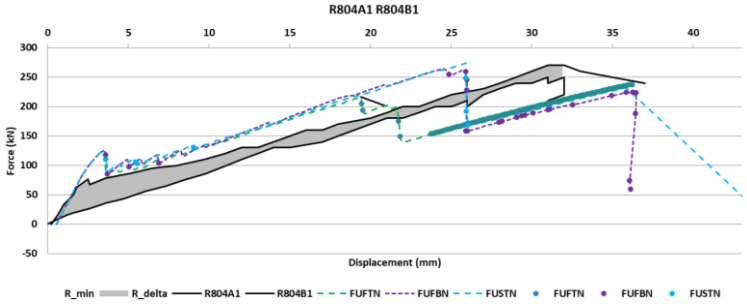

Figure 110 R804A1 Force-displacement graph: FIB bond-slip relation with truss elements, Shima bond-slip relation with truss elements, and FIB bond-slip relation with beam elements

Table 59 Maximum reinforcement stress (top) and shear traction (bottom)

Cases:	***A121A3 FUFTN***	***A121A3 FUFBN***	***B701B2 FUFTN***	***B701B2 FUFBN***	***R804A1 FUFTN***	***R804A1 FUFBN***	***H601A FUFTN***	***H601A FUFBN***
Reinforcement stress [Mpa]	376	314	399	352	441	501	387	418
Shear traction [Mpa]	8	10	9	10	9	11	8	10

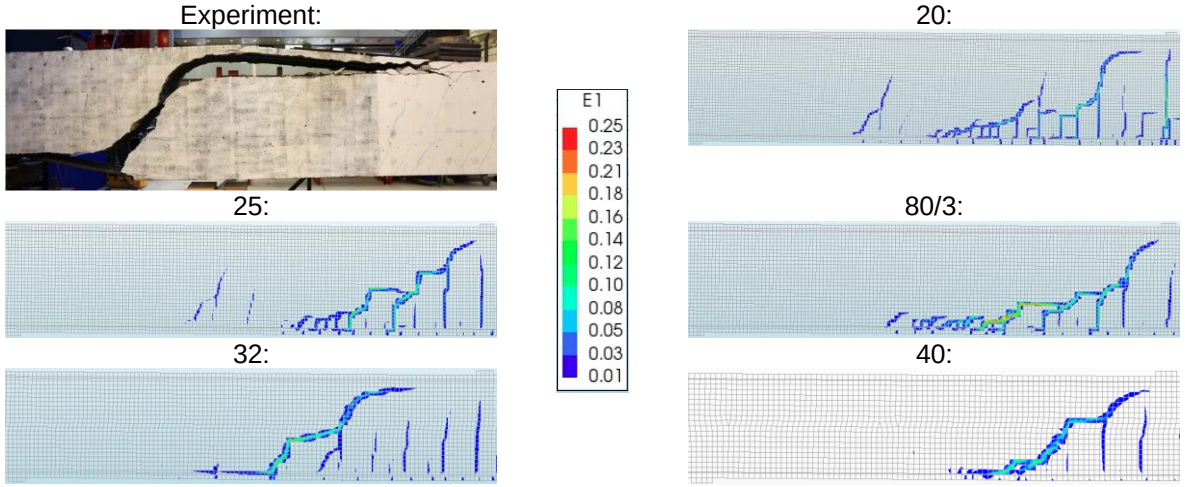

Figure 111 R804A1 element size sensitivity analysis: crack pattern

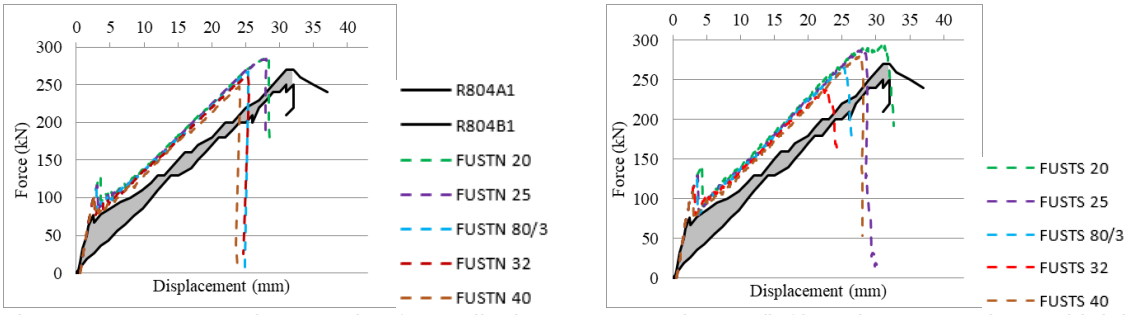

Figure 112 R804A1 element size force-displacement graph: NR (left) and Secant scheme (right)

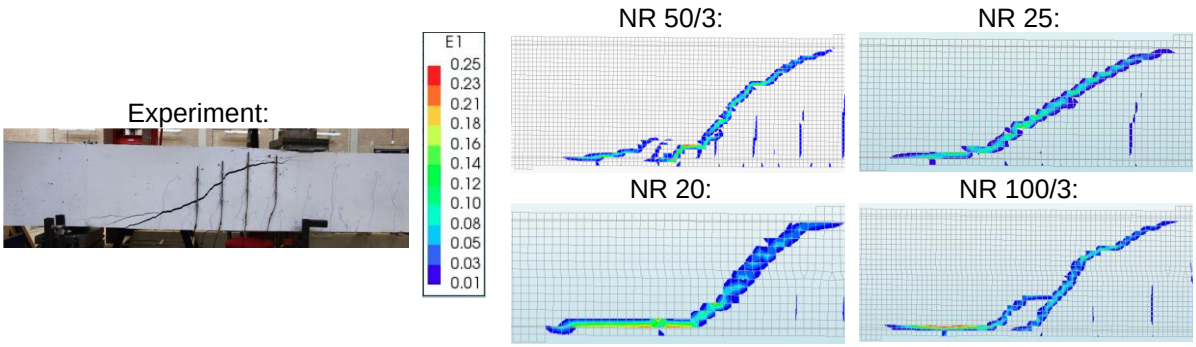

Figure 113 B702B1 element size sensitivity analysis: crack pattern

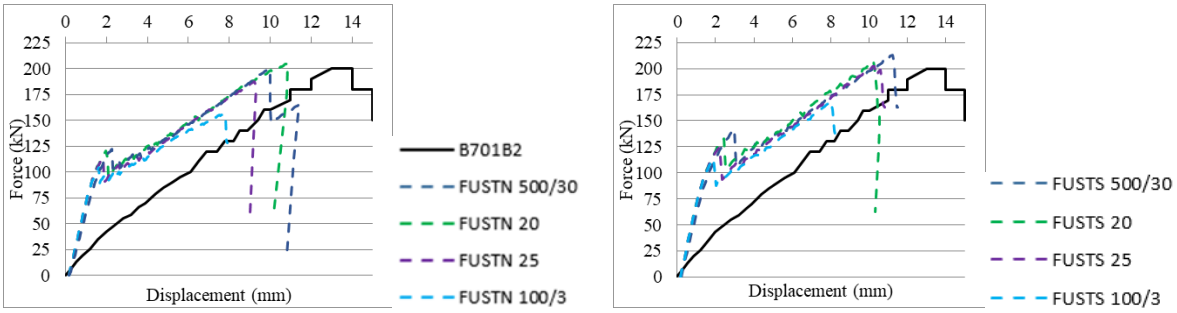

Figure 114 B702B1 element size force-displacement graph: NR (left) and Secant scheme (right)

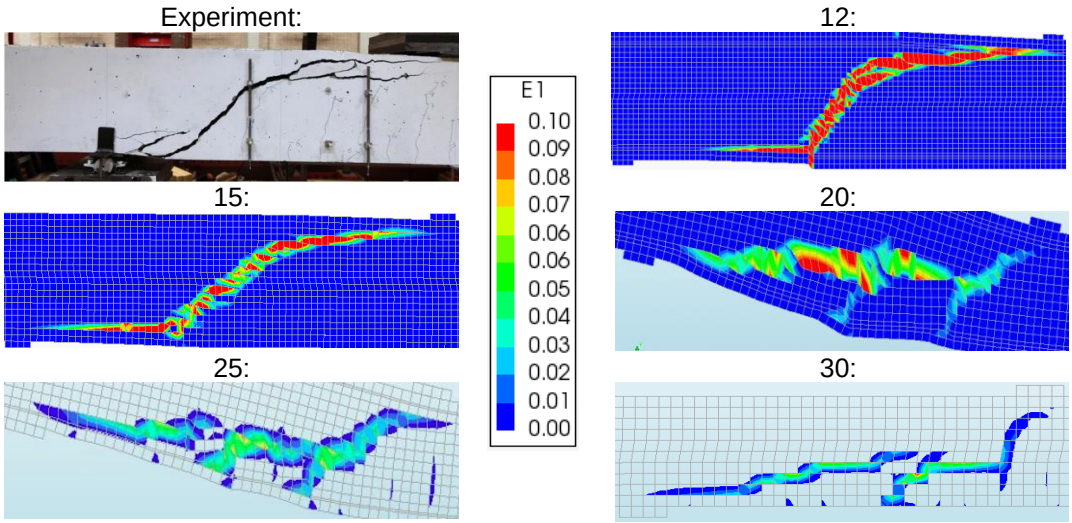

Figure 115 A121A3 element size sensitivity analysis: crack pattern

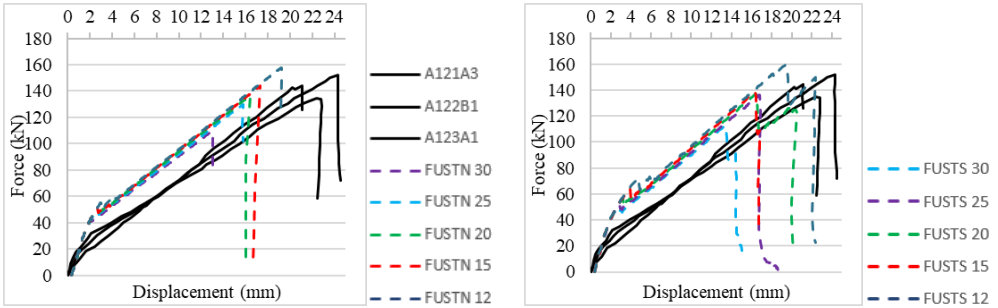

Figure 116 A121A3 element size force-displacement graph: NR (left) and Secant scheme(right)

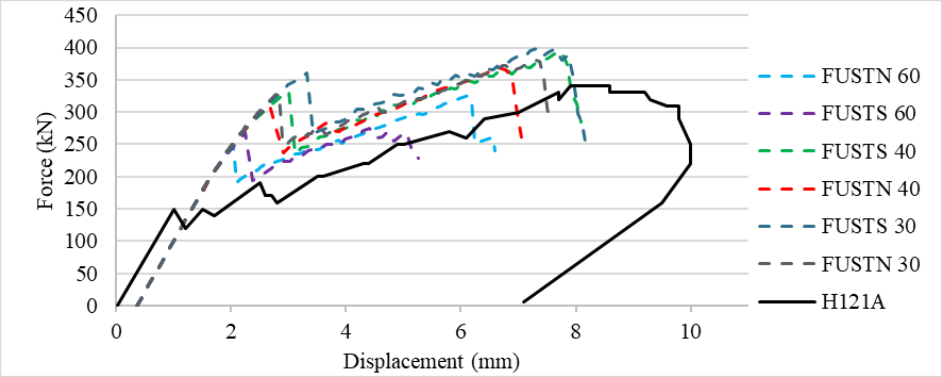

Figure 117 H121A element size and iteration schemes sensitivity analysis

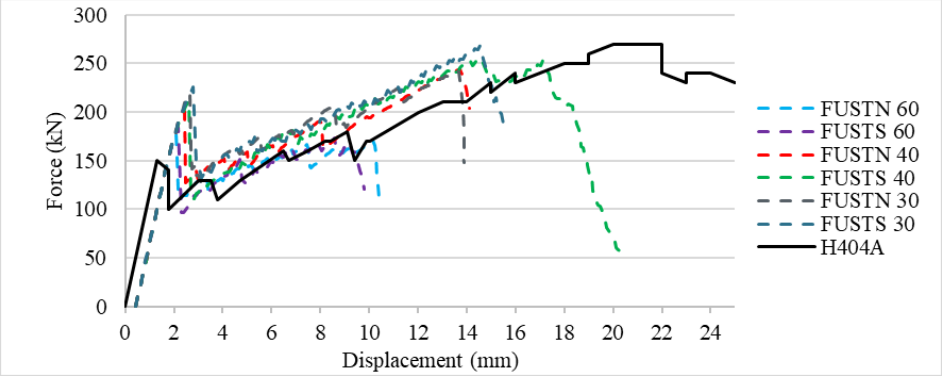

Figure 118 H404A element size and iteration schemes sensitivity analysis

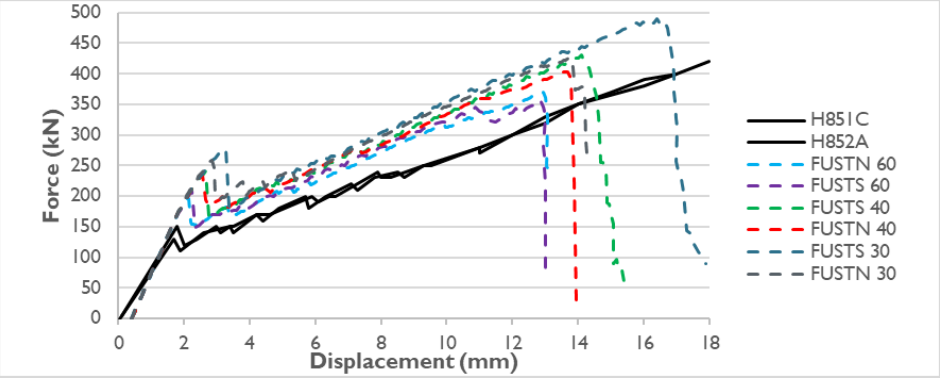

Figure 119 H851C element size and iteration schemes sensitivity analysis

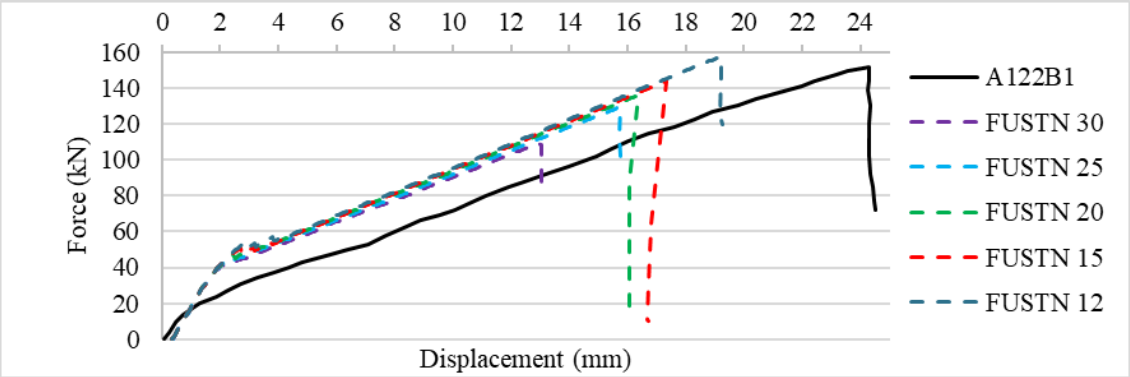

Figure 120 A751B1 element size sensitivity analysis

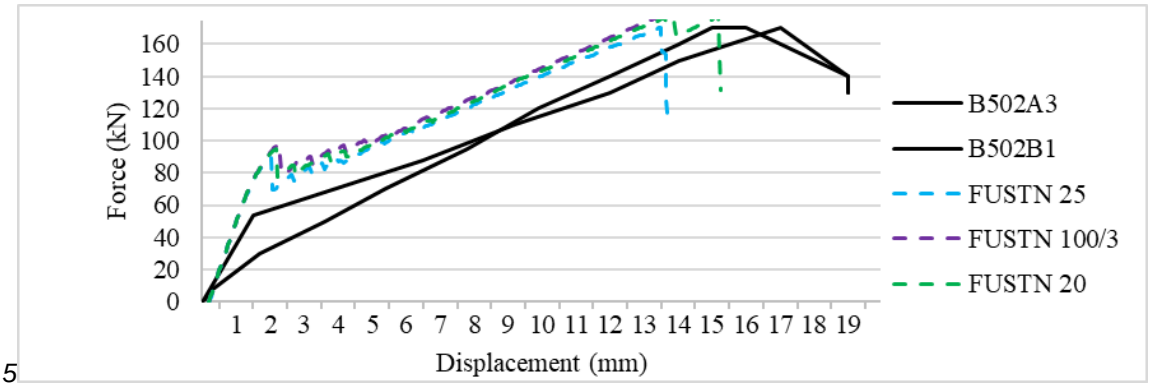

5

Figure 121 B502A3 element size sensitivity analysis

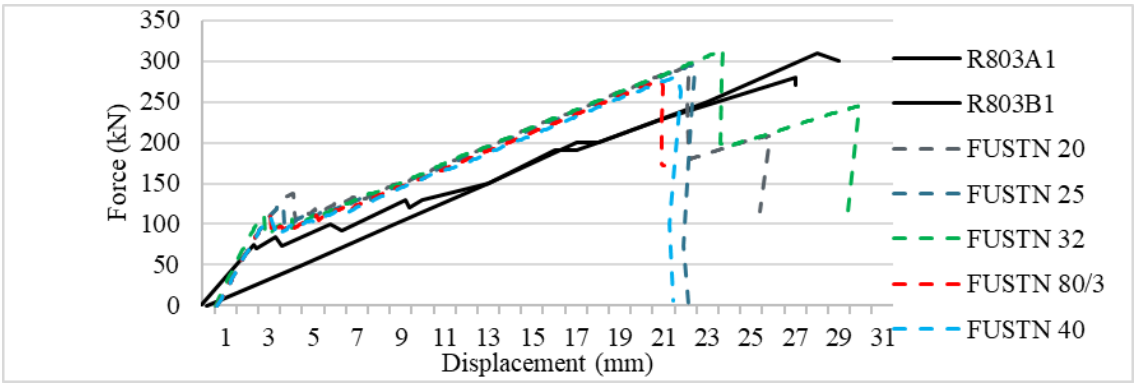

Figure 122 R803A1 element size sensitivity analysis

The tables' vertical rows with experiment 1, experiment 2, and experiment 3 indicate beams with equivalent properties tested more than once.

Table 60 Sensitivity analysis cases with d: 300mm, 500mm, and 800 mm

Newton Raphson	A121 A3 V [kN]	$\frac{V_{exp}}{V_{num}}$	B70 1B2 V [kN]	$\frac{V_{exp}}{V_{num}}$	R804 A1 V [kN]	$\frac{V_{exp}}{V_{num}}$	A751 B1 V [kN]	$\frac{V_{exp}}{V_{num}}$	B502 A3 V [kN]	$\frac{V_{exp}}{V_{num}}$	R803 A1 V [kN]	$\frac{V_{exp}}{V_{num}}$
Num	136.52		187.63		247.82		106.70		170.60		282.04	
Exp 1	144.60	1.0592	202.40	1.0787	269.40	1.0871	108.70	1.0187	173.60	1.0176	279.30	0.9903
Exp 2	152.30	1.1156			249.90	1.0084			173.20	1.0152	307.90	1.0917
Exp 3	136.50	0.9999										

Table 61 Sensitivity analysis cases with d 1200 mm

Newton Raphson	H601A V [kN]	$\frac{V_{exp}}{V_{num}}$	H121A V [kN]	$\frac{V_{exp}}{V_{num}}$	H404A V [kN]	$\frac{V_{exp}}{V_{num}}$	H815C V [kN]	$\frac{V_{exp}}{V_{num}}$
Numerical	321.04		367.93		244.88		403.64	
Experiment 1	306.00	0.9532	341.00	0.9268	269.00	1.1025	421.00	1.0430
Experiment 2	306.00	0.9532					406.00	1.0058

Annex IV Robust numerical model

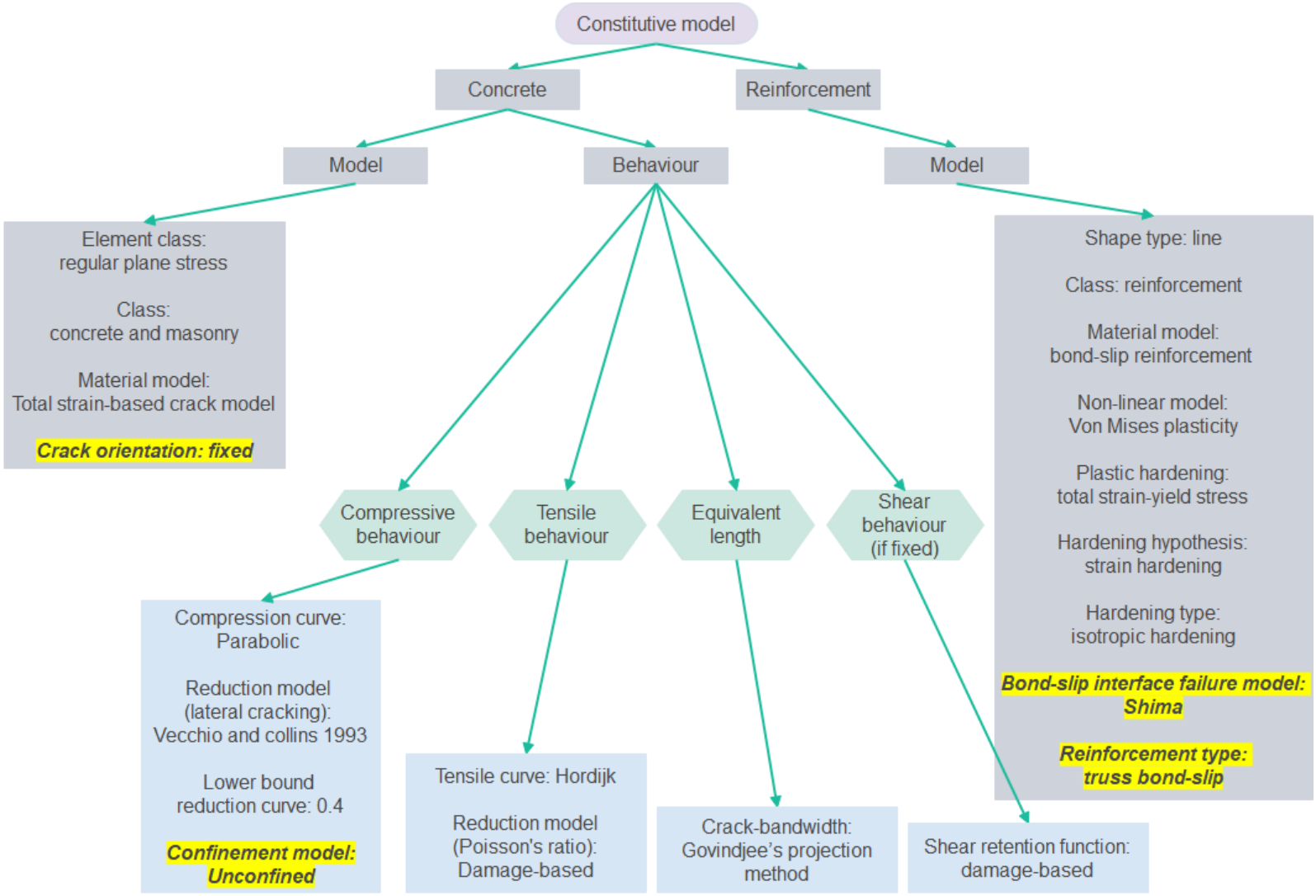

Figure 123 Robust numerical model: constitutive model

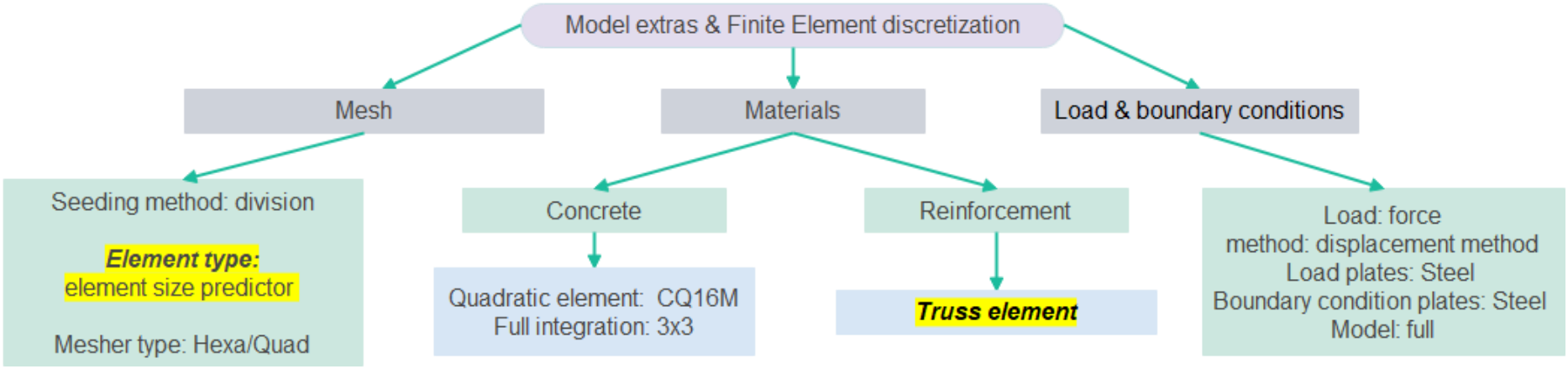

Figure 124 Robust numerical model: finite element discretization

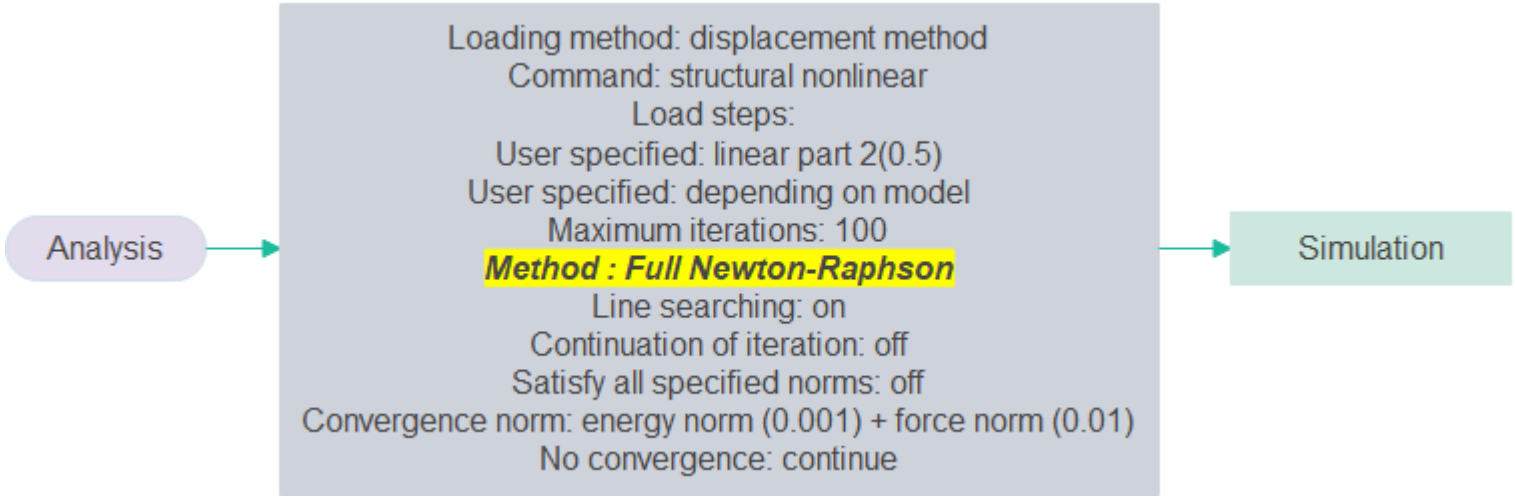

Figure 125 Robust numerical model: analysis procedure

Annex V Sensitivity analysis with the DPC system

The numerical simulations will be compared with the experimental results to grade the simulations' reliability. Collins (91) introduced a Demerit Point Classification (DPC) to classify predictions. The advantage of this classification is accuracy considerations for a calculation model to grade the models' safety. An overview of the DPC system can be found in the table below:

Table 62 Collin's DPC system classification

Range	Demerit penalty	Classification
$\frac{Vexperimental}{Vnumerical} \leq 2$	10	Extreme dangerous
$1.179 \leq \frac{Vexperimental}{Vnumerical} < 2$	5	Dangerous
$0.869 \leq \frac{Vexperimental}{Vnumerical} < 1.179$	0	Safe
$0.5 \leq \frac{Vexperimental}{Vnumerical} < 0.869$	1	conservative
$\frac{Vexperimental}{Vnumerical} < 0.5$	2	Extreme conservative

The demerit penalty will be used to calculate the value of safety for $0 \leq \frac{Vexperimental}{Vnumerical} < 2$. The closer the result is to one, the better the numerical model performs. These values will be plotted as a function of four parameters: the effective depth, the effective span-to-depth ratio, the concrete strength, and the reinforcement ratio.

The boundaries in the plots will be 0.869 and 1.179. These plots will give an overview in case one parameter of the four causes dangerous or conservative results. Suppose the numerical simulations are in extremely dangerous or extremely conservative regions. In that case, the chosen numerical model will be seen as unacceptable. Further sensitivity analysis will be done for the numerical model. The plots will be scattered, as the discrepancy ratio variation supplies a clear safety overview.
The legend for this system is given below:

Table 63 Collin's DPC system boundaries

DPC Legend	*< 0.8035*	*0.8363*	***0.869***	*0.9018*	*0.9345*	*0.9673*	*1*	*1.0448*	*1.0895*	*1.1343*	***1.179***	*1.2238*	*> 1.2685*

Sensitivity analysis initial cases:
The experimental results and numerical simulations comparison for the best numerical model has also been plotted with the $\frac{V_{exp}}{V_{num}}$, against the four parameters which will be used to grade the size effect. This graph shows if a parameter can cause a numerical model to result in unsatisfactory results when graded by the DPC system. The report's two parameters, "effective depth and reinforcement ratio, " vary the most.

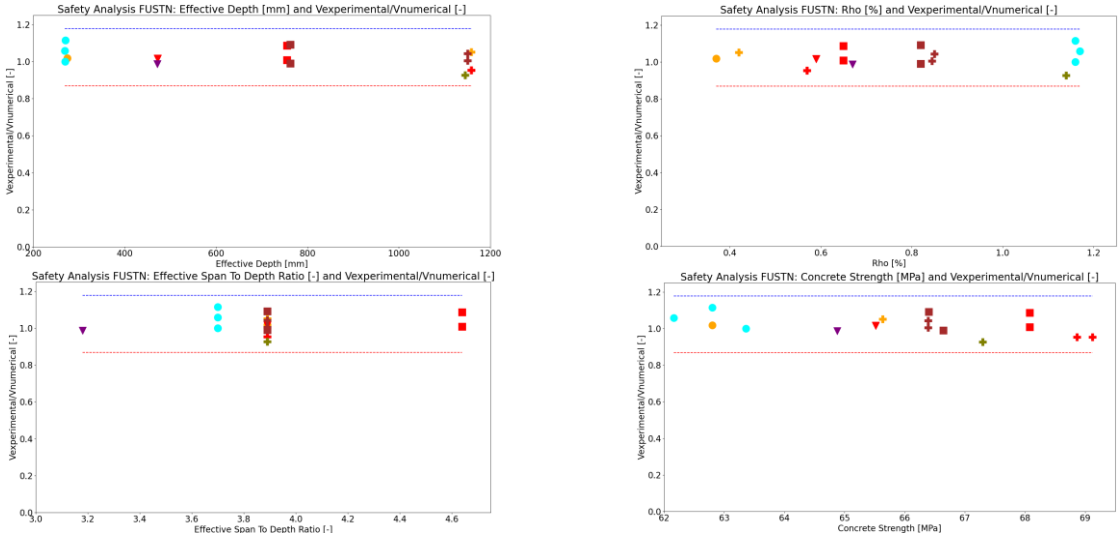

Figure 126 Robust numerical model with DPC boundaries

In addition, similar plots have been added below for the other alternative numerical setup that did not perform as well as the chosen numerical one when graded with the DPC system. The plots in the annex clearly show that one of the four parameters can cause the specific numerical model to simulate inaccurate results.

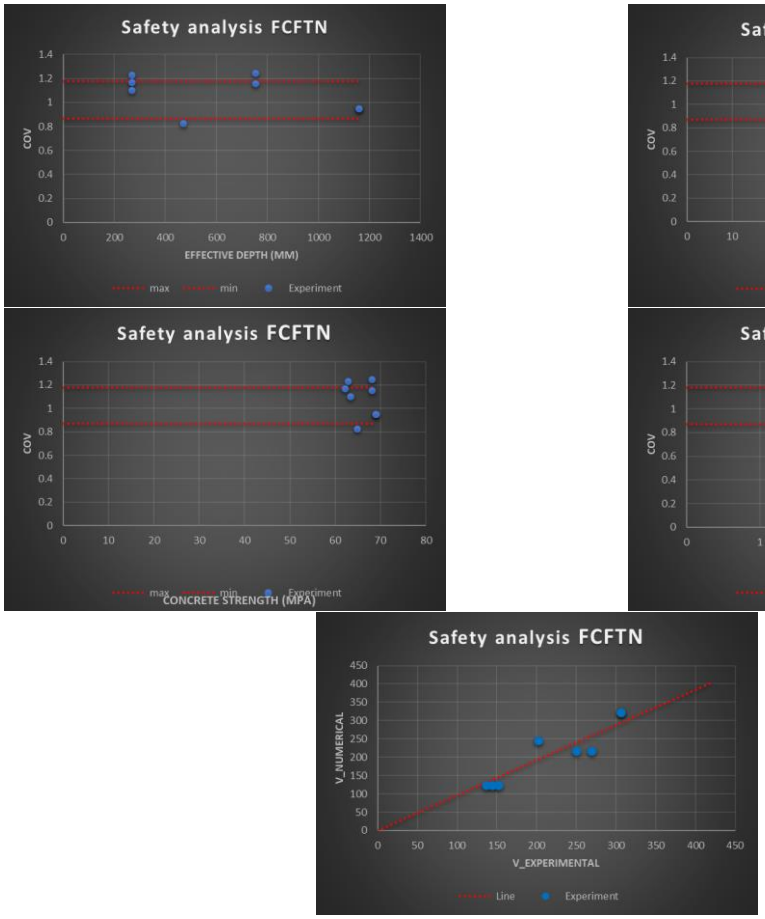

Figure 127 FCFTN with DPC boundaries

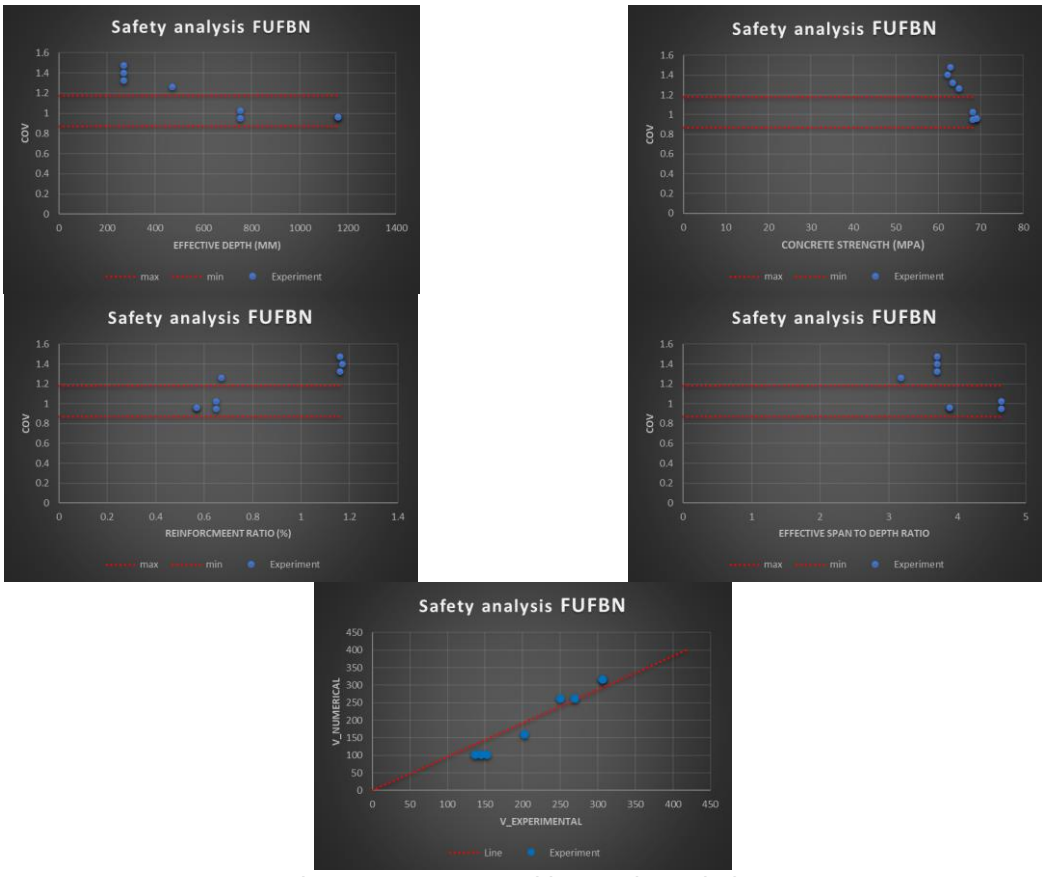

Figure 128 FUFBN with DPC boundaries

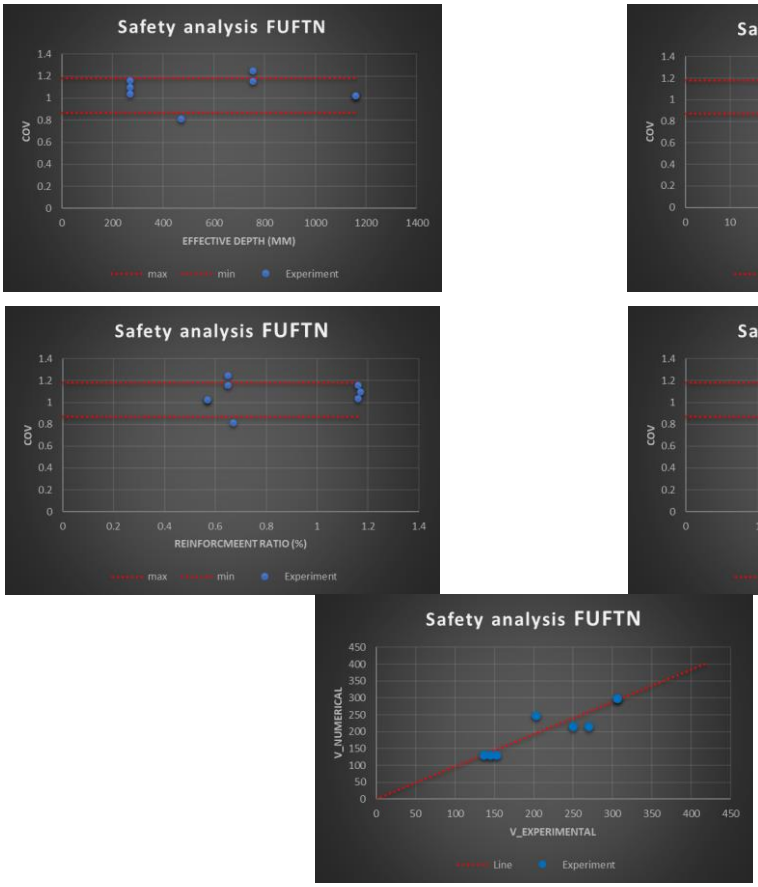

Figure 129 FUFTN with DPC boundaries

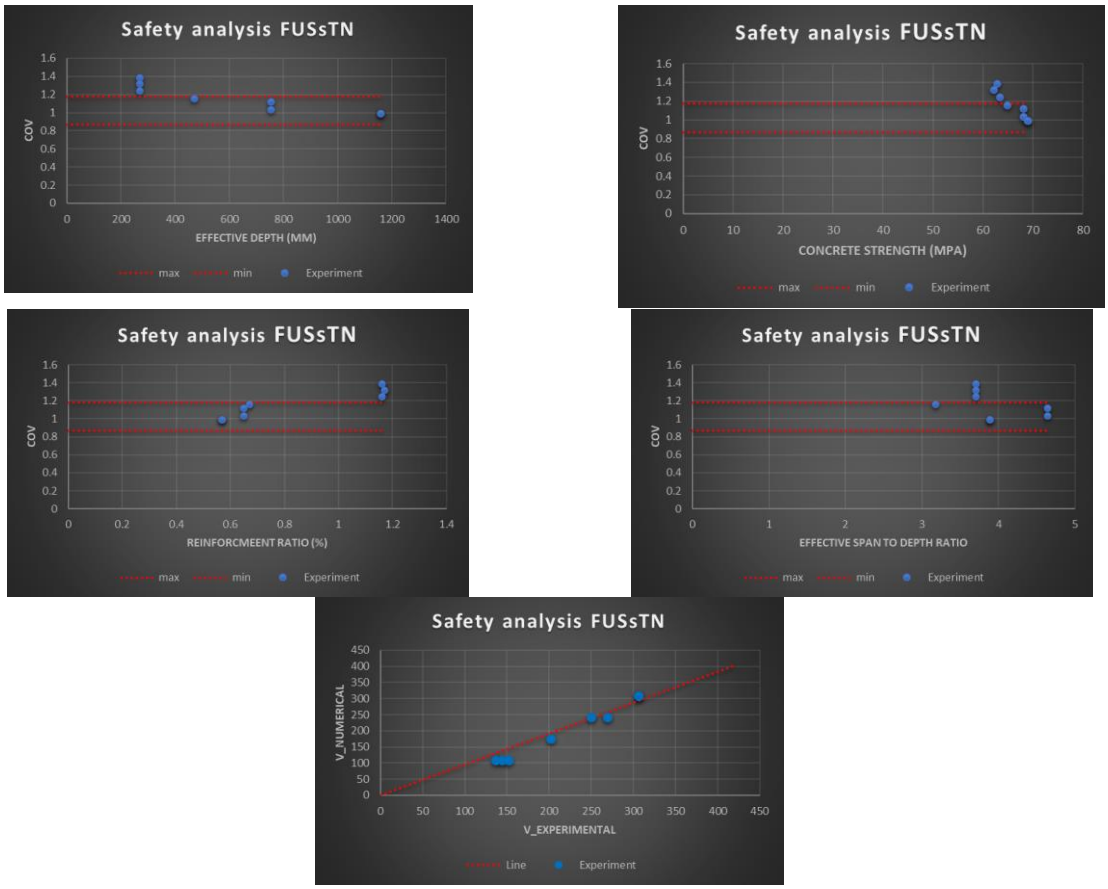

Figure 130 FUSsTN with DPC boundaries

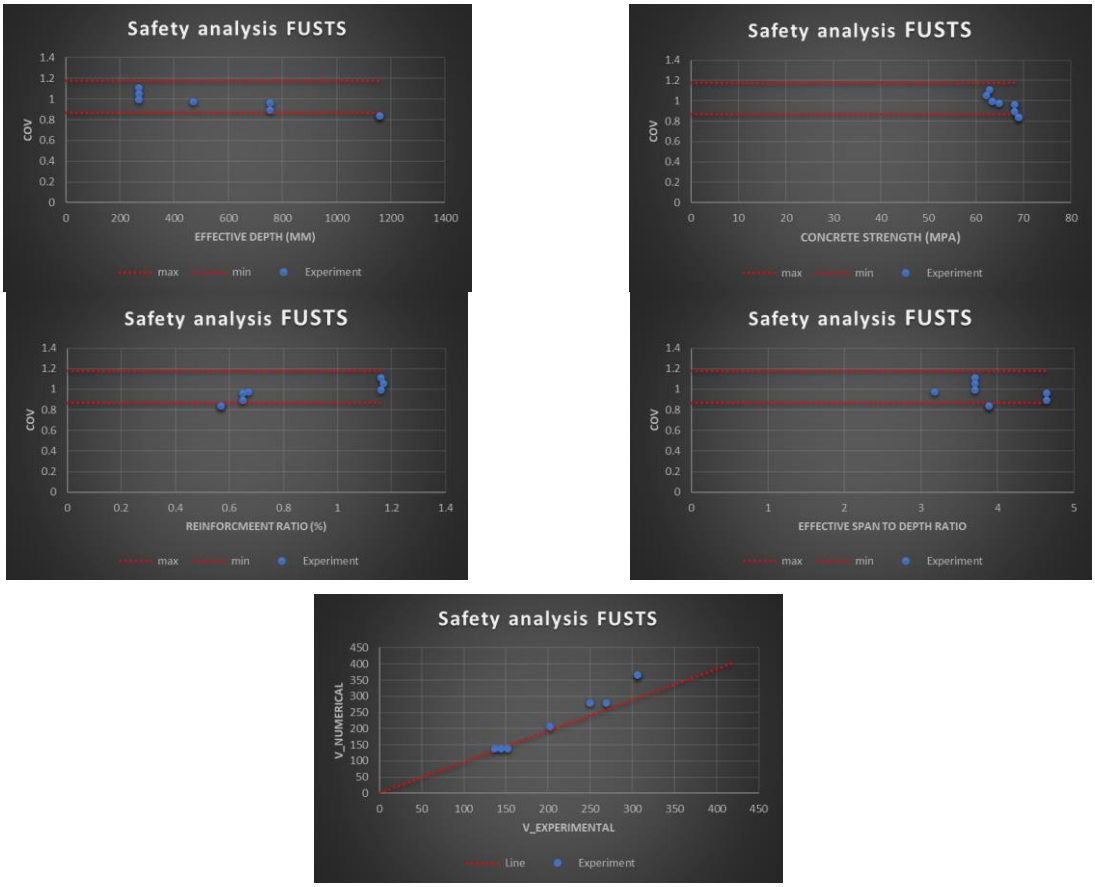

Figure 131 FUSTS with DPC boundaries

Annex VI Quantitative analysis with the DPC system

In this annex, the DPC system is addressed, for which the four graphs in Figure 132 are plotted against four parameters to analyze the result.

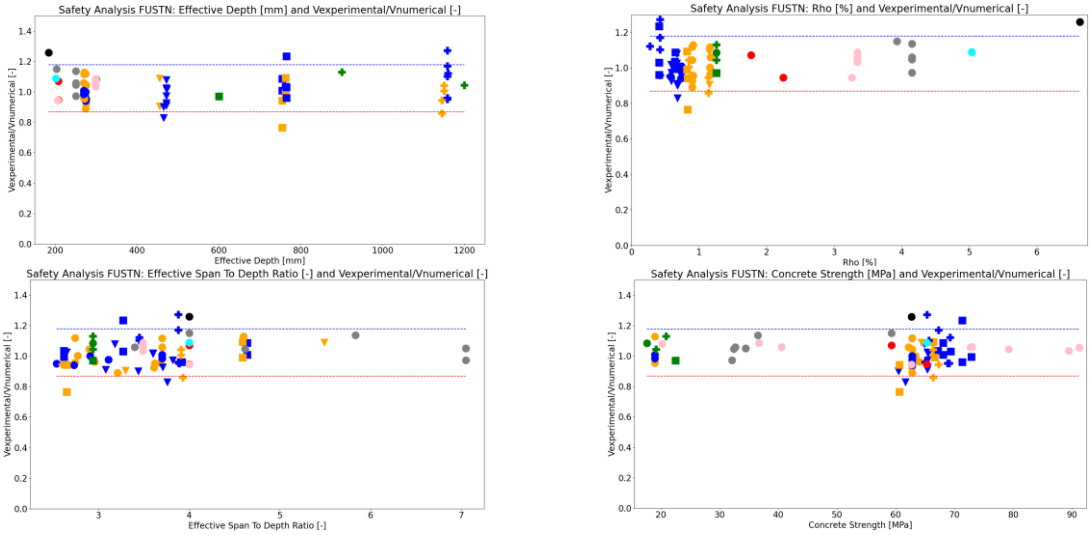

Figure 132 Quantitative analysis with DPC boundaries

For all numerical cases based on the failure load, 92% gave an acceptable according to the DPC system. According to the DPC system, the following cases were unacceptable: Rho_6.6, R502B1, R802A1, E402A, H403A, and H123A. From the numerical analysis, the six cases did result in the expected damage progression and failure mode.

The three cases subjected to an overestimated failure load are R502B1, R802A1, and H123A of the failure load. In case R802A1, stress-locking is noticed for the model due to the fixed crack orientation. This phenomenon is noticeable from the force-displacement graph, where a too-stiff behavior is noticed. The global stiffness from the numerical model leads to a much steeper (positive) slope compared to the experimental model and can be seen in the picture below:

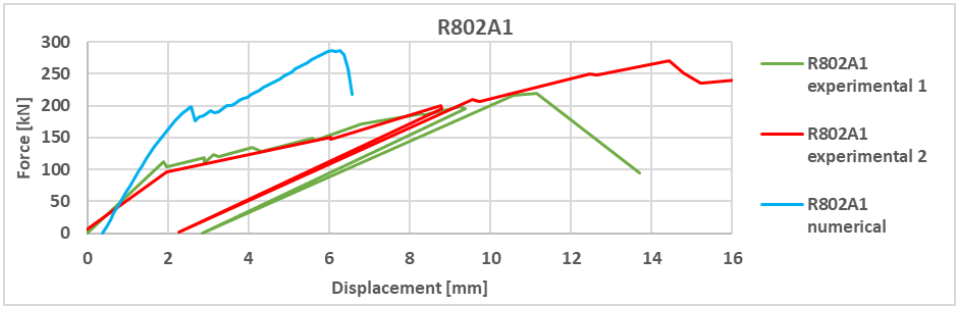

Figure 133 R802A1: force-displacement graph

In Figure 133, the experimental force drops to zero between 2 mm and 2.5 mm displacement due to unloading and reloading. Even though stress-locking is a known problem for the fixed crack orientation, this only happens in one case during the quantitative analysis. The other two overestimating models, namely R502B1 and H123A, are not subjected to stress-locking. There is still an overestimation for these models, of 17% and 16% for each, respectively. This overestimation is because of the damage-based shear retention model, which overestimates the aggregate interlock contribution. A remedy to fix this overestimation is an alternative shear retention model.

The remaining three numerical models were subjected to underestimating the failure load. However, their numerical analysis shows a good damage progression. After an in-depth analysis of the Rho_6.6 model, no problems were found with the numerical model. However, if all the cases from Ahmad et al. used for this study are analyzed, the following results in Table 64 are found.

Table 64 Ahmad et al. cases experimental and simulated failure loads

Test [#]	ρ [%]	V experimental [kN]	V numerical [kN]	h [mm]	d [mm]
rho_1.7	1.77	47.18	44.06	254	208
rho_2.2	2.25	44.96	47.54	254	208
rho_3.3	3.26	45.85	48.54	254	207
rho_3.9	3.93	58.30	50.70	254	203
rho_5.0	5.03	51.68	47.44	254	202
rho_6.6	6.64	54.71	43.46	254	184

From Table 64 above, there is no proper trend for the experimental failure load, with no clear sign if the failure load is decreasing or increasing due to an increasing reinforcement ratio. The numerical simulations show an increase in failure load until a reinforcement ratio of 3.9 %. After this increase, a decrease in the failure load is noticed. A logical explanation for this can be the following: Even though there is a constant beam depth, the effective depth varies to keep a sufficient concrete cover while increasing the reinforcement ratio. The reduction of the effective depth caused a lower failure load even though the reinforcement ratio was increasing. This study was meant to study only the change in the reinforcement ratio. However, due to changes in the effective depth, this study is not ideal for studying only this parameter. In future research, more on this can be researched. A second reason for such results can be that after reaching a percentage of a high reinforcement ratio, an increased reinforcement ratio does not increase the failure load. However, more on this can only be said after further research.

Finally, the other two cases for which the results are underestimated can be addressed, which are H403A and E402A. H403A is analyzed first. Two more experiments with similar beam properties to H403A were performed at Stevin Lab, namely H401A and H402A. The numerical failure load is sufficient for cases H401A and H402A. In contrast, the H403A failure load differs significantly from the result of these two cases. If the failure load from H401A is compared with H403A, a 75% overestimation is noticed for the latter case. This overestimation indicates that the error is in the experiment instead of the numerical model. During experiments, external factors can potentially hugely influence the failure load. These factors are, for example, gravel proportion or the gravel size and explain why an experiment with the same case properties is repeated multiple times. The same conclusion as in this case is made regarding case E402A.

Annex VII Size effect analyses

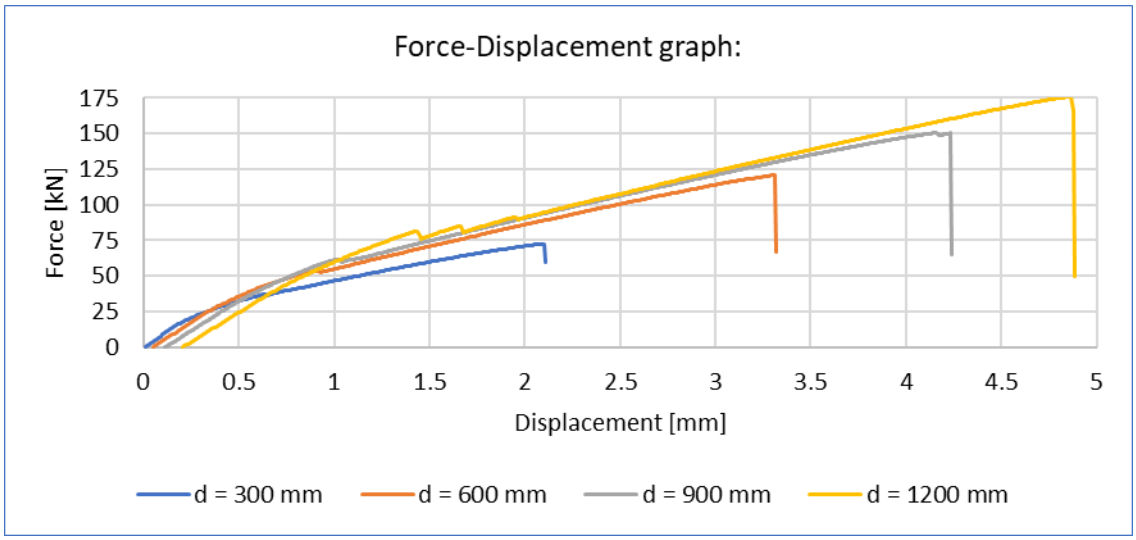

Figure 134 Bhal cases force-displacement graph: effective depths

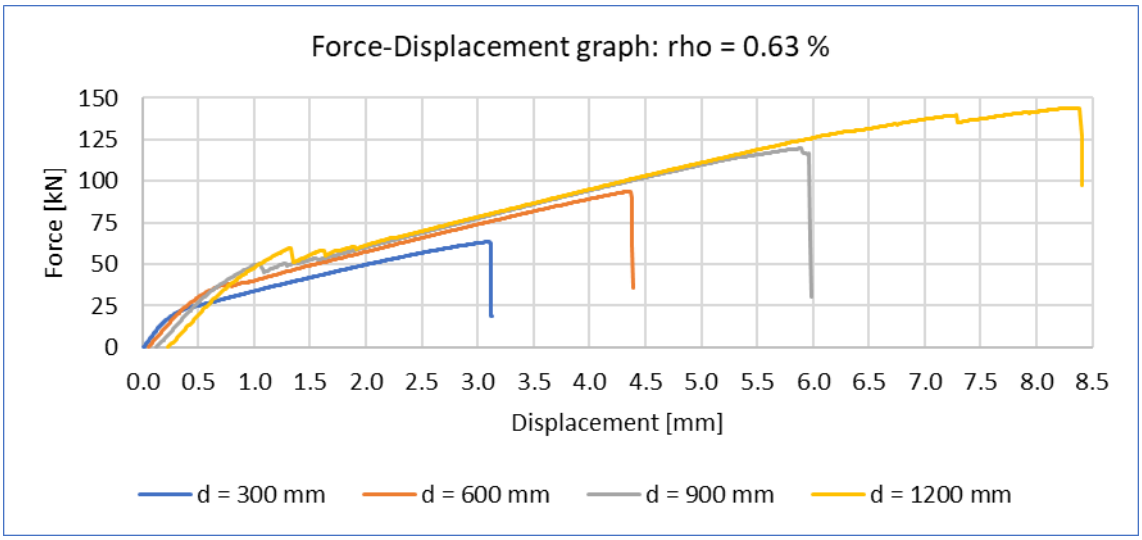

Figure 135 Force-displacement graph: reinforcement ratio 0.63 %

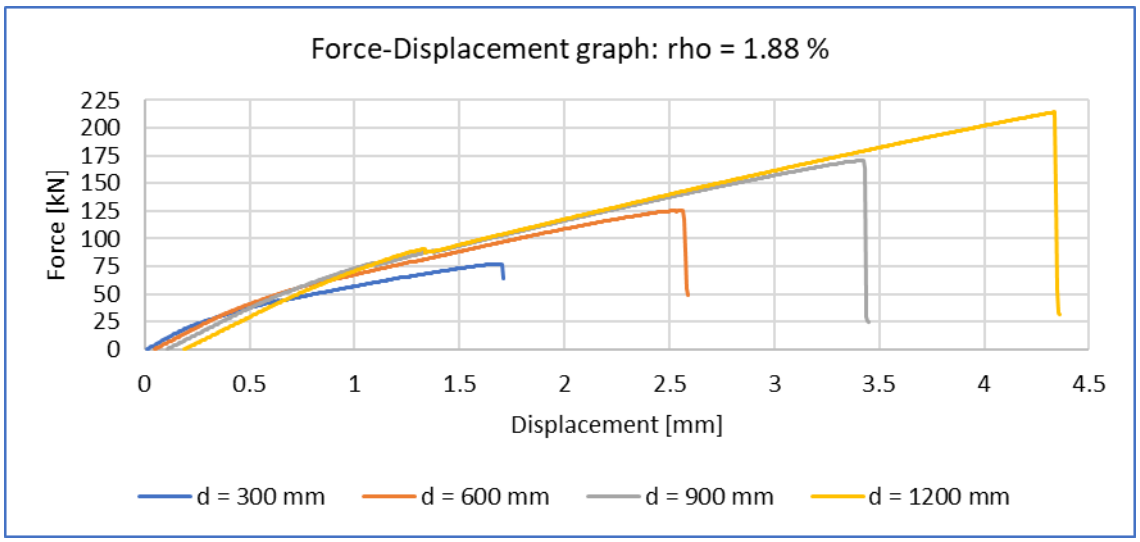

Figure 136 Force-displacement graph: reinforcement ratio 1.88 %

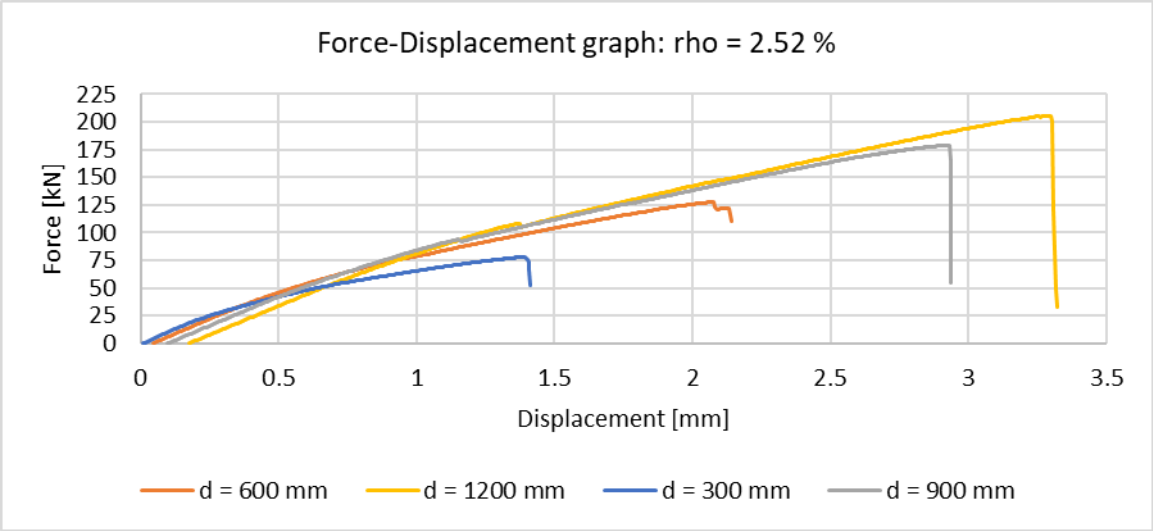

Figure 137 Force-displacement graph: reinforcement ratio 2.52 %

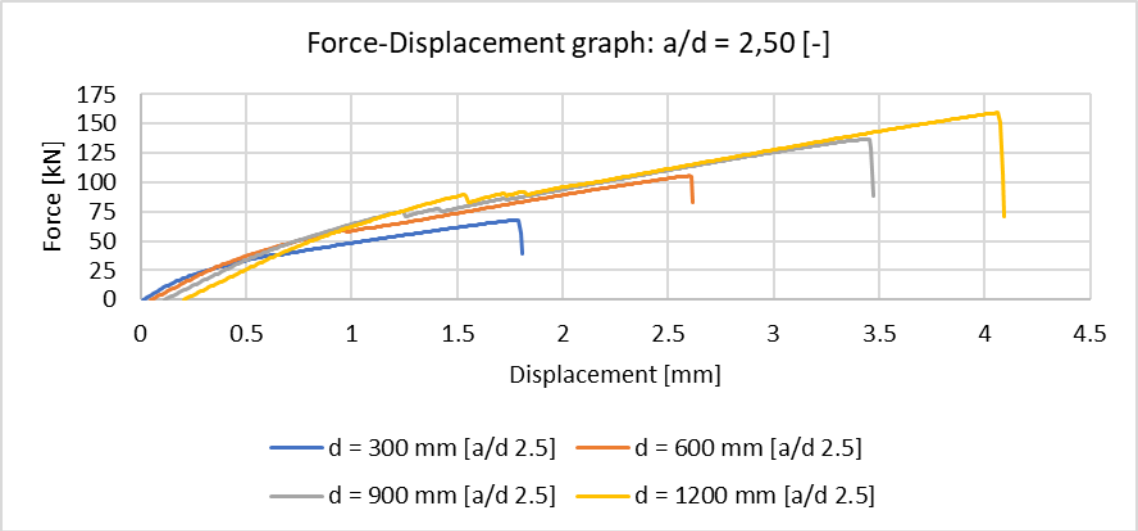

Figure 138 Force-displacement graph: effective span-to-depth ratio 2.50

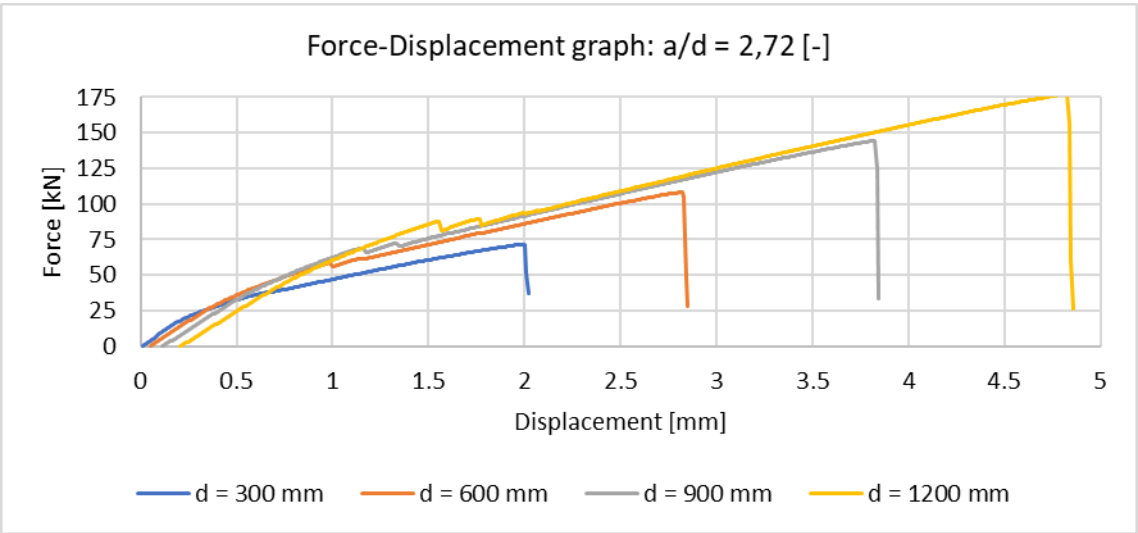

Figure 139 Force-displacement graph: effective span-to-depth ratio 2.72

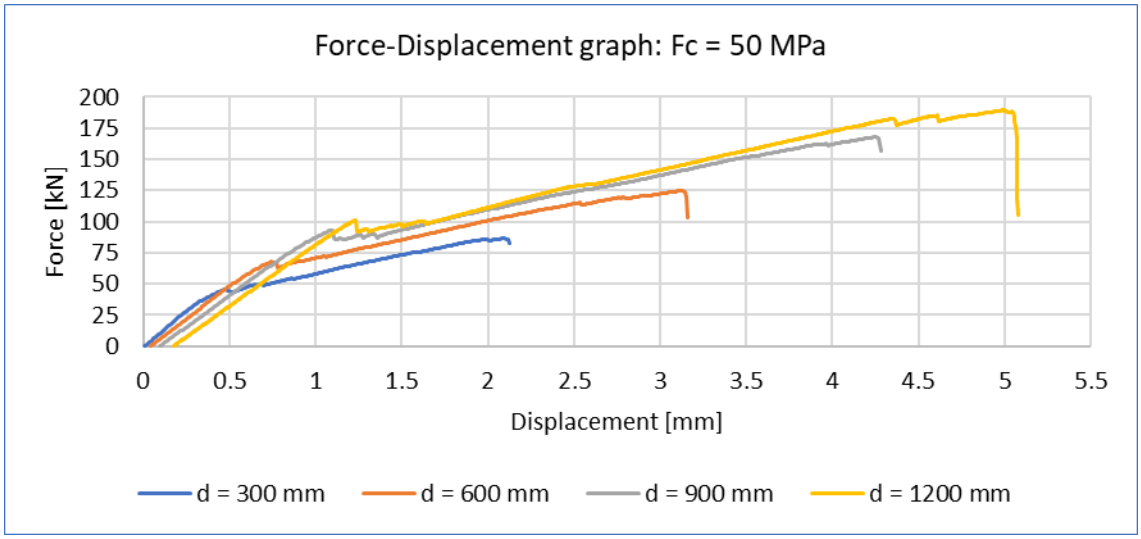

Figure 140 Force-displacement graph: concrete strength 50 MPa

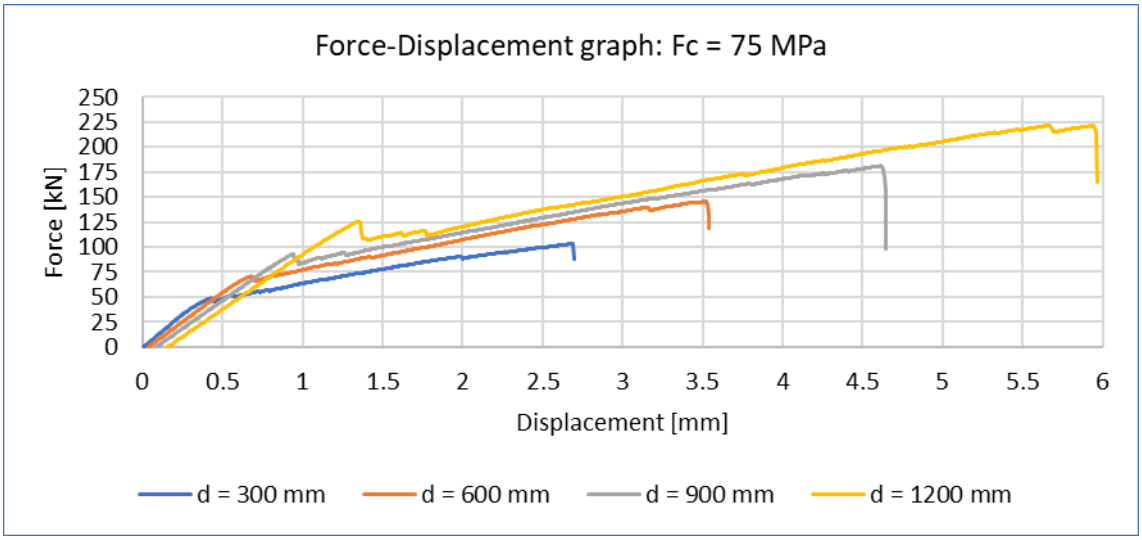

Figure 141 Force-displacement graph: concrete strength 75 Mpa

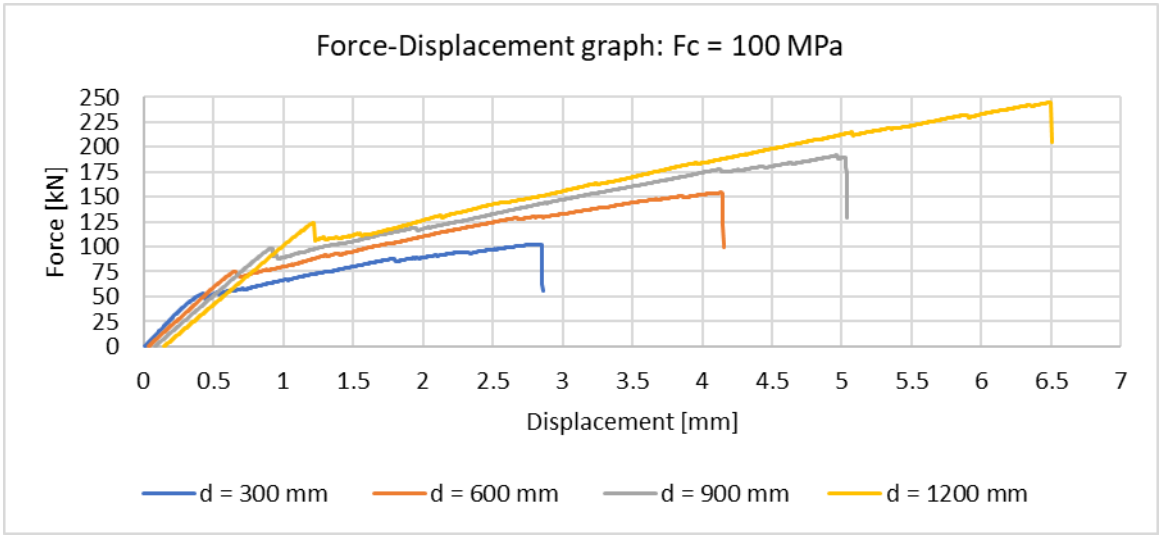

Figure 142 Force-displacement graph: concrete strength 100 MPa

Table 65 Reinforcement ratio variation slopes

Reinforcement ratio	0.63 %	1.26 %	1.88 %	2.52 %
0.3 m < d < 0.6 m	-0.65	-0.58	-0.56	-0.54
0.6 m < d < 0.9 m	-0.45	-0.44	-0.41	-0.39
0.9 m < d < 1.2 m	-0.26	-0.31	-0.26	-0.24

Table 66 Effective span-to-depth ratio variation slopes

Effective span-to-depth ratio	2.50 [-]	2.72 [-]	2.94 [-]
0.3 m < d < 0.6 m	-0.43	-0.6	-0.58
0.6 m < d < 0.9 m	-0.31	-0.39	-0.44
0.9 m < d < 1.2 m	-0.18	-0.18	-0.31

Table 67 Concrete strength variation slopes

Concrete strength	25 MPa	50 MPa	75 MPa	100 MPa
0.3 m < d < 0.6 m	-0.58	-0.92	-1.06	-1.16
0.6 m < d < 0.9 m	-0.44	-0.58	-0.63	-0.65
0.9 m < d < 1.2 m	-0.31	-0.24	-0.19	-0.15

Annex VIII Size effect analysis geometrically scaled fictitious cases

Variation in reinforcement ratio

An analysis is done with different reinforcement ratios on the four Bhal beams to study this potential influence on the size effect. During the numerical model sensitivity analysis, the range of cases with varying reinforcement ratios for all the cases (Chapter 3) was between 0.26 % and 6.64 %. Different reinforcement ratios were chosen within this calibrated range for the size effect analysis, as the results were within an acceptable percentage difference. The chosen reinforcement ratios for the size effect analysis have a significant enough difference between them to better observe the differences in the size effect. The selected reinforcement ratios are:

- 0.63 % (0.5 * 1.26 %)
- 1.26 % (initially used for the configuration of the Bhal experiments)
- 1.88 % (1.5 * 1.26 %)
- 2.52 % (2.0 * 1.26 %)

The fifth reinforcement ratio within the calibrated experiments range would have been 3.15 (2.5 * 1.26 %). However, such high reinforcement ratios were not analyzed because there was not much difference between the ratios of 1.88 % and 2.52 % in the size effect analysis. In Annex VII, the force-displacement graphs are given for each reinforcement ratio configuration. Next, the nominal shear strength of all the different reinforcement ratios is plotted against the effective depth in a log-log plot in Figure 143.

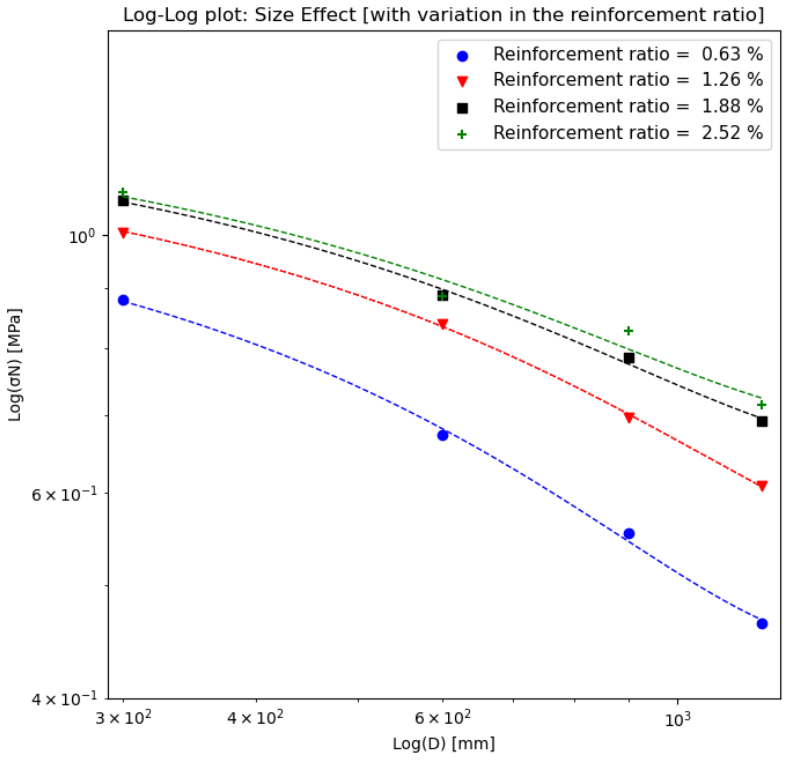

Figure 143 Size effect analysis with variation in the reinforcement ratio

With the increase of the reinforcement ratio, the nominal shear strength also increases for the exact beam sizes. However, the speed with which the reinforcement ratio decreases for geometrically scaled beams is essential to find the influence of the parameter on the size effect. If the results had been analyzed according to the SEL figure (*Figure 8*), all the nominal shear strength values would be in the second section (the nonlinear fracture mechanics influenced by the size effect). The analysis of Figure 143 indicates a slightly steeper slope for cases with lower reinforcement. This slope difference signifies a more pronounced decrease in the nominal shear strength as the reinforcement ratio decreases for RC beams without stirrups. This result concludes that a more significant size effect exists for beams with lower reinforcement ratios. However, these slope differences for the same beam size are minimal and almost neglectable. An increased reinforcement ratio leads to better control of the cracks.

Comparing the reinforcement ratios of 1.88 % to 2.52 % shows interesting behavior. After a high enough reinforcement is reached for the configuration, a further increase in the reinforcement ratio does not weaken the size effect more. Reinforcement ratios much smaller than 0.63 % may get influenced much more by the size effect. Table 65 from Annex VII specifies the slopes for each configuration. The tables can be studied for a broader understanding of the effect of the reinforcement ratio on the size effect.

Other behavioral changes from the increase in the reinforcement ratio are also analyzed. The force-displacement graph analysis in Annex VII showed that the reinforcement ratio affects the beams' global stiffness. The global stiffness increases as the reinforcement ratio increases, as the additional reinforcement helps better distribute the load. The same elastic stiffness for all beams makes sense, as the concrete has not yet cracked during this phase. With the rise in global stiffness, the failure load also increases, but the beam deforms less. The two examples in Figure 144 demonstrate the increase in stiffness. The first example (left) is for the smallest beam with a depth of 300mm, while the second (right) is for the largest beam with an effective depth of 1200 mm. The small beam has a relative failure load increase of 24 % and a relative displacement decrease of 55 % between the maximum and minimum reinforcement ratio. The differences are 43 % and 60 % for the larger one, respectively, showing a more significant capacity gain. This higher increase in capacity for the larger beam is because the large beams with low reinforcement are influenced more by the size effect. The effect is weakened for the case with high reinforcement.

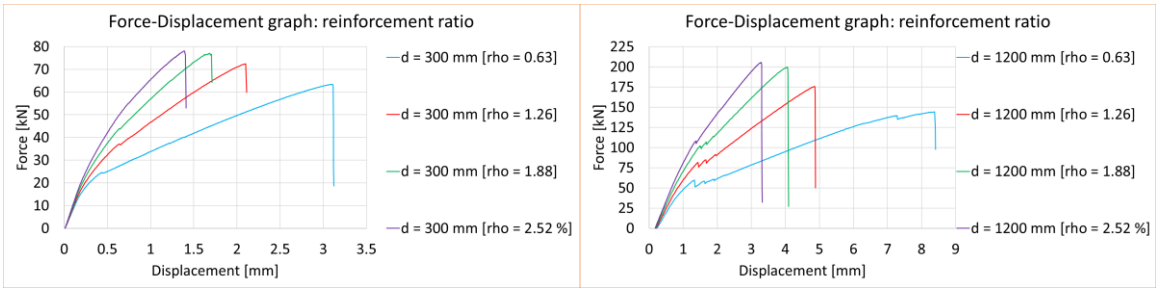

Figure 144 Force-displacement graph: d = 300 mm (left) and d = 1200 mm (right)

Variation in effective span-to-depth ratio

The third parameter that will be studied for its influence on the size effect is the effective span-to-depth ratio. As previously stated, the parameter must be limited to an effective span-to-depth ratio between 2.5 and 7.0 to capture the flexural shear failure. Moving out of this range results in another expected failure mode, which is not considered in this report. The initial effective span-to-depth ratio (2.94) is already at the center of the beam for the size effect analysis. Therefore, considering the effective span-to-depth boundary, the following ratios are chosen when calculated from the left side of the beam:

- 2.94 (initial and maximum ratio)
- 2.72 ($2.94 - \frac{2.94-2.50}{0.5}$)
- 2.50 (minimum ratio)

An overview of the effective span-to-depth ratio locations is shown in Figure 145. In addition, nominal shear strengths for the effective span-to-depth ratio variation are plotted in Figure 146, with the analysis of its influence followed by it.

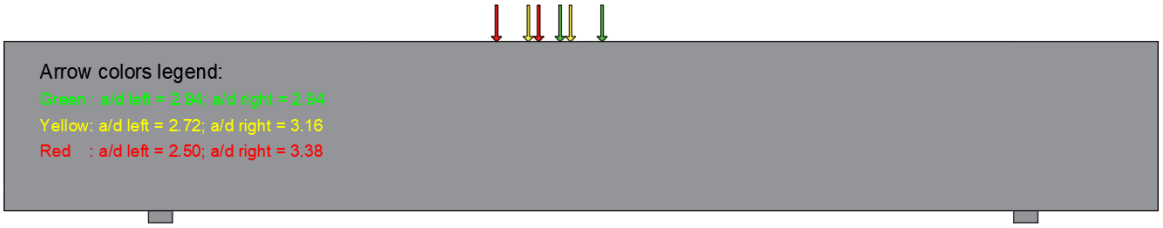

Figure 145 Effective span-to-depth ratio variation

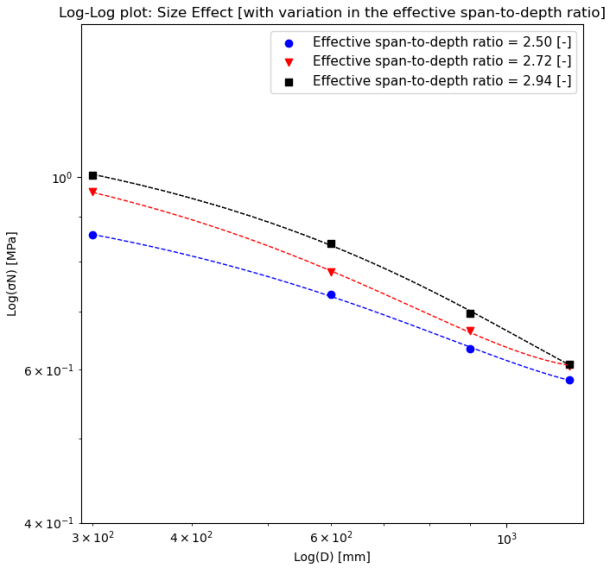

Figure 146 Size effect analysis with variation in the effective span-to-depth ratio

In the previous section, an increase in the reinforcement ratio results in a slightly flatter but almost neglectable slope difference. However, this is the reverse situation for the effective span-to-depth ratio. There is an increase in the steepness of the curves' slope with an increase in the ratio. Unlike the reinforcement ratio, the slope difference is more noticeable from the log-log plot. This difference indicates that the effective span-to-depth ratio has a more significant influence. It should also be noted that the different effective span-to-depth ratios have a difference of just 0.22 (0.50, 0.72, and 0.94), which is not much. With this observation, it can be concluded that the increase in the effective span-to-depth ratio increases the size effect. Table 66 can be viewed from Annex VII to indicate better this parameter's influence on the size effect with the help of the slope measurements for each ratio.

Besides increasing the size effect due to an increasing effective-span-to-depth ratio, this parameter is also a deciding factor in the failure mode and crack pattern, as previously explained. In addition, the failure load increases as the effective span-to-depth ratio increases (moves more central of the beam). This response is seen in the force-displacement graphs for every effective span-to-depth ratio in Annex VII. The failure load increases, but the displacement significantly increases, as seen in Figure 147. This simulated result makes sense from a structural mechanics perspective when the force distribution of the 'vergeet-mij-nietjes/forget-me-not' formulas are applied. The beam capacity will be more significant when loaded at the midspan than when loaded away from it. This result is because a beam loaded at the midspan will be more evenly distributed over the beam's cross-section, resulting in lower stress concentrations. The relative difference in failure load is 4 % for the smallest beam and 8% for the largest beam. The relative difference in displacement between the effective span-to-depth ratio of 2.5 and 2.94 is 17 % for both plotted beams.

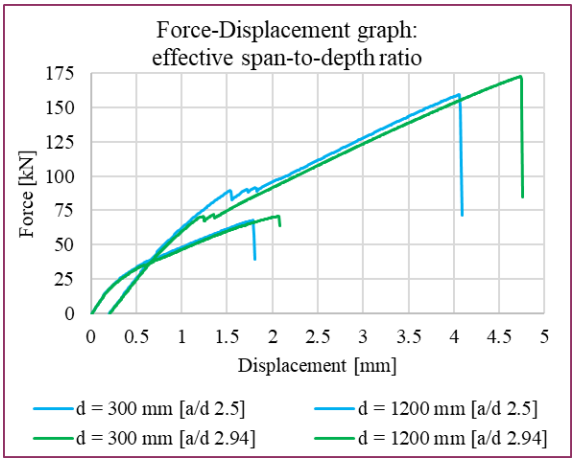

Figure 147 Effective span-to-depth ratio: force-displacement graph

Variation in concrete strength

The concrete strength is the final parameter studied for its influence on the size effect. During the numerical model sensitivity analysis and comparisons with experimental results, the range of simulated models had concrete strengths from 22MPa to 114 MPa. Over the entire range mentioned, reliable results were found with the robust numerical model. Because the results were sufficient according to the failure load percentage difference between the numerical simulations and experimental results, a wide range of concrete strengths can be applied to the analysis in this section. The

concrete strengths used for the size effect analysis are 25 Mpa, 50 Mpa, 75 Mpa, and 100 Mpa. For further analysis, the nominal shear strength for geometrically scaled beams with different concrete strengths is in Figure 148 (left).

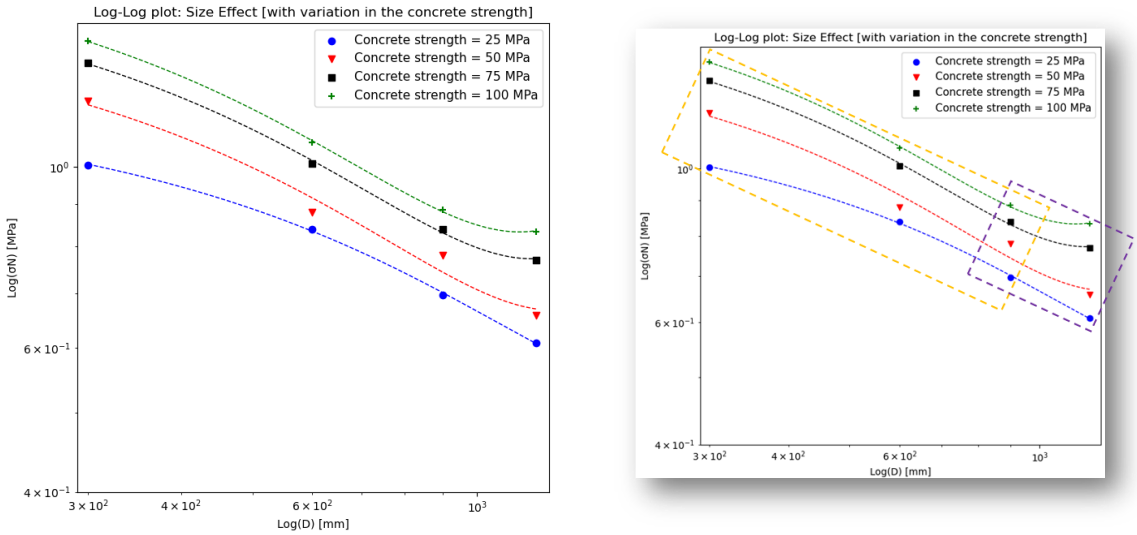

Figure 148 Size effect analysis with variation in the concrete strength

Increasing the concrete strength increases the nominal shear strength for the same beam sizes. Differences in the slopes for the different concrete strengths are also visible. The slopes become steeper consistently as the concrete strength increases for the three smallest beams (effective depth is 300 mm, 600 mm, and 900 mm). The results show an increase in the size effect as the concrete strength increases. A similar type of increase in steepness of the slope was noticed for the effective span-to-depth ratio. The increased size effect with increased concrete strength is reduced as the beam sizes increase for the three smallest beam sizes.

The beam size of 1200 mm requires a separate analysis as a different behavior is noticed here. While the beam with concrete strength seems to continue its steep slope for the nominal shear strength, this is not the case for the higher concrete strength ones. With a higher concrete strength, the large beams show an increasing material randomness sensitivity influencing the nominal shear strength. The energetic size effect dominated the previous beam configurations, but the energetic-statistical size effect is now noticed. Bažant et al. have also acknowledged this size effect as SEL type I, for which the size effect is found using a formula and asymptotic matching. The statistical size effect influence is evident for the two highest concrete strength beams. However, it can also be expected for the other LSC beams. It should be noted that for this behavior, larger beams than the ones simulated must be done. The switch from the energetic size effect to the statistical-energetic size effect can be seen in Figure 148 on the right with the orange and purple blocks. A better overview of the slope change for the nominal shear strength of all the geometrically scaled beams can be found in Table 67 from Annex VII.

The force-displacement graph results in Annex VII show an increase in failure load as the concrete strength increases. The failure load increase between the lowest and highest concrete strength is between 28 % and 42% for the different beam sizes. The increase in concrete strength affects the beam's brittleness. The more brittle the beam, the wider the cracks at failure. This relationship between concrete strength and brittleness is essential, especially with large beams. As the flexural shear failure is already brittle, it is not easy to study the brittleness of the beams. However, an experiment was done after the maximum load was reached using the displacement method. Three small and equal load steps were applied for each beam configuration with different concrete strengths applied. A more gradual decrease in force means a more brittle behavior. This experiment gave the following results:

- The beam with d = 300 mm drops 19 kN more for a concrete strength of 100 MPa compared to one with a concrete strength of 25 MPa
- The beam with d = 1200mm drops 54 kN more for a concrete strength of 100 MPa compared to one with a concrete strength of 25 MPa

The numerical simulation analysis shows that the beams with a more brittle response from increased concrete strength exhibit a more substantial size effect. The energetic-statistical size effect is also visible for large beams with HSC. The different force-displacement curves of this example are plotted in Figure 149.

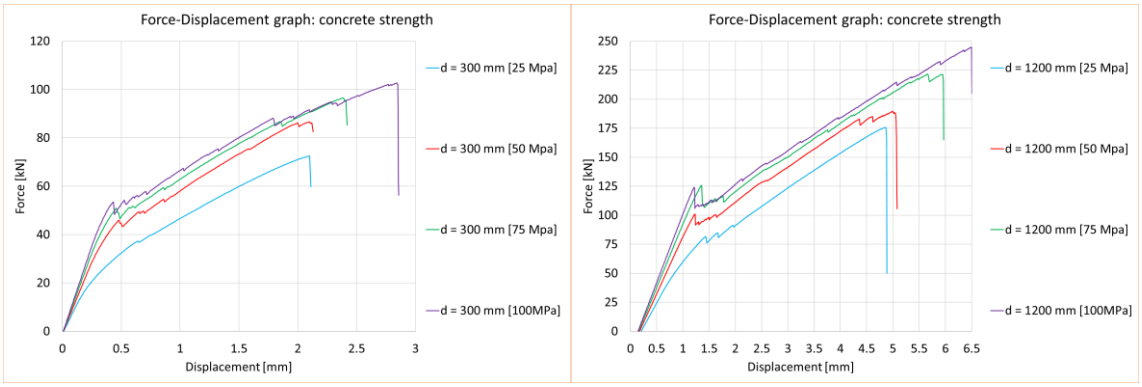

Figure 149 Concrete strength: force-displacement graph

Annex IX Python code: three-point numerical model

Example: R804A1_40

```
    setAnalysisCommandDetail( "NLFEA_NR", "Structural nonlinear 1",
"EXECUT(2)/LOAD/STEPS/EXPLIC/SIZES", steps )
    setAnalysisCommandDetail( "NLFEA_NR", "Structural nonlinear 1",
"EXECUT(2)/ITERAT/MAXITE", 100 )
    setAnalysisCommandDetail( "NLFEA_NR", "Structural nonlinear 1",
"EXECUT(2)/ITERAT/METHOD/METNAM", "NEWTON" )
    setAnalysisCommandDetail( "NLFEA_NR", "Structural nonlinear 1",
"EXECUT(2)/ITERAT/LINESE", True )
    setAnalysisCommandDetail( "NLFEA_NR", "Structural nonlinear 1",
"EXECUT(2)/ITERAT/CONTIN", False )
    setAnalysisCommandDetail( "NLFEA_NR", "Structural nonlinear 1",
"EXECUT(2)/ITERAT/CONVER/ENERGY", True )
    setAnalysisCommandDetail( "NLFEA_NR", "Structural nonlinear 1",
"EXECUT(2)/ITERAT/CONVER/ENERGY/TOLCON", 0.001 )
    setAnalysisCommandDetail( "NLFEA_NR", "Structural nonlinear 1",
"EXECUT(2)/ITERAT/CONVER/DISPLA", False )
    setAnalysisCommandDetail( "NLFEA_NR", "Structural nonlinear 1",
"EXECUT(2)/ITERAT/CONVER/ENERGY/NOCONV", "CONTIN" )
    setAnalysisCommandDetail( "NLFEA_NR", "Structural nonlinear 1",
"EXECUT(2)/ITERAT/CONVER/FORCE/NOCONV", "CONTIN" )

    # Output
    # Analysis
    setAnalysisCommandDetail( "NLFEA_NR", "Structural nonlinear 1",
"OUTPUT(1)/SELTYP", "USER" )
    addAnalysisCommandDetail( "NLFEA_NR", "Structural nonlinear 1",
"OUTPUT(1)/USER" )
    # Displacement
    addAnalysisCommandDetail("NLFEA_NR", "Structural nonlinear
1","OUTPUT(1)/USER/DISPLA(1)/TOTAL/TRANSL/GLOBAL")
    # Force
    addAnalysisCommandDetail("NLFEA_NR", "Structural nonlinear 1",
"OUTPUT(1)/USER/FORCE(1)/REACTI/TRANSL/GLOBAL")
    addAnalysisCommandDetail("NLFEA_NR", "Structural nonlinear 1",
"OUTPUT(1)/USER/FORCE(2)/EXTERN/TRANSL/GLOBAL")
    addAnalysisCommandDetail( "NLFEA_NR", "Structural nonlinear 1",
"OUTPUT(1)/USER/NODFOR(1)/TOTAL/TRANSL/GLOBAL")
    addAnalysisCommandDetail("NLFEA_NR", "Structural nonlinear
1","OUTPUT(1)/USER/NODFOR(2)/ELEMEN/TRANSL/GLOBAL")
    addAnalysisCommandDetail("NLFEA_NR", "Structural nonlinear
1","OUTPUT(1)/USER/NODFOR(3)/REINFO/TRANSL/GLOBAL")
    addAnalysisCommandDetail("NLFEA_NR", "Structural nonlinear 1",
"OUTPUT(1)/USER/ELMFOR(1)/TOTAL/TRANSL/GLOBAL")
    addAnalysisCommandDetail("NLFEA_NR", "Structural nonlinear
1","OUTPUT(1)/USER/ELMFOR(2)/ELEMEN/TRANSL/GLOBAL")
    addAnalysisCommandDetail("NLFEA_NR", "Structural nonlinear
1","OUTPUT(1)/USER/ELMFOR(3)/REINFO/TRANSL/GLOBAL")
    # Total strain
    # Overview
    addAnalysisCommandDetail("NLFEA_NR", "Structural nonlinear 1",
"OUTPUT(1)/USER/STRAIN(1)/TOTAL/GREEN/PRINCI")
    # Concrete
    addAnalysisCommandDetail("NLFEA_NR", "Structural nonlinear 1",
"OUTPUT(1)/USER/STRAIN(2)/TOTAL/GREEN/GLOBAL")
```

```
    addAnalysisCommand( "NLFEA_NR", "PHASE", "Phase" )
    setActivePhase( "NLFEA_NR", "Phase" )
    setActiveInPhase( "NLFEA_NR", "GEOMETRYSUPPORTSET", [ "Load support"
], [ "Phase" ], False )
    addAnalysisCommand( "NLFEA_NR", "NONLIN", "Structural nonlinear" )
    setAnalysisCommandDetail( "NLFEA_NR", "Structural nonlinear",
"EXECUT(1)/LOAD/LOADNR", 2 )
    setAnalysisCommandDetail( "NLFEA_NR", "Structural nonlinear",
"EXECUT(1)/ITERAT/MAXITE", 100 )
    setAnalysisCommandDetail( "NLFEA_NR", "Structural nonlinear",
"EXECUT(1)/ITERAT/METHOD/METNAM", "NEWTON" )
    setAnalysisCommandDetail( "NLFEA_NR", "Structural nonlinear",
"EXECUT(1)/ITERAT/LINESE", True )
    setAnalysisCommandDetail( "NLFEA_NR", "Structural nonlinear",
"EXECUT(1)/ITERAT/CONTIN", False )
    setAnalysisCommandDetail( "NLFEA_NR", "Structural nonlinear",
"EXECUT(1)/ITERAT/CONVER/ENERGY", True )
    setAnalysisCommandDetail( "NLFEA_NR", "Structural nonlinear",
"EXECUT(1)/ITERAT/CONVER/ENERGY/TOLCON", 0.001 )
    setAnalysisCommandDetail( "NLFEA_NR", "Structural nonlinear",
"EXECUT(1)/ITERAT/CONVER/DISPLA", False )
    setAnalysisCommandDetail( "NLFEA_NR", "Structural nonlinear",
"EXECUT(1)/ITERAT/CONVER/ENERGY/NOCONV", "CONTIN" )
    setAnalysisCommandDetail( "NLFEA_NR", "Structural nonlinear",
"EXECUT(1)/ITERAT/CONVER/FORCE/NOCONV", "CONTIN" )
    addAnalysisCommand( "NLFEA_NR", "PHASE", "Phase 1" )
    setActivePhase( "NLFEA_NR", "Phase 1" )
    addAnalysisCommand( "NLFEA_NR", "NONLIN", "Structural nonlinear 1" )
    removeAnalysisCommandDetail( "NLFEA_NR", "Structural nonlinear 1",
"EXECUT(1)" )
    setAnalysisCommandDetail( "NLFEA_NR", "Structural nonlinear 1",
"EXECUT(1)/EXETYP", "START" )
    setAnalysisCommandDetail( "NLFEA_NR", "Structural nonlinear 1",
"EXECUT(1)/ITERAT/MAXITE", 100 )
    setAnalysisCommandDetail( "NLFEA_NR", "Structural nonlinear 1",
"EXECUT(1)/ITERAT/METHOD/METNAM", "NEWTON" )
    setAnalysisCommandDetail( "NLFEA_NR", "Structural nonlinear 1",
"EXECUT(1)/ITERAT/LINESE", True )
    setAnalysisCommandDetail( "NLFEA_NR", "Structural nonlinear 1",
"EXECUT(1)/ITERAT/CONTIN", False )
    setAnalysisCommandDetail( "NLFEA_NR", "Structural nonlinear 1",
"EXECUT(1)/ITERAT/CONVER/ENERGY", True )
    setAnalysisCommandDetail( "NLFEA_NR", "Structural nonlinear 1",
"EXECUT(1)/ITERAT/CONVER/ENERGY/TOLCON", 0.001 )
    setAnalysisCommandDetail( "NLFEA_NR", "Structural nonlinear 1",
"EXECUT(1)/ITERAT/CONVER/DISPLA", False )
    setAnalysisCommandDetail( "NLFEA_NR", "Structural nonlinear 1",
"EXECUT(1)/ITERAT/CONVER/ENERGY/NOCONV", "CONTIN" )
    setAnalysisCommandDetail( "NLFEA_NR", "Structural nonlinear 1",
"EXECUT(1)/ITERAT/CONVER/FORCE/NOCONV", "CONTIN" )
    setAnalysisCommandDetail( "NLFEA_NR", "Structural nonlinear 1",
"EXECUT(2)/EXETYP", "LOAD" )
    setAnalysisCommandDetail( "NLFEA_NR", "Structural nonlinear 1",
"EXECUT(2)/LOAD/LOADNR", 1 )
```

```
addMaterial( "Interface", "INTERF", "ELASTI", [] )
setParameter( "MATERIAL", "Interface", "LINEAR/IFTYP", "LIN2D" )
setParameter( "MATERIAL", "Interface", "LINEAR/ELAS2/DSNY",
interf_normal_stiff )
setParameter( "MATERIAL", "Interface", "LINEAR/ELAS2/DSSX",
interf_shear_stiff )
addGeometry( "Interface", "LINE", "STLIIF", [] )
setParameter( "GEOMET", "Interface", "LIFMEM/THICK", beam_thickness )
imprintIntersection("Beam", "Load plate", True)
imprintIntersection("Beam", "Left support plate", True)
imprintIntersection("Beam", "Right support plate", True)
createConnection( "Interface", "INTER", "SHAPEEDGE" )
setParameter( "GEOMETRYCONNECTION", "Interface", "MODE", "AUTO" )
setParameter( "GEOMETRYCONNECTION", "Interface", "FLIP", False )
attachTo( "GEOMETRYCONNECTION", "Interface", "SOURCE", "Left support
plate", [[ ls, 0, 0 ]] )
attachTo( "GEOMETRYCONNECTION", "Interface", "SOURCE", "Beam", [[ ls, 0,
0 ]] )
attachTo( "GEOMETRYCONNECTION", "Interface", "SOURCE", "Right support
plate", [[ ls+beam_eff_length, 0, 0 ]] )
attachTo( "GEOMETRYCONNECTION", "Interface", "SOURCE", "Beam",
[[ls+beam_eff_length, 0, 0 ]] )
attachTo( "GEOMETRYCONNECTION", "Interface", "SOURCE", "Load plate", [[
ls+a, beam_height, 0 ]] )
attachTo( "GEOMETRYCONNECTION", "Interface", "SOURCE", "Beam", [[ls+a,
beam_height, 0 ]] )
setElementClassType( "GEOMETRYCONNECTION", "Interface", "STLIIF" )
assignMaterial( "Interface", "GEOMETRYCONNECTION", "Interface" )
assignGeometry( "Interface", "GEOMETRYCONNECTION", "Interface" )
resetElementData( "GEOMETRYCONNECTION", "Interface" )

#Mesh
setElementSize( [ "Beam" ], mesh_size, -1, True )
setMesherType( [ "Beam" ], "HEXQUAD" )
setMidSideNodeLocation( [ "Beam" ], "LINEAR" )
setElementSize( [ "Beam" ], mesh_size, -1, True )
setMesherType( [ "Beam" ], "HEXQUAD" )
setMidSideNodeLocation( [ "Beam" ], "LINEAR" )
setElementSize( "Reinf bottom", 1, [[ 0.5*beam_length, reinf_height, 0
]], mesh_size, 0, True )
setElementSize( "Reinf top", 1, [[ 0.5*beam_length, beam_height-
reinf_height, 0 ]], mesh_size, 0, True )
setElementSize( [ "Left support plate", "Right support plate", "Load
plate" ], mesh_size, -1, True )
setMesherType( [ "Left support plate", "Right support plate", "Load
plate" ], "HEXQUAD" )
setMidSideNodeLocation( [ "Left support plate", "Right support plate",
"Load plate" ], "LINEAR" )
generateMesh( [] )

if analysis=='on':
    # Analysis Commands
    steps="0.1("+str(displacement*10)+")"
    addAnalysis( "NLFEA_NR" )
```

```
setParameter( "MATERIAL", "Bond-slip Reinforcement",
"REBARS/PLASTI/TRESSH", "EPSSIG" )
setParameter( "MATERIAL", "Bond-slip Reinforcement",
"REBARS/PLASTI/EPSSIG", [0, 0, eps, fyk, eps_uk, ftk] )
setParameter( "MATERIAL", "Bond-slip Reinforcement", "RESLIP/DSNY",
reinf_normal_stiff)
setParameter( "MATERIAL", "Bond-slip Reinforcement", "RESLIP/DSSX",
reinf_shear_stiff)
if bond_slip=="FIB":
    setParameter( "MATERIAL", "Bond-slip Reinforcement", "RESLIP/SHFTYP",
"BONDS6")
    setParameter( "MATERIAL", "Bond-slip Reinforcement",
"RESLIP/BONDS6/SLPVAL", [thau_max, thau_f, s0, s1, s2, s3, alpha])  # max
shear stress, ultimate shear stress, s0, s1, s2, s3, alpha
elif bond_slip=="Shima":
    setParameter( "MATERIAL", "Bond-slip Reinforcement", "RESLIP/SHFTYP",
"BONDS4" )
    setParameter( "MATERIAL", "Bond-slip Reinforcement",
"RESLIP/BONDS4/SLPVAL", Ecm )
addGeometry( "Reinforcement truss", "RELINE", "REBAR", [] )
setParameter( "GEOMET", "Reinforcement truss", "REITYP", "REITRU" )
setParameter( "GEOMET", "Reinforcement truss", "REITRU/CROSSE", As )
setParameter( "GEOMET", "Reinforcement truss", "REITRU/PERIME", Cp )
addElementData( "Reinforcement truss data" )
setParameter( "DATA", "Reinforcement truss data", "./INTERF", [] )
setParameter( "DATA", "Reinforcement truss data", "INTERF", "TRUSS" )
setReinforcementAspects( [ "Reinf bottom", "Reinf top" ] )
setReinforcementType( "REINFORCEMENTSHAPE", [ "Reinf bottom", "Reinf top"
], "TRUSS_BOND_SLIP" )
assignMaterial( "Bond-slip Reinforcement", "SHAPE", [ "Reinf bottom",
"Reinf top" ] )
assignGeometry( "Reinforcement truss", "SHAPE", [ "Reinf bottom", "Reinf
top" ] )
assignElementData( "Reinforcement truss data", "SHAPE", [ "Reinf bottom",
"Reinf top" ] )
setReinforcementDiscretization( [ "Reinf bottom", "Reinf top" ],
"ELEMENT" )

#Steel plate
addMaterial( "Plates", "MCSTEL", "ISOTRO", [] )
setParameter( "MATERIAL", "Plates", "LINEAR/ELASTI/YOUNG", Es )
setParameter( "MATERIAL", "Plates", "LINEAR/ELASTI/POISON", vs )
setParameter( "MATERIAL", "Plates", "LINEAR/MASS/DENSIT", rho_s )
addGeometry( "Plates", "SHEET", "MEMBRA", [] )
setParameter( "GEOMET", "Plates", "THICK", beam_thickness )
setParameter( "GEOMET", "Plates", "LOCAXS", True )
setElementClassType( "SHAPE", [ "Left support plate", "Load plate",
"Right support plate" ], "MEMBRA" )
assignMaterial( "Plates", "SHAPE", [ "Left support plate", "Load plate",
"Right support plate" ] )
assignGeometry( "Plates", "SHAPE", [ "Left support plate", "Load plate",
"Right support plate" ] )

#Interface
```

```
assignElementData( "Concrete and plate", "SHAPE", [ "Left support plate"
] )
assignElementData( "Concrete and plate", "SHAPE", [ "Right support plate"
] )

# Concrete
addMaterial( "Concrete", "CONCR", "TSCR", [] )
setParameter( "MATERIAL", "Concrete", "LINEAR/ELASTI/YOUNG", Ecm )
setParameter( "MATERIAL", "Concrete", "LINEAR/ELASTI/POISON", vc )
setParameter( "MATERIAL", "Concrete", "LINEAR/MASS/DENSIT", rho_c )
if concrete=="rotating":
    setParameter( "MATERIAL", "Concrete", "MODTYP/TOTCRK", "ROTATE" )
elif concrete=="fixed":
    setParameter( "MATERIAL", "Concrete", "MODTYP/TOTCRK", "FIXED" )
    setParameter( "MATERIAL", "Concrete", "SHEAR/SHRCRV", "DAMAGE" )
setParameter( "MATERIAL", "Concrete", "TENSIL/TENCRV", "HORDYK" )
setParameter( "MATERIAL", "Concrete", "TENSIL/TENSTR", fctm)
setParameter( "MATERIAL", "Concrete", "TENSIL/GF1", Gfk)
setParameter( "MATERIAL", "Concrete", "TENSIL/CBSPEC", "GOVIND")
setParameter( "MATERIAL", "Concrete", "TENSIL/RESTST", tensile_residual )
setParameter( "MATERIAL", "Concrete", "TENSIL/POISRE/POIRED", "DAMAGE" )
setParameter( "MATERIAL", "Concrete", "COMPRS/COMCRV", "PARABO" )
setParameter( "MATERIAL", "Concrete", "COMPRS/COMSTR", fcm )
setParameter( "MATERIAL", "Concrete", "COMPRS/GC", Gck)
setParameter( "MATERIAL", "Concrete", "COMPRS/RESCST",
compression_residual )
setParameter( "MATERIAL", "Concrete", "COMPRS/REDUCT/REDCRV", "VC1993" )
setParameter( "MATERIAL", "Concrete", "COMPRS/REDUCT/REDMIN",
LB_lateral_cracking)
if confinement=='yes':
    setParameter( "MATERIAL", "Concrete", "COMPRS/CONFIN/CNFCRV",
"VECCHI" )
elif confinement=='no':
    setParameter( "MATERIAL", "Concrete", "COMPRS/CONFIN/CNFCRV", "NONE"
)
addGeometry( "Concrete", "SHEET", "MEMBRA", [] )
setParameter( "GEOMET", "Concrete", "THICK", beam_thickness)
setParameter( "GEOMET", "Concrete", "LOCAXS", True )
setElementClassType( "SHAPE", [ "Beam" ], "MEMBRA" )
assignMaterial( "Concrete", "SHAPE", [ "Beam" ] )
assignGeometry( "Concrete", "SHAPE", [ "Beam" ] )
assignElementData( "Concrete and plate", "SHAPE", [ "Beam" ] )

#FIB-BS Reinforcement
addMaterial( "Bond-slip Reinforcement", "REINFO", "REBOND", [] )
setParameter( "MATERIAL", "Bond-slip Reinforcement",
"REBARS/ELASTI/YOUNG", Es )
setParameter( "MATERIAL", "Bond-slip Reinforcement",
"REBARS/POISON/POISON", vs)
setParameter( "MATERIAL", "Bond-slip Reinforcement",
"REBARS/MASS/DENSIT", rho_s )
setParameter( "MATERIAL", "Bond-slip Reinforcement", "REBARS/PLATYP",
"VMISES")
```

```
createSheet( "Beam", [[ 0, 0, 0 ],[ beam_length, 0, 0 ],[ beam_length,
beam_height, 0 ],[ 0, beam_height, 0 ]] )
createLine( "Reinf bottom", [ 0, reinf_height, 0 ], [ beam_length,
reinf_height, 0 ] )
createLine( "Reinf top", [ 0, d, 0 ], [ beam_length, d , 0 ] )
createSheet( "Load plate", [[xl1, yl1, 0 ],[ xl1, yl2, 0 ], [ ls+a, yl2,
0 ],[ xl2,yl2, 0 ],[ xl2,yl1, 0 ]] )
createSheet( "Left support plate", [[xls1, ys1, 0 ],[ xls1, ys2, 0 ],[
ls, ys2, 0 ],[ xls2,ys2, 0 ],[ xls2,ys1, 0 ]] )
createSheet( "Right support plate", [[xrs1, ys1, 0 ],[ xrs1, ys2, 0 ],[
ls+beam_eff_length, ys2, 0 ],[ xrs2,ys2, 0 ],[ xrs2,ys1, 0 ]] )

#Support
addSet( "GEOMETRYSUPPORTSET", "Supports" )
createPointSupport( "Left support", "Supports" )
setParameter( "GEOMETRYSUPPORT", "Left support", "AXES", [ 1, 2 ] )
setParameter( "GEOMETRYSUPPORT", "Left support", "TRANSL", [ 1, 1, 0 ] )
setParameter( "GEOMETRYSUPPORT", "Left support", "ROTATI", [ 0, 0, 0 ] )
attach( "GEOMETRYSUPPORT", "Left support", "Left support plate", [[ ls,
ys2, 0]])
createPointSupport( "Right support", "Supports" )
setParameter( "GEOMETRYSUPPORT", "Right support", "AXES", [ 1, 2 ] )
setParameter( "GEOMETRYSUPPORT", "Right support", "TRANSL", [ 0, 1, 0 ] )
setParameter( "GEOMETRYSUPPORT", "Right support", "ROTATI", [ 0, 0, 0 ] )
attach( "GEOMETRYSUPPORT", "Right support", "Right support plate", [[
ls+beam_eff_length, ys2, 0 ]] )
addSet( "GEOMETRYSUPPORTSET", "Load support" )
createPointSupport( "Displacement method", "Load support" )
setParameter( "GEOMETRYSUPPORT", "Displacement method", "AXES", [ 1, 2 ]
)
setParameter( "GEOMETRYSUPPORT", "Displacement method", "TRANSL", [ 0, 1,
0 ] )
setParameter( "GEOMETRYSUPPORT", "Displacement method", "ROTATI", [ 0, 0,
0 ] )
attach( "GEOMETRYSUPPORT", "Displacement method", "Load plate", [[ ls+a,
beam_height+xl2, 0 ]] )

#Load
addSet( "GEOMETRYLOADSET", "Point load" )
createPointLoad( "Point load", "Point load" )
setParameter( "GEOMETRYLOAD", "Point load", "LODTYP", "DEFORM" )
setParameter( "GEOMETRYLOAD", "Point load", "DEFORM/TR/VALUE", -1 )
setParameter( "GEOMETRYLOAD", "Point load", "DEFORM/TR/DIRECT", 2 )
attach( "GEOMETRYLOAD", "Point load", "Load plate", [[ ls+a, yl2, 0 ]] )
addSet( "GEOMETRYLOADSET", "Self-weight" )
createModelLoad( "Self-weight", "Self-weight" )

#Material property
#Element data
addElementData( "Concrete and plate" )
setParameter( "DATA", "Concrete and plate", "./INTEGR", [] )
setParameter( "DATA", "Concrete and plate", "INTEGR", "HIGH" )
assignElementData( "Concrete and plate", "SHAPE", [ "Load plate" ] )
```

```
elif C50_60 == 'larger':
    fctm = 2.12*ln(1+0.1*fcm)
rho_c=2.5e-09 # Mass Density [T/mm3]
Gfk=0.073*fcm**0.18 # Tensile Fracture Energy [N/mm]
Gck=250*Gfk # Compressive Fracture Energy [N/mm]
tensile_residual = 0.001
compression_residual = 0.01

# Reinforcement
vs=0.3 # Poisson Ratio [-]
Es=200000 # Young's Modulus
rho_s=7.85e-09 # Mass Density [T/mm3]
reinf_normal_stiff=(100*Ecm/mesh_size) # Normal Stiffness of bond-slip
interface [N/mm3]
reinf_shear_stiff=0.1*reinf_normal_stiff # Tangential Stiffness of bond-
slip interface [N/mm3]
As=(0.25*bar_numbers*pi*(bar_diamater**2))+(0.25*bar_numbers2*pi*(bar_dia
mater2**2)) # Area of Reinforcement [mm2]
Cp=(bar_numbers*pi*bar_diamater)+(bar_numbers2*pi*bar_diamater2) #
Perimeter of Reinforcement [mm]
LB_lateral_cracking = 0.4 # [-]
eps = (fyk/Es) # [-]
if steel_class == "A":
    ftk = 1.05 * fyk
    eps_uk = 2.5/100
elif steel_class == "B":
    ftk = 1.08 * fyk
    eps_uk = 5/100
elif steel_class == "C":
    ftk = 1.15 * fyk
    eps_uk = 7.5/100
if rebar == "ribbed":
    thau_max = 2.5*sqrt(fck)  # Pullout test
    s0 = 0.001  # Close to zero should be chosen
    s1 = 1
    s2 = 2
    s3 = 0.7*bar_diamater # Estimation from literature
    alpha = 0.4
    thau_f = 0.4*thau_max
elif rebar == "smooth":
    thau_max = 0.1*sqrt(fcm)  # Pullout
    s0 = 0.001  # Close to zero
    s1 = 0.01
    s2 = s1
    s3 = s1
    alpha = 0.5
    thau_f = thau_max

#Interface Between Load/Support Plate and Beam
interf_normal_stiff=Ecm/mesh_size #Normal Stiffness [N/mm3]
interf_shear_stiff=0.01*interf_normal_stiff #Shear Stiffness [N/mm3]

#Layout of the Beam
rename("SHAPESET", "Shapes", "Beam elements")
```

```
# Setup
setModelAnalysisAspects(["STRUCT"])
setModelDimension("2D")
setDefaultMeshOrder("QUADRATIC")
setDefaultMesherType("HEXQUAD")
setDefaultMidSideNodeLocation("LINEAR")
showWorkingPlane(True)

# units
setUnit("LENGTH", "MM")
setUnit("MASS", "KG")
setUnit("FORCE", "N")
setUnit("TIME", "SEC")
setUnit("TEMPER", "CELSIU")
setUnit("ANGLE", "DEGREE")

#Calculations
#Geometry
#Beam and Reinforcement
beam_length= beam_eff_length+2*ls #Length of the beam [mm]
reinf_height= beam_height-d #Concrete Cover [mm]

# Mesh
if beam_height<=800:
    mesh_size=beam_height/20 # 20 elements over the beam height [mm]
elif beam_height>800:
    mesh_size=40 # a mesh size of 40 mm [mm]

#Support Plate
plate_length=2*mesh_size # Plate length [mm]
plate_Sheight=-mesh_size # End of the support plate (Y-direction)
ys1=0
ys2=plate_Sheight
xls1=ls-0.5*plate_length
xls2=ls+0.5*plate_length
xrs1=xls1+beam_eff_length
xrs2=xls2+beam_eff_length

#Load Plate
plate_Lheight=mesh_size # Height of Load Plate [mm]
xl1=ls+a-0.5*plate_length
xl2=ls+a+0.5*plate_length
yl1=beam_height
yl2=beam_height+plate_Lheight

# Concrete
vc=0.2 # Poisson Ratio [-]
fcm=0.8*fcc # Cylinder Compressive Strength [MPa]
delta_f = 8 # [MPa]
fck=fcm-delta_f # Characteristic Strength [MPa]
Ecm= (1-Ecm_reduction)*21500*(0.1*fcm)**0.33 # Young's Modulus [MPa]
if C50_60 == 'smaller_equal': # Concrete class [-]
    fctm = 0.3*fck**(2/3)
```

```
"""
User input
"""

dpf_folder_name = "R804A1_40"

# Geometry
beam_eff_length=1800 # Effective span of the beam [mm]
beam_thickness=240 # Width of the beam [mm]
beam_height=350 # Height of the beam [mm]
ls=300 # Start of the left support plate [x-direction] [mm]
a=881.25 # Shear Span of the beam [mm]
d=300 # Effective depth of the beam [mm]

# Material Properties
# Concrete
fcc = 85  # Cubic Compressive Strength [MPa]
C50_60 = 'larger'  # Ooncrete class options: smaller_equal or larger
Ecm_reduction=0.00 # Maximum allowed=0.15 [RTD guidelines]

# Reinforcement
bar_numbers=3 # Number of Rebars with first dimater [-]
bar_diamater=25 # Diameter_1 of Reinforcement [mm]
bar_numbers2=0 # Number of Rebars with second diameter [-]
bar_diamater2=0 # Diameter_2 of Reinforcement [mm]
fyk=550 # Yield Strength [MPa]
steel_class = "B"  # Options: A, B, C
rebar = "ribbed"  # Options: ribbed or smooth; smooth coded according the
FIB guidelines

# Displacement from experiments
displacement= 50 # [mm]
# Numerical model options
concrete="fixed" # Options: fixed or rotating
bond_slip="Shima"# Options: Shima or FIB
confinement='no'# Options: yes or no
analysis= 'on' # Autorun analysis: on or off
folder_location = "C:/Diana_numerical models/" # Safe_location: current
code saves to C drive ("C:/Diana_numerical models/"), change if required

# pacakage imports
from math import log as ln
from math import sqrt, pi

"""
Automated model
"""
# Pacakage imports
from math import log as ln
from math import sqrt, pi

# Create project
dpf_location = folder_location+dpf_folder_name
newProject(dpf_location, 1000, {})
    # Reinforcement
    addAnalysisCommandDetail("NLFEA_NR", "Structural nonlinear 1",
"OUTPUT(1)/USER/STRAIN(3)/TOTAL/GREEN/LOCAL")
    # Plastic strain
    # Concrete
    addAnalysisCommandDetail("NLFEA_NR", "Structural nonlinear 1",
"OUTPUT(1)/USER/STRAIN(4)/PLASTI/GREEN/GLOBAL")
    # Reinforcement
    addAnalysisCommandDetail("NLFEA_NR", "Structural nonlinear 1",
"OUTPUT(1)/USER/STRAIN(5)/PLASTI/GREEN/VONMIS")
    # Crackwidth
    addAnalysisCommandDetail("NLFEA_NR", "Structural nonlinear 1",
"OUTPUT(1)/USER/STRAIN(6)/CRKWDT/GREEN/PRINCI")
    addAnalysisCommandDetail("NLFEA_NR", "Structural nonlinear 1",
"OUTPUT(1)/USER/STRAIN(7)/CRKWDT/GREEN/GLOBAL")
    # Stress
    # Overview
    addAnalysisCommandDetail("NLFEA_NR", "Structural nonlinear 1",
"OUTPUT(1)/USER/STRESS(1)/TOTAL/CAUCHY/GLOBAL")
    # Concrete
    addAnalysisCommandDetail("NLFEA_NR", "Structural nonlinear 1",
"OUTPUT(1)/USER/STRESS(2)/TOTAL/CAUCHY/PRINCI")
    # Reinforcement
    addAnalysisCommandDetail("NLFEA_NR", "Structural nonlinear 1",
"OUTPUT(1)/USER/STRESS(3)/TOTAL/CAUCHY/LOCAL")

    # Solve
    setUnit( "FORCE", "KN")
    #runSolver( [] )
    # Save
    saveProject()
    # Export .dat and .dcf files
    dpf_location
    dpf_folder_name
    data_file=dpf_location+".dat"
    exportModel( dpf_location+".dat", 5 )
    saveAnalysisCommands( "NLFEA_NR", dpf_location+"_NLFEA_NR.dcf", 6 )
```

Annex X Python code: four-point numerical model

Example: d_350_75

```
    addAnalysisCommandDetail( "NLFEA_NR", "Structural nonlinear 1",
"OUTPUT(1)/USER" )
    # Displacement
    addAnalysisCommandDetail("NLFEA_NR", "Structural nonlinear
1","OUTPUT(1)/USER/DISPLA(1)/TOTAL/TRANSL/GLOBAL")
    # Force
    addAnalysisCommandDetail("NLFEA_NR", "Structural nonlinear 1",
"OUTPUT(1)/USER/FORCE(1)/REACTI/TRANSL/GLOBAL")
    addAnalysisCommandDetail("NLFEA_NR", "Structural nonlinear 1",
"OUTPUT(1)/USER/FORCE(2)/EXTERN/TRANSL/GLOBAL")
    addAnalysisCommandDetail( "NLFEA_NR", "Structural nonlinear 1",
"OUTPUT(1)/USER/NODFOR(1)/TOTAL/TRANSL/GLOBAL")
    addAnalysisCommandDetail("NLFEA_NR", "Structural nonlinear
1","OUTPUT(1)/USER/NODFOR(2)/ELEMEN/TRANSL/GLOBAL")
    addAnalysisCommandDetail("NLFEA_NR", "Structural nonlinear
1","OUTPUT(1)/USER/NODFOR(3)/REINFO/TRANSL/GLOBAL")
    addAnalysisCommandDetail("NLFEA_NR", "Structural nonlinear 1",
"OUTPUT(1)/USER/ELMFOR(1)/TOTAL/TRANSL/GLOBAL")
    addAnalysisCommandDetail("NLFEA_NR", "Structural nonlinear
1","OUTPUT(1)/USER/ELMFOR(2)/ELEMEN/TRANSL/GLOBAL")
    addAnalysisCommandDetail("NLFEA_NR", "Structural nonlinear
1","OUTPUT(1)/USER/ELMFOR(3)/REINFO/TRANSL/GLOBAL")
    # Total strain
    # Overview
    addAnalysisCommandDetail("NLFEA_NR", "Structural nonlinear 1",
"OUTPUT(1)/USER/STRAIN(1)/TOTAL/GREEN/PRINCI")
    # Concrete
    addAnalysisCommandDetail("NLFEA_NR", "Structural nonlinear 1",
"OUTPUT(1)/USER/STRAIN(2)/TOTAL/GREEN/GLOBAL")
    # Reinforcement
    addAnalysisCommandDetail("NLFEA_NR", "Structural nonlinear 1",
"OUTPUT(1)/USER/STRAIN(3)/TOTAL/GREEN/LOCAL")
    # Plastic strain
    # Concrete
    addAnalysisCommandDetail("NLFEA_NR", "Structural nonlinear 1",
"OUTPUT(1)/USER/STRAIN(4)/PLASTI/GREEN/GLOBAL")
    # Reinforcement
    addAnalysisCommandDetail("NLFEA_NR", "Structural nonlinear 1",
"OUTPUT(1)/USER/STRAIN(5)/PLASTI/GREEN/VONMIS")
    # Crackwidth
    addAnalysisCommandDetail("NLFEA_NR", "Structural nonlinear 1",
"OUTPUT(1)/USER/STRAIN(6)/CRKWDT/GREEN/PRINCI")
    addAnalysisCommandDetail("NLFEA_NR", "Structural nonlinear 1",
"OUTPUT(1)/USER/STRAIN(7)/CRKWDT/GREEN/GLOBAL")
    # Stress
    # Overview
    addAnalysisCommandDetail("NLFEA_NR", "Structural nonlinear 1",
"OUTPUT(1)/USER/STRESS(1)/TOTAL/CAUCHY/GLOBAL")
    # Concrete
    addAnalysisCommandDetail("NLFEA_NR", "Structural nonlinear 1",
"OUTPUT(1)/USER/STRESS(2)/TOTAL/CAUCHY/PRINCI")
    # Reinforcement
    addAnalysisCommandDetail("NLFEA_NR", "Structural nonlinear 1",
"OUTPUT(1)/USER/STRESS(3)/TOTAL/CAUCHY/LOCAL")
```

```
    setActivePhase( "NLFEA_NR", "Phase 1" )
    addAnalysisCommand( "NLFEA_NR", "NONLIN", "Structural nonlinear 1" )
    removeAnalysisCommandDetail( "NLFEA_NR", "Structural nonlinear 1",
"EXECUT(1)" )
    setAnalysisCommandDetail( "NLFEA_NR", "Structural nonlinear 1",
"EXECUT(1)/EXETYP", "START" )
    setAnalysisCommandDetail( "NLFEA_NR", "Structural nonlinear 1",
"EXECUT(1)/ITERAT/MAXITE", 100 )
    setAnalysisCommandDetail( "NLFEA_NR", "Structural nonlinear 1",
"EXECUT(1)/ITERAT/METHOD/METNAM", "NEWTON" )
    setAnalysisCommandDetail( "NLFEA_NR", "Structural nonlinear 1",
"EXECUT(1)/ITERAT/LINESE", True )
    setAnalysisCommandDetail( "NLFEA_NR", "Structural nonlinear 1",
"EXECUT(1)/ITERAT/CONTIN", False )
    setAnalysisCommandDetail( "NLFEA_NR", "Structural nonlinear 1",
"EXECUT(1)/ITERAT/CONVER/ENERGY", True )
    setAnalysisCommandDetail( "NLFEA_NR", "Structural nonlinear 1",
"EXECUT(1)/ITERAT/CONVER/ENERGY/TOLCON", 0.001 )
    setAnalysisCommandDetail( "NLFEA_NR", "Structural nonlinear 1",
"EXECUT(1)/ITERAT/CONVER/DISPLA", False )
    setAnalysisCommandDetail( "NLFEA_NR", "Structural nonlinear 1",
"EXECUT(1)/ITERAT/CONVER/ENERGY/NOCONV", "CONTIN" )
    setAnalysisCommandDetail( "NLFEA_NR", "Structural nonlinear 1",
"EXECUT(1)/ITERAT/CONVER/FORCE/NOCONV", "CONTIN" )
    setAnalysisCommandDetail( "NLFEA_NR", "Structural nonlinear 1",
"EXECUT(2)/EXETYP", "LOAD" )
    setAnalysisCommandDetail( "NLFEA_NR", "Structural nonlinear 1",
"EXECUT(2)/LOAD/LOADNR", 1 )
    setAnalysisCommandDetail( "NLFEA_NR", "Structural nonlinear 1",
"EXECUT(2)/LOAD/STEPS/EXPLIC/SIZES", steps )
    setAnalysisCommandDetail( "NLFEA_NR", "Structural nonlinear 1",
"EXECUT(2)/ITERAT/MAXITE", 100 )
    setAnalysisCommandDetail( "NLFEA_NR", "Structural nonlinear 1",
"EXECUT(2)/ITERAT/METHOD/METNAM", "NEWTON" )
    setAnalysisCommandDetail( "NLFEA_NR", "Structural nonlinear 1",
"EXECUT(2)/ITERAT/LINESE", True )
    setAnalysisCommandDetail( "NLFEA_NR", "Structural nonlinear 1",
"EXECUT(2)/ITERAT/CONTIN", False )
    setAnalysisCommandDetail( "NLFEA_NR", "Structural nonlinear 1",
"EXECUT(2)/ITERAT/CONVER/ENERGY", True )
    setAnalysisCommandDetail( "NLFEA_NR", "Structural nonlinear 1",
"EXECUT(2)/ITERAT/CONVER/ENERGY/TOLCON", 0.001 )
    setAnalysisCommandDetail( "NLFEA_NR", "Structural nonlinear 1",
"EXECUT(2)/ITERAT/CONVER/DISPLA", False )
    setAnalysisCommandDetail( "NLFEA_NR", "Structural nonlinear 1",
"EXECUT(2)/ITERAT/CONVER/ENERGY/NOCONV", "CONTIN" )
    setAnalysisCommandDetail( "NLFEA_NR", "Structural nonlinear 1",
"EXECUT(2)/ITERAT/CONVER/FORCE/NOCONV", "CONTIN" )

    # Output
    # Analysis
    setAnalysisCommandDetail( "NLFEA_NR", "Structural nonlinear 1",
"OUTPUT(1)/SELTYP", "USER" )
```

```
setElementClassType( "GEOMETRYCONNECTION", "Interface", "STLIIF" )
assignMaterial( "Interface", "GEOMETRYCONNECTION", "Interface" )
assignGeometry( "Interface", "GEOMETRYCONNECTION", "Interface" )
resetElementData( "GEOMETRYCONNECTION", "Interface" )

# Mesh
setElementSize( [ "Beam" ], mesh_size, -1, True )
setMesherType( [ "Beam" ], "HEXQUAD" )
setMidSideNodeLocation( [ "Beam" ], "LINEAR" )
setElementSize( [ "Beam" ], mesh_size, -1, True )
setMesherType( [ "Beam" ], "HEXQUAD" )
setMidSideNodeLocation( [ "Beam" ], "LINEAR" )
setElementSize( "Reinf bottom", 1, [[ 0.5*beam_length, reinf_height, 0
]], mesh_size, 0, True )
setElementSize( "Reinf top", 1, [[ 0.5*beam_length, beam_height-
reinf_height, 0 ]], mesh_size, 0, True )
setElementSize( [ "Left support plate", "Left load plate", "Right support
plate", "Right load plate" ], mesh_size, -1, True )
setMesherType( [ "Left support plate", "Left load plate", "Right support
plate", "Right load plate" ], "HEXQUAD" )
setMidSideNodeLocation( [ "Left support plate", "Left load plate", "Right
support plate", "Right load plate" ], "LINEAR" )
generateMesh( [] )

if analysis=='on':
    # Analysis Commands
    steps="0.1("+str(displacement*10)+")"
    addAnalysis( "NLFEA_NR" )
    addAnalysisCommand( "NLFEA_NR", "PHASE", "Phase" )
    setActivePhase( "NLFEA_NR", "Phase" )
    setActiveInPhase( "NLFEA_NR", "GEOMETRYSUPPORTSET", [ "Load support"
], [ "Phase" ], False )
    addAnalysisCommand( "NLFEA_NR", "NONLIN", "Structural nonlinear" )
    setAnalysisCommandDetail( "NLFEA_NR", "Structural nonlinear",
"EXECUT(1)/LOAD/LOADNR", 2 )
    setAnalysisCommandDetail( "NLFEA_NR", "Structural nonlinear",
"EXECUT(1)/ITERAT/MAXITE", 100 )
    setAnalysisCommandDetail( "NLFEA_NR", "Structural nonlinear",
"EXECUT(1)/ITERAT/METHOD/METNAM", "NEWTON" )
    setAnalysisCommandDetail( "NLFEA_NR", "Structural nonlinear",
"EXECUT(1)/ITERAT/LINESE", True )
    setAnalysisCommandDetail( "NLFEA_NR", "Structural nonlinear",
"EXECUT(1)/ITERAT/CONTIN", False )
    setAnalysisCommandDetail( "NLFEA_NR", "Structural nonlinear",
"EXECUT(1)/ITERAT/CONVER/ENERGY", True )
    setAnalysisCommandDetail( "NLFEA_NR", "Structural nonlinear",
"EXECUT(1)/ITERAT/CONVER/ENERGY/TOLCON", 0.001 )
    setAnalysisCommandDetail( "NLFEA_NR", "Structural nonlinear",
"EXECUT(1)/ITERAT/CONVER/DISPLA", False )
    setAnalysisCommandDetail( "NLFEA_NR", "Structural nonlinear",
"EXECUT(1)/ITERAT/CONVER/ENERGY/NOCONV", "CONTIN" )
    setAnalysisCommandDetail( "NLFEA_NR", "Structural nonlinear",
"EXECUT(1)/ITERAT/CONVER/FORCE/NOCONV", "CONTIN" )
    addAnalysisCommand( "NLFEA_NR", "PHASE", "Phase 1" )
```

```
assignGeometry( "Reinforcement truss", "SHAPE", [ "Reinf bottom", "Reinf
top" ] )
assignElementData( "Reinforcement truss data", "SHAPE", [ "Reinf bottom",
"Reinf top" ] )
setReinforcementDiscretization( [ "Reinf bottom", "Reinf top" ],
"ELEMENT" )

# Steel plate
addMaterial( "Plates", "MCSTEL", "ISOTRO", [] )
setParameter( "MATERIAL", "Plates", "LINEAR/ELASTI/YOUNG", Es )
setParameter( "MATERIAL", "Plates", "LINEAR/ELASTI/POISON", vs )
setParameter( "MATERIAL", "Plates", "LINEAR/MASS/DENSIT", rho_s )
addGeometry( "Plates", "SHEET", "MEMBRA", [] )
setParameter( "GEOMET", "Plates", "THICK", beam_thickness )
setParameter( "GEOMET", "Plates", "LOCAXS", True )
setElementClassType( "SHAPE", [ "Left support plate", "Left load plate",
"Right support plate", "Right load plate" ], "MEMBRA" )
assignMaterial( "Plates", "SHAPE", [ "Left support plate", "Left load
plate", "Right support plate", "Right load plate" ] )
assignGeometry( "Plates", "SHAPE", [ "Left support plate", "Left load
plate", "Right support plate", "Right load plate" ] )

# Interface
addMaterial( "Interface", "INTERF", "ELASTI", [] )
setParameter( "MATERIAL", "Interface", "LINEAR/IFTYP", "LIN2D" )
setParameter( "MATERIAL", "Interface", "LINEAR/ELAS2/DSNY",
interf_normal_stiff )
setParameter( "MATERIAL", "Interface", "LINEAR/ELAS2/DSSX",
interf_shear_stiff )
addGeometry( "Interface", "LINE", "STLIIF", [] )
setParameter( "GEOMET", "Interface", "LIFMEM/THICK", beam_thickness )
imprintIntersection("Beam", "Left load plate", True)
imprintIntersection("Beam", "Right load plate", True)
imprintIntersection("Beam", "Left support plate", True)
imprintIntersection("Beam", "Right support plate", True)
createConnection( "Interface", "INTER", "SHAPEEDGE" )
setParameter( "GEOMETRYCONNECTION", "Interface", "MODE", "AUTO" )
setParameter( "GEOMETRYCONNECTION", "Interface", "FLIP", False )
attachTo( "GEOMETRYCONNECTION", "Interface", "SOURCE", "Left support
plate", [[ ls, 0, 0 ]] )
attachTo( "GEOMETRYCONNECTION", "Interface", "SOURCE", "Beam", [[ ls, 0,
0 ]] )
attachTo( "GEOMETRYCONNECTION", "Interface", "SOURCE", "Right support
plate", [[ ls+beam_eff_length, 0, 0 ]] )
attachTo( "GEOMETRYCONNECTION", "Interface", "SOURCE", "Beam",
[[ls+beam_eff_length, 0, 0 ]] )
attachTo( "GEOMETRYCONNECTION", "Interface", "SOURCE", "Left load plate",
[[ ls+a, beam_height, 0 ]] )
attachTo( "GEOMETRYCONNECTION", "Interface", "SOURCE", "Beam", [[ls+a,
beam_height, 0 ]] )
attachTo( "GEOMETRYCONNECTION", "Interface", "SOURCE", "Right load
plate", [[ ls+a+c, beam_height, 0 ]] )
attachTo( "GEOMETRYCONNECTION", "Interface", "SOURCE", "Beam", [[ls+a+c,
beam_height, 0 ]] )
```

```
if confinement=='yes':
    setParameter( "MATERIAL", "Concrete", "COMPRS/CONFIN/CNFCRV",
"VECCHI" )
elif confinement=='no':
    setParameter( "MATERIAL", "Concrete", "COMPRS/CONFIN/CNFCRV", "NONE"
)
addGeometry( "Concrete", "SHEET", "MEMBRA", [] )
setParameter( "GEOMET", "Concrete", "THICK", beam_thickness)
setParameter( "GEOMET", "Concrete", "LOCAXS", True )
setElementClassType( "SHAPE", [ "Beam" ], "MEMBRA" )
assignMaterial( "Concrete", "SHAPE", [ "Beam" ] )
assignGeometry( "Concrete", "SHAPE", [ "Beam" ] )
assignElementData( "Concrete and plate", "SHAPE", [ "Beam" ] )

# FIB-BS Reinforcement
addMaterial( "Bond-slip Reinforcement", "REINFO", "REBOND", [] )
setParameter( "MATERIAL", "Bond-slip Reinforcement",
"REBARS/ELASTI/YOUNG", Es )
setParameter( "MATERIAL", "Bond-slip Reinforcement",
"REBARS/POISON/POISON", vs)
setParameter( "MATERIAL", "Bond-slip Reinforcement",
"REBARS/MASS/DENSIT", rho_s )
setParameter( "MATERIAL", "Bond-slip Reinforcement", "REBARS/PLATYP",
"VMISES")
setParameter( "MATERIAL", "Bond-slip Reinforcement",
"REBARS/PLASTI/TRESSH", "EPSSIG" )
setParameter( "MATERIAL", "Bond-slip Reinforcement",
"REBARS/PLASTI/EPSSIG", [0, 0, eps, fyk, eps_uk, ftk] )
setParameter( "MATERIAL", "Bond-slip Reinforcement", "RESLIP/DSNY",
reinf_normal_stiff)
setParameter( "MATERIAL", "Bond-slip Reinforcement", "RESLIP/DSSX",
reinf_shear_stiff)
if bond_slip=="FIB":
    setParameter( "MATERIAL", "Bond-slip Reinforcement", "RESLIP/SHFTYP",
"BONDS6")
    setParameter( "MATERIAL", "Bond-slip Reinforcement",
"RESLIP/BONDS6/SLPVAL", [thau_max, thau_f, s0, s1, s2, s3, alpha])
elif bond_slip=="Shima":
    setParameter( "MATERIAL", "Bond-slip Reinforcement", "RESLIP/SHFTYP",
"BONDS4" )
    setParameter( "MATERIAL", "Bond-slip Reinforcement",
"RESLIP/BONDS4/SLPVAL", Ecm )
addGeometry( "Reinforcement truss", "RELINE", "REBAR", [] )
setParameter( "GEOMET", "Reinforcement truss", "REITYP", "REITRU" )
setParameter( "GEOMET", "Reinforcement truss", "REITRU/CROSSE", As )
setParameter( "GEOMET", "Reinforcement truss", "REITRU/PERIME", Cp )
addElementData( "Reinforcement truss data" )
setParameter( "DATA", "Reinforcement truss data", "./INTERF", [] )
setParameter( "DATA", "Reinforcement truss data", "INTERF", "TRUSS" )
setReinforcementAspects( [ "Reinf bottom", "Reinf top" ] )
setReinforcementType( "REINFORCEMENTSHAPE", [ "Reinf bottom", "Reinf top"
], "TRUSS_BOND_SLIP" )
assignMaterial( "Bond-slip Reinforcement", "SHAPE", [ "Reinf bottom",
"Reinf top" ] )
```

```
setParameter( "GEOMETRYLOAD", "Left load", "DEFORM/SUPP", "Left support"
)
setParameter( "GEOMETRYLOAD", "Left load", "DEFORM/TR/VALUE", -1 )
setParameter( "GEOMETRYLOAD", "Left load", "DEFORM/TR/DIRECT", 2 )
attach( "GEOMETRYLOAD", "Left load", "Left load plate", [ [ ls+a, yl2, 0
] ] )
createPointLoad( "Right load", "Point load" )
setParameter( "GEOMETRYLOAD", "Right load", "LODTYP", "DEFORM" )
setParameter( "GEOMETRYLOAD", "Right load", "DEFORM/SUPP", "Left support"
)
setParameter( "GEOMETRYLOAD", "Right load", "DEFORM/TR/VALUE", -1 )
setParameter( "GEOMETRYLOAD", "Right load", "DEFORM/TR/DIRECT", 2 )
attach( "GEOMETRYLOAD", "Right load", "Right load plate", [ [ ls+a+c,
yl2, 0 ] ] )
addSet( "GEOMETRYLOADSET", "Self-weight" )
createModelLoad( "Self-weight", "Self-weight" )

# Material property
# Element data
addElementData( "Concrete and plate" )
setParameter( "DATA", "Concrete and plate", "./INTEGR", [] )
setParameter( "DATA", "Concrete and plate", "INTEGR", "HIGH" )
assignElementData( "Concrete and plate", "SHAPE", [ "Left load plate" ] )
assignElementData( "Concrete and plate", "SHAPE", [ "Right load plate" ]
)
assignElementData( "Concrete and plate", "SHAPE", [ "Left support plate"
] )
assignElementData( "Concrete and plate", "SHAPE", [ "Right support plate"
] )

# Concrete
addMaterial( "Concrete", "CONCR", "TSCR", [] )
setParameter( "MATERIAL", "Concrete", "LINEAR/ELASTI/YOUNG", Ecm )
setParameter( "MATERIAL", "Concrete", "LINEAR/ELASTI/POISON", vc )
setParameter( "MATERIAL", "Concrete", "LINEAR/MASS/DENSIT", rho_c )
if concrete=="rotating":
    setParameter( "MATERIAL", "Concrete", "MODTYP/TOTCRK", "ROTATE" )
elif concrete=="fixed":
    setParameter( "MATERIAL", "Concrete", "MODTYP/TOTCRK", "FIXED" )
    setParameter( "MATERIAL", "Concrete", "SHEAR/SHRCRV", "DAMAGE" )
setParameter( "MATERIAL", "Concrete", "TENSIL/TENCRV", "HORDYK" )
setParameter( "MATERIAL", "Concrete", "TENSIL/TENSTR", fctm)
setParameter( "MATERIAL", "Concrete", "TENSIL/GF1", Gfk)
setParameter( "MATERIAL", "Concrete", "TENSIL/CBSPEC", "GOVIND")
setParameter( "MATERIAL", "Concrete", "TENSIL/RESTST", tensile_residual )
setParameter( "MATERIAL", "Concrete", "TENSIL/POISRE/POIRED", "DAMAGE" )
setParameter( "MATERIAL", "Concrete", "COMPRS/COMCRV", "PARABO" )
setParameter( "MATERIAL", "Concrete", "COMPRS/COMSTR", fcm )
setParameter( "MATERIAL", "Concrete", "COMPRS/GC", Gck)
setParameter( "MATERIAL", "Concrete", "COMPRS/RESCST",
compression_residual )
setParameter( "MATERIAL", "Concrete", "COMPRS/REDUCT/REDCRV", "VC1993" )
setParameter( "MATERIAL", "Concrete", "COMPRS/REDUCT/REDMIN",
LB_lateral_cracking)
```

```
# Layout of the Beam
rename("SHAPESET", "Shapes", "Beam elements")
createSheet( "Beam", [[ 0, 0, 0 ],[ beam_length, 0, 0 ],[ beam_length,
beam_height, 0 ],[ 0, beam_height, 0 ]] )
createLine( "Reinf bottom", [ 0, reinf_height, 0 ], [ beam_length,
reinf_height, 0 ] )
createLine( "Reinf top", [ 0, d, 0 ], [ beam_length, d , 0 ] )
createSheet( "Left load plate", [[xl1, yl1, 0 ],[ xl1, yl2, 0 ], [ ls+a,
yl2, 0 ],[ xl2,yl2, 0 ],[ xl2,yl1, 0 ]] )
createSheet( "Right load plate", [[xl3, yl1, 0 ],[ xl3, yl2, 0 ], [
ls+a+c, yl2, 0 ],[ xl4,yl2, 0 ],[ xl4,yl1, 0 ]] )
createSheet( "Left support plate", [[xls1, ys1, 0 ],[ xls1, ys2, 0 ],[
ls, ys2, 0 ],[ xls2,ys2, 0 ],[ xls2,ys1, 0 ]] )
createSheet( "Right support plate", [[xrs1, ys1, 0 ],[ xrs1, ys2, 0 ],[
ls+beam_eff_length, ys2, 0 ],[ xrs2,ys2, 0 ],[ xrs2,ys1, 0 ]] )

# Support
addSet( "GEOMETRYSUPPORTSET", "Supports" )
createPointSupport( "Left support", "Supports" )
setParameter( "GEOMETRYSUPPORT", "Left support", "AXES", [ 1, 2 ] )
setParameter( "GEOMETRYSUPPORT", "Left support", "TRANSL", [ 1, 1, 0 ] )
setParameter( "GEOMETRYSUPPORT", "Left support", "ROTATI", [ 0, 0, 0 ] )
attach( "GEOMETRYSUPPORT", "Left support", "Left support plate", [[ ls,
ys2, 0]])
createPointSupport( "Right support", "Supports" )
setParameter( "GEOMETRYSUPPORT", "Right support", "AXES", [ 1, 2 ] )
setParameter( "GEOMETRYSUPPORT", "Right support", "TRANSL", [ 0, 1, 0 ] )
setParameter( "GEOMETRYSUPPORT", "Right support", "ROTATI", [ 0, 0, 0 ] )
attach( "GEOMETRYSUPPORT", "Right support", "Right support plate", [[
ls+beam_eff_length, ys2, 0 ]] )
addSet( "GEOMETRYSUPPORTSET", "Load support" )
createPointSupport( "Left displacement method", "Load support" )
setParameter( "GEOMETRYSUPPORT", "Left displacement method", "AXES", [ 1,
2 ] )
setParameter( "GEOMETRYSUPPORT", "Left displacement method", "TRANSL", [
0, 1, 0 ] )
setParameter( "GEOMETRYSUPPORT", "Left displacement method", "ROTATI", [
0, 0, 0 ] )
attach( "GEOMETRYSUPPORT", "Left displacement method", "Left load plate",
[[ ls+a, beam_height+xl2, 0 ]] )
createPointSupport( "Right displacement method", "Load support" )
setParameter( "GEOMETRYSUPPORT", "Right displacement method", "AXES", [
1, 2 ] )
setParameter( "GEOMETRYSUPPORT", "Right displacement method", "TRANSL", [
0, 1, 0 ] )
setParameter( "GEOMETRYSUPPORT", "Right displacement method", "ROTATI", [
0, 0, 0 ] )
attach( "GEOMETRYSUPPORT", "Right displacement method", "Right load
plate", [[ ls+a+c, beam_height+xl2, 0 ]] )

# Load
addSet( "GEOMETRYLOADSET", "Point load" )
createPointLoad( "Left load", "Point load" )
setParameter( "GEOMETRYLOAD", "Left load", "LODTYP", "DEFORM" )
```

```
if C50_60 == 'smaller_equal': # Concrete class [-]
    fctm = 0.3*fck**(2/3)
elif C50_60 == 'larger':
    fctm = 2.12*ln(1+0.1*fcm)
rho_c=2.5e-09 # Mass Density [T/mm3]
Gfk=0.073*fcm**0.18 # Tensile Fracture Energy [N/mm]
Gck=250*Gfk # Compressive Fracture Energy [N/mm]
tensile_residual = 0.001
compression_residual = 0.01

# Reinforcement
vs=0.3 # Poisson Ratio [-]
Es=200000 # Young's Modulus
rho_s=7.85e-09 # Mass Density [T/mm3]
reinf_normal_stiff=(100*Ecm/mesh_size) # Normal Stiffness of bond-slip
interface [N/mm3]
reinf_shear_stiff=0.1*reinf_normal_stiff # Tangential Stiffness of bond-
slip interface [N/mm3]
As=(0.25*bar_numbers*pi*(bar_diamater**2))+(0.25*bar_numbers2*pi*(bar_dia
mater2**2)) # Area of Reinforcement [mm2]
Cp=(bar_numbers*pi*bar_diamater)+(bar_numbers2*pi*bar_diamater2) #
Perimeter of Reinforcement [mm]
LB_lateral_cracking = 0.4 # [-]
eps = (fyk/Es) # [-]
if steel_class == "A":
    ftk = 1.05 * fyk
    eps_uk = 2.5/100
elif steel_class == "B":
    ftk = 1.08 * fyk
    eps_uk = 5/100
elif steel_class == "C":
    ftk = 1.15 * fyk
    eps_uk = 7.5/100
if rebar == "ribbed":
    thau_max = 2.5*sqrt(fck)  # Pullout test
    s0 = 0.001  # Close to zero should be chosen
    s1 = 1
    s2 = 2
    s3 = 0.7*bar_diamater # Estimation from literature
    alpha = 0.4
    thau_f = 0.4*thau_max
elif rebar == "smooth":
    thau_max = 0.1*sqrt(fcm)  # Pullout
    s0 = 0.001  # Close to zero
    s1 = 0.01
    s2 = s1
    s3 = s1
    alpha = 0.5
    thau_f = thau_max

# Interface Between Load/Support Plate and Beam
interf_normal_stiff=Ecm/mesh_size # Normal Stiffness [N/mm3]
interf_shear_stiff=0.01*interf_normal_stiff # Shear Stiffness [N/mm3]
```

```
setModelAnalysisAspects(["STRUCT"])
setModelDimension("2D")
setDefaultMeshOrder("QUADRATIC")
setDefaultMesherType("HEXQUAD")
setDefaultMidSideNodeLocation("LINEAR")
showWorkingPlane(True)

# Units
setUnit("LENGTH", "MM")
setUnit("MASS", "KG")
setUnit("FORCE", "N")
setUnit("TIME", "SEC")
setUnit("TEMPER", "CELSIU")
setUnit("ANGLE", "DEGREE")

# Calculations
# Geometry
# Beam and Reinforcement
beam_length= beam_eff_length+2*ls # Length of the beam [mm]
reinf_height= beam_height-d # Concrete Cover [mm]

# Mesh
if beam_height<=800:
    mesh_size=beam_height/20 # 20 elements over the beam height [mm]
elif beam_height>800:
    mesh_size=40 # a mesh size of 40 mm [mm]

# Support Plate
plate_length=2*mesh_size # Plate length [mm]
plate_Sheight=-mesh_size # End of the support plate (Y-direction)
ys1=0
ys2=plate_Sheight
xls1=ls-0.5*plate_length
xls2=ls+0.5*plate_length
xls3=ls+beam_eff_length-0.5*plate_length
xls4=ls+beam_eff_length+0.5*plate_length
xrs1=xls1+beam_eff_length
xrs2=xls2+beam_eff_length

# Load Plate
plate_Lheight=mesh_size # Height of Load Plate [mm]
xl1=ls+a-0.5*plate_length
xl2=ls+a+0.5*plate_length
xl3=ls+a+c-0.5*plate_length
xl4=ls+a+c+0.5*plate_length
yl1=beam_height
yl2=beam_height+plate_Lheight

# Concrete
vc=0.2 # Poisson Ratio [-]
fcm=0.8*fcc # Cylinder Compressive Strength [MPa]
delta_f = 8 # [MPa]
fck=fcm-delta_f # Characteristic Strength [MPa]
Ecm= (1-Ecm_reduction)*21500*(0.1*fcm)**0.33 # Young's Modulus [MPa]
```

```
"""
User input
"""

# File name
dpf_folder_name = "d_350_75"

# Geometry
beam_eff_length=1800 # Effective span of the beam [mm]
beam_thickness=240 # Width of the beam [mm]
beam_height=350 # Height of the beam [mm]
ls=300 # Start of the left support plate [x-direction] [mm]
a=881.25 # Shear Span of the beam [mm]
d=300 # Effective depth of the beam [mm]
c=37.50 # Distance between loading points of the beam [mm]

# Material Properties
# Concrete
fcc=75 # Cubic Compressive Strength [MPa]
C50_60 = 'larger'  # Ooncrete class options: smaller_equal or larger
Ecm_reduction=0.00 # Maximum allowed=0.15 [RTD guidelines]

# Reinforcement
bar_numbers=2 # Number of Rebars with first dimater [-]
bar_diamater=24 # Diameter_1 of Reinforcement [mm]
bar_numbers2=0 # Number of Rebars with second diameter [-]
bar_diamater2=0 # Diameter_2 of Reinforcement [mm]
fyk=425.75 # Yield Strength [MPa]
steel_class = "B"  # Options: A, B, C
rebar = "ribbed"  # Options: ribbed or smooth; smooth coded according the
FIB guidelines

# Displacement from experiments
displacement= 50 # [mm]
# Numerical model options
concrete="fixed" # Options: fixed or rotating
bond_slip="Shima"# Options: Shima or FIB
confinement='no'# Options: yes or no
analysis= 'on' # Autorun analysis: on or off
folder_location = "C:/Diana_numerical models/" # Safe_location: current
code saves to C drive ("C:/Diana_numerical models/"), change if required

"""
Automated model
"""
# Pacakage imports
from math import log as ln
from math import sqrt, pi

# Create project
dpf_location = folder_location+dpf_folder_name
newProject(dpf_location, 1000, {})

# Setup
```

```
# Solve
setUnit( "FORCE", "KN")
#runSolver( [] )
# Save
saveProject()
# Export .dat and .dcf files
dpf_location
dpf_folder_name
data_file=dpf_location+".dat"
exportModel( dpf_location+".dat", 5 )
saveAnalysisCommands( "NLFEA_NR", dpf_location+"_NLFEA_NR.dcf", 6 )
```